025921-30-T

TECHNICAL REPORT

for NASA Grant NAG-2-541

NASA Technical Monitor: Alex Woo

Grant Title:	Development of 3D Electromagnetic Modeling Tools for Airborne Vehicles
Report Title:	Electromagnetic Scattering by Coated Convex Surfaces and Wedges Simulated by Approximate Boundary Conditions
Institution:	Radiation Laboratory Department of Electrical Engineering and Computer Science The University of Michigan Ann Arbor MI 48109-2122
Period Covered:	Feb. 1992 – Sept. 1992
Report Authors:	H.H. Syed and J.L. Volakis
Principal Investigator:	John L. Volakis Telephone: (313) 764-0500

Electromagnetic scattering by coated convex surfaces and wedges simulated by approximate boundary conditions

H.H. Syed and J.L. Volakis*

Radiation Laboratory
Department of Electrical Engineering
and Computer Science
The University of Michigan
Ann Arbor MI 48109-2122

*The work reported here was also used as a dissertation submitted to the University of Michigan Department of Electrical Engineering and Computer Science in partial fulfillment of the requirements for the Doctor of Philosophy degree.

engm

UMR0529

ABSTRACT

ELECTROMAGNETIC SCATTERING BY COATED CONVEX SURFACES AND WEDGES SIMULATED BY APPROXIMATE BOUNDARY CONDITIONS

Asymptotic/high-frequency solutions are developed for analyzing the non- specular scattering mechanisms associated with coated convex surfaces and edges simulated by approximate boundary conditions. In particular, the standard impedance boundary conditions (SIBCs) and the second order generalized impedance boundary conditions (GIBCs) are employed for a characterization of the edge diffraction, creeping wave and surface diffracted wave contributions. To study the creeping wave and surface diffracted wave mechanisms, rigorous UTD (uniform geometrical theory of diffraction) diffraction coefficients are developed for a convex coated cylinder simulated with SIBCs and GIBCs. The ray solutions obtained remain valid in the transition region and reduce uniformly to those in the deep lit and shadow regions. A uniform asymptotic solution is also presented for observations in the close vicinity of the cylinder. The diffraction coefficients for a convex cylinder are obtained via a generalization of the corresponding ones for the circular cylinder. To validate the asymptotic/high-

frequency solution integral equations are derived for both E and H-polarization and solved numerically using the method of moments. Results are presented for a single and three layered coated convex cylinder. Some insights are also provided on the accuracy of the employed GIBCs versus SIBCs for application to curved surfaces. To characterize the scattering by impedance wedges illuminated at skew incidence, diffraction coefficients are derived from an approximate solution of the governing functional difference equations. This solution exactly recovers the known ones for an impedance half plane or an arbitrary wedge at normal incidence and to validate it for other wedge angles a moment method code was used. Finally, to test the usefulness of the approximate skew incidence impedance wedge diffraction coefficient for three dimensional structures, equivalent currents are derived in the context of PTD for a finite length impedance wedge of arbitrary internal angle. These are incorporated in a standard general purpose physical theory of diffraction (PTD) code and results are presented for a number of different impedance structures.

TABLE OF CONTENTS

LIST OF FIGURES

CHAPTER I

INTRODUCTION

The subject of this dissertation deals with the characterization of the non- specular electromagnetic scattering from coated and impedance structures in the context of asymptotic/high-frequency techniques. Nowadays, the study of both specular and non-specular electromagnetic scattering mechanisms is crucial in the design of all high performance airborne vehicles with low radar cross section (RCS). Shaping and radar absorbing materials are commonly employed to reduce the radar reflectivity of these vehicles. However, in most cases, only the specular contributions from electrically large structures can be effectively reduced by shaping. This leaves non-specular or diffraction contributions primarily caused by edges, creeping waves and surface diffracted waves, as the dominant terms. It is, therefore, important to examine the effect of radar absorbing materials in controlling non-specular scattering.

A common technique for RCS control is to use radar absorbing coatings and over the past few years much attention has been given to the electromagnetic characterization of such coatings. Methods have been developed to simulate the material coatings by approximate boundary conditions which offer several advantages in both asymptotic and numerical analyses of electromagnetic problems. For example, in the case of asymptotic/high-frequency analysis, the coating can be replaced by a single

boundary condition suitable for the application of the Wiener-Hopf technique [1,2] or some other function theoretic approach [3,11]. In numerical analysis, the replacement of the profile of the coating with a single boundary condition eliminates the need to introduce unknown polarization currents inside the coating. This, significantly, reduces the total number of unknowns and results in a more efficient solution.

The standard impedance boundary condition (SIBC) [4] has been frequently employed to simulate composite material coatings on metallic structures. However, it is well-known that the SIBC simulation is accurate only if the coating is very thin and has a high index of refraction. One of the major reasons for this is because the SIBC cannot model the polarization current components which are normal to the coating. To improve the accuracy of the SIBC simulation, higher order impedance boundary conditions were recently developed [5] and found to be capable of simulating thicker coatings with greater accuracy. These conditions involve higher order derivatives of the fields beyond the first and can be thought as a generalization to the SIBC. They are ,therefore, referred to as the generalized impedance boundary conditions (GIBC) and one of their advantages is again a simplification in the analysis.

In our study, the SIBC and second order GIBC will be used for a characterization of the edge diffraction, creeping wave and surface diffracted wave contributions. The characterizations will be carried out via asymptotic/function theoretic methods which have been traditionally used in high-frequency studies (i.e. where the scatterer is many wavelengths in size). An important advantage of the asymptotic/high-frequency techniques over numerical methods is that the scattered field from a complex structure is a priori subdivided into contributions from its different components. This gives an insight into the importance of each scattering contributor which is particularly useful for designing vehicles with given radar cross section. Among the most

popular asymptotic/high-frequency methods are the geometrical theory of diffraction (GTD) and physical theory of diffraction (PTD). The GTD/PTD formulations can permit characterizations of non- metallic geometries but require the appropriate diffraction coefficients associated with a specific discontinuity in surface curvature or material composition. These diffraction coefficients play a role similar to the reflection and transmission coefficients of the GO reflected and transmitted rays and can be determined from an exact analytical solution of a corresponding canonical geometry. Unfortunately, this has only been rigorously accomplished for a handful of geometries which primarily include metallic edges and wedges at normal and skew incidences [6]–[8], second order surface discontinuity [9,10], impedance wedges at normal incidence [11], thin dielectric and resistive edges at normal and skew incidences [12,13], impedance or material discontinuities in a plane [14,15] and the right-angled wedge at skew incidence with one of its faces perfectly conducting [16]. Solutions may be also found in the literature for creeping wave characterizations and for some non-generic configurations.

The main goal of this dissertation is to develop asymptotic/high-frequency solutions for analyzing the non-specular scattering mechanisms produced by coated convex surfaces and edges simulated by the approximate boundary conditions. Also, to validate the accuracy of these asymptotic solutions, integral equations are derived on the basis of the employed SIBCs and GIBCs. The integral equation solutions are then used for benchmarking the proposed asymptotic expressions. Some insights are also provided on the accuracy of the employed GIBCs for the subject geometries.

The organization of this dissertation is as follows. In chapter two, both the SIBCs and the GIBCs are presented for simulating a material coating on a metallic substrate. The GIBCs involve higher order derivatives having coefficients which are

determined using the exact reflection coefficient of the metal-backed coating. As an illustration, the simulation of metal-baked uniform and three layer dielectric coatings is given.

Chapter three deals with numerical solutions on the basis of a second order GIBC. The GIBCs have so far been presented for simple planar surfaces such as a uniform coating on a ground plane [5,17] and a resistive sheet [17,18]. Of practical interest, however, is the application of these conditions to multilayer and inhomogeneous coatings and layers forming arbitrarily curved surfaces. In this case, the derived GIBC for a planar coating is extended to the curved surface by postulation. The accuracy of such an extension as a function of curvature is, of course, in question and its examination for surfaces other than circular, spherical or elliptical requires a numerical solution. In chapter three, a numerical implementation of a second order GIBC, simulating the coating on a metallic cylinder of arbitrary shape, is considered. Integral equations, for both E and H- polarization, are derived and solved numerically using the method of moments. Results are presented for a single and three layered coated circular and ogival cylinder and the accuracy of the given GIBCs verses SIBCs is discussed. This numerical implementation is, also, needed to validate the asymptotic/high-frequency solutions, for a convex coated cylinder which is presented in chapter four.

In chapter four, the non-specular scattering mechanisms like creeping waves and surface diffracted waves are considered as applied to a coated convex cylinder. Rigorous UTD (uniform geometrical theory of diffraction) diffraction coefficients are presented for this geometry simulated with SIBCs and GIBCs. In particular, ray solutions are obtained which remain valid in the transition region and reduce uniformly to those in the deep lit and shadow regions. These involve new transition functions

in place of the usual Fock-type integrals, characteristic to the perfectly conducting cylinder. A uniform asymptotic solution is also presented for observations in the close vicinity of the cylinder. The diffraction coefficients for a convex cylinder are obtained via a generalization of the corresponding ones for the circular cylinder. Results are presented which validate the accuracy of the ray solutions by comparing them with those obtained from the eigenfunction solution and the numerical solution of chapter three.

Chapter five deals with a most crucial source of non-specular electromagnetic scattering, that of diffraction by an impedance wedge. A normal incidence solution for the diffraction by an impedance (SIBC) wedge having arbitrary included angle is already available [11]. On the contrary, for skew incidence, solutions have only been obtained for impedance wedges having included angles of 0 (half plane) [12,13,14,15,19], $\pi/2$ (with one face perfectly conducting) [14,15,16,20], π and $3\pi/2$ (with one face perfectly conducting) [14,15,19]. This is because enforcement of the SIBCs on the wedge faces leads to a set of four coupled functional difference equations which can only be decoupled for the special cases mentioned above. In chapter five, we present an approximate solution of the coupled difference equations by again employing Maliuzhinets' method [11]. The derived solution recovers those for an impedance wedge of arbitrary included angle at normal incidence and an impedance half plane at skew incidence. The reduction of the approximate solution to that for the right- angled wedge (the only other known exact solution) is done numerically.

In chapter six, we examine the accuracy of the approximate skew incidence dyadic diffraction coefficient (developed in chapter five) for a variety of different wedge angles. This is accomplished by comparison with numerical data obtained from a new moment method solution of the coupled set of integral equations for skew incidence

on an impedance polygonal cylinder. The solution of this coupled set of integral equations provides the surface currents which are integrated to yield the scattered field on the diffraction cone. The corresponding (first order) high-frequency solution for the far zone scattered field for the polygonal cylinder is then compared to the results from the moment method code.

The skew incidence diffraction coefficient for an impedance wedge is essential for computing the electromagnetic scattering of practical three dimensional impedance structures. To test the usefulness of the approximate skew incidence solution for such 3-D structures, equivalent currents are presented in the context of PTD for a finite length impedance wedge of arbitrary internal angle. These are derived in chapter seven and are incorporated in a standard general purpose physical theory of diffraction (PTD) code [21]. Many patterns are computed on the basis of this code which demonstrate the accuracy of the formulation for a number of different impedance structures. These include typical shapes such as plates, finite length cones and cylinders which have been partially or fully coated. The PTD implementation required a dyadic physical optics (PO) diffraction coefficient which is derived in appendix A.

CHAPTER II

SIMULATION OF COATED STRUCTURES BY APPROXIMATE BOUNDARY CONDITIONS

The use of composite materials, in the form of a uniform or non-uniform coating applied to a metallic substrate, has led to the development of methods for simulating material effects in electromagnetic scattering. A possible approach is to employ approximate boundary conditions which offer several advantages in both asymptotic and numerical analyses of electromagnetic problems. For example, in the case of asymptotic/high frequency analysis, it allows an accurate replacement of a coating or a layer with a single boundary condition amenable to a Wiener-Hopf analysis [1,2] or some other function theoretic approach [3]. In numerical analysis, the profile of a coating can be replaced by a single boundary condition on the surface of the coating. This eliminates a need for introducing unknown polarization currents within the coating and thus leading to a more efficient solution.

Traditionally, the standard impedance boundary condition (SIBC) [4] has been employed to simulate dielectric coatings on perfectly conducting objects. However, as is well known, the SIBC provides limited accuracy and is only applicable to lossy and/or high contrast coatings. One of the major reasons for this is because it cannot model the polarization current components that are normal to the dielectric layer.

The SIBC has, therefore, been found to be best suited for near normal incidence unless the coating's material properties are such that penetration within the coating is limited.

The SIBC is a first order condition in that its definition involves a single normal derivative of the component of the field normal to the modeled surface. Recently [5], however, a class of boundary conditions were proposed whose major characteristic is the inclusion of higher order derivatives (along the direction of the surface normal) of the normal field components. These were originally introduced by Kane and Karp [22], Karp and Karal [23], and Wienstein [17] to simulate surface wave effects, but have been found to be rather general in nature. In fact, they can be employed to simulate any material profile with a suitable choice of the (constant) derivative coefficients. Appropriately, they are referred to as generalized impedance boundary conditions (GIBCs) and can be written either in terms of tangential or normal derivatives provided a duality condition is satisfied [5]. Unlike the SIBCs they offer several degrees of freedom and allow an accurate prediction of the surface reflected fields at oblique incidences. This was demonstrated in [5] for the infinite planar surface formed by a uniform dielectric layer on a ground plane. It was found that the maximum coating thickness accurately simulated by a given GIBC is related to the highest order derivative included in the condition.

2.1 Standard Impedance Boundary Conditions (SIBCs)

The most common approximate boundary condition is the standard impedance boundary condition (SIBC). It allows us to solve a two media problem while solving explicitly for the fields only in one. This is achieved by relating the tangential fields along the surface which takes into account the effective material composition of the

second medium. The idea of impedance boundary conditions was first introduced by Leontovich (see [24]) and, later, Senior [25]–[27] reviewed and expounded upon the use and limitations of this principle. For the metal-backed dielectric layer shown in figure 2.1, the impedance boundary condition can be mathematically written as

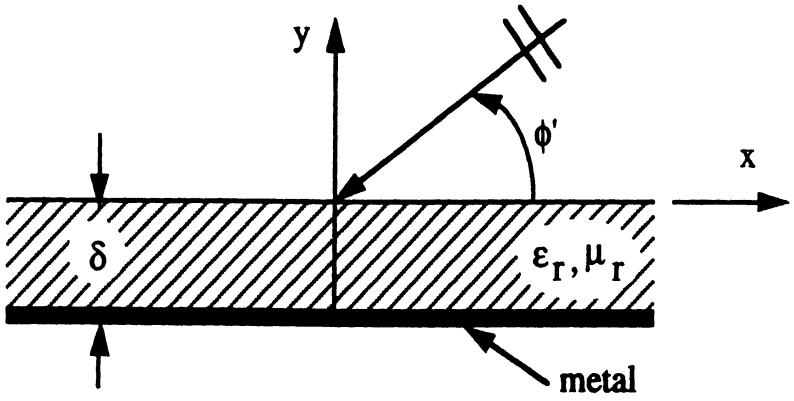

Figure 2.1: Metal-backed dielectric layer.

$$\overline{E} - (\hat{n} \cdot \overline{E})\hat{n} = \eta Z(\hat{n} \times \overline{H}) \tag{2.1}$$

where $\hat{n}$ is the normal to the surface, η is the surface impedance, Z is the free space impedance and $\overline{E}$ and $\overline{H}$ are the total electric and magnetic fields respectively. For the metal-backed layer of thickness δ in figure 2.1, η is given by (an $e^{j\omega t}$ time dependance has been assumed and suppressed throughout)

$$\eta = j\frac{N}{\epsilon_r}\tan(Nk\delta) \tag{2.2}$$

where $k = 2\pi/\lambda$ is the free space wave number, $N = \sqrt{\epsilon_r \mu_r}$ is the index of refraction whose magnitude is assumed to be large, ϵ_r and μ_r are the relative permittivity and permeability of the layer, respectively. Senior [26,27] has shown that a dual relationship exists for (2.1) where $Z\overline{H} \rightarrow -\overline{E}/Z$, $\overline{E} \rightarrow \overline{H}$ and $\eta \rightarrow \frac{1}{\eta}$ giving

$$\overline{H} - (\hat{n} \cdot \overline{H})\hat{n} = -\frac{1}{\eta Z}(\hat{n} \times \overline{E}) \tag{2.3}$$

The vector form of the SIBCs given in (2.1) and (2.3) can also be applied to curved surfaces. However, it is required that the penetration depth of the electromagnetic field must be small compared with the minimum thickness and minimum radius of curvature ρ_g of the body, and the local wavelength in the material must also be small compared with ρ_g. These conditions can be summarized as [27]

$$|ImN|k\rho_g \gg 1 \tag{2.4}$$

It is to be noted that SIBCs support both electric and magnetic surface currents $\overline{J}$ and $\overline{M}$, respectively, where

$$\overline{J} = \hat{n} \times \overline{H}, \qquad \overline{M} = -\hat{n} \times \overline{E} \tag{2.5}$$

and the use of (2.1) yields the relationship between the two currents as

$$\overline{M} = -\eta Z \hat{n} \times \overline{J} \tag{2.6}$$

2.2 Generalized Impedance Boundary Conditions (GIBCs)

2.2.1 Single Layer Coating

Consider the planar single-layer coating shown in figure 2.1. An appropriate boundary condition that simulates the coated structure takes the form [5,23]

$$\sum_{m=0}^{M} \frac{a_m}{(-jk)^m} \frac{\partial^m}{\partial y^m} E_y = 0 \tag{2.7a}$$

$$\sum_{m=0}^{M} \frac{a'_m}{(-jk)^m} \frac{\partial^m}{\partial y^m} H_y = 0 \tag{2.7b}$$

where the constants a_m and a'_m are specific to the material and geometrical properties of the simulated structure and must be derived to allow an accurate reproduction of the field in the region $y > 0$.

Expressions given in (2.7) are scalar forms of a class of GIBCs. Because, however, they involve normal derivatives, they are not convenient to implement numerically neither do they provide a physical meaning of what they represent. It is, therefore, important to express (2.7) in terms of tangential derivatives. As shown in [5], this can be accomplished provided a_m and a'_m are not chosen independently. For example, when $M = 1$, (2.7a) and (2.7b) can be reduced to (2.1) and (2.3), respectively, where we identify $\eta = a_0/a_1 = a'_1/a'_0$ as the surface impedance. For $M = 2$, (2.7) becomes

$$\begin{aligned} \frac{\partial^2 E_y}{\partial y^2} - \frac{a_1}{jka_2}\frac{\partial E_y}{\partial y} - \frac{a_0}{k^2 a_2}E_y &= 0 \\ \frac{\partial^2 H_y}{\partial y^2} - \frac{a'_1}{jka'_2}\frac{\partial H_y}{\partial y} - \frac{a'_0}{k^2 a'_2}H_y &= 0 \end{aligned} \tag{2.8}$$

which can also be written in terms of tangential derivatives and, thus, exposing their non-local character. From [5] we have that (2.8) are equivalent to

$$\hat{y} \times \left(\hat{y} \times \left[\overline{E} - \frac{a_2}{jka_1} \nabla \left(\hat{y} \cdot \overline{E} \right) \right] \right) = -\frac{a_2 + a_0}{a_1} Z \hat{y} \times \left[\overline{H} - \frac{a'_2}{jka'_1} \nabla \left(\hat{y} \cdot \overline{H} \right) \right] \tag{2.9}$$

provided the duality condition

$$\frac{a'_1}{a'_2 + a'_0} = \frac{a_2 + a_0}{a_1} \tag{2.10}$$

is satisfied.

The vector form of the boundary conditions (2.9) allows us to write it in a coordinate-free form, thus, making it applicable to non-planar surfaces. Referring to figure 2.1, (2.9) may be rewritten as

$$\hat{n} \times \left(\hat{n} \times \left[\overline{E} - \frac{a_2}{jka_1} \nabla \left(\hat{n} \cdot \overline{E} \right) \right] \right) = -\frac{a_2 + a_0}{a_1} Z \hat{n} \times \left[\overline{H} - \frac{a'_2}{jka'_1} \nabla \left(\hat{n} \cdot \overline{H} \right) \right] \tag{2.11}$$

where $\hat{n}$ denotes the unit normal to the surface at the point of application.

There are a number of methods that can be employed for deriving the constant coefficients a_m and a'_m. One approach is to expand the plane wave reflection coefficient in a suitable form leading to the identification of the constants. A second method is a generalization of that employed in [1], where the boundary condition at $y = 0$ is derived by transferring the fields from the ground plane to $y = 0$ via a Taylor series expansion. Below we derive a second order GIBC by using the first of the methods mentioned above.

Consider the plane wave

$$H_z^i = e^{jk(x\cos\phi' + y\sin\phi')} \tag{2.12}$$

incident on the surface $y = 0$, shown in figure 2.1, satisfying the GIBC given in (2.7). The implied reflection coefficient is then

$$R(\phi') = -\frac{\sum_{m=0}^{M}(-1)^m a_m \sin^m\phi'}{\sum_{m=0}^{M} a_m \sin^m\phi'} \tag{2.13}$$

with an analogous expression for the reflection coefficient associated with E_z-incidence. We are interested in finding the constants a_m when the GIBC simulates the single layer coating shown in figure 2.1. This can be accomplished by expanding the exact reflection coefficient corresponding to the given coating in a form comparable to (2.13) and thus allowing identification of the constants a_m. For an H-polarized plane wave incidence, the exact reflection coefficient can be written as

$$R_h(\phi') = -\frac{\sqrt{N^2-\cos^2\phi'}\tan\left(k\delta\sqrt{N^2-\cos^2\phi'}\right) + j\epsilon_r\sin\phi'}{\sqrt{N^2-\cos^2\phi'}\tan\left(k\delta\sqrt{N^2-\cos^2\phi'}\right) - j\epsilon_r\sin\phi'} \tag{2.14}$$

The corresponding reflection coefficient for E-polarization is

$$R_e(\phi') = -\frac{\sqrt{N^2-\cos^2\phi'} - j\mu_r\sin\phi'\tan\left(k\delta\sqrt{N^2-\cos^2\phi'}\right)}{\sqrt{N^2-\cos^2\phi'} + j\mu_r\sin\phi'\tan\left(k\delta\sqrt{N^2-\cos^2\phi'}\right)} \tag{2.15}$$

where $R_h(\phi')$ and $R_e(\phi')$ are both referred to $y = 0^+$.

2.2.1.1 Low Contrast GIBCs

The low contrast conditions can be derived by introducing the approximation $\tan x \approx x$ in (2.14) for $|N|$ small [28], giving

$$R_h(\phi') \approx -\frac{k\delta \sin^2 \phi' + j\epsilon_r \sin^2 \phi' + k\delta(N^2-1)}{k\delta \sin^2 \phi' - j\epsilon_r \sin^2 \phi' + k\delta(N^2-1)} \tag{2.16}$$

from which the constants a_m are easily found to be

$$a_o = \frac{(N^2-1)k\delta}{\epsilon_r} \tag{2.17a}$$

$$a_1 = -j \tag{2.17b}$$

$$a_2 = \frac{k\delta}{\epsilon_r} \tag{2.17c}$$

Following a similar procedure, we may also derive the constants a'_m corresponding to E_z-incidence. We have

$$a'_o = 1 \tag{2.18a}$$

$$a'_1 = jk\mu_r\delta \tag{2.18b}$$

$$a'_2 \approx 0 \tag{2.18c}$$

2.2.1.2 High Contrast GIBCs

The high contrast conditions assume $|N|$ to be large and, therefore, using the approximations

$$\sqrt{N^2 - \cos^2 \phi'} \approx N - \frac{1}{2N} + \frac{\sin^2 \phi'}{2N} \tag{2.19}$$

$$\tan\left(\frac{k\delta}{2N}\sin^2\phi'\right) \approx \frac{k\delta}{2N}\sin^2\phi' \tag{2.20}$$

in (2.14) leads to the constants

$$a_o = \left(N - \frac{1}{2N}\right)\left[\tan(k\delta N) - \tan\left(\frac{k\delta}{2N}\right)\right] \tag{2.21a}$$

$$a_1 = -j\epsilon_r\left[1 + \tan(k\delta N)\tan\left(\frac{k\delta}{2N}\right)\right] \tag{2.21b}$$

$$\begin{aligned} a_2 = \frac{1}{2N}\Bigg[&\tan(k\delta N) - \tan\left(\frac{k\delta}{2N}\right) + k\delta\left(N - \frac{1}{2N}\right) \\ &\cdot\left\{1 + \tan(k\delta N)\tan\left(\frac{k\delta}{2N}\right)\right\}\Bigg] \end{aligned} \tag{2.21c}$$

$$a_o' = \left(N - \frac{1}{2N}\right)\left[1 + \tan(k\delta N)\tan\left(\frac{k\delta}{2N}\right)\right] \tag{2.22a}$$

$$a_1' = j\mu_r\left[\tan(k\delta N) - \tan\left(\frac{k\delta}{2N}\right)\right] \tag{2.22b}$$

$$\begin{aligned} a_2' = \frac{1}{2N}\Bigg[&1 + \tan(k\delta N)\tan\left(\frac{k\delta}{2N}\right) - k\delta\left(N - \frac{1}{2N}\right) \\ &\cdot\left\{\tan(k\delta N) - \tan\left(\frac{k\delta}{2N}\right)\right\}\Bigg] \end{aligned} \tag{2.22c}$$

In the above, the boundary conditions implied by (2.17)–(2.22) are referred to the surface $y = 0^+$.

2.2.2 Three Layer Coating

The simulation of multilayer coatings is of more practical interest and in this section we consider the derivation of GIBCs applicable to a three layer coating with

arbitrary constitutive parameters. The geometry of the coating is illustrated in figure 2.2. For H-polarization the exact reflection coefficient referenced to $y = 0$ can be written as

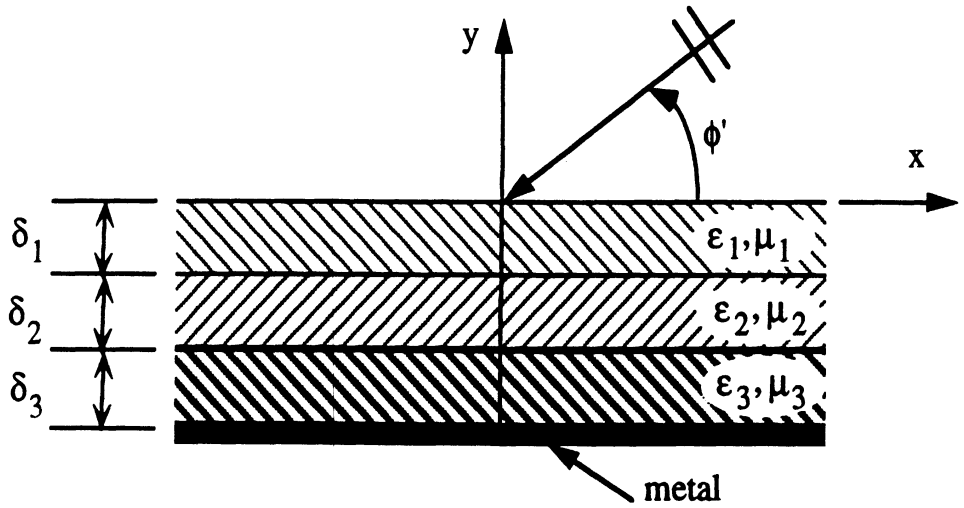

Figure 2.2: Illustration of a three-layer metal-backed coating.

$$R_h(\phi') = \frac{F_N(\phi')}{F_D(\phi')} \tag{2.23}$$

where

$$\begin{aligned} F_{N,D}(\phi') \;=\; & \epsilon_1\epsilon_2\epsilon_3 k_{y0}k_{y1}k_{y2}\cos(k_{y3}\delta_3)\cos(k_{y2}\delta_2)\cos(k_{y1}\delta_1) \\ & - \epsilon_1^2\epsilon_3 k_{y0}k_{y2}^2\cos(k_{y3}\delta_3)\sin(k_{y2}\delta_2)\sin(k_{y1}\delta_1) \\ & - \epsilon_1\epsilon_2^2 k_{y0}k_{y1}k_{y3}\sin(k_{y3}\delta_3)\sin(k_{y2}\delta_2)\cos(k_{y1}\delta_1) \\ & - \epsilon_1^2\epsilon_2 k_{y0}k_{y2}k_{y3}\sin(k_{y3}\delta_3)\cos(k_{y2}\delta_2)\sin(k_{y1}\delta_1) \end{aligned}$$

$$\mp j\epsilon_2\epsilon_3 k_{y1}^2 k_{y2}\cos(k_{y3}\delta_3)\cos(k_{y2}\delta_2)\sin(k_{y1}\delta_1)$$

$$\mp j\epsilon_1\epsilon_3 k_{y1} k_{y2}^2\cos(k_{y3}\delta_3)\sin(k_{y2}\delta_2)\cos(k_{y1}\delta_1)$$

$$\pm j\epsilon_2^2 k_{y1}^2 k_{y3}\sin(k_{y3}\delta_3)\sin(k_{y2}\delta_2)\sin(k_{y1}\delta_1)$$

$$\mp j\epsilon_1\epsilon_2 k_{y1} k_{y2} k_{y3}\sin(k_{y3}\delta_3)\cos(k_{y2}\delta_2)\cos(k_{y1}\delta_1) \qquad (2.24)$$

with

$$k_{yn} = k\sqrt{N_n^2 - \cos^2\phi'} \qquad (2.25)$$

$N_n = \sqrt{\epsilon_n\mu_n}$ and $k_{y0} = k\sin\phi'$.

2.2.2.1 Low Contrast GIBCs

To put (2.23) in a form compatible with (2.13) we must now expand the terms $\sin(k_{yn}\delta_n)$ and $\cos(k_{yn}\delta_n)$ in powers of $\sin\phi'$. The simplest case is to assume that $k_{yn}\delta_n$ is sufficiently small allowing us to set

$$\sin(k_{yn}\delta_n) \approx k_{yn}\delta_n \qquad (2.26)$$

and

$$\cos(k_{yn}\delta_n) \approx 1 \qquad (2.27)$$

Clearly (2.26)–(2.27) also implies that $N_n\delta_n$ must be small and thus the resulting boundary conditions will be valid for low contrast and thin coatings.

Substituting (2.26)–(2.27) into (2.23) and retaining only terms up to and including $O(\delta_n)$ we obtain

$$a_0 = \frac{(N_1^2 - 1)\,k\delta_1}{\epsilon_1} + \frac{(N_2^2 - 1)\,k\delta_2}{\epsilon_2} + \frac{(N_3^2 - 1)\,k\delta_3}{\epsilon_3} \qquad (2.28a)$$

$$a_1 = -j \tag{2.28b}$$

$$a_2 = k\left(\frac{\delta_1}{\epsilon_1} + \frac{\delta_2}{\epsilon_2} + \frac{\delta_3}{\epsilon_3}\right) \tag{2.28c}$$

When these are subsequently introduced into (2.9) or (2.11) we have a second order (low contrast) GIBC for simulating a thin three-layer coating. The generalization of (2.28) to any arbitrary number of layers is obvious provided the total coating thickness remains small.

Following a similar procedure we may also derive the constants a'_m corresponding to E_z-incidence. We have

$$a'_0 = 1 \tag{2.29a}$$

$$a'_1 = jk(\mu_1\delta_1 + \mu_2\delta_2 + \mu_3\delta_3) \tag{2.29b}$$

$$a'_2 = 0 \tag{2.29c}$$

These imply a first order condition, but by retaining higher order terms in the expansion we find that

$$a'_0 = \mu_1\mu_2 - \alpha_1\left(N_1^2 - 1\right) - \alpha_2\left(N_2^2 - 1\right) \tag{2.30a}$$

$$a'_1 = jk\mu_1\mu_2\left(\mu_1\delta_1 + \mu_2\delta_2 + \mu_3\delta_3\right) \tag{2.30b}$$

$$a'_2 = -(\alpha_1 + \alpha_2) \tag{2.30c}$$

in which

$$\alpha_1 = k^2\mu_1\mu_3\delta_2\left[-j\mu_1 k\delta_1\delta_3 + \delta_3\right]$$

and

$$\alpha_2 = k^2 \mu_2 \delta_1 \left[\mu_2 \delta_2 + \mu_3 \delta_3 \right]$$

2.2.2.2 High Contrast GIBCs

For large N_n, the approximations (2.26)–(2.27) are not valid. In this case it is more appropriate to set

$$k_n = k\sqrt{N_n^2 - \cos^2\phi'} \approx k\left(N_n - \frac{1}{2N_n} + \frac{\sin^2\phi'}{2N_n}\right) \tag{2.31}$$

and expand the resulting sine and cosine terms appearing in (2.24). This, however, leads to a 12th order GIBC that is obviously impractical to employ analytically and numerically. Instead, a more reasonable approach is to assume that the three layers comprising the coating have varying refractive indices. In practice, the top layer usually has a small refractive index whereas the bottom layer has a larger refractive index. With this assumption we set

$$\sin(k_{y1}\delta_1) \approx k_{y1}\delta_1 \tag{2.32}$$

$$\cos(k_{y1}\delta_1) \approx 1 \tag{2.33}$$

$$k_{y2} = k\sqrt{N_2^2 - \cos^2\phi'} \approx k\left(N_2 - \frac{1}{2N_2} + \frac{sin^2\phi'}{2N_2}\right) \tag{2.34}$$

$$\sin\left(\frac{k\delta_2}{2N_2}\sin^2\phi'\right) \approx \frac{k\delta_2}{2N_2}\sin^2\phi' \tag{2.35}$$

$$\cos\left(\frac{k\delta_2}{2N_2}\sin^2\phi'\right) \approx 1 \tag{2.36}$$

and

$$k_{y3} = k\sqrt{N_3^2 - \cos^2\phi'} \approx kN_3 \tag{2.37}$$

Employing (2.32)–(2.37) into (2.23), after much tedious algebra we find that a sixth order GIBC is required [28] to recover the resulting reflection coefficient. This can be truncated to a second order GIBC with the pertinent constants for H-polarization given by

$$\begin{aligned} a_0 = & -j\epsilon_2\epsilon_3\left(N_1^2-1\right)\left(N_2-\frac{1}{2N_2}\right)k\delta_1 \\ & - j\epsilon_1\epsilon_3\left(N_2^2-1\right)\tan\left[\left(N_2-\frac{1}{2N_2}\right)k\delta_2\right] \\ & + j\epsilon_2^2\left(N_1^2-1\right)N_3k\delta_1\tan\left[\left(N_2-\frac{1}{2N_2}\right)k\delta_2\right]\tan(N_3k\delta_3) \\ & - j\epsilon_1\epsilon_2\left(N_2-\frac{1}{2N_2}\right)N_3\tan(N_3k\delta_3) \end{aligned} \tag{2.38a}$$

$$\begin{aligned} a_1 = & -\epsilon_1\epsilon_2\epsilon_3\left(N_2-\frac{1}{2N_2}\right) \\ & + \epsilon_1^2\epsilon_3\left(N_2^2-1\right)k\delta_1\tan\left[\left(N_2-\frac{1}{2N_2}\right)k\delta_2\right] \\ & + \epsilon_1\epsilon_2^2N_3\tan\left[\left(N_2-\frac{1}{2N_2}\right)k\delta_2\right]\tan(N_3k\delta_3) \\ & + \epsilon_1^2\epsilon_2\left(N_2-\frac{1}{2N_2}\right)N_3k\delta_1\tan(N_3k\delta_3) \end{aligned} \tag{2.38b}$$

$$a_2 = j\epsilon_2\epsilon_3(N_1^2-1)\left(N_2-\frac{1}{2N_2}\right)k\delta_1\frac{k\delta_2}{2N_2}\tan\left[\left(N_2-\frac{1}{2N_2}\right)k\delta_2\right]$$

$$-\ j\epsilon_2\epsilon_3\left(N_2-\frac{1}{2N_2}\right)k\delta_1 - j\epsilon_2\epsilon_3(N_1^2-1)\frac{1}{2N_2}k\delta_1$$

$$-\ j\epsilon_1\epsilon_3\left(N_2^2-1\right)\frac{k\delta_2}{2N_2} - j\epsilon_1\epsilon_3\tan\left[\left(N_2-\frac{1}{2N_2}\right)k\delta_2\right]$$

$$+\ j\epsilon_2^2\left(N_1^2-1\right)N_3k\delta_1\frac{k\delta_2}{2N_2}\tan(N_3k\delta_3)$$

$$+\ j\epsilon_2^2N_3k\delta_1\tan\left[\left(N_2-\frac{1}{2N_2}\right)k\delta_2\right]\tan(N_3k\delta_3)$$

$$+\ j\epsilon_1\epsilon_2\left(N_2-\frac{1}{2N_2}\right)N_3\frac{k\delta_2}{2N_2}\tan\left[\left(N_2-\frac{1}{2N_2}\right)k\delta_2\right]\tan(N_3k\delta_3)$$

$$-\ j\epsilon_1\epsilon_2\frac{1}{2N_2}N_3\tan(N_3k\delta_3) \qquad (2.38c)$$

Similarly, for E-polarization, we find

$$a_0' = \mu_2\mu_3\left(N_1^2-1\right)\left(N_2-\frac{1}{2N_2}\right)k\delta_1\tan(N_3k\delta_3)$$

$$+\ \mu_1\mu_3\left(N_2^2-1\right)\tan\left[\left(N_2-\frac{1}{2N_2}\right)k\delta_2\right]\tan(N_3k\delta_3)$$

$$+\ \mu_2^2(N_1^2-1)N_3k\delta_1\tan\left[\left(N_2-\frac{1}{2N_2}\right)k\delta_2\right]$$

$$-\ \mu_1\mu_2\left[\left(N_2-\frac{1}{2N_2}\right)N_3\right] \qquad (2.39a)$$

$$a_1' = -j\mu_1\mu_2\mu_3\left(N_2 - \frac{1}{2N_2}\right)\tan(N_3 k\delta_3)$$

$$+\ j\mu_1^2\mu_3\left(N_2^2-1\right)k\delta_1\tan\left[\left(N_2-\frac{1}{2N_2}\right)k\delta_2\right]\tan(N_3k\delta_3)$$

$$-\ j\mu_1\mu_2^2N_3\tan\left[\left(N_2-\frac{1}{2N_2}\right)k\delta_2\right]$$

$$-\ j\mu_1^2\mu_2\left(N_2-\frac{1}{2N_2}\right)N_3k\delta_1 \qquad (2.39b)$$

$$a_2' = \mu_2\mu_3\left(N_1^2-1\right)\frac{1}{2N_2}k\delta_1\tan(N_3k\delta_3)$$

$$+\ \mu_2\mu_3\left(N_2-\frac{1}{2N_2}\right)\delta_1\tan(N_3k\delta_3)$$

$$-\ \mu_2\mu_3\left(N_1^2-1\right)\left(N_2-\frac{1}{2N_2}\right)k\delta_1\frac{k\delta_2}{2N_2}\tan\left[\left(N_2-\frac{1}{2N_2}\right)k\delta_2\right]\tan(N_3k\delta_3)$$

$$+\ \mu_1\mu_3\tan\left[\left(N_2-\frac{1}{2N_2}\right)k\delta_2\right]\tan(N_3k\delta_3)$$

$$+\ \mu_1\mu_3(N_2^2-1)\frac{k\delta_2}{2N_2}\tan(N_3k\delta_3)$$

$$+\ \mu_2^2N_3k\delta_1\tan\left[\left(N_2-\frac{1}{2N_2}\right)k\delta_2\right]+\mu_2^2(N_2^2-1)N_3k\delta_1\frac{k\delta_2}{2N_2}$$

$$-\ \mu_1\mu_2\frac{1}{2N_2}N_3+\mu_1\mu_2\left(N_2-\frac{1}{2N_2}\right)N_3\frac{k\delta_2}{2N_2}\tan\left[\left(N_2-\frac{1}{2N_2}\right)k\delta_2\right] \qquad (2.39c)$$

CHAPTER III

NUMERICAL IMPLEMENTATION OF GIBC

In this chapter, we pursue a numerical implementation of the boundary conditions (2.11) in a manner similar to that employed in conjunction with the standard impedance boundary conditions (2.1)–(2.3) [29,30,31]. Of interest in this implementation is an examination of the accuracy of the second order GIBCs over that of the SIBCs in simulating a dielectric coating over a metallic structure. So far, GIBCs have been generated for simple planar surfaces such as a uniform coating on a ground plane [5,17] and a resistive sheet [17,18]. Of practical interest, however, is the application of these conditions to multilayer and inhomogeneous coatings and layers forming arbitrarily curved surfaces. In this case, the GIBC as derived from the corresponding planar structure/surface is extended to the curved surface by postulation. The accuracy of such an extension as a function of curvature is, of course, in question and its examination for surfaces other than circular or elliptical requires a numerical solution. For a closed surface, the GIBCs equivalently replace the entire effect of the coating, thus, eliminating a need to introduce polarization currents within the dielectric. This is an important advantage of the GIBCs leading to a simpler formulation and a reduction of unknowns in the numerical implementation.

3.1 Integral Equation Formulation

3.1.1 H_z-incidence

Consider the plane wave

$$H_z^i = e^{jk(x\cos\phi' + y\sin\phi')} \tag{3.1}$$

incident upon a three-layer coated cylinder of arbitrary cross section as shown in figure 3.1. For a two dimensional curved surface having large radius of curvature, the GIBC given in (2.11) simplifies to

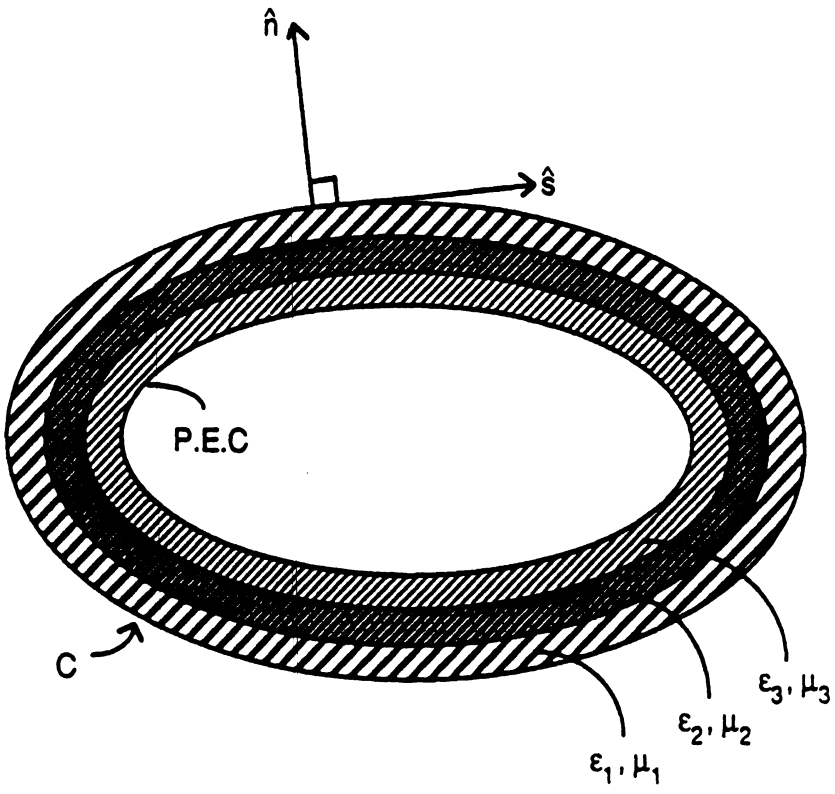

Figure 3.1: Illustration of a three-layer coated cylinder.

$$E_s = \frac{a_0 + a_2}{a_1} Z H_z + \frac{Z a_2}{k^2 a_1} \frac{\partial^2}{\partial s^2} H_z \tag{3.2}$$

where we have also employed the relation

$$E_n = \frac{jZ}{k}\frac{\partial H_z}{\partial s} \tag{3.3}$$

We note that (3.2) is identical to that implied by (2.9) if we let $E_x \rightarrow E_s$, $E_y \rightarrow E_n$ and $\partial/\partial x \rightarrow \partial/\partial s$.

To compute the scattered field by the configuration in figure 3.1, a traditional approach is to introduce the electric and magnetic surface equivalent currents (see figure 3.2)

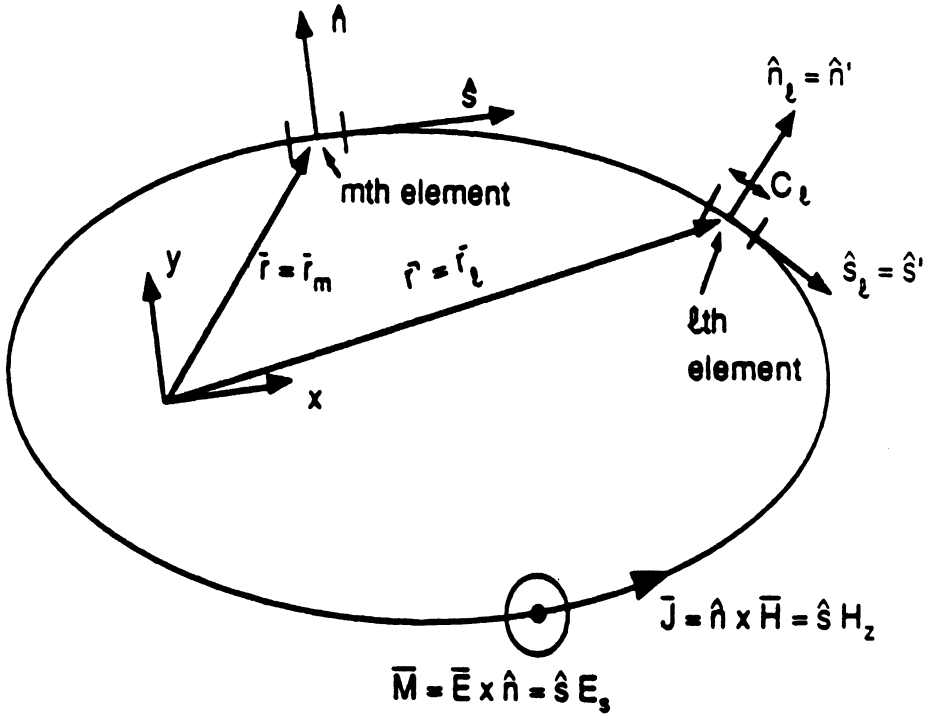

Figure 3.2: Equivalent current model and illustration of the discretization parameters.

$$\overline{J} = \hat{n} \times \overline{H} = \hat{s} H_z = \hat{s} J_s \tag{3.4}$$

$$\overline{M} \;=\; \overline{E} \times \hat{n} = \hat{z} E_s = \hat{z} M_z \tag{3.5}$$

on the outer surface of the coating where $\overline{E}$ and $\overline{H}$ denote the total fields on C. From (3.2) and (3.4)–(3.5) we then find

$$M_z(\overline{r}) = \left[\frac{a_0 + a_2}{a_1} + \frac{a_2}{k^2 a_1} \frac{\partial^2}{\partial s^2} \right] Z \, J_s(\overline{r}), \quad \overline{r} \in C \tag{3.6}$$

Enforcement of the GIBC, thus, eliminates one of the unknown current components. In the case of a first order GIBC (SIBC) the relationship between M_z and J_s is linear as implied by (2.6). The appearance of the second derivative in (3.6) is therefore attributed to the higher order condition and provides an added accuracy in the simulation of the coating.

To construct an integral equation for the surface current J_s, we now enforce the condition

$$H_z = J_s = H_z^i + H_z^s \tag{3.7}$$

on C where

$$H_z^s = -\frac{Yk}{4} \int_C M_z(\overline{r}') H_0^{(2)}(k\rho) ds' + \frac{j}{4} \int_C J_{s'}(\overline{r}') \frac{d}{dn'} H_0^{(2)}(k\rho) ds' \tag{3.8}$$

is the scattered field. In (3.8), $H_0^{(2)}$ represents the zeroth order Hankel function of the second kind and d/dn' denotes differentiation along the direction normal to C at the integration point. Also,

$$\rho = |\overline{r} - \overline{r}'| \tag{3.9}$$

where $\overline{r}$ and $\overline{r}'$ are the two dimensional position vectors defining the observation and integration points, respectively. The differential element ds' denotes arc length along the integration contour C.

Substituting (3.8) into (3.7) and making use of (3.6) leads to the integral equation

$$H_z^i(\bar{r}) = J_s(\bar{r}) + \frac{1}{4}\int_C J_{s'}(\bar{r}')\left[k\frac{a_0+a_2}{a_1} - j\frac{d}{dn'} + \frac{a_2}{ka_1}\frac{\partial^2}{\partial s'^2}\right]H_0^{(1)}(k\rho)ds', \quad \bar{r}\in C \tag{3.10}$$

To solve this numerically we may discretize C into N straight segments, as shown in figure 3.2, and assume a constant current distribution on each segment. By enforcing (3.10) at the center of each of the N segments, we then obtain the discrete system

$$[V_m] = [Z_{m\ell}][J_{s\ell}] \tag{3.11}$$

for a solution of the current distribution J_s. In (3.11), $[J_{s\ell}]$ is a column matrix with $J_{s\ell}$, $\ell = 1,2,...,N$ denoting the current on the ℓth element of C. $[V_m]$ is the excitation column matrix whose elements are given by

$$V_m = H_z^i(\bar{r}_m), \quad m = 1,2,\ldots,N \tag{3.12}$$

in which $\bar{r}_m$ denotes the location of the observation/test point (see figure 3.2). Finally, $[Z_{m\ell}]$ is a square impedance matrix whose elements can be expressed as

$$Z_{m\ell} = 1 + Z_{m\ell}^1 + Z_{m\ell}^2 + Z_{m\ell}^3 \tag{3.13}$$

with

$$Z_{m\ell}^1 = \frac{k}{4}\frac{a_0+a_2}{a_1}\int_{C_\ell} H_0^{(2)}(k\rho)ds', \qquad \bar{r} = \bar{r}_m \tag{3.14}$$

$$Z_{m\ell}^2 = -\frac{j}{4}\int_{C_\ell}\frac{d}{dn'}H_0^{(2)}(k\rho)ds', \qquad \bar{r} = \bar{r}_m \tag{3.15}$$

$$Z_{m\ell}^3 = \frac{a_2}{4ka_1}\int_{C_\ell}\frac{\partial^2}{\partial s'^2}H_0^{(2)}(k\rho)ds', \qquad \bar{r} = \bar{r}_m$$

$$= \frac{a_2}{4ka_1}\left[(\hat{s}_\ell\cdot\hat{\rho})H_1^{(2)}(k\rho)\right]_{s_\ell-\frac{\Delta}{2}}^{s_\ell+\frac{\Delta}{2}}, \quad \bar{r} = \bar{r}_m \tag{3.16}$$

in which

$$\bar{r}_\ell = s_\ell \hat{s}_\ell + n_\ell \hat{n}_\ell$$

denotes the center of the ℓth integration cell of width Δ. The vectors $\hat{s}_\ell$ and $\hat{n}_\ell$ represent the unit tangent and unit normal, respectively, to the surface at $\bar{r}_\ell$. It is necessary to evaluate the integrals in (3.14) and (3.15) analytically for small r and this can easily be accomplished after $Z^1_{m\ell}$ and $Z^2_{m\ell}$ are written in terms of local coordinates. To do so, we define the observation vector $\bar{r}_m$ as

$$\bar{r}_m = s_m \hat{s}_m + n_m \hat{n}_m = s_{m\ell} \hat{s}_\ell + n_{m\ell} \hat{n}_\ell \tag{3.17}$$

$$\bar{r}' = s' \hat{s}_\ell + n' \hat{n}_\ell \tag{3.18}$$

and by substituting these into (3.14) we obtain

$$Z^1_{m\ell} = \frac{k}{4} \frac{a_0 + a_2}{a_1} \int_{s_\ell - s_{m\ell} - \frac{\Delta}{2}}^{s_\ell - s_{m\ell} + \frac{\Delta}{2}} H_0^{(2)}(k\sqrt{\tilde{s}^2 + \tilde{n}^2}) d\tilde{s} \tag{3.19}$$

where $\tilde{n} = n_{m\ell} - n_\ell$. Similarly, for $Z^2_{m\ell}$ we have

$$Z^2_{m\ell} = \frac{j}{4} \frac{d}{d\tilde{n}} \int_{s_\ell - s_{m\ell} - \frac{\Delta}{2}}^{s_\ell - s_{m\ell} + \frac{\Delta}{2}} H_0^{(2)} \left(k\sqrt{\tilde{s}^2 + \tilde{n}^2}\right) d\tilde{s} \tag{3.20}$$

The analytical expressions for the integrals in (3.19) and (3.20) have been developed in [32] by using a small argument expansion of the Hankel function to $O(\rho^4, \rho^4 \ln \rho)$.

Once the current distribution has been determined from (3.11), the far zone fields can be easily evaluated using (3.8). By introducing the large argument approximation of the Hankel function into (3.8) we find

$$H^s_z|_{r\to\infty} = \frac{e^{-jkr}}{\sqrt{r}} \Delta \sqrt{\frac{k}{8\pi}} e^{j\frac{\pi}{4}} \sum_{\ell=1}^{N} J_{s\ell} e^{jk(n_\ell \nu_\ell + 2s_\ell \xi_\ell)}$$

$$\cdot \frac{\sin(k\Delta\xi_\ell)}{k\Delta\xi_\ell} \left[\hat{n}_\ell \cdot \hat{r} - \frac{a_0 + a_2}{a_1} - \frac{a_2}{a_1} \xi_\ell^2\right] \tag{3.21}$$

where

$$\nu_\ell = (\hat{n}_\ell \cdot \hat{x}) \cos\phi + (\hat{n}_\ell \cdot \hat{y}) \sin\phi$$

$$2\xi_\ell = (\hat{s}_\ell \cdot \hat{x}) \cos\phi + (\hat{s}_\ell \cdot \hat{y}) \sin\phi \tag{3.22}$$

and (r, ϕ) denote the usual cylindrical coordinates of the far-zone observation point.

The echowidth of the structure is defined by

$$\sigma_H = \lim_{r \to \infty} 2\pi r \frac{|H_z^s|^2}{|H_z^i|^2} \tag{3.23}$$

and can be computed via (3.21).

3.1.2 E_z-incidence

When the coated cylinder is illuminated by the plane wave

$$E_z^i = e^{jk(x\cos\phi' + y\sin\phi')} \tag{3.24}$$

the equation (2.11) simplifies to

$$E_z = -\frac{a_0 + a_2}{a_1} Z H_s - \frac{a_2'}{k^2(a_2' + a_0')} \frac{\partial^2}{\partial s^2} E_z \tag{3.25}$$

and we observe that this is the dual of (3.2) upon letting $a_m \to a_m'$ and invoking (2.10). The equivalent currents are given by

$$\overline{J} = \hat{n} \times \overline{H} = -\hat{z} H_s = \hat{z} J_z \tag{3.26}$$

$$\overline{M} = \overline{E} \times \hat{n} = -\hat{s} E_z = \hat{s} M_s \tag{3.27}$$

From (3.25) we also have

$$J_z(\overline{r}) = -\left(\frac{a_0' + a_2'}{a_1'} + \frac{a_2'}{k^2 a_1'} \frac{\partial^2}{\partial s^2} \right) Y\, M_s(\overline{r}), \quad \overline{r} \in C \tag{3.28}$$

which is dual to (3.6).

To construct an integral equation for the magnetic current M_s we follow the same procedure as that employed in the case of H_z-incidence. On C,

$$E_z = -M_s = E_z^i + E_z^s \tag{3.29}$$

where E_z^s is the scattered field given by

$$E_z^s = -\frac{Zk}{4}\int_C J_z(\overline{r}')H_o^{(2)}(k\rho)ds' - \frac{j}{4}\int_C M_{s'}(\overline{r}')\frac{d}{dn'}H_0^{(2)}(k\rho)ds' \tag{3.30}$$

Introducing (3.28) into (3.30) and substituting into (3.29) leads to the integral equation

$$-E_z^i(\overline{r}) = M_s(\overline{r}) + \frac{1}{4}\int_C M_s(\overline{r}')\left[k\left(\frac{a_0'+a_2'}{a_1'}\right) - j\frac{d}{dn'} + \frac{a_2'}{ka_1'}\frac{\partial^2}{\partial s'^2}\right]H_0^{(2)}(k\rho)ds', \tag{3.31}$$

$$\overline{r} \in C$$

This is dual to (3.10) and its numerical solution can be accomplished in a manner parallel to that employed for (3.10). Also the far zone field is given by the dual of (3.21).

3.2 Numerical Results

This section addresses the numerical accuracy of the high and low contrast second order GIBCs in comparison with the SIBCs and other standard formulations. A determination of the GIBC's range of validity by comparison with simulations based on exact solutions or other validated numerical techniques is also presented.

Figure 3.3 presents a numerical comparison between the GIBC, SIBC and the exact solution with TE-incidence on a uniformly coated circular cylinder. As seen, the SIBC is quite accurate in simulating thin coatings. However, as the coating

thickness increases, it no longer remains accurate and this is demonstrated in figures 3.3(b) and 3.3(c). We note that the low and high contrast GIBCs employed to generate the curves in figure 3.3 were obtained by setting $\delta_1 = \delta_3 = 0$.

Figures 3.4 and 3.5 show a comparison of results based on the low and high GIBCs for different permitivities and coating thicknesses. In particular, figure 3.4 includes data corresponding to constant thickness, single coatings. As expected, the low contrast GIBC shows a better agreement with the exact solution in the case of low contrast material and the high contrast GIBC is more accurate for higher permitivities. The curves in figure 3.5 correspond to constant permittivity coatings and it is now seen that the high contrast GIBC is more accurate over the low contrast GIBC as the thickness of the coating is increased. Data obtained from numerous tests suggest that the agreement between the low contrast GIBC and exact solutions is acceptable for $\sqrt{\epsilon}\,\delta < 0.15\lambda$ with H-polarization and for $\sqrt{\epsilon}\,\delta < 0.20\lambda$ with E-polarization. The range of validity of the high contrast GIBC is unfortunately a function of the refractive index and thickness as depicted by the plot in figure 3.6.

The aforementioned conclusions on the range of validity of the high and low contrast GIBCs were based on data for a single uniform coating on a circular cylinder of radius 1λ. Of course, other parameters such as the radius of the cylinder and homogeneity of the coating are of importance. Although these were not accounted for in this preliminary study, some general suggestions can be noted based on our experience. In particular, when the relative permeability is not unity, it is reasonable to assume that the range of validity of the conditions will be between those stated for the E and H polarizations. Also, when the conditions are applied to model multiple layer coatings, an average permittivity can be computed before making use of the criteria given above. Representative scattering patterns from a multilayer cylinder

are given in figure 3.7 and as seen, the agreement with corresponding numerical data [32] is good.

Since the presented GIBCs were derived on the assumption of a planar surface, it is of interest to examine their accuracy in simulating surfaces having small radii of curvature and/or discontinuities in the first derivative. With regard to the first issue, the conditions have been employed to model smooth coated cylinders down to at least $\lambda/4$ in radius without any appreciable deterioration of their accuracy. The second is addressed by using a second order GIBC to simulate a uniformly coated ogival cylinder. Scattering data based on the low and high contrast GIBC are shown in figure 3.8 and compared with data based on a finite element boundary integral [33] method. We note that the accuracy of the GIBC formulation tends to decrease with increasing eccentricity of the ogive. In general, though, the agreement between the exact and GIBC-based solutions remains good for tip angles (α) greater than 60 degrees. However, the accuracy of the GIBC simulation can be greatly improved by replacing the sharp tip of the ogive with a rounded one (having radius of about 0.01λ) and increasing the sampling around the tip. This is demonstrated in figures 3.9 and 3.10 for tip angles of 36° and 30°, respectively. The agreement between the FEM and the GIBC solutions tends to deteriorate as the tip angle goes below 30 degrees.

The results presented up to this point correspond to uniform coatings. As noted earlier, though, the GIBCs can be employed to simulate coatings of varying thickness and layered material composition. Figure 3.11 presents data for an ogive coated with a constant thickness coating having non- uniform ϵ and/or μ.

3.3 Summary

Second order generalized impedance boundary conditions (GIBCs) were used to derive integral equations for scattering by two-dimensional coated structures of arbitrary cross-section and implemented using a moment method procedure. Results based on this numerical implementation were then compared with corresponding data based on an exact solution or from other validated computer codes. It was found that the proposed second order boundary conditions provide an improved simulation of the coating in comparison with the traditional standard impedance boundary condition and guidelines were given for their region of validity. The primary reason for the improved simulation is because the second order GIBC includes the effect of the polarization current components normal to the coating in addition to the tangential ones. In general, the presence of edges deteriorates the accuracy of the simulation particularly for thicker coatings. This is due to the inherent non-uniqueness of these boundary conditions at abrupt terminations, a situation which can only be remedied by introducing additional field constraints at the terminations [51,52]. The second order GIBCs were found to be equally effective in simulating non- planar coatings having laterally non-uniform but smoothly varying material properties or thickness.

(a)

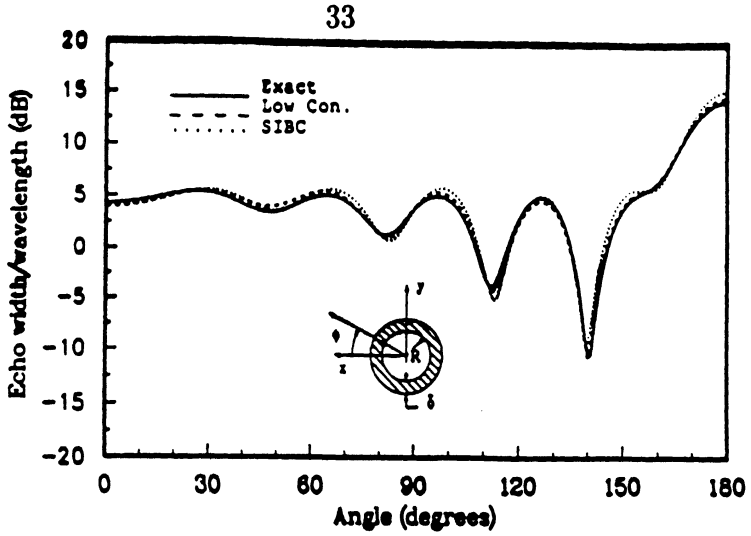

(b)

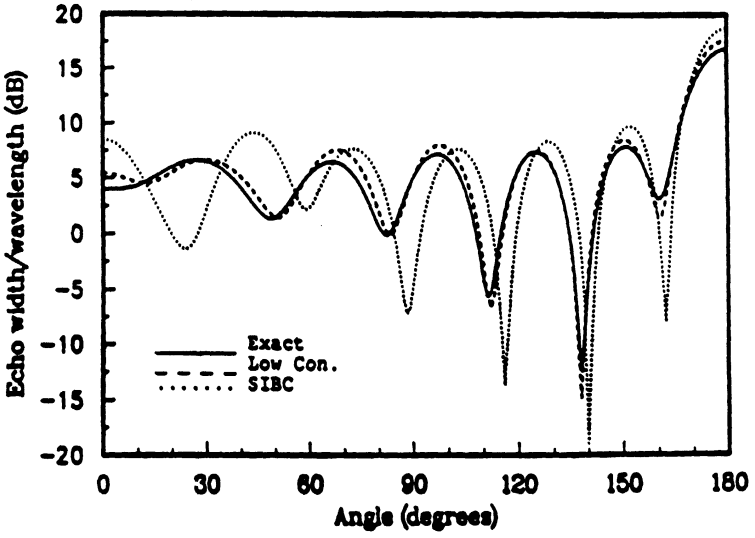

(c)

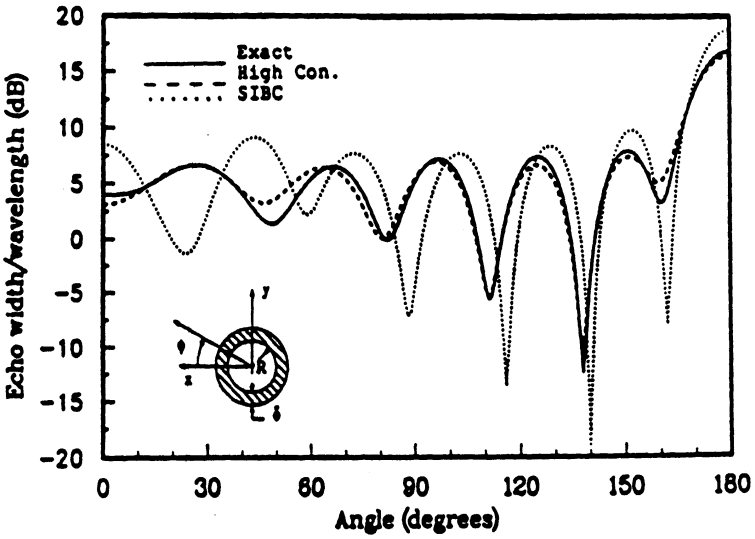

Figure 3.3: H-polarization bistatic echowidth ($\phi' = 0°$) for a coated cylinder having $R = 1\lambda$ (includes coating). (a) $\delta_1 = 0$, $\delta_2 = 0.03\lambda$, $\delta_3 = 0$, $\epsilon = 4$, $\mu = 1$. (b) $\delta_1 = 0$, $\delta_2 = 0.07\lambda$, $\delta_3 = 0$, $\epsilon = 4$, $\mu = 1$. (c) $\delta_1 = 0$, $\delta_2 = 0.07\lambda$, $\delta_3 = 0$, $\epsilon = 4$, $\mu = 1$.

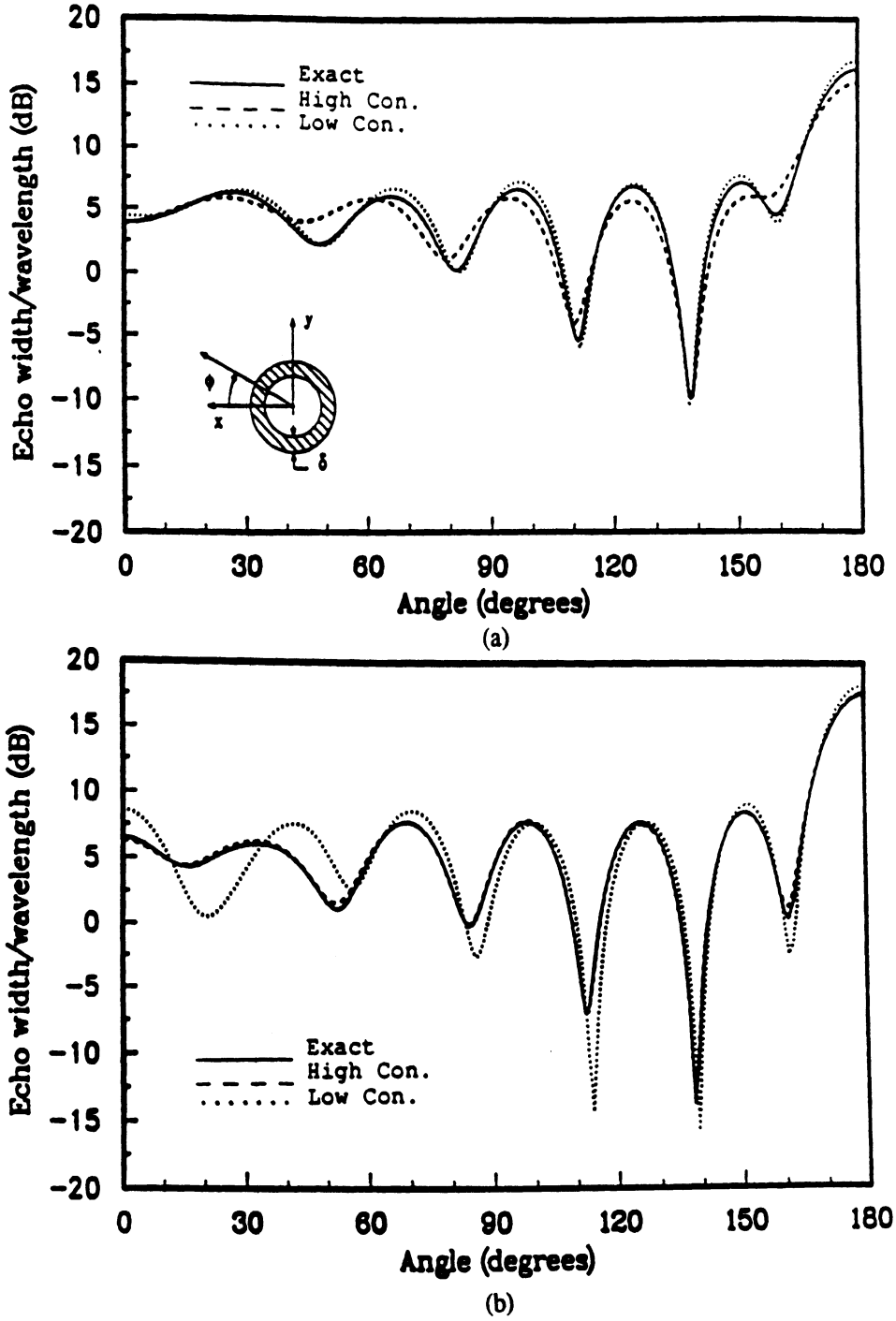

Figure 3.4: H-polarization bistatic echowidth ($\phi' = 0°$) for a coated cylinder having $R = 1\lambda$ (includes coating). (a) $\delta_1 = 0$, $\delta_2 = 0.06\lambda$, $\delta_3 = 0$, $\epsilon = 4$, $\mu = 1$. (b) $\delta_1 = 0$, $\delta_2 = 0.06\lambda$, $\delta_3 = 0$, $\epsilon = 8$, $\mu = 1$.

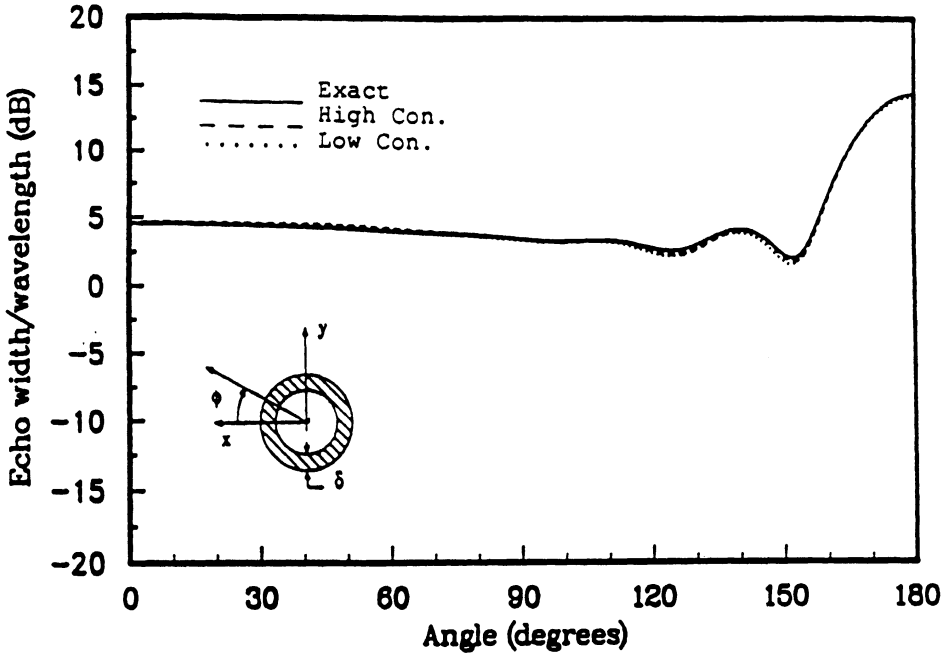

(a)

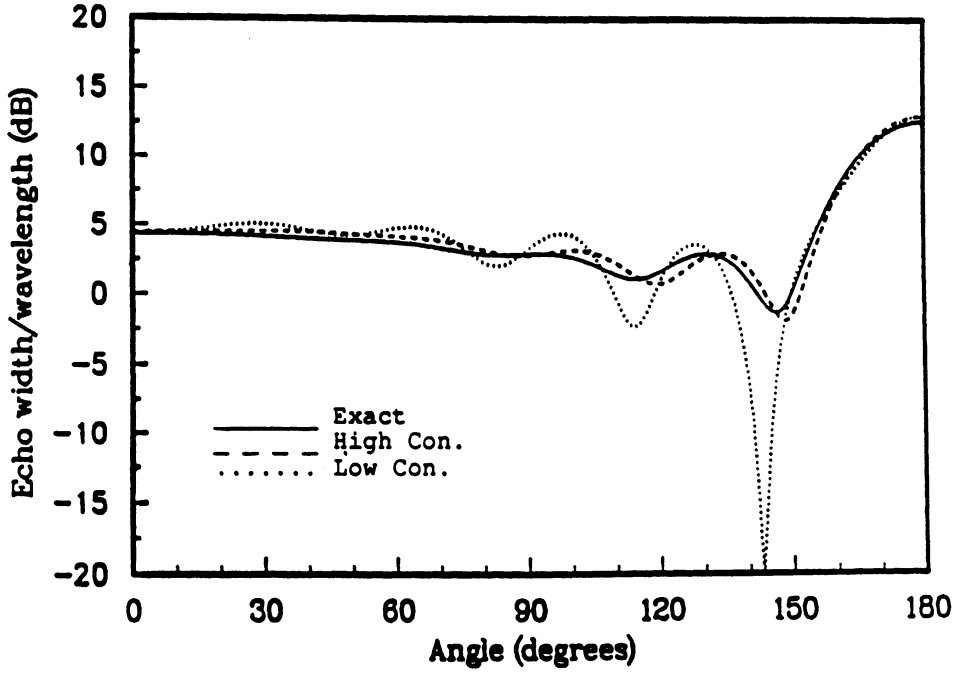

(b)

Figure 3.5: E-polarization bistatic echowidth ($\phi' = 0°$) for a coated cylinder having $R = 1\lambda$ (includes coating). (a) $\delta_1 = 0$, $\delta_2 = 0.08\lambda$, $\delta_3 = 0$, $\epsilon = 4$, $\mu = 1$. (b) $\delta_1 = 0$, $\delta_2 = 0.12\lambda$, $\delta_3 = 0$, $\epsilon = 4$, $\mu = 1$.

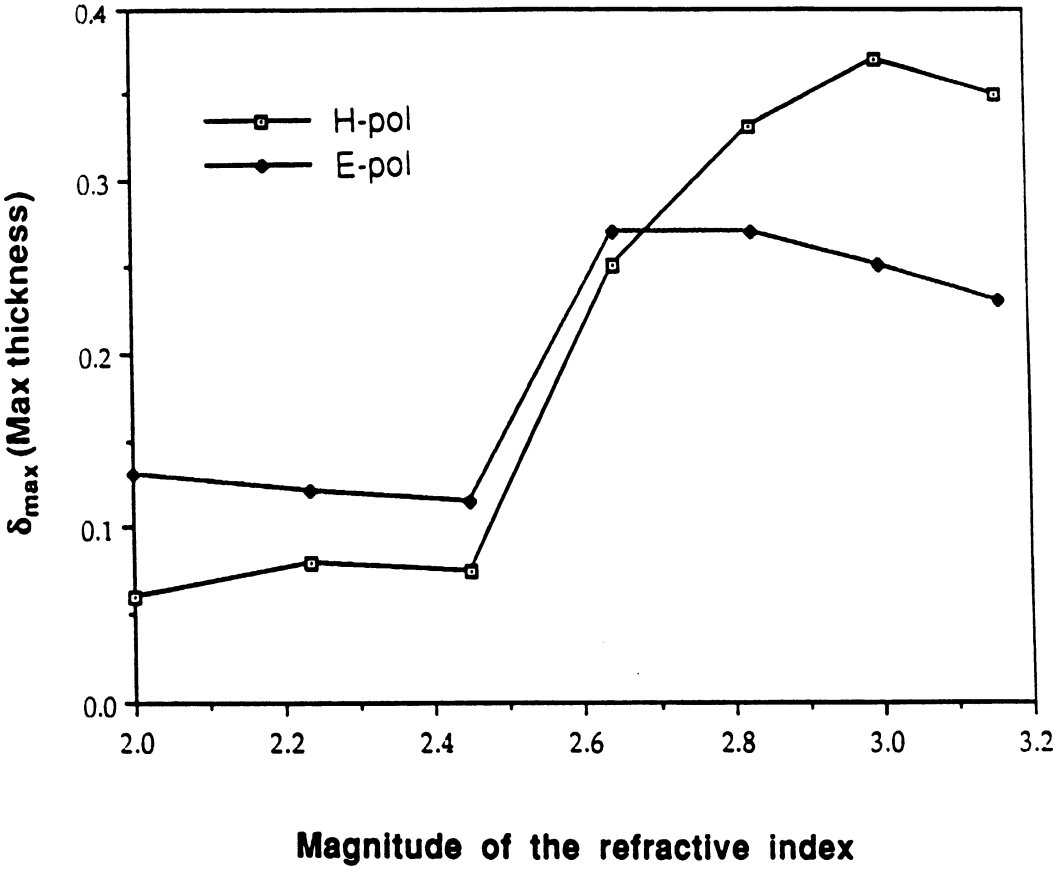

Figure 3.6: Maximum allowable coating thickness for applying the high contrast second order GIBC as a function of refractive index ($\epsilon^{-1/2}$) with an acceptable error of $\pm$ 2 dB in the field magnitude.

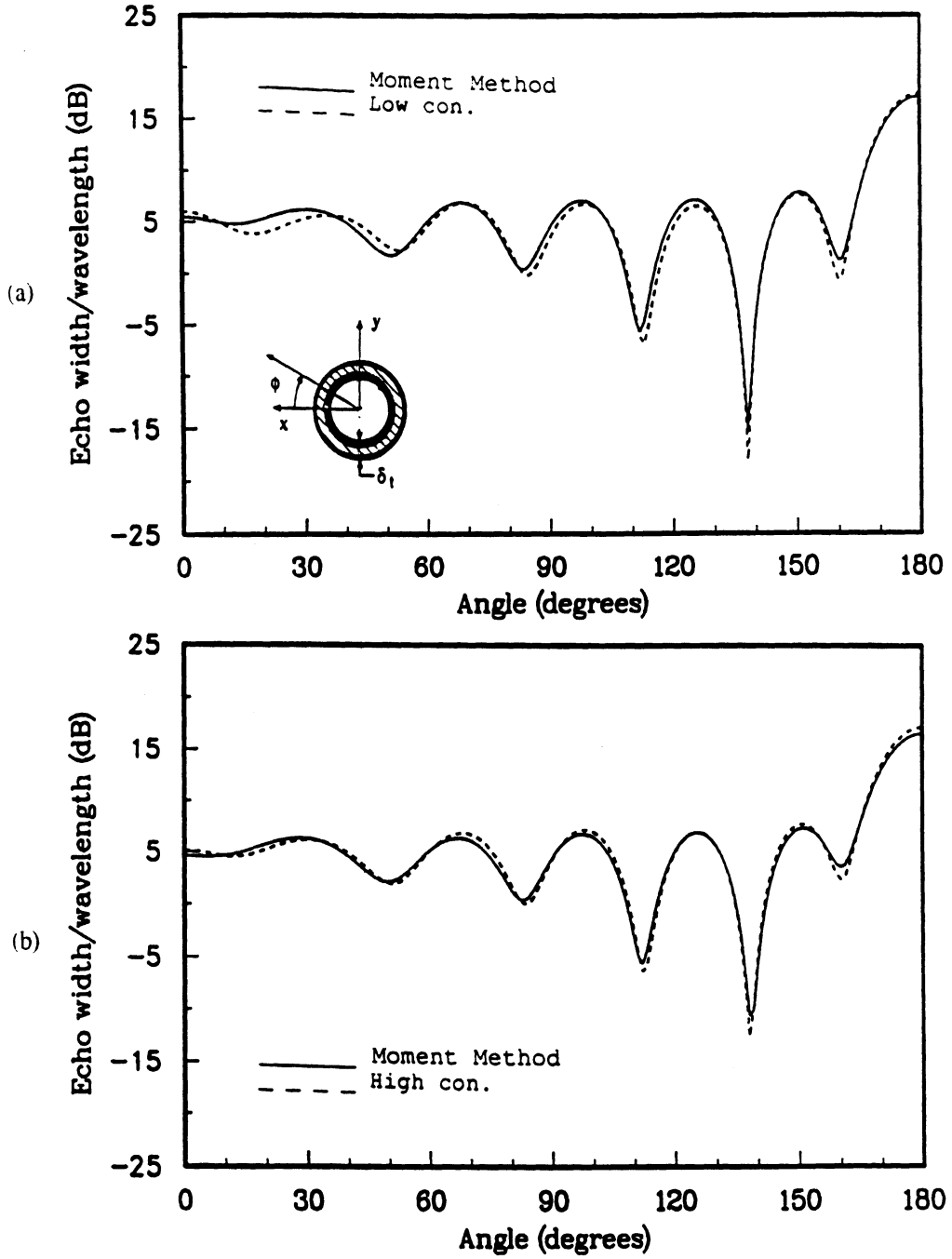

Figure 3.7: H-polarization bistatic echowidth ($\phi' = 0°$) for a three- layer coated cylinder having $R = 1\lambda$ (included coating). (a) $\delta_1 = 0.01\lambda$, $\delta_2 = 0.02\lambda$, $\delta_3 = 0.03\lambda$, $\epsilon_1 = 3 - j0.1$, $\epsilon_2 = 4 - j0.3$, $\epsilon_3 = 7 - j1.5$, $\mu_1 = \mu_2 = \mu_3 = 1.2$. (b) $\delta_1 = 0.01\lambda$, $\delta_2 = 0.02\lambda$, $\delta_3 = 0.03\lambda$, $\epsilon_1 = 3 - j0.1$, $\epsilon_2 = 4 - j0.3$, $\epsilon_3 = 7 - j1.5$, $\mu_1 = \mu_2 = \mu_3 = 1$.

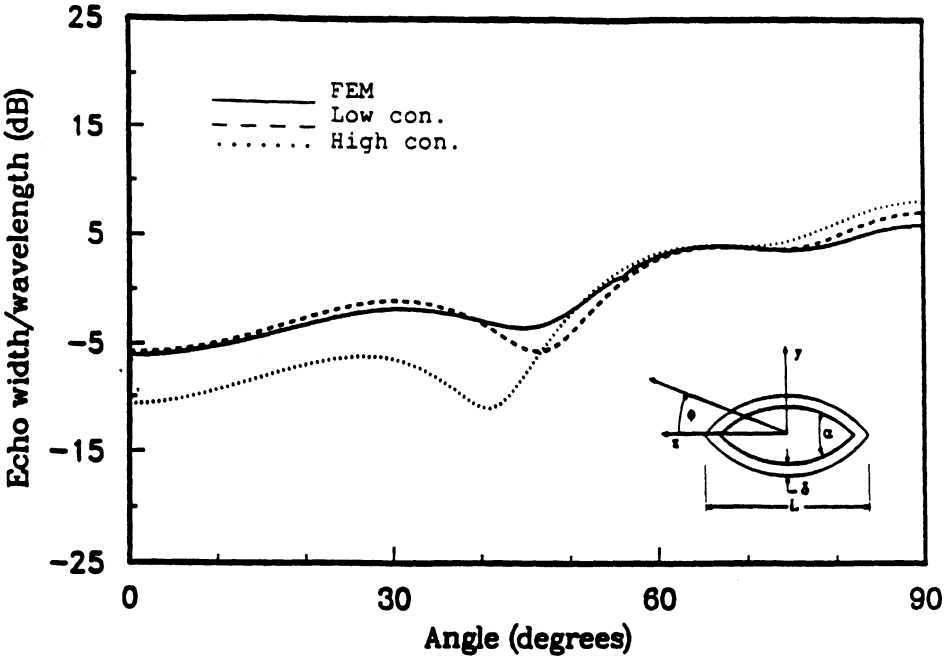

(a)

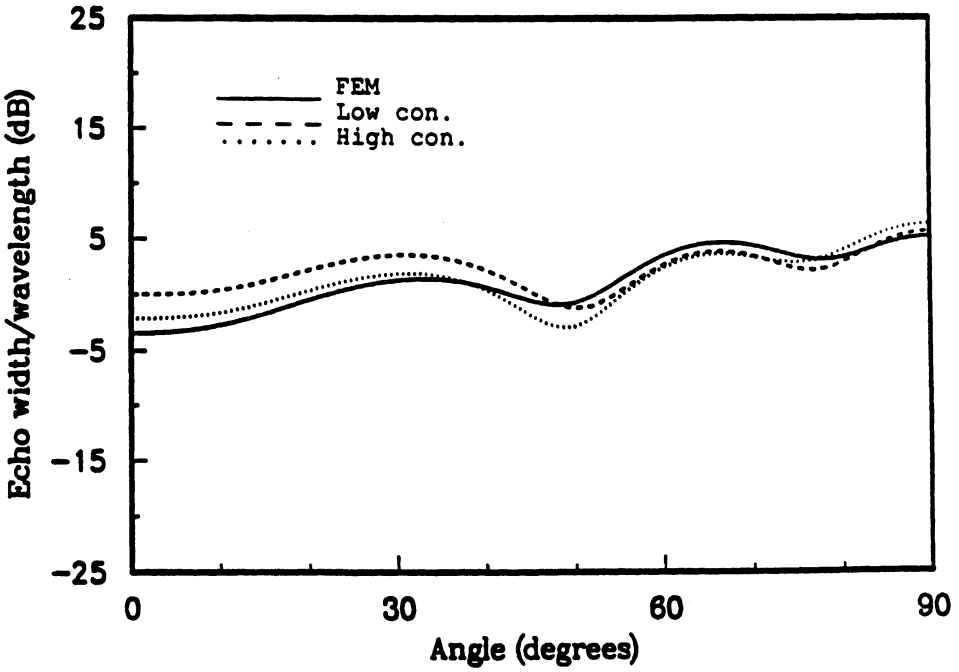

(b)

Figure 3.8: H-polarization backscatter echowidth from an ogival cylinder having total length $L = 1.32\lambda$ (includes coating) and tip angle $\alpha = 90°$. (a) $\delta_1 = 0$, $\delta_2 = 0.06\lambda$, $\delta_3 = 0$, $\epsilon = 3$. (b) $\delta_1 = 0$, $\delta_2 = 0.06\lambda$, $\delta_3 = 0$, $\epsilon = 8$.

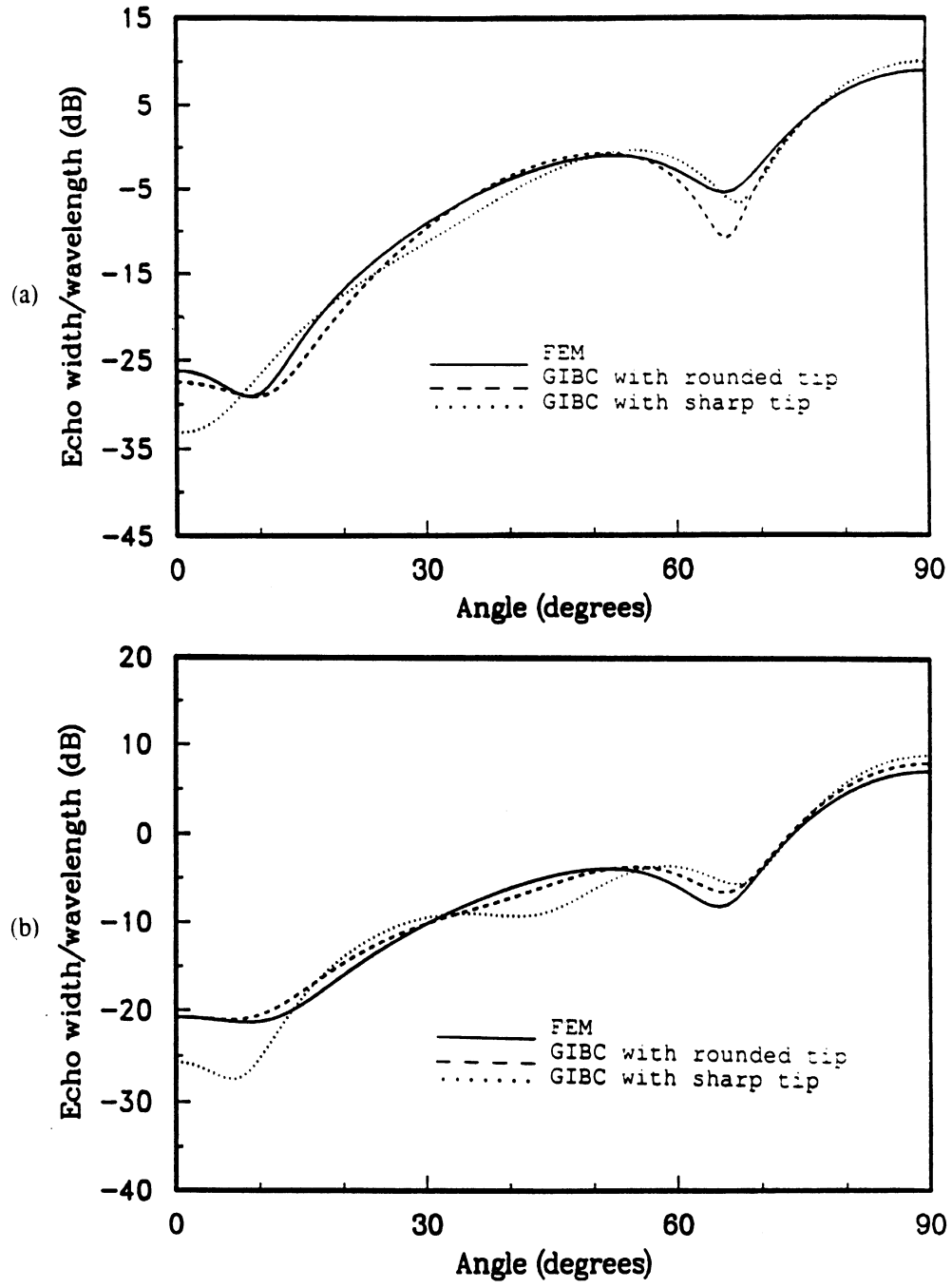

Figure 3.9: H-polarization backscatter echowidth from an ogival cylinder having total length $L = 1.26\lambda$ (includes coating) and tip angle $\alpha = 36°$. (a) $\delta_1 = 0$, $\delta_2 = 0.03\lambda$, $\delta_3 = 0$, $\epsilon = 4$. (b) $\delta_1 = 0$, $\delta_2 = 0.03\lambda$, $\delta_3 = 0$, $\epsilon = 3 - j1$, $\mu = 2 - j0.5$.

(a)

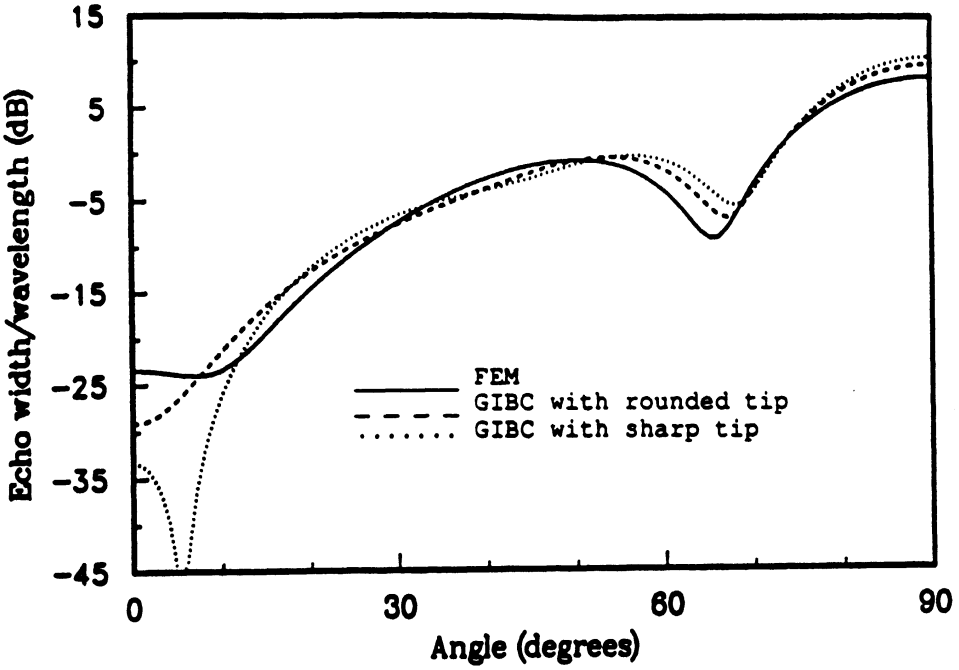

(b)

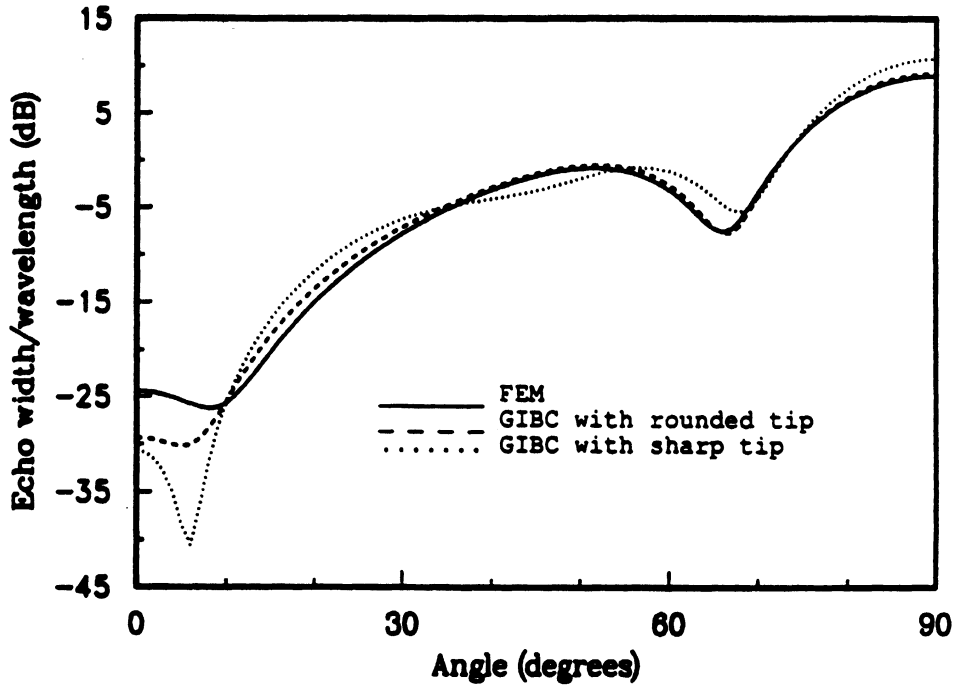

Figure 3.10: H-polarization backscatter echowidth from an ogival cylinder having total length $L = 1.26\lambda$ (includes coating) and tip angle $\alpha = 30°$. (a) $\delta_1 = 0$, $\delta_2 = 0.03\lambda$, $\delta_3 = 0$, $\epsilon = 4$. (b) $\delta_1 = 0$, $\delta_2 = 0.03\lambda$, $\delta_3 = 0$, $\epsilon = 3 - j1$, $\mu = 2 - j0.5$.

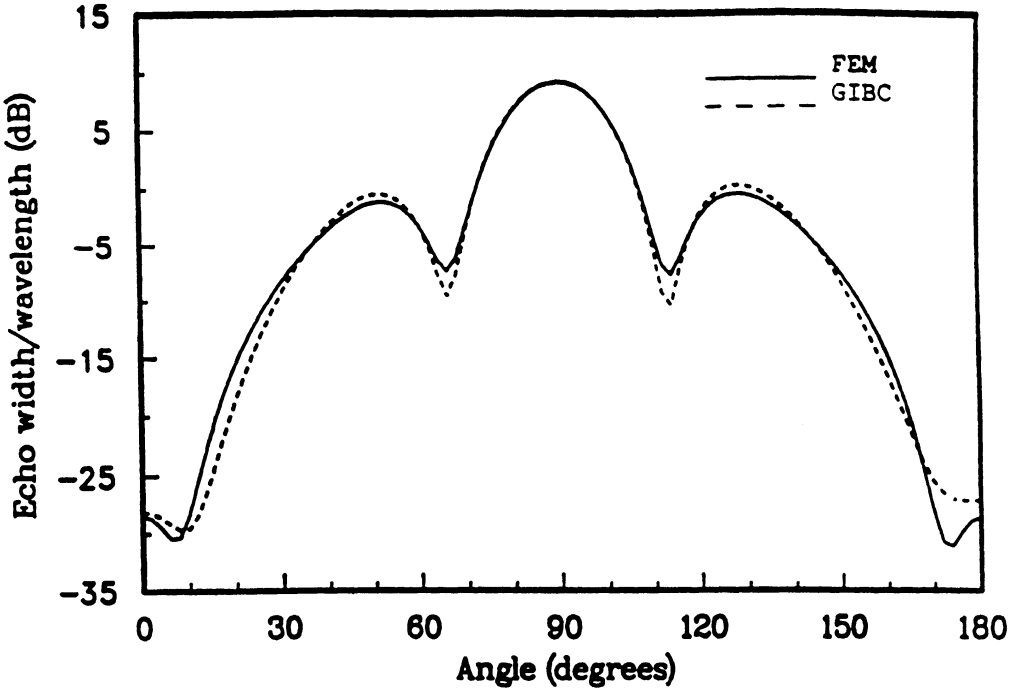

(b)

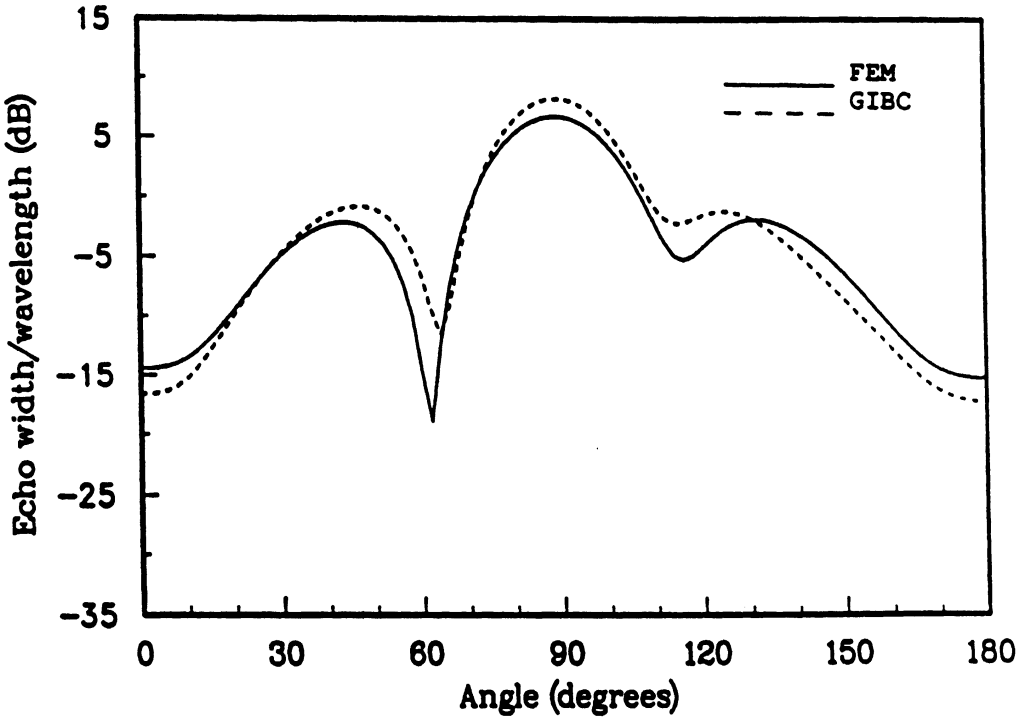

(a)

Figure 3.11: H-polarization backscatter echowidth from an ogival cylinder having total length $L = 1.26\lambda$ (includes coating) and tip angle $\alpha = 36°$. (a) Variable right hand side coating using a linear taper; $\epsilon = 4$ to $5 - j1.5$ from center to tip, $\delta_1 = 0$, $\delta_2 = 0.03$, $\delta_3 = 0$ ($\mu = 1$). (b) Variable right hand side coating using a linear taper; $\mu = 2$ to $3 - j1.5$ from center to tip, $\delta_1 = 0$, $\delta_2 = 0.03$, $\delta_3 = 0$, ($\epsilon = 1$).

CHAPTER IV

HIGH FREQUENCY SCATTERING BY A SMOOTH COATED CONVEX CYLINDER SIMULATED BY APPROXIMATE BOUNDARY CONDITIONS

This chapter deals with the subject of non-specular scattering mechanisms arising due to creeping waves and curved surface diffraction. A rigorous UTD solution is developed here for the diffraction by a coated convex cylinder simulated with the approximate boundary conditions (SIBCs and GIBCs). In addition, a uniform asymptotic solution is obtained which remains valid when the observation point is in the close vicinity of the cylinder. One of the objectives of this exercise is to demonstrate the use of the approximate boundary conditions, presented in chapter two, for the development of analytical solutions for curved surfaces. These asymptotic solutions are then validated using the eigenfunction solution for a coated circular cylinder and using the numerical data based on the integral equation formulation developed in chapter three for a general convex cylinder.

The problem of scattering by a smooth convex impedance cylinder has received much attention. Wang [34,35] presented ray-optical solutions for the impedance and coated cylinders. His results are valid only in the deep lit and shadow regions and do not apply to the case where the observation point is in the transition region. Wait

and Conda [36,37] developed a solution which is valid in the transition region and for observation points on and off the surface. However, as pointed out by Pathak [38] it does not uniformly reduce to the ray solution [39,40] exterior to the transition regions. Also, it is not valid on the portion of the surface in the transition region and these limitations were the primary motivation in Pathak's work [38] for the perfectly conducting convex cylinder. Recently, Kim and Wang [41] presented a solution applicable to a coated cylinder that remained valid in the transition region. They employed a heuristic approach to obtain the numerical values of the resulting transition integral applicable to a coated cylinder. Their solution is uniform but is not applicable in the close vicinity of the cylinder.

The UTD solution to be presented here parallels that given by Pathak [38] for the circular perfectly conducting cylinder. However, in the case of the coated cylinder the resulting UTD expressions are in terms of Fock-type integrals whose efficient evaluation is of primary interest. In the following, we first present the eigenfunction solution based on the second order GIBC simulation of a circular coated cylinder. By employing Watson's transformation this is written in integral form which is then cast in a ray representation. The ray solution is subsequently generalized to the case of a general convex cylinder. Finally, the evaluation of the Fock-type integrals is discussed and some results are presented which validate the accuracy of the GIBC ray solutions.

4.1 Eigenfunction and Integral Representation

Before considering the problem of scattering by a convex impedance suface, it is instructive to first develop a solution for the diffraction by the canonical geometry of a circular impedance cylinder. Generalizations to any convex surface can then be

made on the basis of the expressions obtained for the circular cylinder.

Consider the plane wave

$$u^i = u_o e^{jkx} = u_o e^{jk\rho\cos\phi} \tag{4.1}$$

incident on the coated circular cylinder shown in figure 4.1a, where u_o is the amplitude of the wave and u^i denotes either the E_z or H_z component of the incident field. We propose to simulate the circular cylinder with an equivalent one (see figure 4.1b) satisfying the GIBCs. This implies that (2.11) takes the form

$$E_\phi = -\frac{(a_2 + a_o)}{a_1} Z H_z - \frac{a_2 Z}{k^2 b^2 a_1} \frac{\partial^2 H_z}{\partial \phi^2} \tag{4.2}$$

for H_z-incidence or

$$E_z = \frac{(a_2 + a_o)}{a_1} Z H_\phi - \frac{a_2'}{k^2 b^2 (a_2' + a_o')} \frac{\partial^2 E_z}{\partial \phi^2} \tag{4.3}$$

in the case of E_z-incidence. In the above, a_m and a_m' were derived in chapter two for the low and high contrast GIBCs.

An eigenfunction representation of the total field in the presence of the cylinder can be generally written as

$$u^t = \sum_{n=-\infty}^{\infty} j^n \left[J_n(k\rho) + A_n H_n^{(2)}(k\rho) \right] e^{-jn\phi} \tag{4.4}$$

where $J_n(\cdot)$ is the Bessel function of order n and $H_n^{(2)}(\cdot)$ denotes the nth order Hankel function of the second kind. To find the constants A_n we enforce the GIBC given by (4.2) or (4.3) at $\rho = b$. This yields

$$A_n = -\frac{J_n'(kb) + Q(n) J_n(kb)}{H_n^{(2)'}(kb) + Q(n) H_n^{(2)}(kb)} \tag{4.5}$$

in which the prime denotes differentiation with respect to the Bessel or Hankel func-

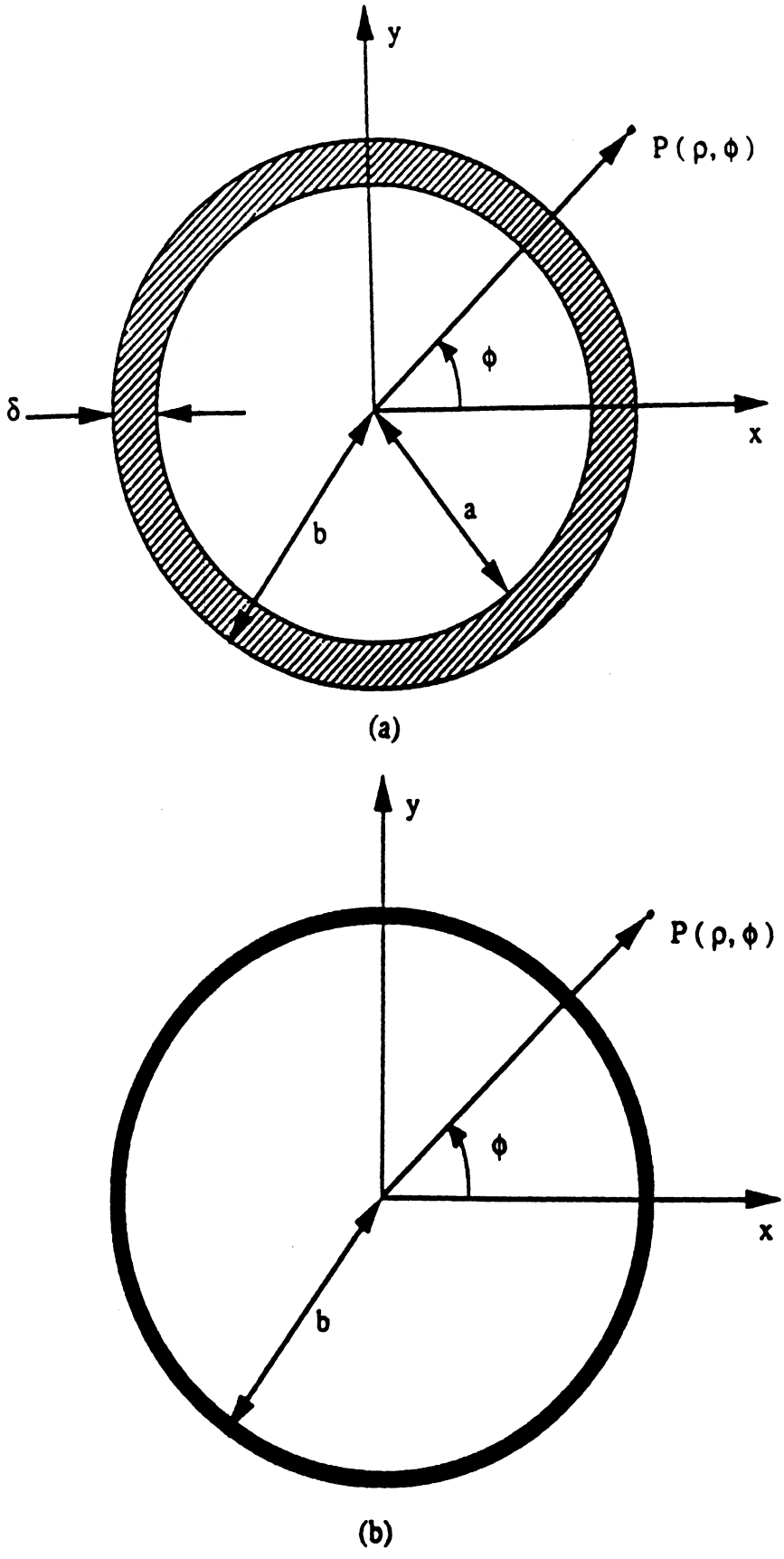

Figure 4.1: (a) Coated circular cylinder (b) equivalent coated cylinder simulated with GIBCs.

tion argument,

$$Q(n) = \begin{cases} -j\left(\frac{a_2+a_o}{a_1} - n^2\frac{a_2}{k^2b^2a_1}\right) & \text{for } H_z\text{-incidence} \\ \\ -j\left(\frac{a_2'+a_o'}{a_1'} - n^2\frac{a_2'}{k^2b^2a_1'}\right) & \text{for } E_z\text{-incidence} \end{cases} \tag{4.6}$$

and when $a_2 = a_2' = 0$, $Q(n)$ reduces to

$$Q(n) = Q = \begin{cases} -j\frac{a_o}{a_1} = -j\eta & \text{for } H_z\text{-incidence} \\ \\ -j\frac{a_o'}{a_1'} = -j\frac{1}{\eta} & \text{for } E_z\text{-incidence} \end{cases} \tag{4.7}$$

Since (4.4) is a slowly convergent series, especially for large kb, our objective is to obtain asymptotic representations for u^t suitable for practical applications. We, therefore, seek uniform expressions for the total field in the lit, shadow and transition regions. Such expressions should also recover the well known geometrical optics field, where applicable. To obtain a ray representation of (4.4) in conjunction with (4.6) we must first recast u^t in integral form. Employing the usual Watson's transformation [6] and noting that $Q(n) = Q(-n)$, we find [38]

$$u^t = u_1 + u_2$$

where

$$u_1 = u_o \int_{-\infty}^{\infty} \left[J_\nu(k\rho) - \frac{J_\nu'(kb) + Q(\nu)J_\nu(kb)}{H_\nu^{(2)'}(kb) + Q(\nu)H_\nu^{(2)}(kb)} H_\nu^{(2)}(k\rho) \right] e^{-j\nu\psi} d\nu \tag{4.8a}$$

or

$$u_1 = \frac{u_o}{2} \int_{-\infty}^{\infty} \left[H_\nu^{(1)}(k\rho) - \frac{H_\nu^{(1)'}(kb) + Q(\nu)H_\nu^{(1)}(kb)}{H_\nu^{(2)'}(kb) + Q(\nu)H_\nu^{(2)}(kb)} H_\nu^{(2)}(k\rho) \right] e^{-j\nu\psi} d\nu \tag{4.8b}$$

and

$$u_2 = u_o \int_{-\infty}^{\infty} \left[J_\nu(k\rho) - \frac{J_\nu'(kb) + Q(\nu)J_\nu(kb)}{H_\nu^{(2)'}(kb) + Q(\nu)H_\nu^{(2)}(kb)} H_\nu^{(2)}(k\rho) \right] e^{j\nu\pi/2}$$

$$\frac{e^{-j\nu(2\pi+\phi)} + e^{-j\nu(2\pi-\phi)}}{1 - e^{-j2\nu\pi}} d\nu \tag{4.9}$$

in which

$$\psi = |\phi| - \frac{\pi}{2} \tag{4.10}$$

and $Q(\nu)$ is given by (4.6) upon letting $n \rightarrow \nu$. The field component u_1, defined above, includes the geometrical optics and dominant surface diffraction contributions whereas u_2 denotes the creeping waves which circulate around the cylinder more than once. We are interested in an asymptotic evaluation of u_1 and to do this we must separately consider each of the space regions illustrated in figure 4.2.

4.2 Field in the Deep Lit and Shadow Regions

In the deep lit region, the geometrical optics incident and reflected rays represent an accurate first-order high-frequency approximation of the total field. The geometrical optics field can be extracted from u_1 upon performing an asymptotic evaluation of (4.8) yielding [42]

$$u^{GO}(P_L) \approx u^i(P_L) + u^i(Q_R) R_{s,h} \sqrt{\frac{\tilde{\rho}}{\tilde{\rho} + \ell}} e^{-jk\ell} \tag{4.11}$$

in which

$$R_s \approx -\frac{a_o' - a_1' \cos\theta^i + a_2' \cos^2\theta^i}{a_o' + a_1' \cos\theta^i + a_2' \cos^2\theta^i} \quad (E_z \text{ - incidence}) \tag{4.12a}$$

$$R_h \approx -\frac{a_o - a_1 \cos\theta^i + a_2 \cos^2\theta^i}{a_o + a_1 \cos\theta^i + a_2 \cos^2\theta^i} \quad (H_z \text{ - incidence}) \tag{4.12b}$$

are the reflection coefficients associated with the coating [5]. The parameter θ^i is illustrated in figure 4.3 and ℓ is the distance (must be large) from the surface reflection

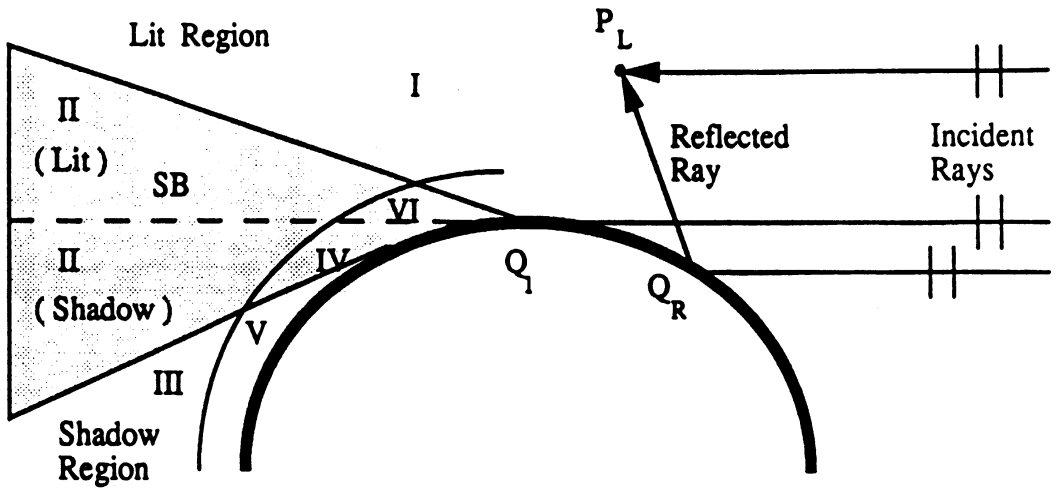

Figure 4.2: Different regions associated with the plane wave scattering from a smooth convex cylinder.

point Q_R to the observation point P_L. Finally, $\tilde{\rho}$ is the reflected ray caustic distance and for a convex cylinder it is given by

$$\tilde{\rho} = \frac{\rho_g(Q_R)\cos\theta^i}{2} \tag{4.13}$$

$\rho_g(Q_R)$ is the radius of curvature of the surface at Q_R and is equal to b for the circular cylinder.

For observations in the deep shadow region, a residue series representation of u_1 is more appropriate. From (4.8), we obtain

$$u_1 = -u_o \frac{4}{kb} \sum_{m=1}^{\infty} \frac{H_{\nu_m}^{(2)}(k\rho) e^{j\nu_m(\phi-\frac{\pi}{2})}}{H_{\nu_m}^{(2)}(kb) \frac{\partial}{\partial\nu}\left[H_\nu^{(2)'}(kb) + Q(\nu) H_\nu^{(2)}(kb)\right]_{\nu=\nu_m}} \tag{4.14}$$

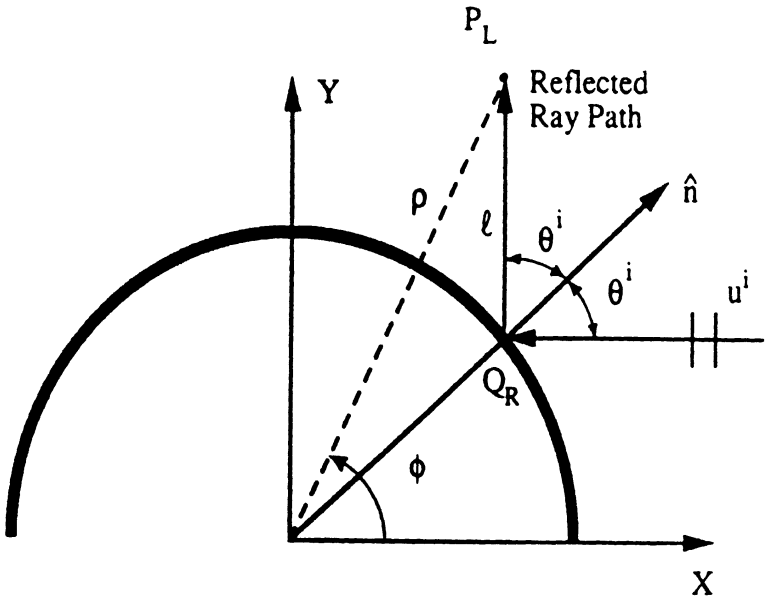

Figure 4.3: Reflected ray path.

where ν_m are the zeros of the transcendental equation

$$H_{\nu_m}^{(2)'}(kb) + Q(\nu_m)H_{\nu_m}^{(2)}(kb) = 0 \tag{4.15}$$

Obviously, (4.14) does not provide a ray-picture interpretation of the creeping-wave diffraction which is desirable for generalizations to non- circular cylinders. To recast (4.14) in a form compatible with the Keller type GTD format, the Debye approximation must be employed for the Hankel function for $k\rho \gg |\nu_m|$. This yields

$$u_1^d(P_s) \approx u^i(Q_1)T_{s,h}\frac{e^{-jks}}{\sqrt{s}} \tag{4.16}$$

where

$$T_{s,h} = -\sum_{m=1}^{\infty} \mathcal{D}_m(Q_1) \cdot e^{-j\nu_m\theta} \cdot \mathcal{D}_m(Q_2) \tag{4.17}$$

is the corresponding diffraction coefficient and for the circular cylinder

$$\begin{aligned} \mathcal{D}_m(Q_1) &= \mathcal{D}_m(Q_2) \\ &= \left[\sqrt{\frac{2}{\pi}}\frac{4}{k^2 b}\frac{e^{j\frac{\pi}{4}}}{H_{\nu_m}^{(2)}(kb)\frac{\partial}{\partial\nu}\left\{H_\nu^{(2)}(kb)+Q(\nu)H_\nu^{(2)}(kb)\right\}_{\nu=\nu_m}}\right]^{\frac{1}{2}} \end{aligned} \tag{4.18}$$

with θ as defined in figure 4.4.

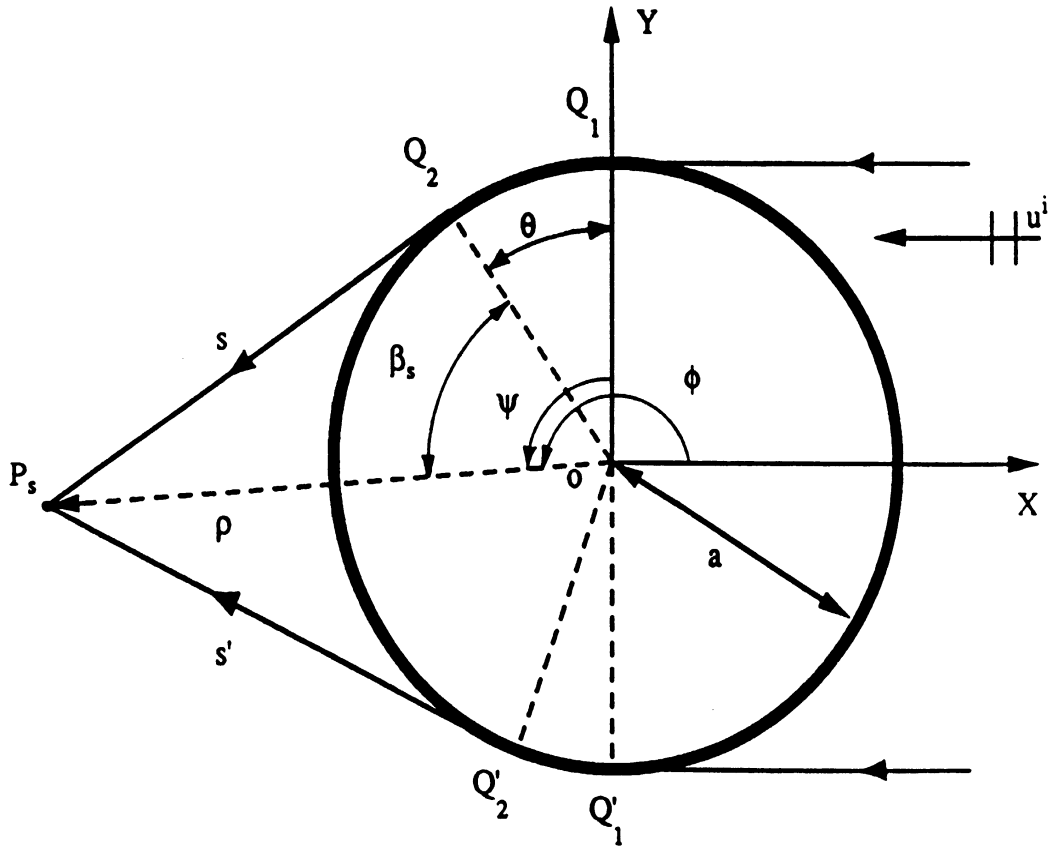

Figure 4.4: Propagation ray paths in the shadow region.

A generalization of (4.16)–(4.18) for convex cylinders is now possible by making the replacements

$$b \rightarrow \rho_g(Q_{1,2}) \tag{4.19}$$

$$e^{-j\nu_m\theta} \rightarrow \exp\left[-j\int_{t'(Q_1)}^{t'(Q_2)} \frac{\nu_m(t')}{\rho_g(t')}dt'\right] \tag{4.20}$$

Consequently, the attachment coefficient $\mathcal{D}_m(Q_1)$ is no longer equal to the launching coefficient $\mathcal{D}_m(Q_2)$.

4.3 Field in the Transition Region

The geometrical optics and creeping wave solutions presented above are not valid in the transition region close to the shadow boundaries as illustrated in figure 4.2. New uniform expressions are, therefore, required to overcome this limitation. These can be derived following the procedure adopted by Pathak [38] for a perfectly conducting convex cylinder. For the lit region we find

$$u_1(P_L) \approx u^i(P_L) + u^i(Q_R)R_{s,h}\sqrt{\frac{\tilde{\rho}}{\tilde{\rho}+\ell}}e^{-jk\ell} \tag{4.21}$$

where $R_{s,h}$ is now given by

$$R_{s,h} = -\sqrt{\frac{-4}{x'}}\exp\left\{-j\frac{(x')^3}{12}\right\}\left[\frac{e^{-j\frac{\pi}{4}}}{2x'\sqrt{\pi}}\left\{1 - F(2k\ell\cos^2\theta^i)\right\} + G(x',q)\right] \tag{4.22}$$

$$F(x) = 2j\sqrt{x}e^{-jx}\int_x^\infty e^{-jx^2}dx \tag{4.23}$$

$$x' = -2m(Q_R)\cos\theta^i \tag{4.24}$$

$$m(Q_R) = \left\{\frac{k\rho_g(Q_R)}{2}\right\}^{\frac{1}{3}} \tag{4.25}$$

and

$$\tilde{\rho} = \frac{\rho_g(Q_R)\cos\theta^i}{2}. \tag{4.26}$$

$F(x)$ is the UTD transition function [43] and $G(x',q)$ is defined by

$$G(x',q) = \frac{e^{-j\frac{\pi}{4}}}{\sqrt{\pi}}\int_{-\infty}^{\infty}\frac{V'(\tau) - q(\tau)V(\tau)}{W_2'(\tau) - q(\tau)W_2(\tau)}e^{-jx\tau}d\tau \tag{4.27}$$

in which

$$q(\tau) = mQ(\nu) \tag{4.28}$$

whereas $V(\tau)$ and $W_{1,2}(\tau)$ are the Fock-type Airy functions [44]

$$2jV(\tau) = W_1(\tau) - W_2(\tau) \tag{4.29}$$

$$W_{1,2}(\tau) = \frac{1}{\sqrt{\pi}} \int_{\Gamma_{1,2}} e^{\tau t - t^3/3} dt \tag{4.30}$$

The contour Γ_1 runs from $\infty e^{-j\frac{2\pi}{3}}$ to $\infty - j\epsilon$ and Γ_2 is the complex conjugate of Γ_1. We remark that in the case of an SIBC simulation, $q(\tau)$ becomes a constant.

For the shadow region, we have

$$u_1(P_s) \approx u^i(Q_1) T_{s,h} \frac{e^{-jks}}{\sqrt{s}} \tag{4.31}$$

where the diffraction coefficient $T_{s,h}$ is now redefined as

$$T_{s,h} = -\sqrt{m(Q_1)m(Q_2)} \sqrt{\frac{2}{k}} e^{-jkt} \left[\frac{e^{-j\frac{\pi}{4}}}{2x\sqrt{\pi}} \{1 - F(ks\tilde{a})\} + G(x,q) \right] \tag{4.32}$$

in which

$$x = \int_{t'(Q_1)}^{t'(Q_2)} \frac{m(t')}{\rho_g(t')} dt' \tag{4.33}$$

$$t = \int_{t'(Q_1)}^{t'(Q_2)} dt' \tag{4.34}$$

and

$$\tilde{a} = \frac{x^2}{2m(Q_1)m(Q_2)} \tag{4.35}$$

As is usually the case, (4.21)-(4.35) were first derived for the circular cylinder and were subsequently generalized for non-circular convex cylinders.

4.4 Field in the Close Vicinity of the Convex Cylinder

In all of the above derivations we have assumed that ℓ is large. Consequently, the given expressions are not adequate for field computations very close to the cylinder. In this case, it is possible to obtain a suitable approximation of the integral (4.8) by replacing the Hankel and Bessel functions in terms of Airy integrals and then employing a Taylor series expansions for these integrals.

Following a procedure similar to the one given in [38], the resulting expressions for an arbitrary smooth convex cylinder are

$$u_1(P) \approx u^i(P_N)\left[e^{-jhz'} - \sum_{n=0}^{5}\frac{(-1)^n}{n!}(jhz')^n + e^{\frac{-j(z')^3}{3}}\{\Lambda_1(z') - \Lambda_2(z')\}\right] \tag{4.36}$$

when P_N is in the lit region, and

$$u_1(P) \approx u^i(Q_1)e^{-jkt}\left[\frac{\rho_g(P_N)}{\rho_g(Q_1)}\right]^{\frac{-1}{6}}\{\Lambda_1(z) - \Lambda_2(z)\} \tag{4.37}$$

when P_N is in the shadow region. In (4.36) and (4.37)

$$\Lambda_1(D) = g_1(D) + j\frac{h^2}{2!}g_1'(D) - \frac{h^3}{3!}g_1(D) - \frac{h^4}{4!}g_1''(D) - j4\frac{h^5}{5!}g_1'(D) \tag{4.38}$$

$$\Lambda_2(D) = hg_2(D) + j\frac{h^3}{3!}g_2'(D) - 2\frac{h^4}{4!}g_2(D) - \frac{h^5}{5!}g_2''(D) \tag{4.39}$$

$$g_1(D) = \frac{1}{\sqrt{\pi}}\int_{-\infty}^{\infty}\frac{e^{-jD\tau}}{W_2'(\tau) - q(\tau)W_2(\tau)}d\tau \tag{4.40}$$

$$g_2(D) = \frac{1}{\sqrt{\pi}}\int_{-\infty}^{\infty}\frac{q(\tau)e^{-jD\tau}}{W_2'(\tau) - q(\tau)W_2(\tau)}d\tau \tag{4.41}$$

$$z' = -m(P_N)\cos\theta^i \tag{4.42}$$

for P_N in the lit region and

$$z = \int_{t'(Q_1)}^{t'(P_N)}\frac{m(t')}{\rho_g(t')}dt' \tag{4.43}$$

for P_N in the shadow region

$$t = \int_{t'(Q_1)}^{t'(P_N)} dt' \tag{4.44}$$

$$h = \frac{kd(P_N)}{m(P_N)} \tag{4.45}$$

$$d(P_N) = \rho - \rho_g(P_N) \tag{4.46}$$

The points P and P_N in the lit and shadow regions are illustrated in figure 4.5. We remark that when the cylinder's surface obeys the SIBC, $g_{1,2}(D)$ simplify to

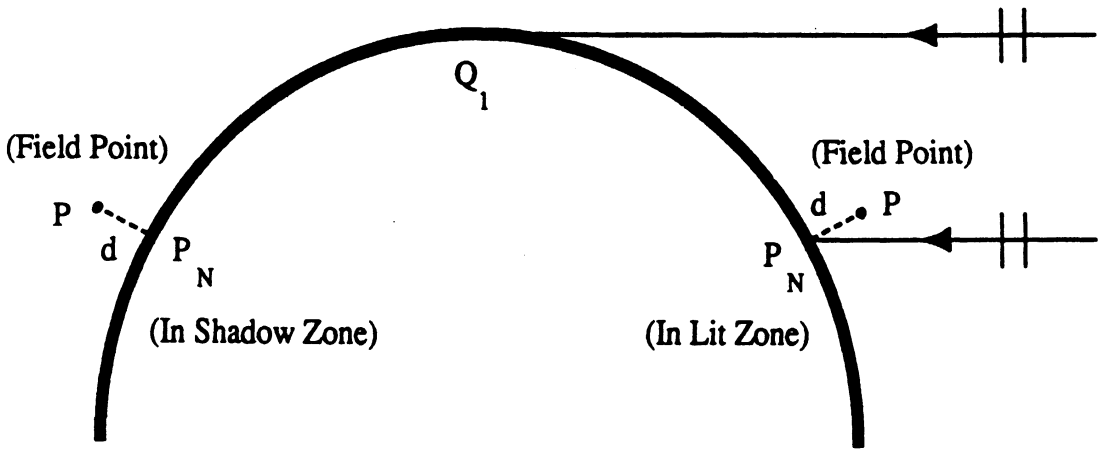

Figure 4.5: Projection of the field point P in the direction normal to the surface at P_N.

$$g_1(D) \rightarrow g(D) = \frac{1}{\sqrt{\pi}} \int_{-\infty}^{\infty} \frac{e^{-jD\tau}}{W_2'(\tau) - qW_2(\tau)} d\tau \tag{4.47}$$

$$g_2(D) \rightarrow mQg(D) \tag{4.48}$$

In the case of slowly attenuating creeping and/or surface waves (4.36) is not adequate and an improved result may be obtained by adding (4.36) and (4.37) with $t > \pi b$ (in case of a circular cylinder of radius b). Clearly, the addition of (4.37) corresponds to the contribution of the creeping wave that has travelled the minimum distance on the cylinder's surface to reach P_N. The contribution of those creeping waves that travelled more than once around the cylinder is given by u_2 and could be added to u_1 if greater accuracy is required.

The functions $g_1(D)$, $g_2(D)$ and $G(x, q)$ are Fock-type integrals that are formally the Fourier transform of a slowly varying factor consisting of a quotient of terms containing Airy functions and their derivatives. A computationally efficient scheme was proposed by Pearson [45] for the evaluation of these integrals. The scheme is an extension of the Fourier trapezoidal rule devised by Tuck [46] to treat the rotated-ray exponential behavior occuring in the integrals. The sampling frequency used in the computation is dictated by the slowly varying Airy-function factor in the integrands. Sufficiently accurate results have been obtained for both lossy and non-lossy coatings on a perfectly conducting cylinder using this scheme.

4.5 Numerical Results

The UTD expressions derived in the previous sections provide a complete set of equations for the computation of the total field in all regions of interest. In this section, we present some calculated data which validate the accuracy of the derived expressions by comparison with data based on the moment method and eigenfunction

solutions.

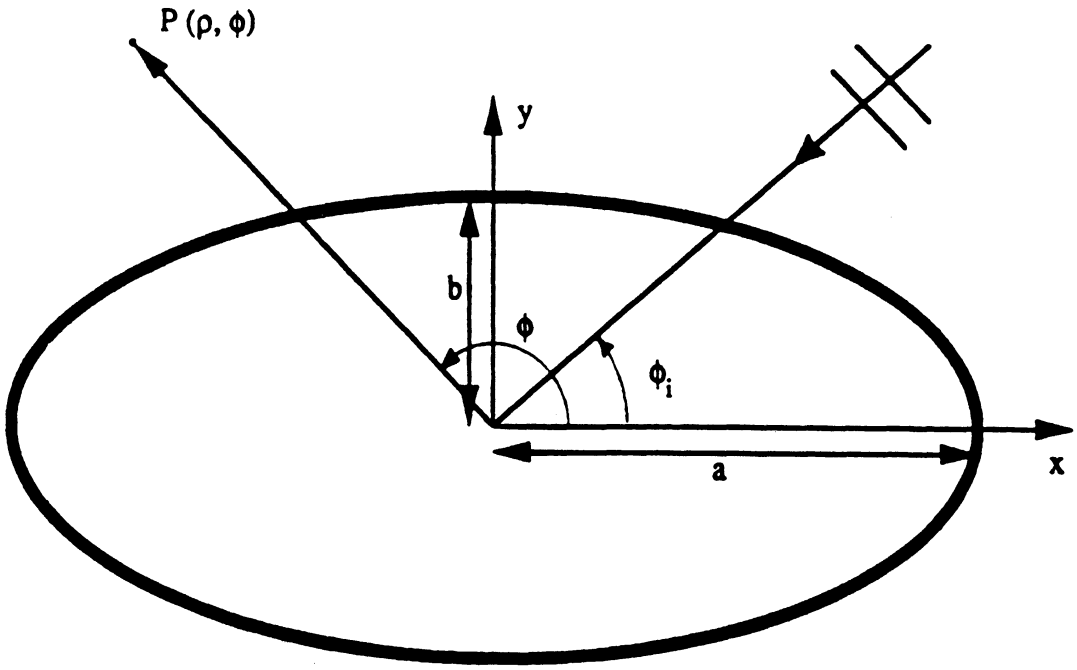

Figure 4.6: Elliptical cylinder configuration.

To show the validity of the UTD solution in the case of a convex cylinder, a special case of an elliptical cylinder (see figure 4.6) is considered in figure 4.7. Data based on the moment method solution are compared with the one obtained from the UTD solution in conjunction with the second order low and high contrast boundary conditions. Figure 4.8 verifies the asymptotic solution, developed for the field point in the close vicinity of a convex cylinder. We remark, however, that the approximations used for the Hankel functions in the derivation of (4.36) and (4.37) become less accurate for some values of ϵ_r and μ_r associated with lossless coatings, and this can be avoided by using more accurate approximations for the Hankel functions. Finally,

figure 4.9 demonstrates the use of GIBC in simulating multilayer coatings by simply redefining the material constants a_m and a'_m as discussed in [47,48].

A difficulty in implementing the expressions derived in this work was the evaluation of the Fock-type integrals $G(x,q)$, $g_1(D)$ and $g_2(D)$ as well as the determination of the zeros corresponding to (4.15). The Fock- type integrals were evaluated by employing the method described in [45] and the zeros of (4.15) were determined using the routine given in [49].

4.6 Summary

Rigorous ray solutions of the scattered fields were presented for a coated convex cylinder. These were developed in the context of the uniform geometrical theory of diffraction and specific expressions were given for the scattered fields in the lit, shadow and transition regions as well as for observations in the near vicinity of the cylinder. That is, UTD expressions were derived for all regions exterior to the coated cylinder. These are suited for engineering computations and are given in terms of the generalized Pekeris or Fock-type functions whose evaluation was efficiently performed via the Fourier Trapezoidal rule suggested by Pearson [45].

In comparison to the solution given by Kim and Wang [41], the ray representations given here are based on a second order generalized impedance boundary conditions which permits the simulation of thin multilayered coating as demonstrated in the included examples. Also, in our implementation of the transition fields we employed a rigorous rather than a heuristic evaluation of the Fock-type integrals. Further, we have presented accurate field representations for observations on or near the vicinity of the coated cylinder and these can also be used for computing the radiated fields by a source or an aperture on the surface of the convex cylinder.

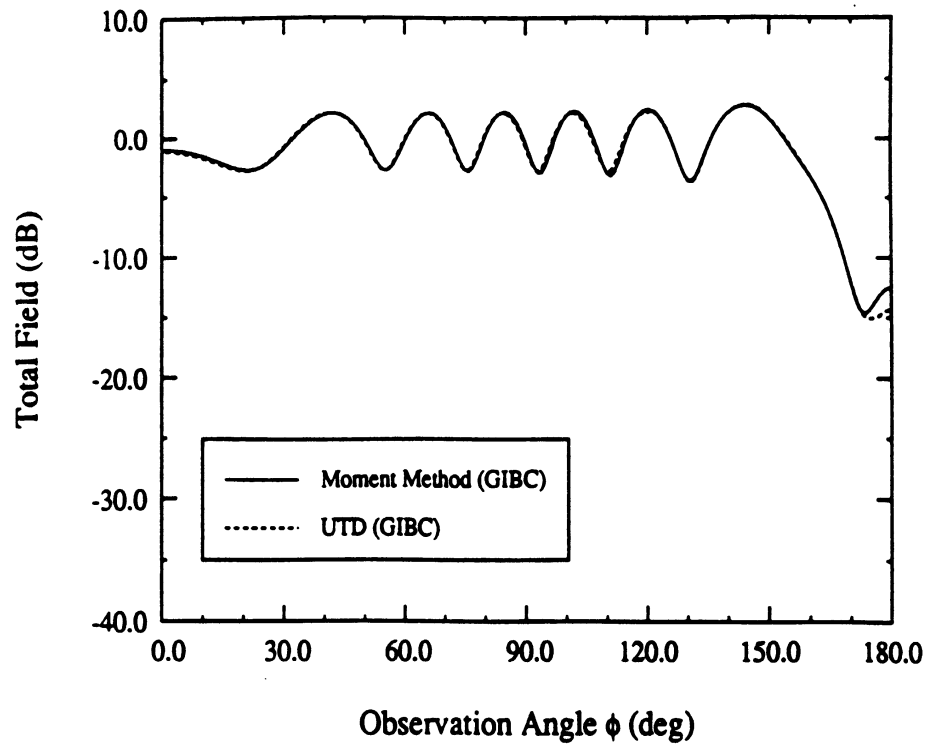

(a)

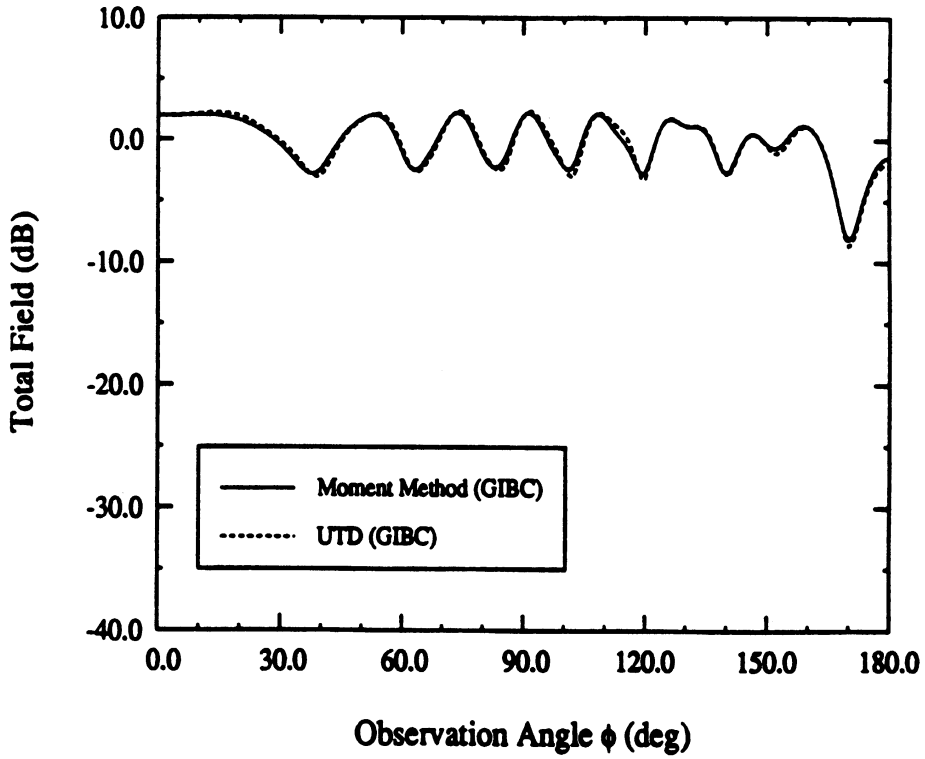

(b)

Figure 4.7: Bistatic scattering pattern for an elliptical cylinder having $a = 2\lambda$, $b = 1\lambda$, $\rho = 5\lambda$, $\phi_i = 0$ (a) E- polarization, $\epsilon_r = 4$, $\mu_r = 1$, $\delta = 0.07\lambda$ (b) H-polarization, $\epsilon_r = 8$, $\mu_r = 1$, $\delta = 0.2\lambda$.

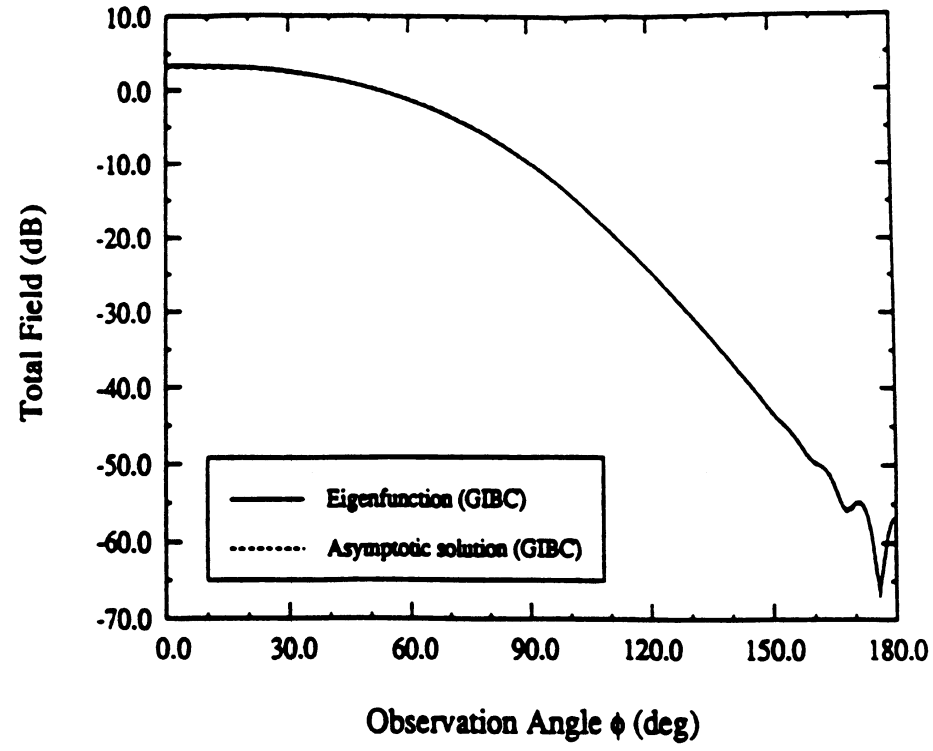

(a)

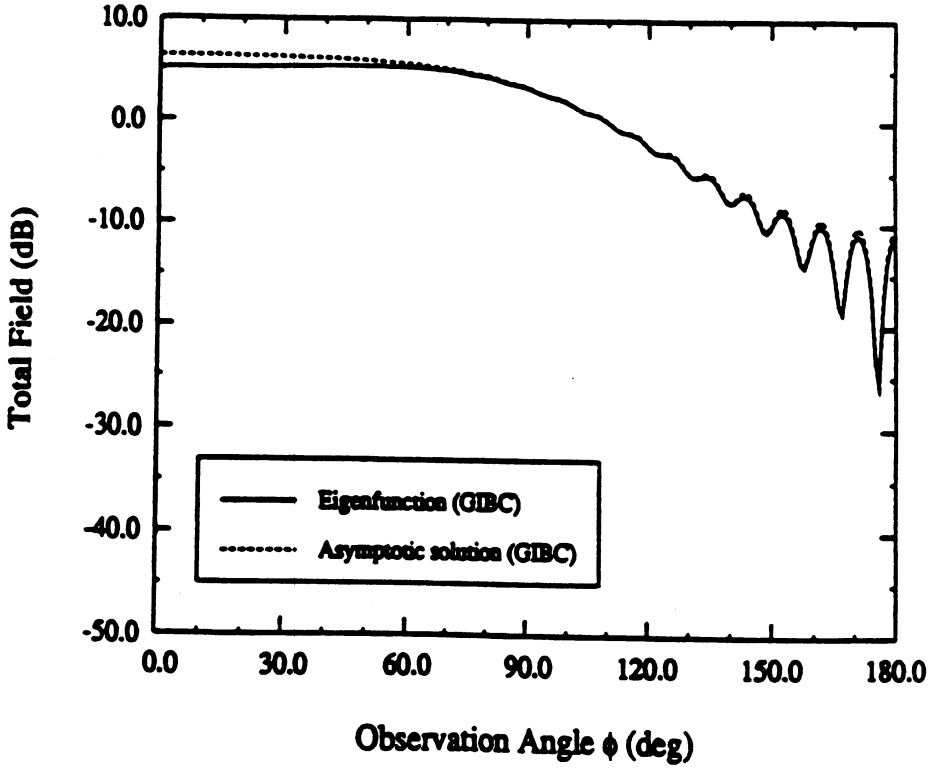

(b)

Figure 4.8: Bistatic scattering pattern of a circular cylinder having $b = 3\lambda$, $\rho = 3.05\lambda$, $\phi_i = 0$ (a) E-polarization, $\epsilon_r = 4$, $\mu_r = 1$, $\delta = 0.07\lambda$ (b) H-polarization, $\epsilon_r = 8$, $\mu_r = 1$, $\delta = 0.2\lambda$.

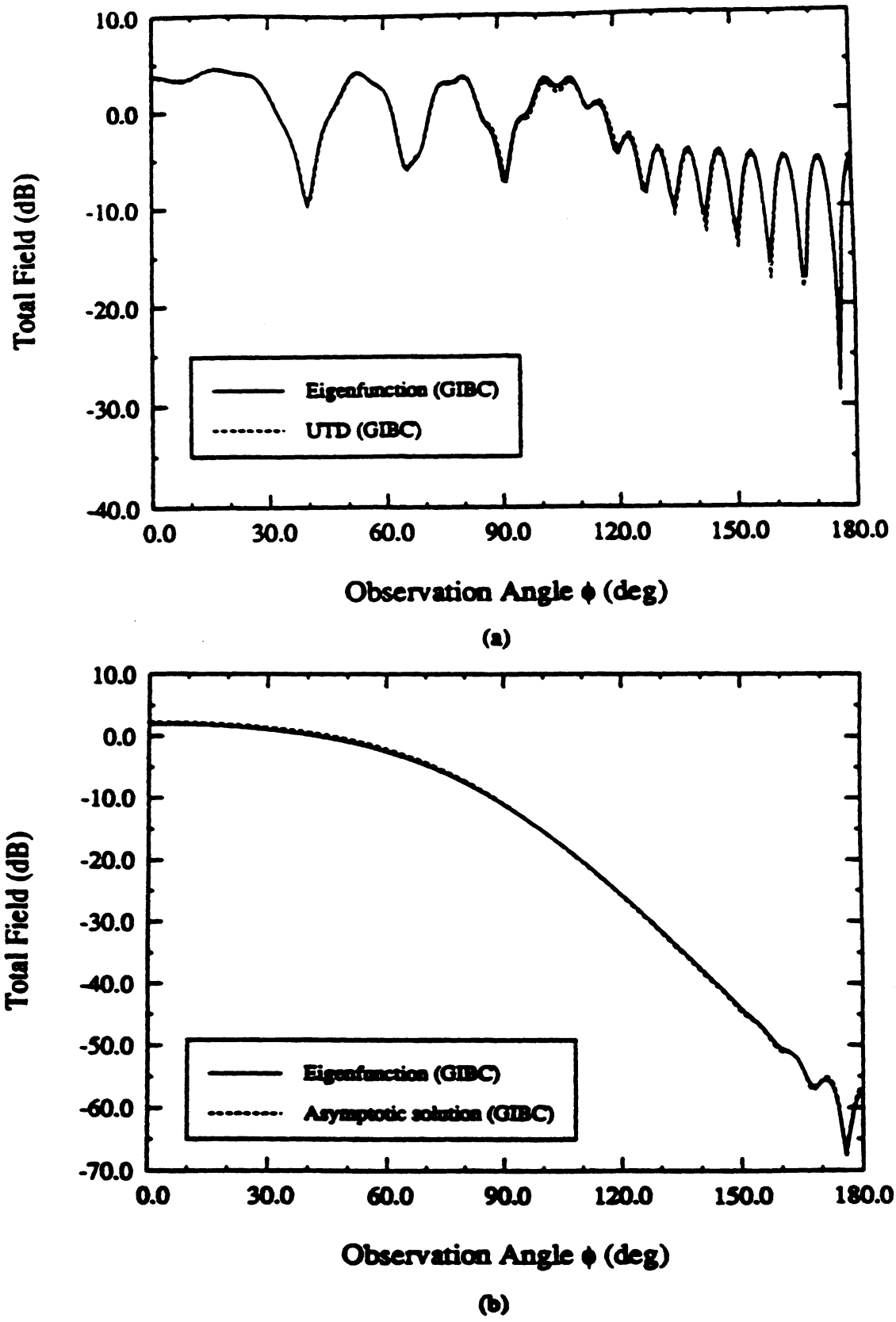

Figure 4.9: Bistatic scattering pattern of a three-layer coated circular cylinder having $b = 3\lambda$, $\phi_i = 0$, $\epsilon_{r1} = 3 - j0.1$, $\epsilon_{r2} = 4 - j0.3$, $\epsilon_{r3} = 7 - j1.5$, $\mu_{r1} = \mu_{r2} = \mu_{r3} = 1$, $\delta_1 = 0.01\lambda$, $\delta_2 = 0.02\lambda$, $\delta_3 = 0.03\lambda$ (a) H-polarization, $\rho = 5\lambda$ (b) E- polarization, $\rho = 3.05\lambda$.

CHAPTER V

AN APPROXIMATE SOLUTION FOR SCATTERING BY AN IMPEDANCE WEDGE AT SKEW INCIDENCE

So far, in the previous chapters we developed and validated diffraction coefficients for smooth coated convex cylinders simulated with the approximate boundary conditions (SIBCs and GIBCs). These diffraction coefficients can be utilized to study the non-specular scattering mechanisms caused by creeping waves and surface diffracted waves. In this chapter we will consider other sources of non-specular electromagnetic scattering, namely those associated with diffraction from first derivative discontinuities as in the case of edges and wedges coated with lossy material.

A normal incidence solution for a wedge with arbitrary included angle and having SIBCs imposed on its faces is already available [11]. However, the diffraction coefficient obtained from this solution is only applicable to two dimensional structures and for practical applications it is necessary to derive coefficients applicable to three dimensional structures. This can be accomplished by solving the impedance wedge problem with a plane wave excitation at skew angles. Unfortunately, the exact solution to this problem has only been obtained for a few wedge angles. In particular, solutions are possible only for wedges having included angles of 0 (half- plane) [12,13,14,15,19], $\pi/2$ (with one face perfectly conducting) [14,15,16,20], π and $3\pi/2$

(with one face perfectly conducting) [14,15,19]. The main difficulty in obtaining the skew incidence solution for the diffraction by an impedance (SIBC) wedge is the lack of techniques to solve the resulting four coupled functional difference equations. For the specific wedges mentioned above the four difference equations can be decoupled yielding the solution given in the references but their decoupling for other wedge angles has so far eluded researchers.

In this chapter, an approximate solution is developed for an impedance wedge at skew incidence using Maliuzhinets' method [11]. This solution exactly recovers the known ones for an impedance half plane and the normal incidence wedge solution. A major effort is devoted to the validation of the approximate solution and for this purpose a moment method code was developed for computing the scattering by an impedance polygonal cylinder excited at skew incidence. The formulation forming the basis of this code is deferred until chapter six.

5.1 Modified Form of the SIBCs

Consider an impedance wedge geometry shown in figure 5.1 having an external angle of $2\Phi = n\pi$ with surface impedances $\eta_+ Z$ and $\eta_- Z$ at $\phi = +\Phi$ and $\phi = -\Phi$, respectively. This impedance (SIBC) wedge is illuminated by a plane wave impinging from the direction

$$\hat{i} = -\hat{x}\sin\beta_o\cos\phi' - \hat{y}\sin\beta_o\sin\phi' + \hat{z}\cos\beta_o \tag{5.1}$$

where $|\phi'| \leq \Phi$ and β_o represents the skewness angle and is equal to $\pi/2$ when the wave is incident normal to the wedge. The z components of the incident field are of the form

$$E_z^i = e_z e^{-jk\hat{i}\cdot\bar{r}} \qquad ZH_z^i = h_z e^{-jk\hat{i}\cdot\bar{r}} \tag{5.2}$$

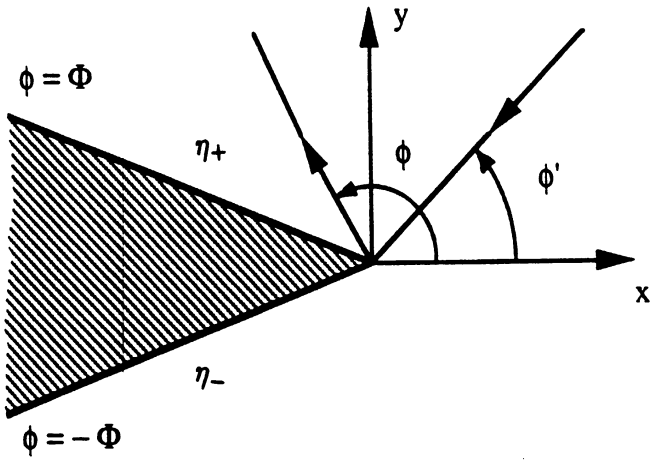

Figure 5.1: Impedance wedge geometry.

with Z being the intrinsic free space impedance.

We observe that the total field must have the same z dependence as the incident field because the wedge is infinite along the z direction and the SIBCs are independent of z. Therefore, from Maxwell's equations

$$E_\rho = \frac{1}{jk\sin^2\beta_o}\left\{\cos\beta_o\frac{\partial E_z}{\partial\rho} + \frac{1}{\rho}\frac{\partial}{\partial\phi}(ZH_z)\right\} \tag{5.3}$$

$$E_\phi = \frac{1}{jk\sin^2\beta_o}\left\{\cos\beta_o\frac{1}{\rho}\frac{\partial E_z}{\partial\phi} - \frac{\partial}{\partial\rho}(ZH_z)\right\} \tag{5.4}$$

$$ZH_\rho = \frac{1}{jk\sin^2\beta_o}\left\{\cos\beta_o\frac{\partial}{\partial\rho}(ZH_z) - \frac{1}{\rho}\frac{\partial E_z}{\partial\phi}\right\} \tag{5.5}$$

$$ZH_\phi = \frac{1}{jk\sin^2\beta_o}\left\{\frac{\partial E_z}{\partial\rho} + \cos\beta_o\frac{1}{\rho}\frac{\partial}{\partial\phi}(ZH_z)\right\} \tag{5.6}$$

and these can be used to rewrite the SIBCs in a more convenient form not involving the z components of the electric and magnetic field. Beginning with the usual forms

of the SIBCs given in terms of the tangential fields, we have

$$E_\rho = \mp\eta_\pm Z H_z \qquad \text{at } \phi = \pm\Phi \tag{5.7}$$

$$E_z = \pm\eta_\pm Z H_\rho \qquad \text{at } \phi = \pm\Phi \tag{5.8}$$

Differentiating these with respect to z we obtain (tangential differentiation of the boundary conditions is allowed)

$$\frac{\partial E_\rho}{\partial z} = \mp\eta_\pm Z \frac{\partial H_z}{\partial z} \tag{5.9}$$

$$\frac{\partial E_z}{\partial z} = \pm\eta_\pm Z \frac{\partial H_\rho}{\partial z} \tag{5.10}$$

Alternatively on multiplying (5.7) with ρ and then differentiating (5.7) and (5.8) with respect to ρ yields

$$\frac{\partial}{\partial \rho}(\rho E_\rho) = \mp\eta_\pm Z \frac{\partial}{\partial \rho}(\rho H_z) \tag{5.11}$$

$$\frac{\partial E_z}{\partial \rho} = \pm\eta_\pm Z \frac{\partial H_\rho}{\partial \rho} \tag{5.12}$$

and these are of course equivalent to the previous two sets.

Other alternative boundary conditions can be obtained by combining the sets (5.9)–(5.10) and (5.11)–(5.12). In particular, by dividing (5.11) with ρ and adding the resulting equation to (5.10) we get

$$-\frac{1}{\rho}\frac{\partial E_\phi}{\partial \phi} = \pm\eta_\pm Z \left(\frac{\partial H_\rho}{\partial z} - \frac{\partial H_z}{\partial \rho} \right) \mp \eta_\pm Z \frac{1}{\rho} H_z \tag{5.13}$$

where we have also used the divergence condition

$$\nabla \cdot \overline{E} = \frac{1}{\rho}\frac{\partial}{\partial \rho}(\rho E_\rho) + \frac{1}{\rho}\frac{\partial E_\phi}{\partial \phi} + \frac{\partial E_z}{\partial z} = 0 \tag{5.14}$$

However, (5.13) can be simplified further upon noting that

$$\left(\frac{\partial H_\rho}{\partial z} - \frac{\partial H_z}{\partial \rho}\right) = jkYE_\phi \tag{5.15}$$

when this is introduced in (5.13) along with (5.7) we obtain the condition

$$\frac{\partial E_\phi}{\partial \phi} \pm j\eta_\pm k\rho E_\phi + E_\rho = 0 \tag{5.16}$$

which is just another form of the SIBC not involving any of the z field components. Proceeding in a similar manner, we can combine (5.9) and (5.12) to obtain

$$\frac{\partial H_\phi}{\partial \phi} \pm j\frac{1}{\eta_\pm} k\rho H_\phi + H_\rho = 0 \tag{5.17}$$

which is obviously the dual of (5.16). As we shall see in the next section, equation (5.16) and (5.17) are the most convenient forms of the SIBCs necessary for the application of Maliuzhinets' method in the case of skew incidence.

5.2 Derivation of the Functional Difference Equations

To apply Maliuzhinets' method [11] for the solution of the impedance wedge diffracted fields we begin by first representing the total fields in the presence of the wedge as

$$E_z = \frac{e^{-jkz\cos\beta_o}}{2\pi j} \int_\gamma e^{jk\rho\sin\beta_o\cos\alpha} S_e(\alpha+\phi)d\alpha \tag{5.18}$$

$$ZH_z = \frac{e^{-jkz\cos\beta_o}}{2\pi j} \int_\gamma e^{jk\rho\sin\beta_o\cos\alpha} S_h(\alpha+\phi)d\alpha \tag{5.19}$$

These are complete spectral representations where γ is the Sommerfeld contour shown in figure 5.2 and $S_{e,h}$ are unknown spectral functions.

The goal in the subsequent steps is the explicit determination of $S_{e,h}$ on the basis of the governing Maxwell's equations and the boundary conditions (5.16)–(5.17). On

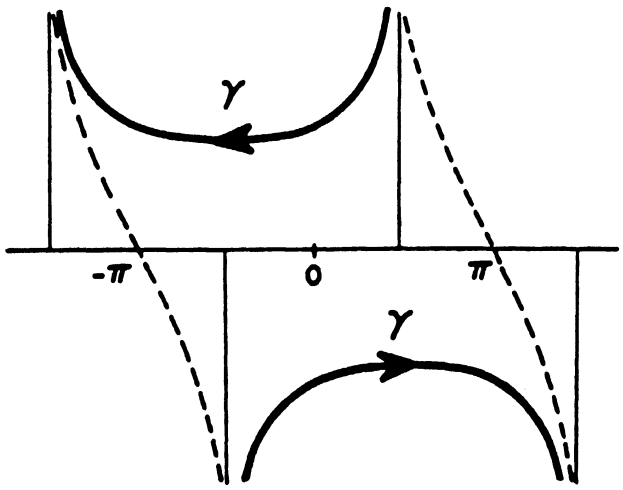

Figure 5.2: Sommerfeld contour γ in the complex α plane.

enforcing the boundary conditions (5.16)- (5.17) at $\phi = \pm\Phi$ along with (5.3)-(5.6) we obtain

$$\int_{\gamma} e^{jk\rho \sin\beta_o \cos\alpha} \left(\sin\alpha \pm \frac{1}{\eta_{\pm} \sin\beta_o}\right) \{\cos\beta_o \sin\alpha S_h(\alpha \pm \Phi) + \cos\alpha S_e(\alpha \pm \Phi)\} = 0 \tag{5.20}$$

$$\int_{\gamma} e^{jk\rho \sin\beta_o \cos\alpha} \left(\sin\alpha \pm \frac{\eta_{\pm}}{\sin\beta_o}\right) \{\cos\beta_o \sin\alpha S_e(\alpha \pm \Phi) - \cos\alpha S_h(\alpha \pm \Phi)\} = 0 \tag{5.21}$$

These are four coupled integral equations and we observe that $S_{e,h}$ are decoupled when $\cos\beta_o = 0$ corresponding to the case of normal incidence. Note that the top and bottom face impedances $\eta_{\pm}$ appear in the dual factor multiplying the integrands and this is a consequence of the new SIBCs (5.16)-(5.17). According to Maliuzhinets [11], the necessary and sufficient condition to satisfy (5.20) and (5.21) is that the

integrands be even functions of α. A mathematical statement of this is

$$A_e^{\pm}(\alpha)\{\cos\alpha S_e(\alpha\pm\Phi)+\cos\beta_o\sin\alpha S_h(\alpha\pm\Phi)\}= \cos\alpha S_e(-\alpha\pm\Phi)-\cos\beta_o\sin\alpha S_h(-\alpha\pm\Phi) \tag{5.22}$$

$$A_h^{\pm}(\alpha)\{\cos\beta_o\sin\alpha S_e(\alpha\pm\Phi)-\cos\alpha S_h(\alpha\pm\Phi)\}= -\cos\beta_o\sin\alpha S_e(-\alpha\pm\Phi)-\cos\alpha S_h(-\alpha\pm\Phi) \tag{5.23}$$

where

$$A_{e,h}^{\pm}(\alpha)=\frac{\sin\alpha\pm\sin\theta_{e,h}^{\pm}}{-\sin\alpha\pm\sin\theta_{e,h}^{\pm}} \tag{5.24}$$

with

$$\sin\theta_e^{\pm}=\frac{1}{\eta_{\pm}\sin\beta_o}\qquad \sin\theta_h^{\pm}=\frac{\eta_{\pm}}{\sin\beta_o} \tag{5.25}$$

Equations (5.22) and (5.23) are functional difference equations which are coupled and cannot in general be solved for $S_{e,h}(\alpha)$ in a closed form. In the case of normal incidence ($\cos\beta_o=0$), the difference equations take the form

$$A_e^{\pm}(\alpha)S_e(\alpha\pm\Phi)=S_e(-\alpha\pm\Phi) \tag{5.26}$$

$$A_h^{\pm}(\alpha)S_h(\alpha\pm\Phi)=S_h(-\alpha\pm\Phi) \tag{5.27}$$

and each of these difference equations can then be solved independently via Maliuzhinets' method. Equations (5.22) and (5.23) can also be decoupled for some special cases by employing certain suitable linear combinations of the spectral functions S_e and S_h [15]. In particular, separation can be achieved for

(a) a half plane ($\Phi=\pi$)

(b) a two part plane ($\Phi=\pi/2$)

(c) a right angled wedge with one face perfectly conducting ($\Phi=3\pi/4$ and $\Phi=\pi/4$).

5.3 Approximate Solution of the Difference Equations

In this section, we shall consider approximate solutions of (5.22)–(5.23) for arbitrary impedance wedge angles and surface impedances $\eta_{\pm}$. As mentioned earlier, these are coupled and cannot be separated for an arbitrary wedge angle Φ ($\Phi \leq \pi$) and β_o ($0 \leq \beta_o \leq \pi/2$). However, approximate solutions can be obtained which will be shown to be of acceptable accuracy over a certain angular sector exterior to the wedge. In the following, three approximate solutions to the difference equations (5.22)–(5.23) are presented whose combined validity range encloses the entire region of interest. Since most wedges of practical interest have $\pi/2 \leq \Phi \leq \pi$, we shall restrict our study to this region.

5.3.1 Separation Method I

For this separation method we shall assume that Φ is near π ($\Phi = \pi$ being the half plane case) and at the same time β_o is close to $\pi/2$ ($\beta_o = \pi/2$ being the normal incidence case). The resulting solution for $S_{e,h}$ is expected to be most accurate for wedges having $\Phi \approx \pi$ and/or $\beta_o \approx \pi/2$. We also expect that the approximation will recover the known half plane solution and that at normal incidence with arbitrary wedge angle. On our way to obtain such an approximate solution, we first divide (5.22) and (5.23) by $\cos\alpha$ giving

$$A_e^{\pm}(\alpha)\left\{\cos\beta_o \tan\alpha S_h(\alpha \pm \Phi) + S_e(\alpha \pm \Phi)\right\} = \\ -\cos\beta_o \tan\alpha S_h(-\alpha \pm \Phi) + S_e(-\alpha \pm \Phi) \tag{5.28}$$

and

$$A_h^{\pm}(\alpha)\left\{\cos\beta_o \tan\alpha S_e(\alpha \pm \Phi) - S_h(\alpha \pm \Phi)\right\} = \\ -\cos\beta_o \tan\alpha S_e(-\alpha \pm \Phi) - S_h(-\alpha \pm \Phi) \tag{5.29}$$

We now have two options in proceeding with the decoupling of (5.28) and (5.29). We may, for example, opt to satisfy the boundary conditions on the upper face ($\phi = +\Phi$) exactly and only approximately on the lower face ($\phi = -\Phi$). Alternatively, we may instead choose to satisfy the boundary conditions on the lower face of the wedge exactly and only approximately on the upper face. Proceeding with the first option, we introduce

$$t_1(\alpha + \Phi) = \cos\beta_o \tan\alpha S_h(\alpha + \Phi) + S_e(\alpha + \Phi) \tag{5.30}$$

$$t_2(\alpha + \Phi) = \cos\beta_o \tan\alpha S_e(\alpha + \Phi) - S_h(\alpha + \Phi) \tag{5.31}$$

Then

$$t_1(\alpha - \Phi) = \cos\beta_o \tan(\alpha - 2\Phi) S_h(\alpha - \Phi) + S_e(\alpha - \Phi) \tag{5.32}$$

$$t_2(\alpha - \Phi) = \cos\beta_o \tan(\alpha - 2\Phi) S_e(\alpha - \Phi) - S_h(\alpha - \Phi) \tag{5.33}$$

and on noting that

$$\cos\beta_o \tan(\alpha - 2\Phi) = \cos\beta_o \tan\alpha - \cos\beta_o \tan 2\Phi \left\{\tan(\alpha - 2\Phi)\tan\alpha + 1\right\} \tag{5.34}$$

we can rewrite (5.32) and (5.33) as

$$t_1(\alpha - \Phi) = \cos\beta_o \tan\alpha S_h(\alpha - \Phi) + S_e(\alpha - \Phi) + b_1(\alpha) \tag{5.35}$$

$$t_2(\alpha - \Phi) = \cos\beta_o \tan\alpha S_e(\alpha - \Phi) - S_h(\alpha - \Phi) + b_2(\alpha) \tag{5.36}$$

where

$$b_{1,2}(\alpha) = -\cos\beta_o \tan 2\Phi \left\{\tan(\alpha - 2\Phi)\tan\alpha + 1\right\} S_{h,e}(\alpha - \Phi) \tag{5.37}$$

Substituting now (5.30), (5.31), (5.35) and (5.36) into (5.28) and (5.29) yields the new difference equations

$$A^{+}_{e,h}(\alpha)t_{1,2}(\alpha+\Phi) = t_{1,2}(-\alpha+\Phi) \tag{5.38}$$

for the upper face and

$$A^{-}_{e,h}(\alpha)t_{1,2}(\alpha-\Phi) = t_{1,2}(-\alpha-\Phi) + p_{1,2}(\alpha) \tag{5.39}$$

for the lower face of the wedge with

$$p_{1,2}(\alpha) = A^{-}_{e,h}(\alpha)b_{1,2}(\alpha) - b_{1,2}(-\alpha) \tag{5.40}$$

To decouple t_1 and t_2 on the basis of (5.39) and (5.40) it is necessary that we set $p_{1,2}(\alpha) = 0$ and this approximation affects primarily the boundary conditions imposed on the lower impedance wedge face. To observe this let us replace α with $\alpha+\Phi$ in (5.38) and with $\alpha-\Phi$ in (5.39). When the resulting equations are subtracted, we obtain

$$A^{+}_{e,h}(\alpha+\Phi)t_{1,2}(\alpha+2\Phi) - A^{-}_{e,h}(\alpha-\Phi)t_{1,2}(\alpha-2\Phi) = f_{1,2}(\alpha) \tag{5.41}$$

where

$$f_{1,2}(\alpha) = -p_{1,2}(\alpha-\Phi) = \frac{2\cos\beta_o \sin 2\Phi}{\cos 2\Phi + \cos 4\Phi \cos 2\alpha + \sin 4\Phi \sin 2\alpha} A^{-}_{e,h}(\alpha-\Phi)$$

$$\cdot S_{h,e}(\alpha-2\Phi) - \frac{2\cos\beta_o \sin 2\Phi}{\cos 2\Phi + \cos 2\alpha} S_{h,e}(-\alpha) \tag{5.42}$$

For $f_{1,2}(\alpha) = 0$, the two difference equations (5.41) become linear first order homogeneous functional difference equations and can be solved via Maliuzhinets' method for t_1 and t_2. It is interesting to note that $f_{1,2}(\alpha)$ is identically zero when $\cos\beta_o \sin 2\Phi = 0$. Thus on setting $f_{1,2}(\alpha) = 0$, the resulting solution for $t_{1,2}(\alpha)$ is the exact one for the cases where

(a) $\beta_o = \pi/2$ (normal incidence with arbitrary wedge angle)

(b) $\Phi = \pi$ (half plane with arbitrary β_o)

(c) $\Phi = \pi/2$ (two part plane with arbitrary β_o).

Therefore, any solution of (5.41), based on the assumption that $\cos\beta_o \sin 2\Phi \approx 0$, will exactly recover all three cases mentioned above.

Once $t_{1,2}(\alpha)$ are found from a solution of (5.41), the corresponding $S_{e,h}(\alpha)$ spectra are obtained by inverting (5.30) and (5.31). First, we rewrite these as

$$t_1(\alpha) = \cos\beta_o \frac{\sin(\alpha-\Phi)}{\cos(\alpha-\Phi)} S_h(\alpha) + S_e(\alpha) \tag{5.43}$$

$$t_2(\alpha) = \cos\beta_o \frac{\sin(\alpha-\Phi)}{\cos(\alpha-\Phi)} S_e(\alpha) - S_h(\alpha) \tag{5.44}$$

and from these we readily find that

$$S_e(\alpha) = \frac{\cos(\alpha-\Phi)}{1-\sin^2\beta_o \sin^2(\alpha-\Phi)} \{\cos(\alpha-\Phi)t_1(\alpha) + \cos\beta_o \sin(\alpha-\Phi)t_2(\alpha)\} \tag{5.45}$$

$$S_h(\alpha) = \frac{\cos(\alpha-\Phi)}{1-\sin^2\beta_o \sin^2(\alpha-\Phi)} \{\cos\beta_o \sin(\alpha-\Phi)t_1(\alpha) - \cos(\alpha-\Phi)t_2(\alpha)\} \tag{5.46}$$

From Maliuzhinets [11], a solution of (5.41), with $f_{1,2}(\alpha) \approx 0$, which is free of poles and zeros in the strip $|Re(\alpha)| \leq \Phi$ is the auxiliary Maliuzhinets' function $\Psi(\alpha, \theta^+_{e,h}, \theta^-_{e,h})$ defined by the product

$$\begin{aligned}\Psi\left(\alpha, \theta^+_{e,h}, \theta^-_{e,h}\right) &= \Psi_\Phi\left(\alpha + \Phi + \frac{\pi}{2} - \theta^+_{e,h}\right) \Psi_\Phi\left(\alpha - \Phi - \frac{\pi}{2} + \theta^-_{e,h}\right) \\ &\cdot \Psi_\Phi\left(\alpha + \Phi - \frac{\pi}{2} + \theta^+_{e,h}\right) \Psi_\Phi\left(\alpha - \Phi + \frac{\pi}{2} - \theta^-_{e,h}\right)\end{aligned} \tag{5.47}$$

where $\Psi_\Phi(\alpha)$ is the Maliuzhinets' function for which simple analytic expressions are given in [50]. For large $|Im(\alpha)|$, this function has the property

$$\lim_{|Im(\alpha)|\to\infty} \Psi_\Phi(\alpha) = O\left\{exp\frac{|Im(\alpha)|}{8\Phi}\right\} \tag{5.48}$$

where $O(\cdot)$ is the Landau symbol. We may thus express $t_{1,2}(\alpha)$ as

$$t_{1,2}(\alpha) = \sigma_{1,2}(\alpha)\frac{\Psi(\alpha, \theta_{e,h}^{+}, \theta_{e,h}^{-})}{\Psi(\phi', \theta_{e,h}^{+}, \theta_{e,h}^{-})} \tag{5.49}$$

where $\sigma_{1,2}(\alpha)$ satisfies the equation

$$\sigma_{1,2}(\alpha \pm \Phi) = \sigma_{1,2}(-\alpha \pm \Phi) \tag{5.50}$$

and from (5.38) and (5.39) its presence is allowable since

$$A_{e,h}^{\pm}(\alpha)\Psi(\alpha \pm \Phi) = \Psi(-\alpha \pm \Phi) \tag{5.51}$$

In accordance with (5.50) the most general solution for $\sigma_{1,2}(\alpha)$ is

$$\sigma_{1,2}(\alpha) = \sin^{m}\left(\frac{\pi\alpha}{2\Phi}\right) \tag{5.52}$$

where m is an integer. However, before proposing any form of $\sigma_{1,2}(\alpha)$, we note certain characteristics that must be satisfied as dictated by the physics of the problem. They are:

(a) $\sigma_{1,2}(\alpha)$ must have a first order pole singularity in the strip $|Re(\alpha)| \leq \Phi$ at $\alpha = \phi'$ to allow recovery of the incident field

(b) $S_{e,h}(\alpha) = O(constant)$ for large $|Im(\alpha)|$ (since the fields at the edge take a constant nonzero value)

(c) $\sigma_{1,2}(\alpha)$ should contain the pole singularities associated with the term $1/\cos(\alpha - \Phi)$ which lie in the strip $|Re(\alpha)| < \pi$. This is a consequence of the solution procedure.

In view of these requirements, $\sigma_{1,2}(\alpha)$ should be of the form

$$\sigma_{1,2}(\alpha) = A_{1,2}\frac{\frac{1}{n}\cos\frac{\phi'}{n}}{\sin\frac{\alpha}{n} - \sin\frac{\phi'}{n}} + \frac{C_{e,h}}{\left(\sin\frac{\alpha}{n} - \sin\frac{\alpha_1}{n}\right)} + \frac{D_{e,h}}{\left(\sin\frac{\alpha}{n} - \sin\frac{\alpha_2}{n}\right)} \tag{5.53}$$

The coefficients $A_{1,2}$, $C_{e,h}$ and $D_{e,h}$ are constants to be determined and $\alpha_1 = \Phi - \frac{\pi}{2}$, $\alpha_2 = \Phi - \frac{3\pi}{2}$ represent the zeros of $\cos(\alpha - \Phi)$ in the strip $|Re(\alpha)| < \pi$.

The constants $A_{1,2}$ are obtained by requiring that the final solution recovers the incident field. For this, it is necessary that

$$e_z = \frac{\cos(\phi' - \Phi)}{1 - \sin^2\beta_o \sin^2(\phi' - \Phi)} \{\cos(\phi' - \Phi)A_1 + \cos\beta_o \sin(\phi' - \Phi)A_2\} \tag{5.54}$$

$$h_z = \frac{\cos(\phi' - \Phi)}{1 - \sin^2\beta_o \sin^2(\phi' - \Phi)} \{\cos\beta_o \sin(\phi' - \Phi)A_1 - \cos(\phi' - \Phi)A_2\} \tag{5.55}$$

giving

$$A_1 = \cos\beta_o \tan(\phi' - \Phi)h_z + e_z \tag{5.56}$$

$$A_2 = \cos\beta_o \tan(\phi' - \Phi)e_z - h_z \tag{5.57}$$

To determine the constants $C_{e,h}$ and $D_{e,h}$, we note that the expressions for $S_{e,h}$ given in (5.45) and (5.46) have four undesirable poles, all in the strip $|Re(\alpha)| < \pi$. These are associated with the multiplying factor $\left\{1 - \sin^2\beta_o \sin^2(\alpha - \Phi)\right\}^{-1}$ and are given by

$$\xi_{1,2} = \left(\Phi - \frac{\pi}{2}\right) \pm \alpha_o, \qquad \xi_{3,4} = \left(\Phi - \frac{3\pi}{2}\right) \pm \alpha_o \qquad (\pi/2 \leq \Phi \leq \pi) \tag{5.58}$$

with

$$\alpha_o = j \ln\left(\tan\frac{\beta_o}{2}\right) \tag{5.59}$$

so that $\cos\alpha_o = \csc\beta_o$ and $\sin\alpha_o = -j\cot\beta_o$. Each one of these poles corresponds to an inhomogeneous plane wave which grows exponentially with increasing $k\rho$ in some region of space and it is thus necessary to remove these poles by choosing the constants $C_{e,h}$ and $D_{e,h}$ such that the numerator of $S_{e,h}$ goes to zero at these poles. From (5.45), the conditions, which must be satisfied to eliminate these undesired poles are

$$\pm jt_1\left(\Phi - \frac{\pi}{2} \pm \alpha_o\right) + t_2\left(\Phi - \frac{\pi}{2} \pm \alpha_o\right) = 0 \tag{5.60}$$

$$\pm jt_1\left(\Phi - \frac{3\pi}{2} \pm \alpha_o\right) + t_2\left(\Phi - \frac{3\pi}{2} \pm \alpha_o\right) = 0 \tag{5.61}$$

which are four equations sufficient for determining the constants $C_{e,h}$ and $D_{e,h}$. A set of conditions, identical to (5.60)–(5.61), can also be obtained by similar arguments imposed on (5.46). Thus cancellation of the undesired poles for $S_e(\alpha)$ is carried over to $S_h(\alpha)$.

To obtain the z components of the far zone diffracted field, we first deform the Sommerfeld contour shown in figure 5.2 into a steepest descent path. A non-uniform evaluation of the integrals via the steepest descent method then yields

$$E_z^d \approx \frac{e^{-jk\rho\sin\beta_o}e^{-j\frac{\pi}{4}}}{\sqrt{2\pi k\rho\sin\beta_o}}\{S_e(\phi-\pi) - S_e(\phi+\pi)\} \tag{5.62}$$

$$ZH_z^d \approx \frac{e^{-jk\rho\sin\beta_o}e^{-j\frac{\pi}{4}}}{\sqrt{2\pi k\rho\sin\beta_o}}\{S_h(\phi-\pi) - S_h(\phi+\pi)\} \tag{5.63}$$

We note that in the far zone, the above z components of the diffracted field are proportional to the corresponding β_o and ϕ components via the relations

$$E_z^d = -\sin\beta_o E_{\beta_o}^d \qquad ZH_z^d = -\sin\beta_o E_\phi^d \tag{5.64}$$

Similarly, for the incident fields

$$E_z^i = \sin\beta_o E_{\beta_o}^i \qquad ZH_z^i = \sin\beta_o E_\phi^i \tag{5.65}$$

The solution of the difference equations (5.28) and (5.29) as presented above recovers the exact solutions for the three special cases, namely those corresponding to, normal incidence ($\beta_o = \pi/2$) with arbitrary wedge angle, a half plane (arbitrary β_o, $\Phi = \pi$) and a two part plane (arbitrary β_o, $\Phi = \pi/2$). An important feature of this solution, lacked by other available solutions [13,14,15,19], is that a single computer code can be employed to compute the scattered field for all three special

cases mentioned above. However, our primary interest is to examine the accuracy of the solution for other wedge angles. We expect, of course, the solution to deteriorate as the wedge angle and/or the skewness angle β_o move away from the values corresponding to the special cases. This is illustrated in figures 5.3–5.6 where far zone backscatter ($\phi = \phi'$) patterns are given as a function of the observation angle ϕ and for different wedge angles. Figures 5.3 and 5.4 show the patterns for internal wedge angles of 0^o, 10^o, 20^o and 30^o with β_o kept at 30^o. In figures 5.5 and 5.6 β_o is varied from 90^o to 40^o while the internal wedge angle is kept constant at 30^o. From the plots in figures 5.4(b) and 5.6(b) we observe that the pattern deteriorates in the region beyond the reflection boundary of the upper face or in other words when the lower face becomes visible. This is concluded from the appearance of a false pole and a false null in the pattern not corresponding to any physical characteristic. Such a behavior is not unexpected because as noted earlier our solution emphasized the upper face boundary condition whereas the boundary condition for the lower face was only approximately satisfied since we arbitrarily had set $f_{1,2}(\alpha) = 0$. Next we introduce new linear combinations t_1 and t_2 to separate the difference equations so that the lower face boundary conditions are satisfied exactly whereas the upper face boundary conditions are only approximately satisfied. The derived solution should be more accurate for observations near the lower face of the wedge.

5.3.2 Separation Method II

To separate the equations for the lower face ($\phi = -\Phi$) of the impedance wedge we introduce the linear combinations

$$t_1(\alpha - \Phi) = \cos\beta_o \tan\alpha S_h(\alpha - \Phi) + S_e(\alpha - \Phi) \tag{5.66}$$

(a)

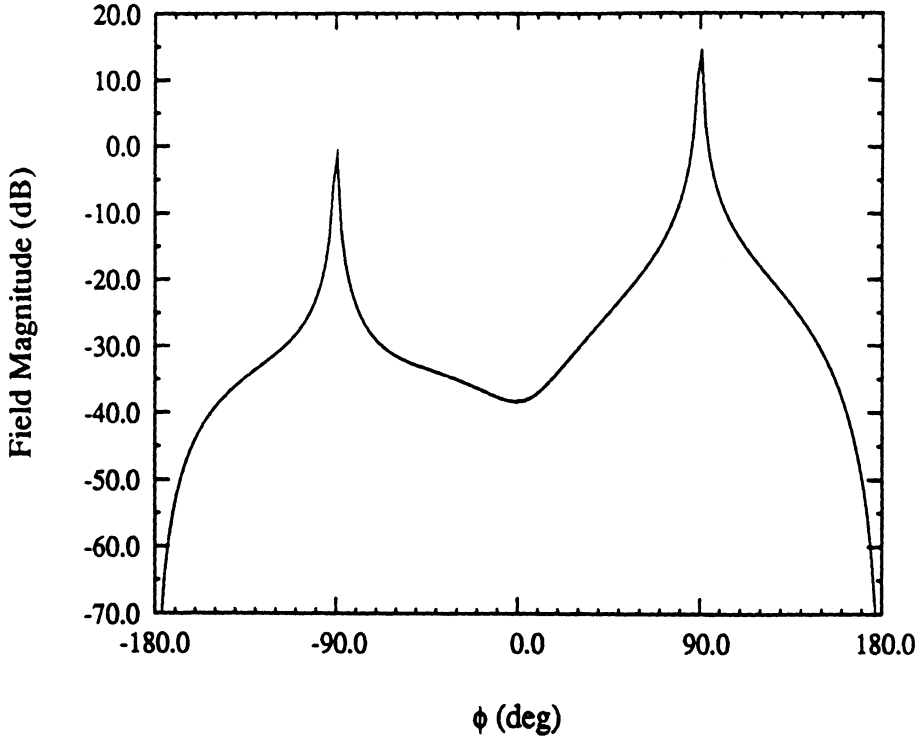

(b)

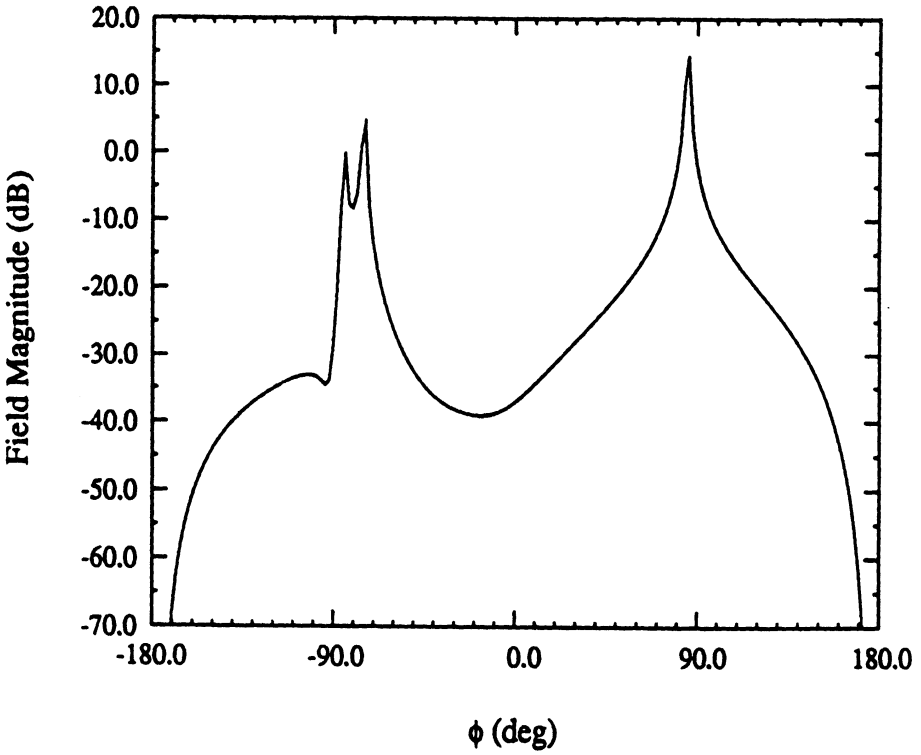

Figure 5.3: Far zone backscatter pattern for an impedance wedge having $\eta_+ = 1.0 - j1.0$, $\eta_- = 0.5 - j0.1$, $\beta_o = 30°$, $E_{\beta_o\beta_o'}$, (a) internal wedge angle = 0°, (b) internal wedge angle = 10°.

(a)

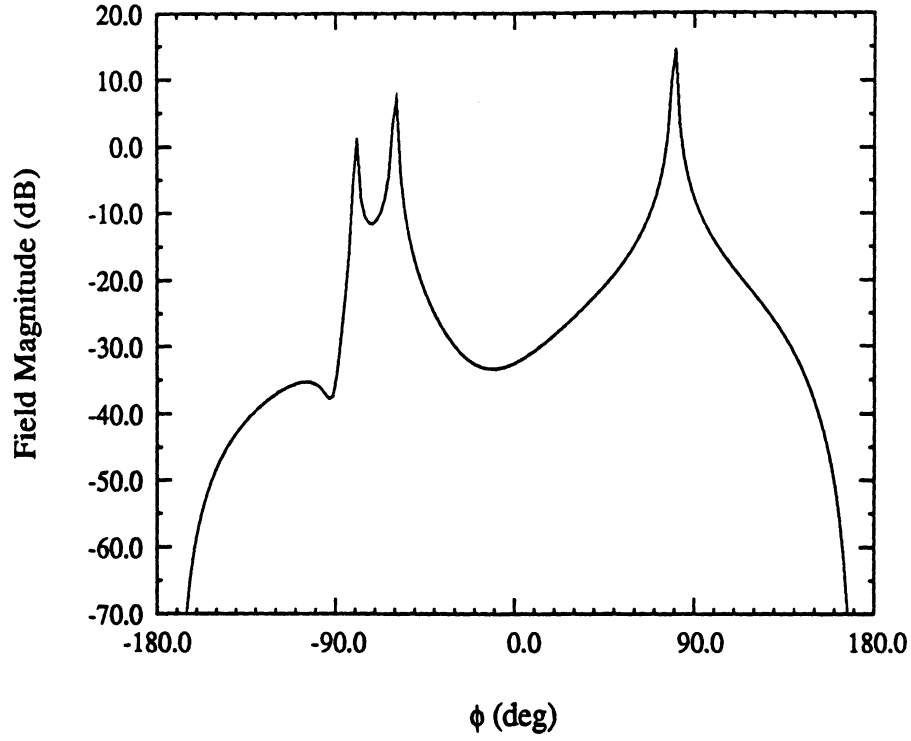

(b)

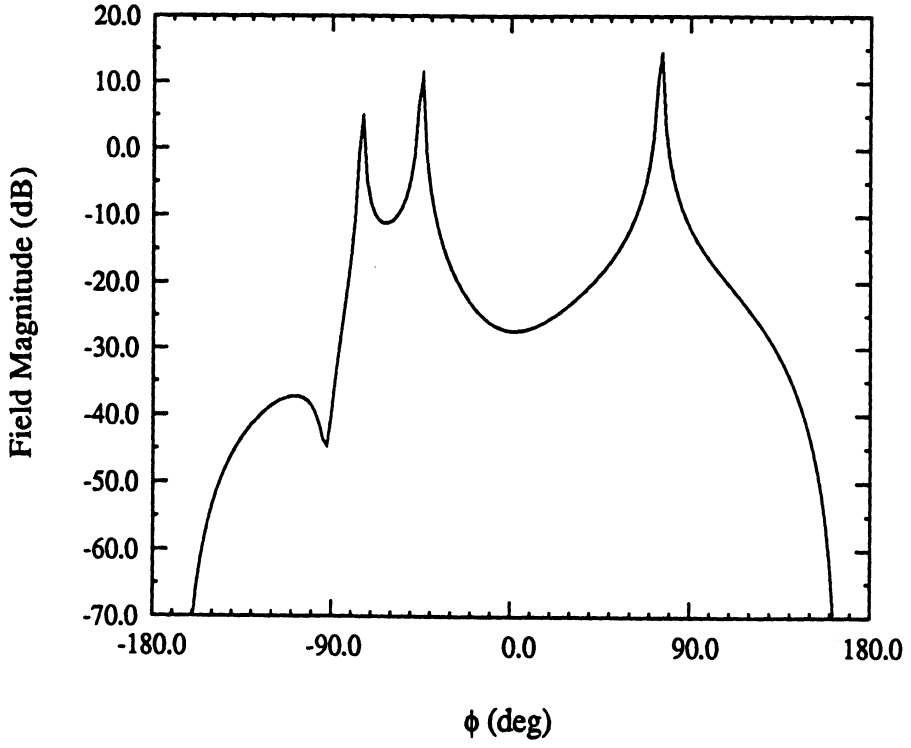

Figure 5.4: Far zone backscatter pattern for an impedance wedge having $\eta_+ = 1.0 - j1.0$, $\eta_- = 0.5 - j0.1$, $\beta_o = 30^o$, $E_{\beta_o\beta_o'}$, (a) internal wedge angle = 20^o, (b) internal wedge angle = 30^o.

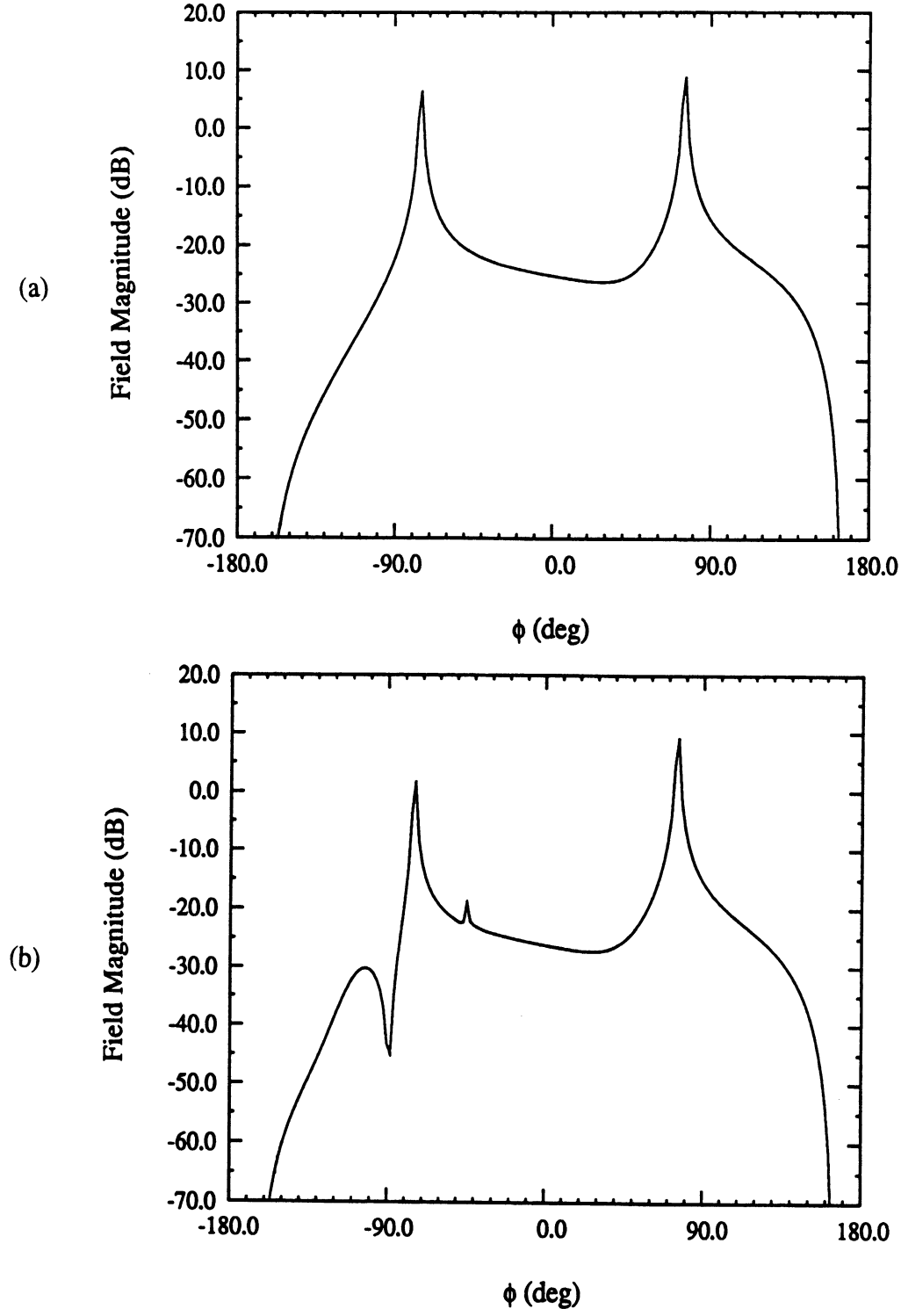

Figure 5.5: Far zone backscatter pattern for an impedance wedge having $\eta_+ = 1.0 - j1.0$, $\eta_- = 0.5 - j0.1$, internal wedge angle = 30°, $E_{\beta_o\beta_o'}$, (a) $\beta_o = 90°$, (b) $\beta_o = 70°$.

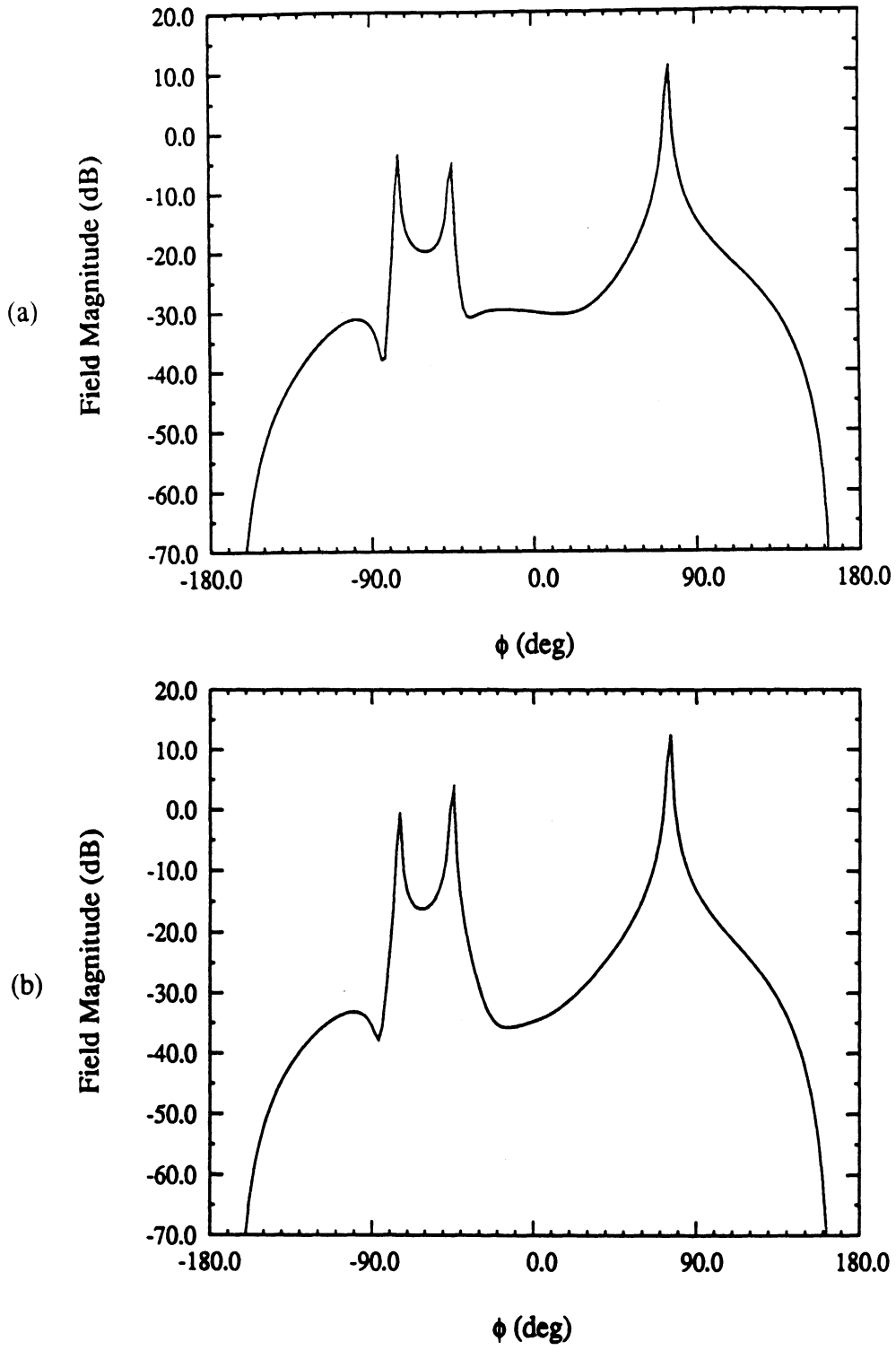

Figure 5.6: Far zone backscatter pattern for an impedance wedge having $\eta_+ = 1.0 - j1.0$, $\eta_- = 0.5 - j0.1$, internal wedge angle = 30°, $E_{\beta_o\beta_o'}$, (a) $\beta_o = 50°$, (b) $\beta_o = 40°$.

$$t_2(\alpha - \Phi) = \cos\beta_o \tan\alpha S_e(\alpha - \Phi) - S_h(\alpha - \Phi) \tag{5.67}$$

This implies that

$$t_1(\alpha + \Phi) = \cos\beta_o \tan(\alpha + 2\Phi) S_h(\alpha + \Phi) + S_e(\alpha + \Phi) \tag{5.68}$$

$$t_2(\alpha + \Phi) = \cos\beta_o \tan(\alpha + 2\Phi) S_e(\alpha + \Phi) - S_h(\alpha + \Phi) \tag{5.69}$$

and on following the procedure outlined in the previous section we get the difference equations

$$A^+_{e,h}(\alpha + \Phi) t_{1,2}(\alpha + 2\Phi) - A^-_{e,h}(\alpha - \Phi) t_{1,2}(\alpha - 2\Phi) = f_{1,2}(\alpha) \tag{5.70}$$

where $f_{1,2}(\alpha)$ is now given by

$$f_{1,2}(\alpha) = p_{1,2}(\alpha + \Phi) = \frac{2\cos\beta_o \sin 2\Phi}{\cos 2\Phi + \cos 4\Phi \cos 2\alpha + \sin 4\Phi \sin 2\alpha} A^+_{e,h}(\alpha + \Phi)$$

$$\cdot S_{h,e}(\alpha + 2\Phi) - \frac{2\cos\beta_o \sin 2\Phi}{\cos 2\Phi + \cos 2\alpha} S_{h,e}(-\alpha) \tag{5.71}$$

Again we note that $f_{1,2}(\alpha)$ is identically zero when $\cos\beta_o \sin 2\Phi = 0$. This implies that on setting $f_{1,2}(\alpha) = 0$ the resulting solution for $t_{1,2}(\alpha)$ is the exact one for the cases where

(a) $\beta_o = \pi/2$ (Normal incidence with arbitrary wedge angle)

(b) $\Phi = \pi$ (Half plane with arbitrary β_o)

(c) $\Phi = \pi/2$ (two part plane with arbitrary β_o).

The new expressions for $S_e(\alpha)$ and $S_h(\alpha)$ are

$$S_e(\alpha) = \frac{\cos(\alpha + \Phi)}{1 - \sin^2\beta_o \sin^2(\alpha + \Phi)} \{\cos(\alpha + \Phi) t_1(\alpha) + \cos\beta_o \sin(\alpha + \Phi) t_2(\alpha)\} \tag{5.72}$$

$$S_h(\alpha) = \frac{\cos(\alpha + \Phi)}{1 - \sin^2\beta_o \sin^2(\alpha + \Phi)} \{\cos\beta_o \sin(\alpha + \Phi) t_1(\alpha) - \cos(\alpha + \Phi) t_2(\alpha)\} \tag{5.73}$$

and the solutions for $t_{1,2}(\alpha)$ are again of the same form as in (5.49). The expressions for $\sigma_{1,2}(\alpha)$ will also be the same as given in (5.53) except for the replacements $\alpha_1 \rightarrow -\alpha_1$ and $\alpha_2 \rightarrow -\alpha_2$. On imposing the requirement for the incident field we get

$$A_1 = \cos\beta_o \tan(\phi' + \Phi) h_z + e_z \tag{5.74}$$

$$A_2 = \cos\beta_o \tan(\phi' + \Phi) e_z - h_z \tag{5.75}$$

and the constants $C_{e,h}$ and $D_{e,h}$ can be found by cancelling the undesired poles of $S_{e,h}$. These are now associated with the term $\left\{1 - \sin^2\beta_o \sin^2(\alpha + \Phi)\right\}^{-1}$ and for $|Re(\alpha)| < \pi$ are given by

$$\xi_{1,2} = \left(\frac{\pi}{2} - \Phi\right) \pm \alpha_o, \qquad \xi_{3,4} = \left(\frac{3\pi}{2} - \Phi\right) \pm \alpha_o \qquad (\pi/2 \leq \Phi \leq \pi) \tag{5.76}$$

where α_o is the same as before. From (5.72), the conditions which must be satisfied to eliminate the undesired poles are

$$\pm j t_1 \left(\frac{\pi}{2} - \Phi \pm \alpha_o\right) + t_2 \left(\frac{\pi}{2} - \Phi \pm \alpha_o\right) = 0 \tag{5.77}$$

$$\pm j t_1 \left(\frac{3\pi}{2} - \Phi \pm \alpha_o\right) + t_2 \left(\frac{3\pi}{2} - \Phi \pm \alpha_o\right) = 0 \tag{5.78}$$

leading to a 4×4 matrix for the solution of the constants $C_{e,h}$ and $D_{e,h}$. A non-uniform steepest descent path evaluation of (5.18) and (5.19) will, then, yield the far zone diffracted field as given in (5.62)–(5.63) with the new expressions for $S_{e,h}$ as given in (5.72)– (5.73).

Figures 5.7 and 5.8 show the far zone backscatter ($\phi = \phi'$) patterns of an impedance wedge for internal wedge angles of 0^o, 10^o, 20^o and 30^o with β_o kept at 30^o. In figures 5.9 and 5.10, β_o is varied from 90^o to 40^o while the internal wedge angle is kept constant at 30^o. Again, we note that the accuracy of the patterns

worsens as we move away from the special cases of a half plane (internal wedge angle=0°) or away from normal incidence wedge ($\beta_o = \pi/2$). When the internal wedge angle is not zero, close inspection of figures 5.8(b) and 5.10(b) reveals that the pattern deteriorates in the region beyond the reflection boundary of the lower face or in other words when the upper face becomes visible. This is concluded from the appearance of a false pole and a false null in the pattern not corresponding to any physical characteristics. Such behavior is not unexpected because our solution emphasized the lower face boundary condition whereas the boundary condition for the upper face was only approximately satisfied. The pattern is reasonable as long as the observation point remains near the lower face.

5.3.3 Separation Method III

We next turn our attention to the case when both faces of the wedge are visible. In order to obtain a solution of acceptable accuracy in this region, the difference equations associated with the upper and lower faces of the wedge have to be decoupled without introducing approximations to the implied boundary conditions. This can only be done if all trignometric terms in $S_{e,h}(\alpha)$ have a period of 2Φ. However, because of the presence of $\sin\alpha$ and $\cos\alpha$ this is not possible unless they are replaced by an expansion having that property. Suitable candidates for functions of this expansion are

$$\sin\frac{m\pi\alpha}{\Phi},\ \cos\frac{m\pi\alpha}{\Phi},\ \sin^m\frac{\pi\alpha}{\Phi},\ \cos^m\frac{\pi\alpha}{\Phi} \tag{5.79}$$

where m is an integer. From equations (5.62) and (5.63), we observe that in the final evaluation of the far zone diffracted field, α eventually takes on the real values of $\phi \pm \pi$. Also, to determine the constants $A_{1,2}$ we substitute ϕ' (a real valued variable) in place of α. This suggests that we may treat α as a real variable and represent

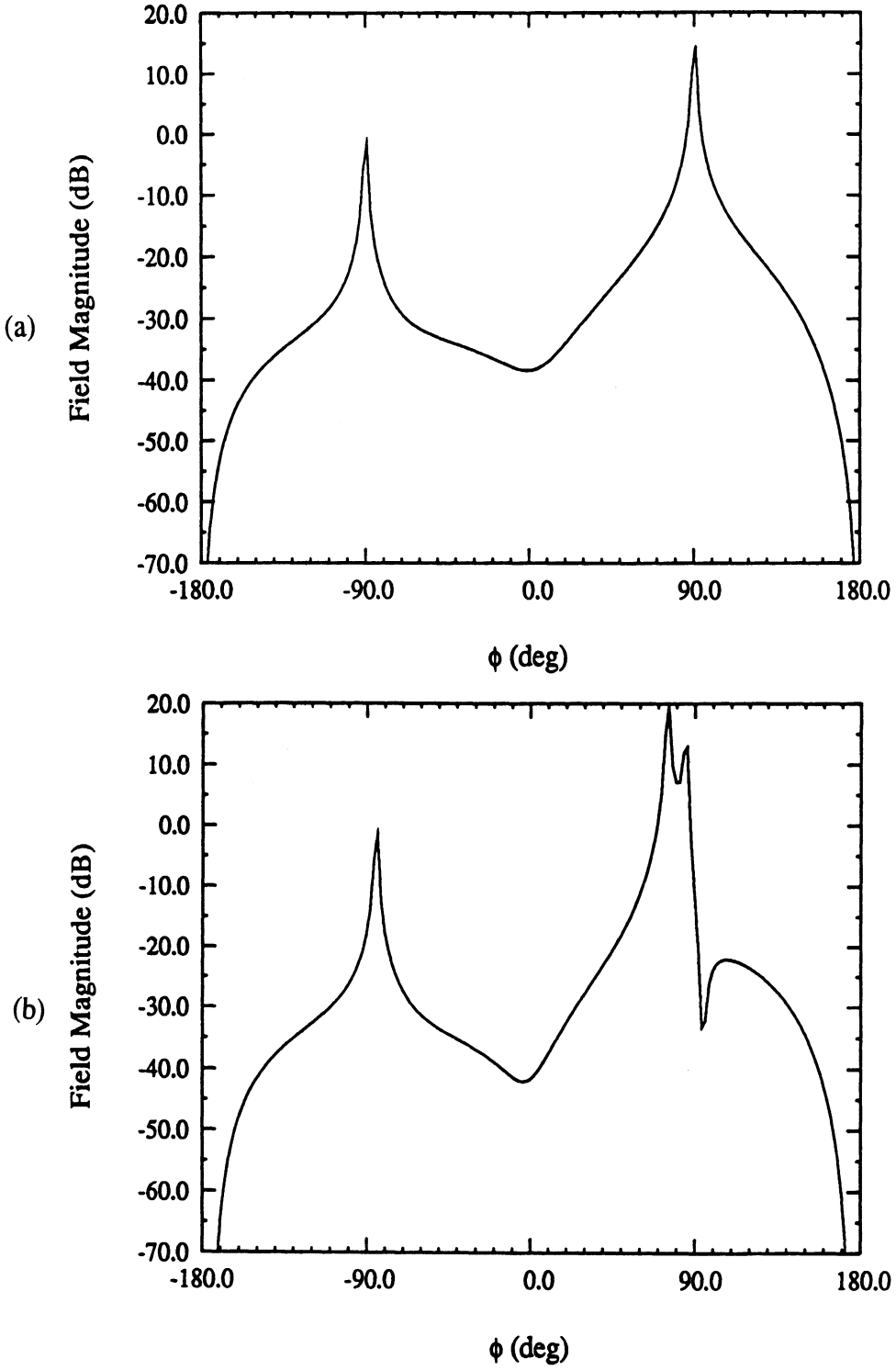

Figure 5.7: Far zone backscatter pattern for an impedance wedge having $\eta_+ = 1.0 - j1.0$, $\eta_- = 0.5 - j0.1$, $\beta_o = 30°$, $E_{\beta_o\beta_o'}$, (a) internal wedge angle = 0°, (b) internal wedge angle = 10°.

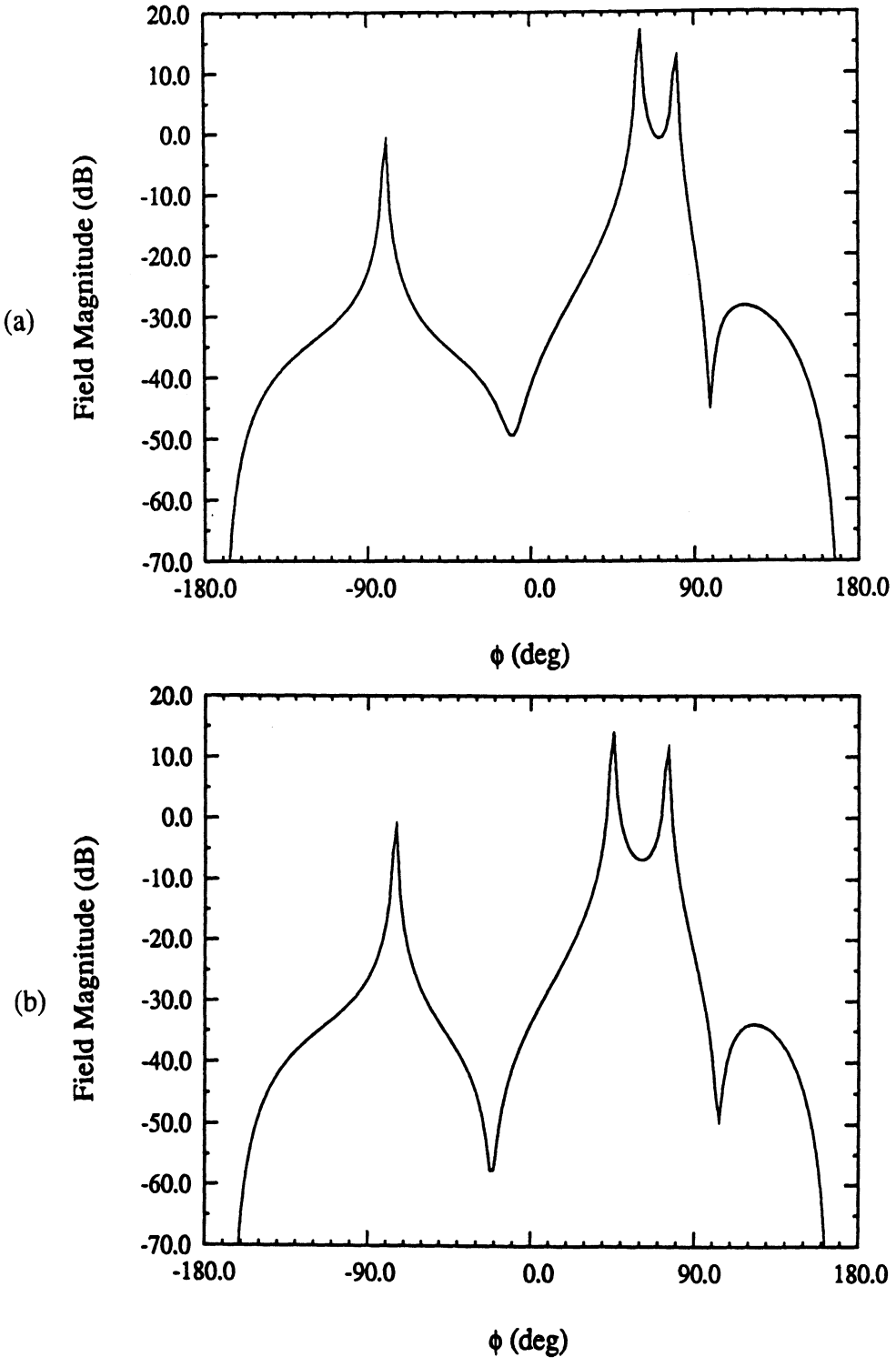

Figure 5.8: Far zone backscatter pattern for an impedance wedge having $\eta_+ = 1.0 - j1.0$, $\eta_- = 0.5 - j0.1$, $\beta_o = 30°$, $E_{\beta_o\beta_o'}$, (a) internal wedge angle = 20°, (b) internal wedge angle = 30°.

(a)

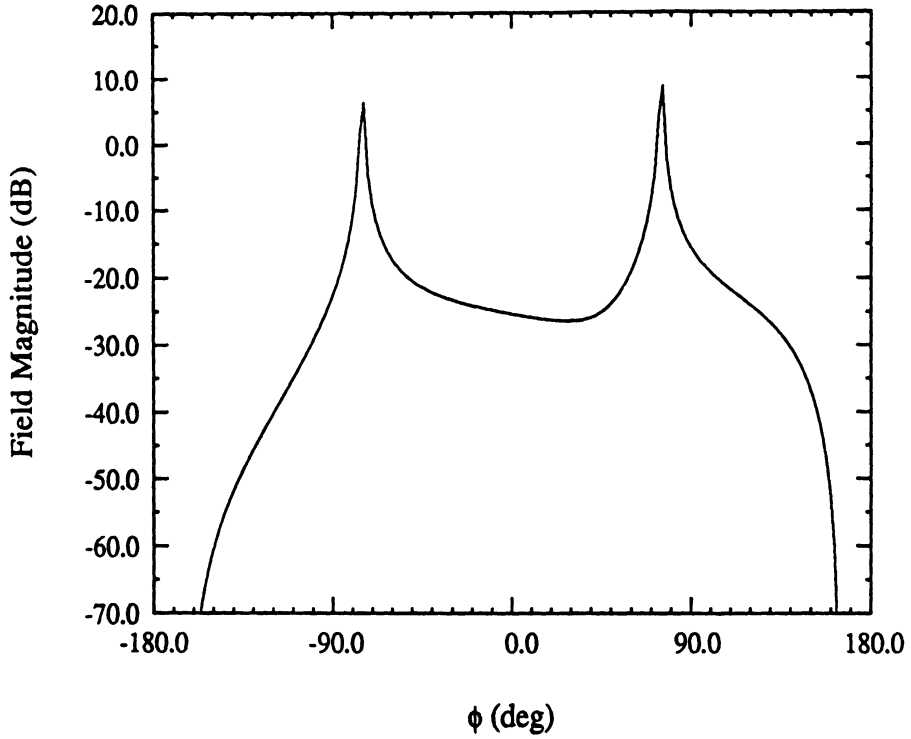

(b)

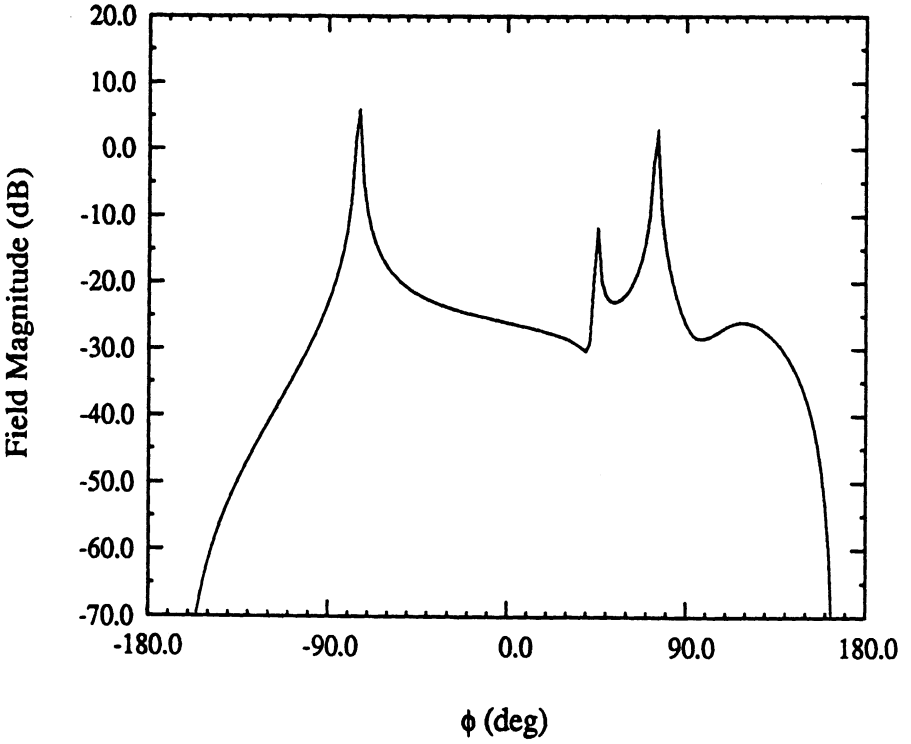

Figure 5.9: Far zone backscatter pattern for an impedance wedge having $\eta_+ = 1.0 - j1.0$, $\eta_- = 0.5 - j0.1$, internal wedge angle = 30°, $E_{\beta_o\beta_o'}$, (a) $\beta_o = 90°$, (b) $\beta_o = 70°$.

(a)

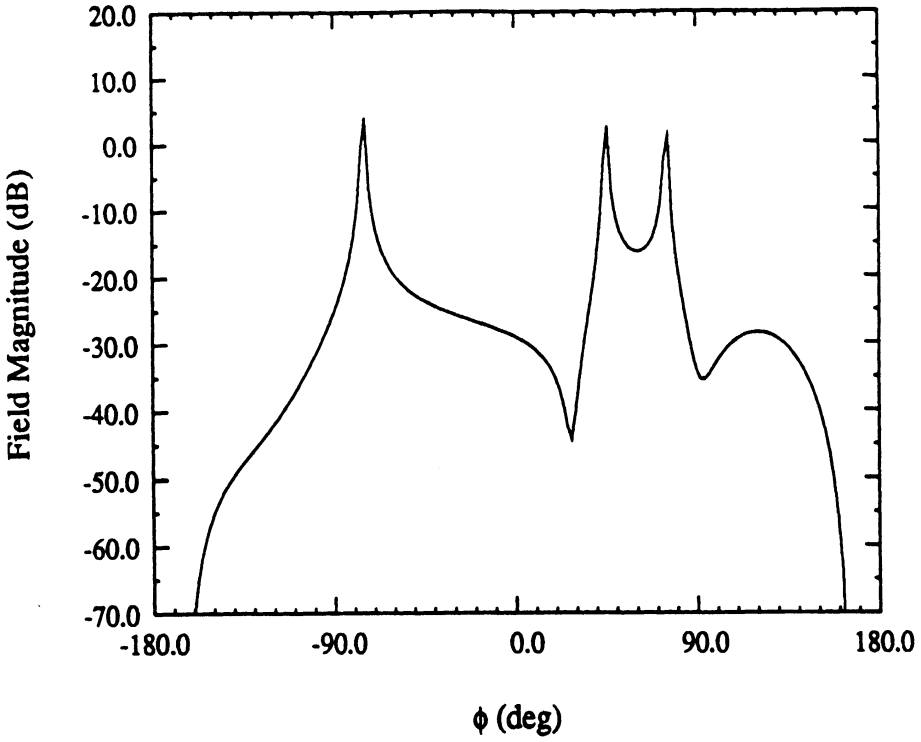

(b)

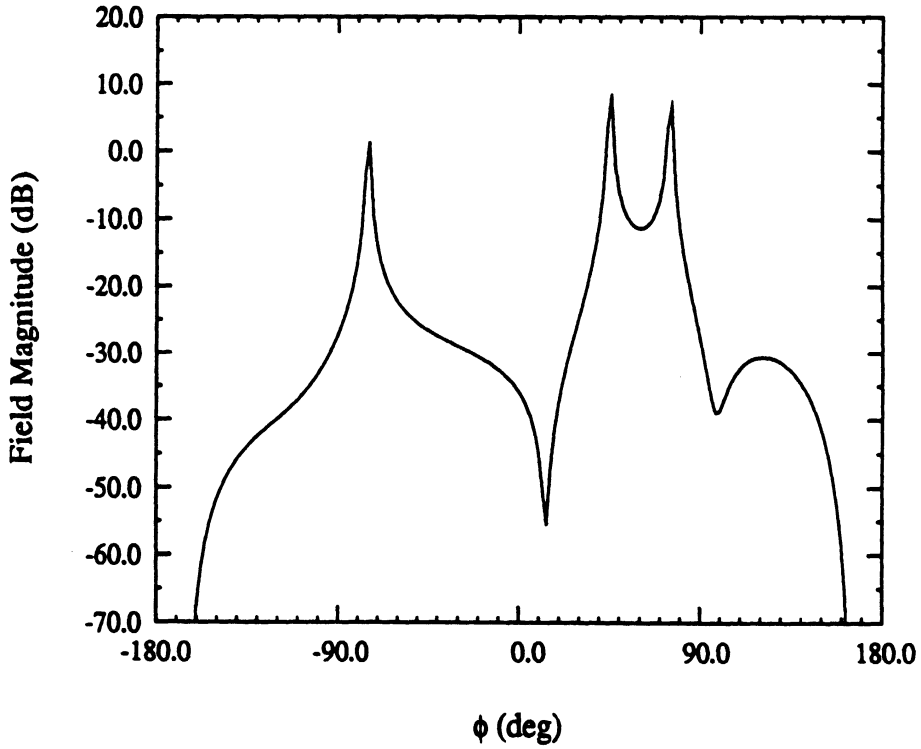

Figure 5.10: Far zone backscatter pattern for an impedance wedge having $\eta_+ = 1.0 - j1.0$, $\eta_- = 0.5 - j0.1$, internal wedge angle = 30°, $E_{\beta_o\beta_o'}$, (a) $\beta_o = 50°$, (b) $\beta_o = 40°$.

$\sin\alpha$ and $\cos\alpha$ in terms of a Fourier series given by

$$\cos\alpha = a_o + \sum_{m=1}^{\infty} a_m \cos\frac{m\pi\alpha}{\Phi} \tag{5.80}$$

$$\sin\alpha = \sum_{m=1}^{\infty} b_m \sin\frac{m\pi\alpha}{\Phi} \tag{5.81}$$

where

$$a_o = \frac{1}{2\Phi}\int_{-\Phi}^{\Phi} \cos\alpha d\alpha, \qquad a_m = \frac{1}{\Phi}\int_{-\Phi}^{\Phi} \cos\alpha\cos\frac{m\pi\alpha}{\Phi} d\alpha \tag{5.82}$$

and

$$b_m = \frac{1}{\Phi}\int_{-\Phi}^{\Phi} \sin\alpha\sin\frac{m\pi\alpha}{\Phi} d\alpha \tag{5.83}$$

The above series representations will approach $\sin\alpha$ and $\cos\alpha$, inside the real interval $[-\Phi, \Phi]$, depending on how many terms in the series are used for the approximation. Obviously, the expansion will deviate substantially from the actual values of $\sin\alpha$ and $\cos\alpha$ outside this interval. Since $\phi \pm \pi$ (with $-\Phi < \phi < \Phi$) replaces α in the evaluation of the far zone field, we would like the expansions (5.80)-(5.81) to remain accurate inside the intervals $[-\Phi - \pi, \Phi - \pi]$ and $[-\Phi + \pi, \Phi + \pi]$. From the above we conclude that this is not the case, and consequently the Fourier series expansion is not a suitable choice.

Another possibility for representing $\sin\alpha$ and $\cos\alpha$ by a function of period 2Φ is to use a few terms of the expansion with a_m, b_m other than those given by (5.82) and (5.83). In particular, we may choose the beginning terms of the series, namely $\sin\frac{\pi\alpha}{\Phi}$ and $\cos\frac{\pi\alpha}{\Phi}$ (where we have chosen $b_1 = 1, a_o = 0$ and $a_1 = 1$ for the time being), to approximate $\sin\alpha$ and $\cos\alpha$, respectively. To establish a measure of this approximation in representing $\sin\alpha$ and $\cos\alpha$ for other Φ, we refer to the plots of $\sin\frac{\pi\alpha}{\Phi}$ and $\cos\frac{\pi\alpha}{\Phi}$ in figure 5.11. Clearly, for $\Phi = \pi$ these approximations precisely

recover $\sin\alpha$ and $\cos\alpha$. Introducing this approximation to replace $\sin\alpha$ and $\cos\alpha$ where they appear in $S_{e,h}(\alpha)$ and in equations (5.22) and (5.23), we obtain

$$A_e^{\pm}(\alpha)\left\{\cos\frac{\pi\alpha}{\Phi}S_e(\alpha\pm\Phi)+\cos\beta_o\sin\frac{\pi\alpha}{\Phi}S_h(\alpha\pm\Phi)\right\}= \cos\frac{\pi\alpha}{\Phi}S_e(-\alpha\pm\Phi)-\cos\beta_o\sin\frac{\pi\alpha}{\Phi}S_h(-\alpha\pm\Phi) \tag{5.84}$$

$$A_h^{\pm}(\alpha)\left\{\cos\beta_o\sin\frac{\pi\alpha}{\Phi}S_e(\alpha\pm\Phi)-\cos\frac{\pi\alpha}{\Phi}S_h(\alpha\pm\Phi)\right\}= -\cos\beta_o\sin\frac{\pi\alpha}{\Phi}S_e(-\alpha\pm\Phi)-\cos\frac{\pi\alpha}{\Phi}S_h(-\alpha\pm\Phi) \tag{5.85}$$

where $A_{e,h}(\alpha)$ is the same as defined in (5.24). To separate the above equations, we introduce the linear combinations

$$t_1(\alpha+\Phi)=\cos\beta_o\sin\frac{\pi\alpha}{\Phi}S_h(\alpha+\Phi)+\cos\frac{\pi\alpha}{\Phi}S_e(\alpha+\Phi) \tag{5.86}$$

$$t_2(\alpha+\Phi)=\cos\beta_o\sin\frac{\pi\alpha}{\Phi}S_e(\alpha+\Phi)-\cos\frac{\pi\alpha}{\Phi}S_h(\alpha+\Phi) \tag{5.87}$$

which also imply that

$$t_1(\alpha-\Phi)=\cos\beta_o\sin\frac{\pi\alpha}{\Phi}S_h(\alpha-\Phi)+\cos\frac{\pi\alpha}{\Phi}S_e(\alpha-\Phi) \tag{5.88}$$

$$t_2(\alpha-\Phi)=\cos\beta_o\sin\frac{\pi\alpha}{\Phi}S_e(\alpha-\Phi)-\cos\frac{\pi\alpha}{\Phi}S_h(\alpha-\Phi) \tag{5.89}$$

Introducing these expressions in (5.84)–(5.85), we obtain

$$A_{e,h}^{+}(\alpha)t_{1,2}(\alpha+\Phi)=t_{1,2}(-\alpha+\Phi) \tag{5.90}$$

$$A_{e,h}^{-}(\alpha)t_{1,2}(\alpha-\Phi)=t_{1,2}(-\alpha-\Phi) \tag{5.91}$$

which can be readily decoupled for a solution of $t_{1,2}(\alpha)$. In particular, on replacing α with $\alpha+\Phi$ in (5.90) and with $\alpha-\Phi$ in (5.91) and then subtracting (5.91) from (5.90) we get

$$A_{e,h}^{+}(\alpha+\Phi)t_{1,2}(\alpha+2\Phi)-A_{e,h}^{-}(\alpha-\Phi)t_{1,2}(\alpha-2\Phi)=0 \tag{5.92}$$

(a) $\sin\frac{\pi\alpha}{\Phi}$

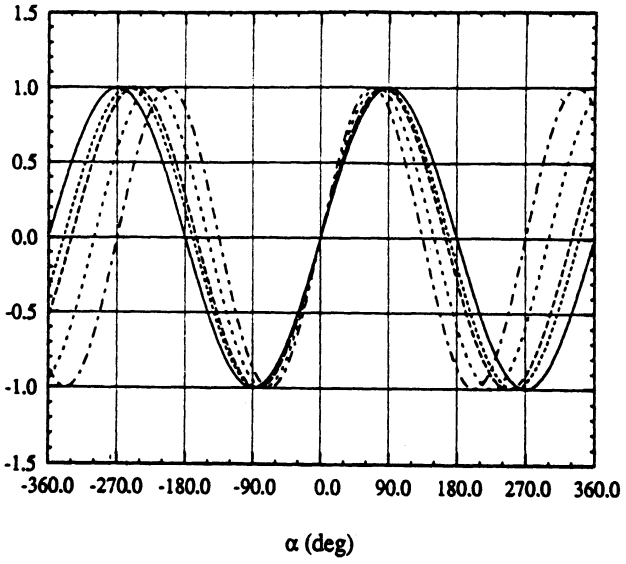

(b) $\cos\frac{\pi\alpha}{\Phi}$

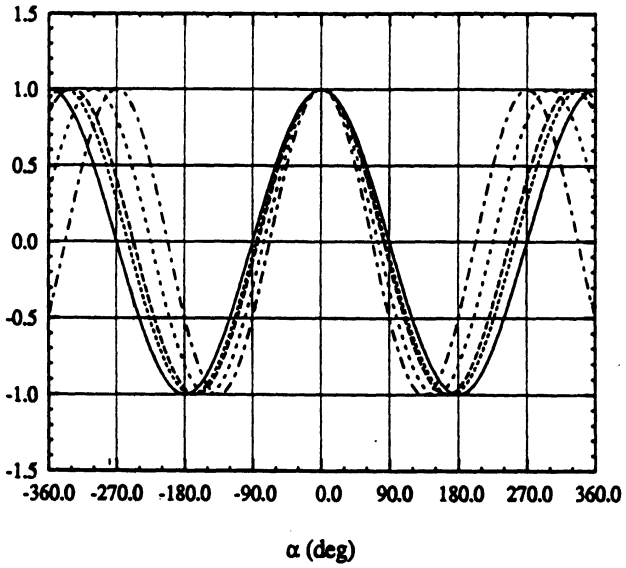

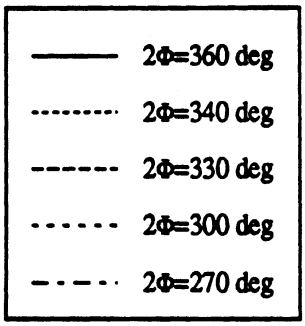

Figure 5.11: A plot of (a) $\sin\frac{\pi\alpha}{\Phi}$, (b) $\cos\frac{\pi\alpha}{\Phi}$.

This is a difference equation identical to (5.41) with $f_{1,2}(\alpha) = 0$ and can be solved via Maliuzhinets' method for all wedge angles. We observe from (5.84) and (5.85) that the solution of (5.92) for an arbitrary wedge angle will recover the exact solutions for the cases when

(a) $\beta_o = \pi/2$ (Normal incidence with arbitrary wedge angle)

and

(b) $\Phi = \pi$ (Half plane with arbitrary β_o).

Once $t_{1,2}(\alpha)$ are determined, the spectra $S_{e,h}(\alpha)$ are found from the relations

$$S_e(\alpha) = \frac{-1}{1 - \sin^2\beta_o \sin^2\frac{\pi\alpha}{\Phi}} \left\{ \cos\frac{\pi\alpha}{\Phi} t_1(\alpha) + \cos\beta_o \sin\frac{\pi\alpha}{\Phi} t_2(\alpha) \right\} \tag{5.93}$$

$$S_h(\alpha) = \frac{-1}{1 - \sin^2\beta_o \sin^2\frac{\pi\alpha}{\Phi}} \left\{ \cos\beta_o \sin\frac{\pi\alpha}{\Phi} t_1(\alpha) - \cos\frac{\pi\alpha}{\Phi} t_2(\alpha) \right\} \tag{5.94}$$

and these were derived by using the expressions

$$t_1(\alpha) = -\cos\beta_o \sin\frac{\pi\alpha}{\Phi} S_h(\alpha) - \cos\frac{\pi\alpha}{\Phi} S_e(\alpha) \tag{5.95}$$

$$t_2(\alpha) = -\cos\beta_o \sin\frac{\pi\alpha}{\Phi} S_e(\alpha) + \cos\frac{\pi\alpha}{\Phi} S_h(\alpha) \tag{5.96}$$

which follow from (5.86)–(5.89).

Let us now solve (5.92) for $t_{1,2}(\alpha)$. Following the procedure outlined before, $t_{1,2}(\alpha)$ can be written as in (5.49) with $\sigma_{1,2}(\alpha)$ changed to

$$\sigma_{1,2}(\alpha) = A_{1,2} \frac{\frac{1}{n}\cos\frac{\phi'}{n}}{\sin\frac{\alpha}{n} - \sin\frac{\phi'}{n}} + C_{e,h} + D_{e,h} \sin\frac{\alpha}{n} \tag{5.97}$$

The above expression for $\sigma_{1,2}(\alpha)$ is chosen to satisfy the conditions

(a) $\sigma_{1,2}(\alpha)$ must have a first order pole singularity in the strip $|Re(\alpha)| \leq \Phi$ at $\alpha = \phi'$ to allow recovery of the incident field

(b) $S_{e,h}(\alpha) = O(constant)$ for large $|Im(\alpha)|$ (since the fields at the edge take

a constant nonzero value).

The constants $A_{1,2}$ are again computed so that the residue of the pole at $\alpha = \phi'$ yields the incident field. We have

$$A_1 = -\cos\beta_o \sin\frac{\pi\phi'}{\Phi} h_z - \cos\frac{\pi\phi'}{\Phi} e_z \tag{5.98}$$

$$A_2 = -\cos\beta_o \sin\frac{\pi\phi'}{\Phi} e_z + \cos\frac{\pi\phi'}{\Phi} h_z \tag{5.99}$$

From (5.93) and (5.94), the undesired poles of $S_{e,h}$ in the strip $|Re(\alpha)| < \pi$ are given by

$$\xi_{1,2} = \alpha_r \pm j\alpha_i, \qquad \xi_{3,4} = -\alpha_r \pm j\alpha_i \tag{5.100}$$

where

$$\alpha_r = \frac{\Phi}{2}, \qquad \alpha_i = \left|\frac{n}{2}\ln\left(\tan\frac{\beta_o}{2}\right)\right| \tag{5.101}$$

The constants $C_{e,h}$ and $D_{e,h}$ are determined in a similar manner as described earlier to cancel these poles.

The specification of $t_{1,2}(\alpha)$ and $S_{e,h}(\alpha)$ is now complete, and the far zone diffracted field can be calculated from the non-uniform steepest descent path evaluation of (5.18) and (5.19). This far zone diffracted field, with $\phi = \phi'$, is plotted in figures (5.12) and (5.13) for a half plane (internal wedge angle=0°) and for a wedge (internal wedge angle=30°). From figure (5.12), it is interesting to see that there is no deterioration (i.e. no false peaks or nulls) in the pattern for the region between the two reflection shadow boundaries. However, in figure (5.13), the comparison of the cross-polarization patterns of the wedge with that of the half plane reveals that in the case of the wedge there are two false poles appearing at $\phi = \pm\frac{\pi}{2} \mp \Phi$ (reflection shadow boundaries). To resolve this problem, we note that for a half plane ($\Phi = \pi$)

(a)

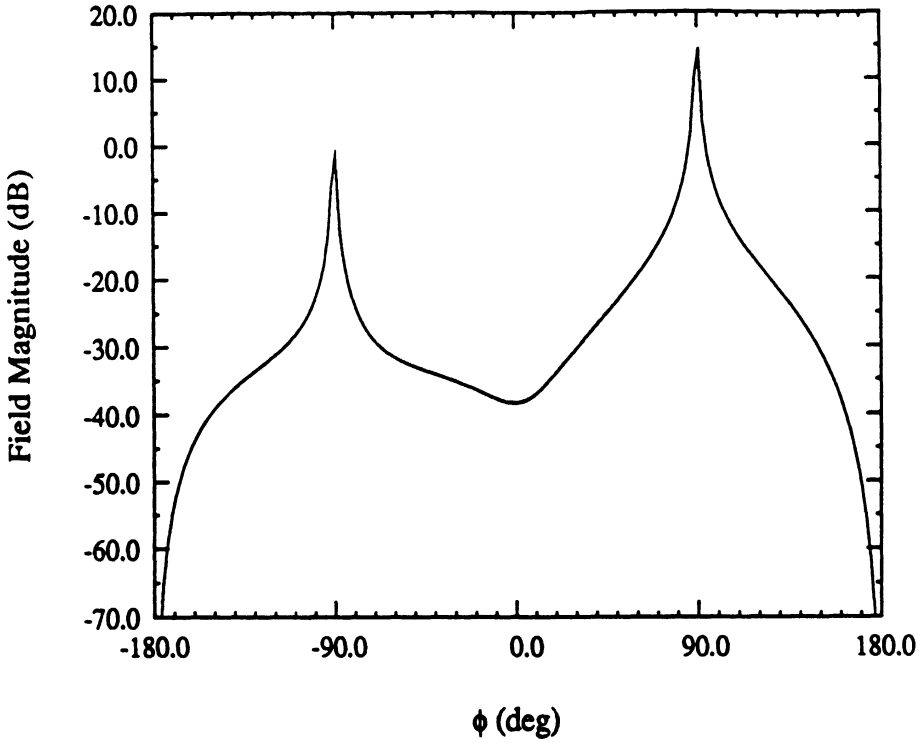

(b)

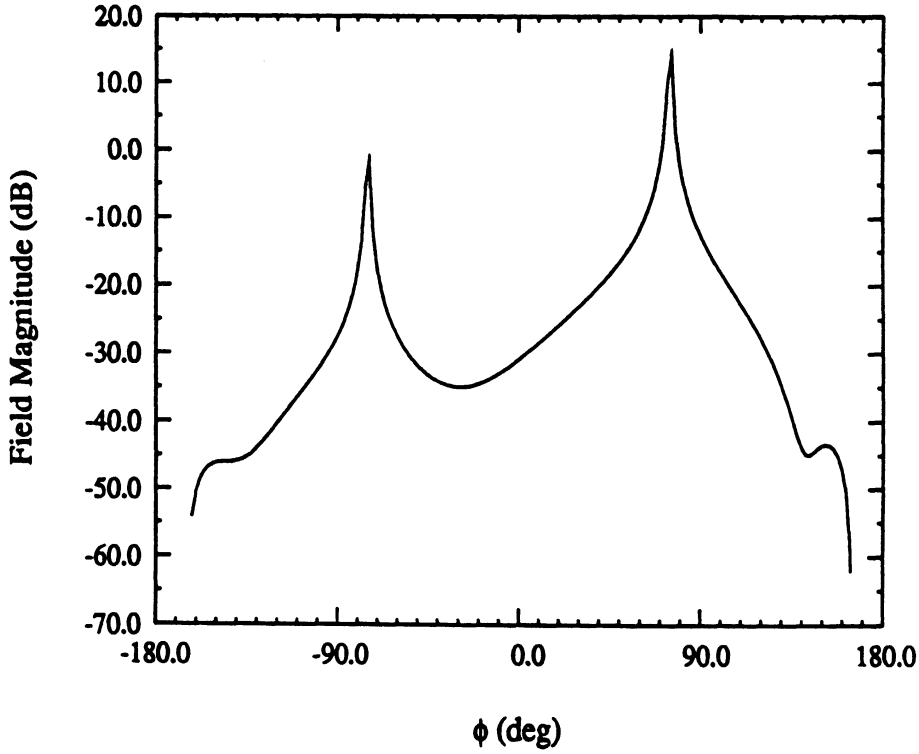

Figure 5.12: Far zone backscatter pattern for an impedance wedge having $\eta_+ = 1.0 - j1.0$, $\eta_- = 0.5 - j0.1$, $\beta_o = 30°$, $E_{\beta_o\beta_o'}$, (a) internal wedge angle = 0°, (b) internal wedge angle = 30°.

(a)

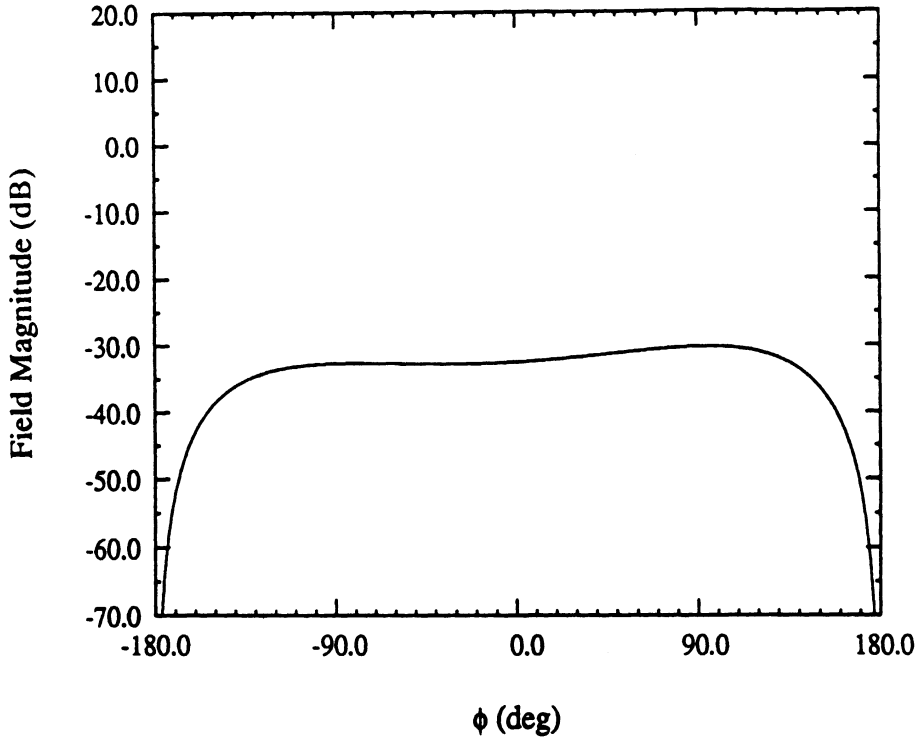

(b)

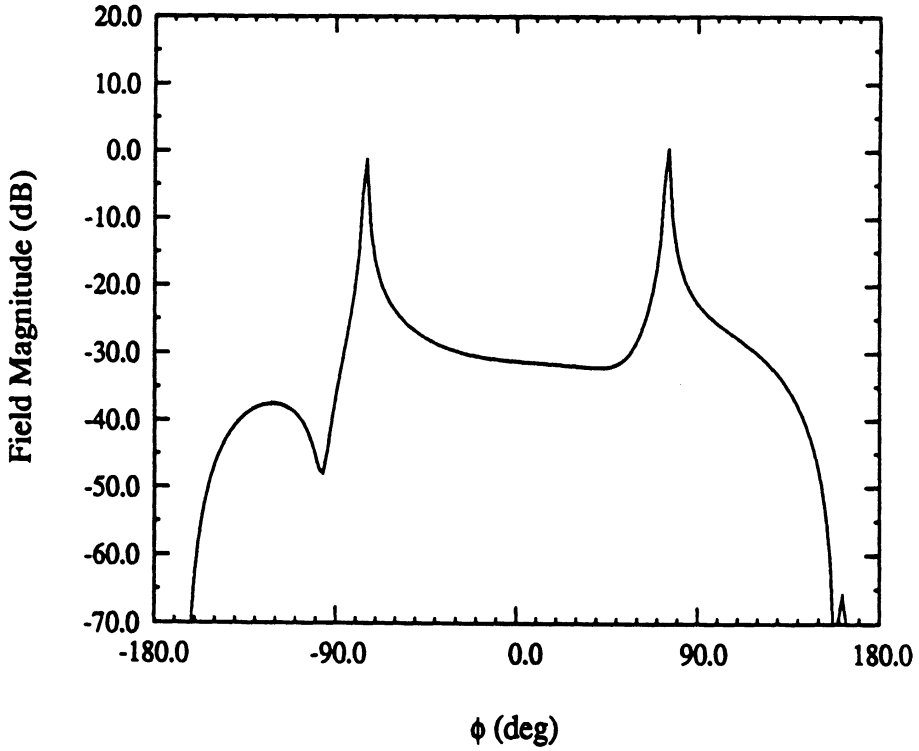

Figure 5.13: Far zone backscatter pattern for an impedance wedge having $\eta_+ = 1.0 - j1.0$, $\eta_- = 0.5 - j0.1$, $\beta_o = 30^o$, $E_{\phi\beta_o'}$, (a) internal wedge angle = 0^o, (b) internal wedge angle = 30^o.

$$\sin\frac{\pi\alpha}{\Phi}=0, \qquad \text{at } \alpha=-\Phi,\ 0,\ \Phi \tag{5.102}$$

and

$$\cos\frac{\pi\alpha}{\Phi}=0, \qquad \text{at } \alpha=-\frac{\pi}{2}+\Phi,\ \frac{\pi}{2}-\Phi \tag{5.103}$$

which ensures that the poles in question do cancel out. However, for an arbitrary wedge angle $\Phi \neq \pi$, (5.103) is no longer true. This suggests that we should replace $\cos\frac{\pi\alpha}{\Phi}$ with $\cos\frac{\pi\alpha}{\Phi}+\cos\frac{\pi}{n}$ which goes to zero at $\alpha=-\frac{\pi}{2}+\Phi,\ \frac{\pi}{2}-\Phi$ cancelling the undesired poles just as it was done in the case of a half plane. We note that this modification still permits our solution to reduce to the exact ones as discussed above. In addition to this, the inspection of (5.84) and (5.85), yields that the normal incidence ($\beta_o=\frac{\pi}{2}$) wedge solution can still be recovered.

Replacing $\cos\frac{\pi\alpha}{\Phi}$ by $\cos\frac{\pi\alpha}{\Phi}+\cos\frac{\pi}{n}$ in (5.93)–(5.96), we obtain that

$$\begin{aligned} S_e(\alpha) \simeq\ & \frac{-1}{\cos^2\beta_o\sin^2\frac{\pi\alpha}{\Phi}+\left(\cos\frac{\pi\alpha}{\Phi}+\cos\frac{\pi}{n}\right)^2} \\ & \cdot\left\{\left(\cos\frac{\pi\alpha}{\Phi}+\cos\frac{\pi}{n}\right)t_1(\alpha)+\cos\beta_o\sin\frac{\pi\alpha}{\Phi}t_2(\alpha)\right\} \end{aligned} \tag{5.104}$$

$$\begin{aligned} S_h(\alpha) \simeq\ & \frac{-1}{\cos^2\beta_o\sin^2\frac{\pi\alpha}{\Phi}+\left(\cos\frac{\pi\alpha}{\Phi}+\cos\frac{\pi}{n}\right)^2} \\ & \cdot\left\{\cos\beta_o\sin\frac{\pi\alpha}{\Phi}t_1(\alpha)-\left(\cos\frac{\pi\alpha}{\Phi}+\cos\frac{\pi}{n}\right)t_2(\alpha)\right\} \end{aligned} \tag{5.105}$$

These expressions imply that

$$A_1=-\cos\beta_o\sin\frac{\pi\phi'}{\Phi}h_z-\left(\cos\frac{\pi\phi'}{\Phi}+\cos\frac{\pi}{n}\right)e_z \tag{5.106}$$

$$A_2=-\cos\beta_o\sin\frac{\pi\phi'}{\Phi}e_z+\left(\cos\frac{\pi\phi'}{\Phi}+\cos\frac{\pi}{n}\right)h_z \tag{5.107}$$

and we observe that the incident field is recovered as required.

The poles of $S_{e,h}$ to be cancelled are now associated with the multiplying factor $\left\{\cos^2\beta_o \sin^2\frac{\pi\alpha}{\Phi} + \left(\cos\frac{\pi\alpha}{\Phi} + \cos\frac{\pi}{n}\right)^2\right\}^{-1}$ and for $|Re(\alpha)| < \pi$, these are

$$\xi_{1,2} = \alpha_r \pm j\alpha_i, \qquad \xi_{3,4} = -\alpha_r \pm j\alpha_i \tag{5.108}$$

where

$$\alpha_r = \frac{n}{2}\cos^{-1}\left|\frac{\cos\frac{\pi}{n}}{\sin\beta_o}\right|, \qquad \alpha_i = \left|\frac{n}{2}\ln\left(\tan\frac{\beta_o}{2}\right)\right| \tag{5.109}$$

provided $\left|\frac{\cos\frac{\pi}{n}}{\sin\beta_o}\right| \leq 1$. When $\left|\frac{\cos\frac{\pi}{n}}{\sin\beta_o}\right| > 1$, the poles are given by

$$\xi_{1,2} = \pm j\alpha_{i_1}, \qquad \xi_{3,4} = \pm j\alpha_{i_2} \tag{5.110}$$

with

$$\alpha_{i_{1,2}} = \left|\frac{n}{2}\ln\left(x_{1,2} + \sqrt{x_{1,2}^2 - 1}\right)\right| \tag{5.111}$$

where

$$x_{1,2} = -\frac{\cos\frac{\pi}{n}}{\sin^2\beta_o} \pm \frac{\cos\beta_o}{\sin^2\beta_o}\sqrt{\cos^2\frac{\pi}{n} - \sin^2\beta_o} \tag{5.112}$$

The constants $C_{e,h}$ and $D_{e,h}$ can now be determined in a similar fashion as described earlier to cancel these poles. Figure 5.14 shows the far zone backscatter ($\phi = \phi'$) patterns of an impedance wedge having an included angle of 30°. It is clear from figure 5.14 (b) that the replacement of $\cos\frac{\pi\alpha}{\Phi}$ by $\cos\frac{\pi\alpha}{\Phi} + \cos\frac{\pi}{n}$ takes care of the false poles.

So far, we have developed three different solutions of the difference equations represented by (5.22) and (5.23). The first and the second solutions were obtained by separating the difference equations associated with the upper ($\phi = +\Phi$) and the lower ($\phi = -\Phi$) faces of the impedance wedge, respectively. The third solution was constructed by approximating the trignometric functions $\sin\alpha$ and $\cos\alpha$ terms with

(a)

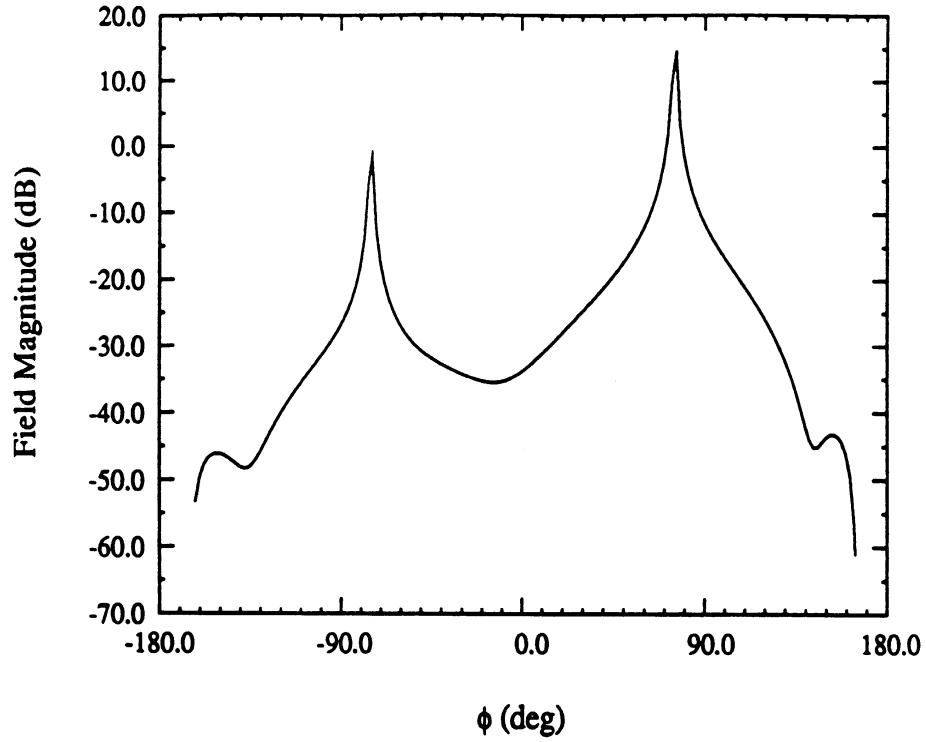

(b)

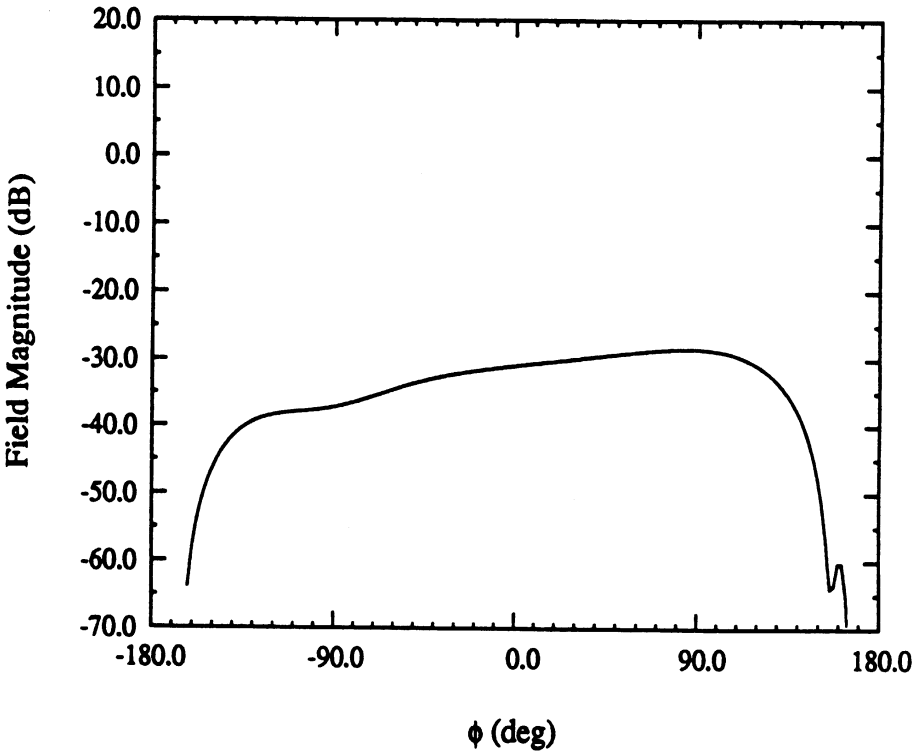

Figure 5.14: Far zone backscatter pattern for an impedance wedge having $\eta_+ = 1.0 - j1.0$, $\eta_- = 0.5 - j0.1$, $\beta_o = 30°$, internal wedge angle = 30°, (a) $E_{\beta_o\beta_o'}$, (b) $E_{\phi\beta_o'}$.

functions which were periodic in 2Φ. This led to the separation of the difference equations associated with both faces of the impedance wedge. We note that all three solutions recover the half plane ($\Phi = \pi$, with arbitrary β_o) and the normal incidence ($\beta_o = \pi/2$, with arbitrary wedge angle) cases exactly. These three solutions can now be employed to compute the far zone diffracted field with each solution to be used in the angular region where it is expected to do better than the others. In particular, the first solution should be employed when the observation angle ϕ is in the region starting from the upper face $\phi = +\Phi$ and ending at the shadow boundary (incident or reflection) reached first from the upper face. The second solution should be employed when the observation angle ϕ is in the region starting from the lower face $\phi = -\Phi$ and ending at the shadow boundary (incident or reflection) reached first from the lower face. The third solution should be used in the region where the observation angle ϕ is between the two shadow boundaries (both reflection shadow boundaries or one incident and one reflection shadow boundary) of the wedge. Figure 5.15 shows the regions where the three solutions should be applied. Using this criterion, the far zone backscatter ($\phi = \phi'$) patterns of an impedance wedge are plotted in figure 5.16 for internal wedge angles of 20° and 30° while β_o is kept constant at 30°. Figure 5.17 shows similar plots for two other values of β_o (namely 50° and 40°) with the internal wedge angle kept at 30°.

5.3.4 Test Results

The presented approximate solutions for an impedance wedge are expected to be accurate when the internal wedge angle of the wedge is close to zero (a half plane) and/or when the skewness angle β_o is near 90° (normal incidence). However, it is interesting to compare the results obtained on the basis of these approximate wedge

(a)

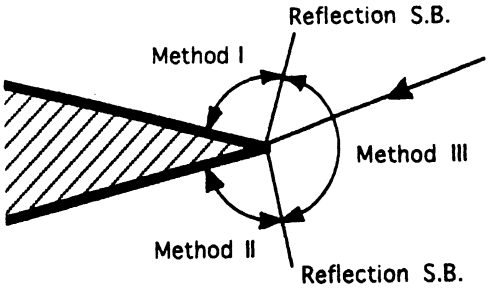

(b)

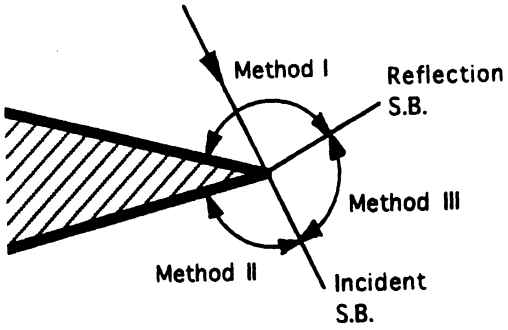

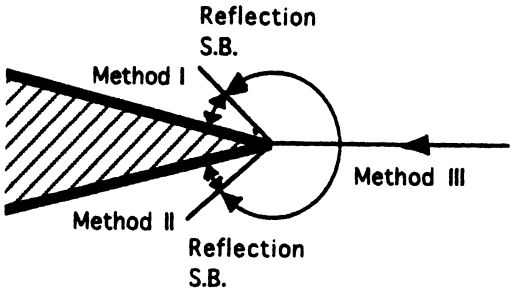

Figure 5.15: Different regions for the applicability of the three solutions. (a) backscatter case (b) bistatic case.

(a)

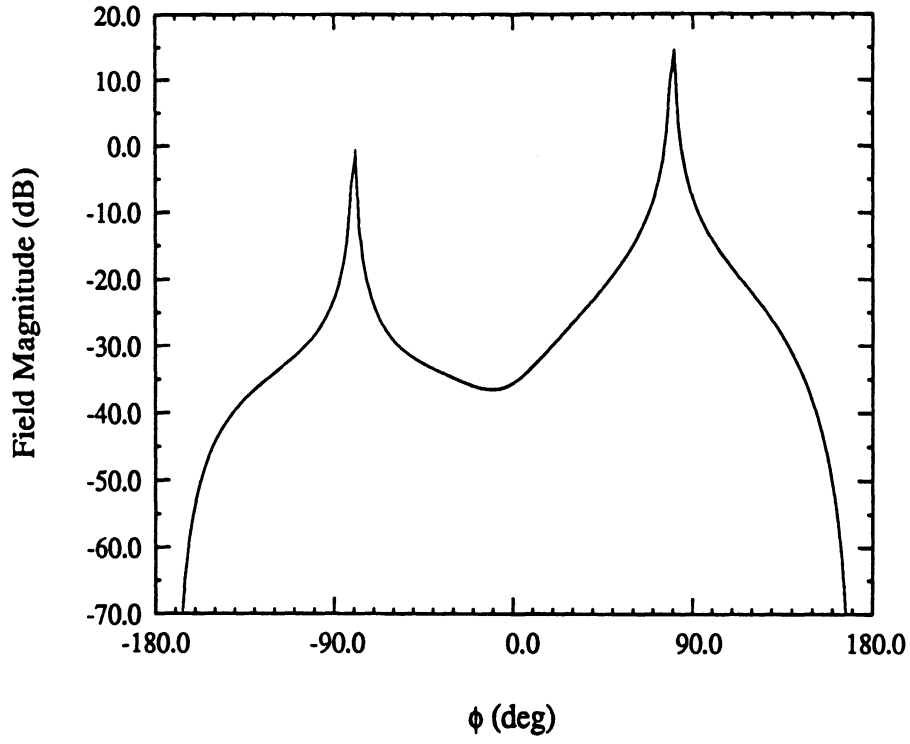

(b)

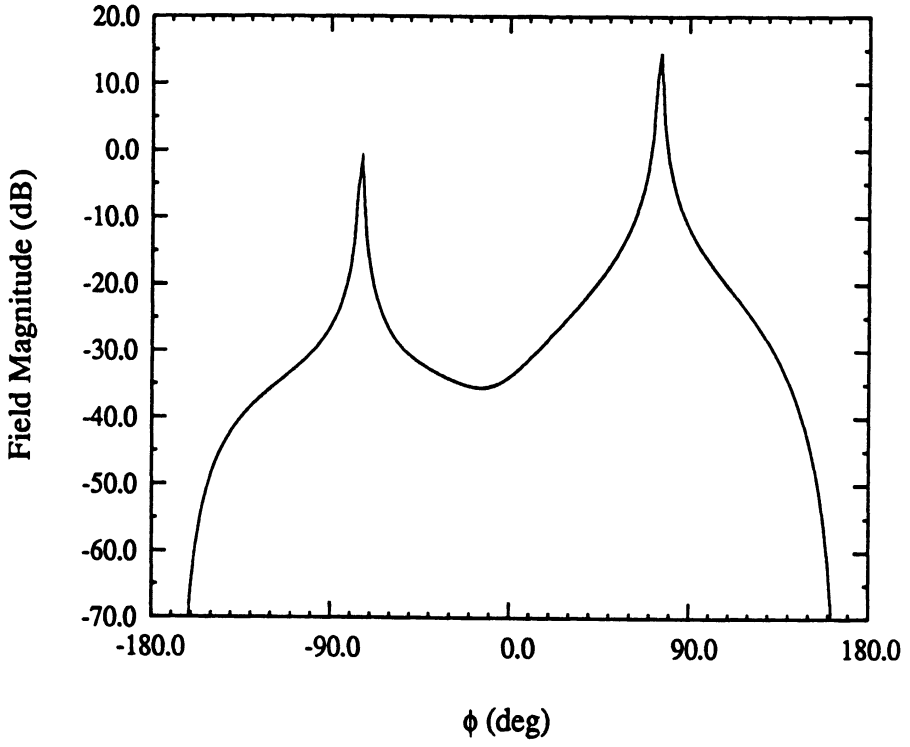

Figure 5.16: Far zone backscatter pattern for an impedance wedge having $\eta_+ = 1.0 - j1.0$, $\eta_- = 0.5 - j0.1$, $\beta_o = 30°$, $E_{\beta_o\beta_o'}$, (a) internal wedge angle = 20°, (b) internal wedge angle = 30°.

(a)

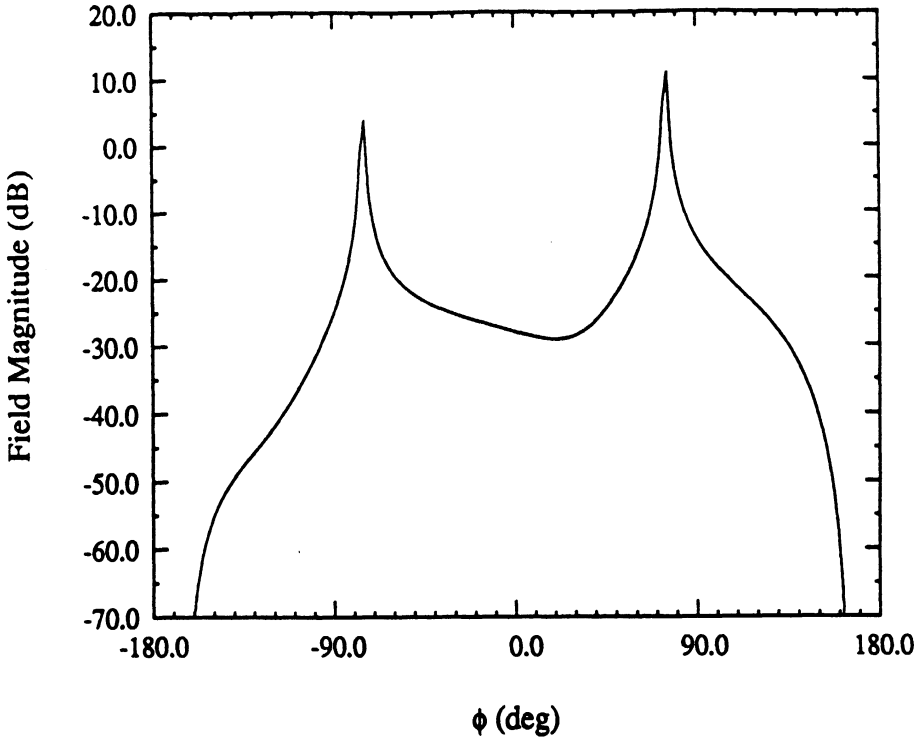

(b)

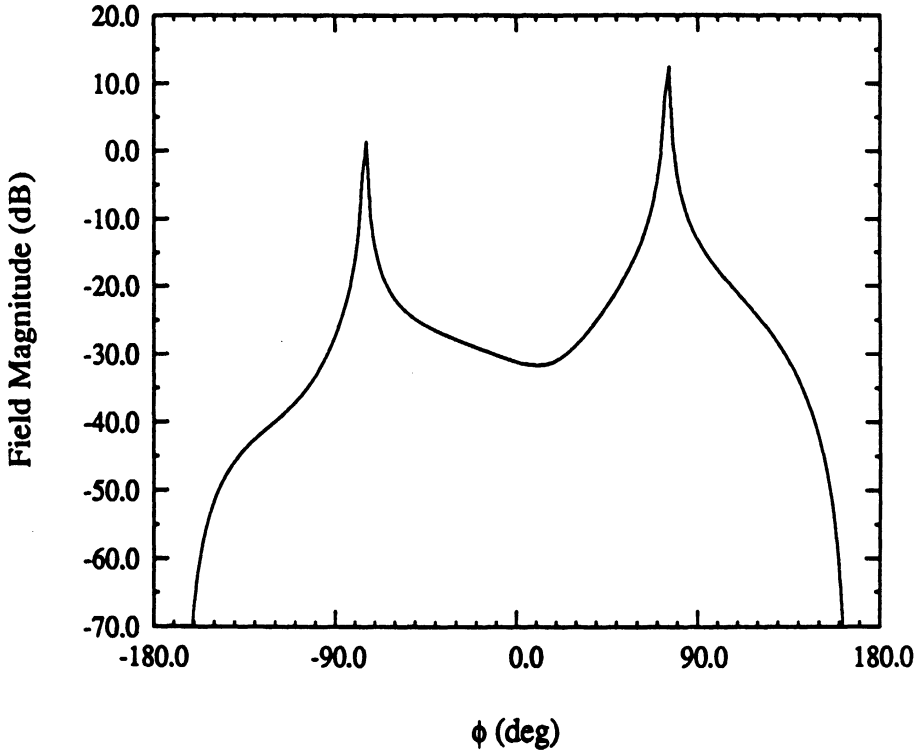

Figure 5.17: Far zone backscatter pattern for an impedance wedge having $\eta_+ = 1.0 - j1.0$, $\eta_- = 0.5 - j0.1$, internal wedge angle = 30°, $E_{\beta_o\beta_o'}$, (a) $\beta_o = 50°$, (b) $\beta_o = 40°$.

solutions with the known exact solution for a right-angled wedge (internal wedge angle = 90°) having one face perfectly conducting. This is the only known solution not recovered by the given approximate ones. The accuracy of the approximate solutions is obviously expected to be low in this case because the internal wedge angle of 90° is quite far from the special cases recovered by the approximate solutions. Figures 5.18–5.21 show backscatter patterns for both like- and cross- polarizations with β_o having values of 60° and 30°. We observe that the approximate solution is more accurate for $\beta_o = 60°$ than it is for $\beta_o = 30°$. This is understandable because $\beta_o = 60°$ is closer to $\beta_o = 90°$, in which case the approximate solution recovers the exact one. We remark that the presented cross-polarization plots were computed everywhere by the approximate solution of method III since the other two approximate solutions become highly inaccurate for this wedge angle.

5.3.5 Summary

In this chapter, we considered the skew incidence scattering from an impedance wedge having arbitrary included angle. Application of the boundary conditions (SIBCs) on the wedge faces resulted in a set of four coupled functional difference equations. Three different approximate solutions were presented to solve these difference equations. The first and the second solutions were obtained by separating the difference equations associated with the upper ($\phi = +\Phi$) and the lower ($\phi = -\Phi$) faces of the impedance wedge, respectively. These solutions were found to recover the exact ones for the three special cases, namely those corresponding to, normal incidence ($\beta_o = 90°$) with arbitrary wedge angle, a half plane (arbitrary β_o, internal wedge angle = 0°) and a two part plane (arbitrary β_o, internal wedge angle = 180°). An important feature of these two solutions, lacked by others [13,14,15,19], is that

a single computer code can be employed to compute the scattered field for all three special cases mentioned above. The third solution was constructed by approximating $\sin\alpha$ and $\cos\alpha$, appearing in the difference equations, with functions having a period of 2Φ. This solution reduces to the exact half plane (arbitrary β_o, internal wedge angle = $0°$) solution and the one for normal incidence ($\beta_o = 90°$). A scheme was suggested to use all three approximate solutions in their respective regions of accuracy. Finally, the results from the approximate solutions were compared with those obtained from the exact solution of a right-angled wedge.

(a)

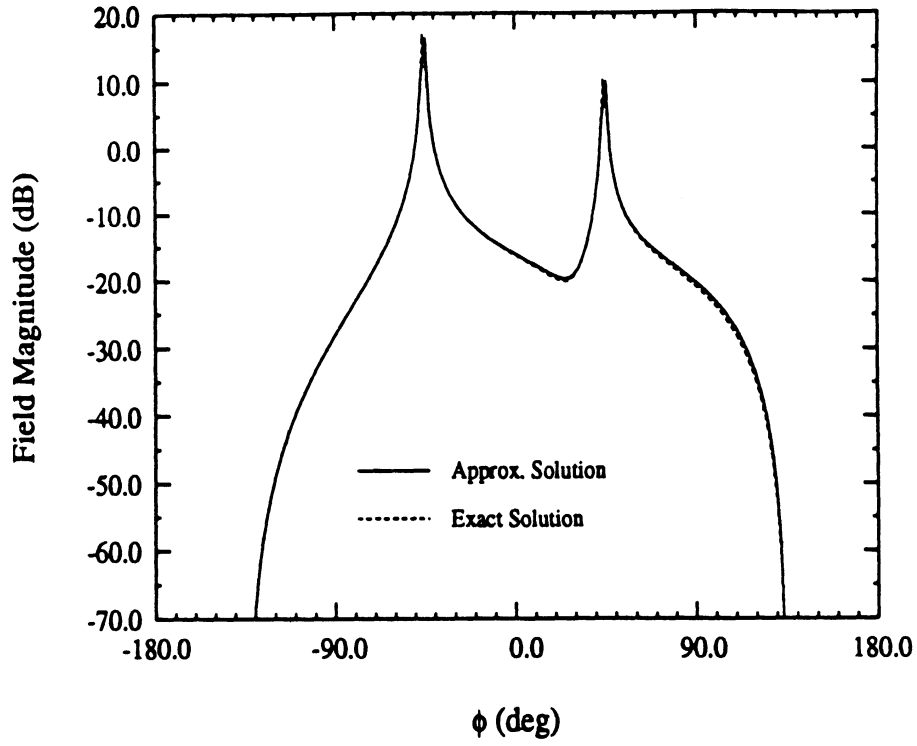

(b)

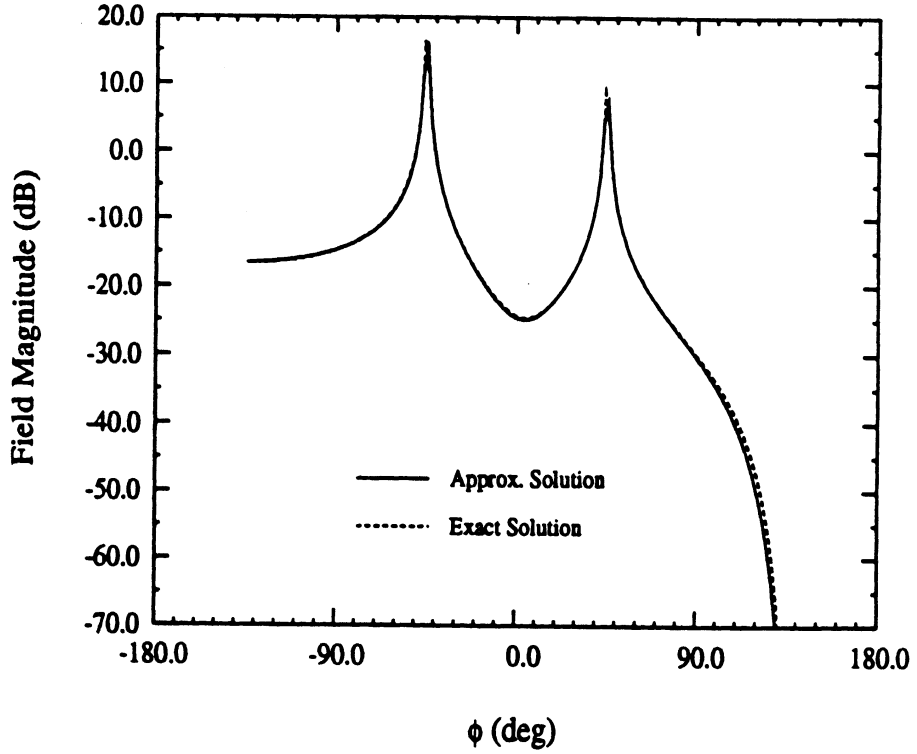

Figure 5.18: Far zone backscatter pattern for a right-angled wedge having $\eta_+ = 1.0 - j1.0$, $\eta_- = 0$, $\beta_o = 60°$, (a) $E_{\beta_o\beta_o'}$, (b) $E_{\phi\phi'}$.

(a)

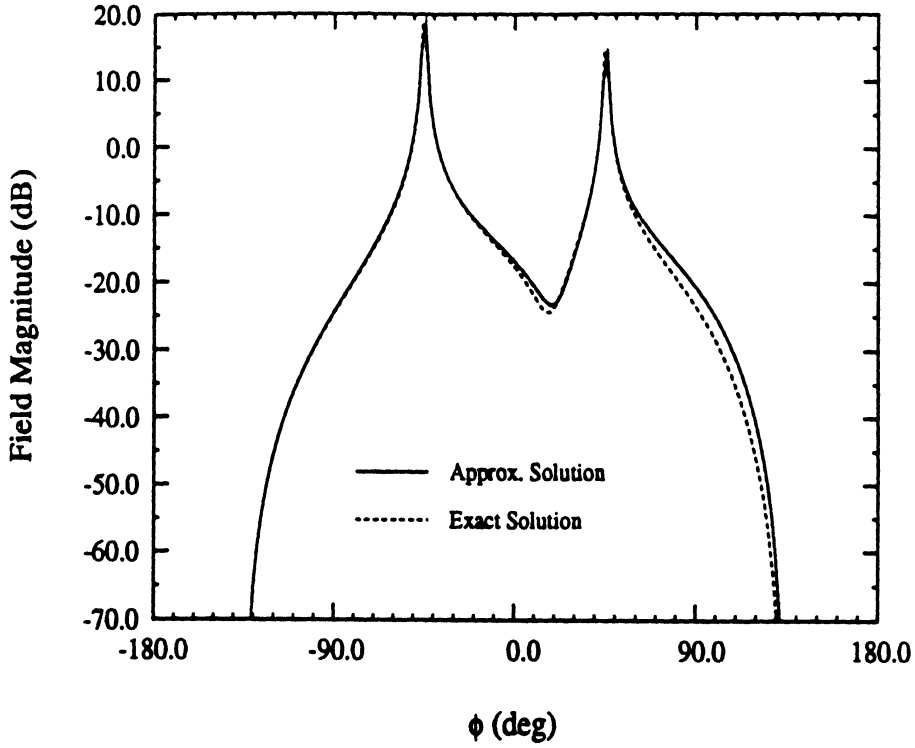

(b)

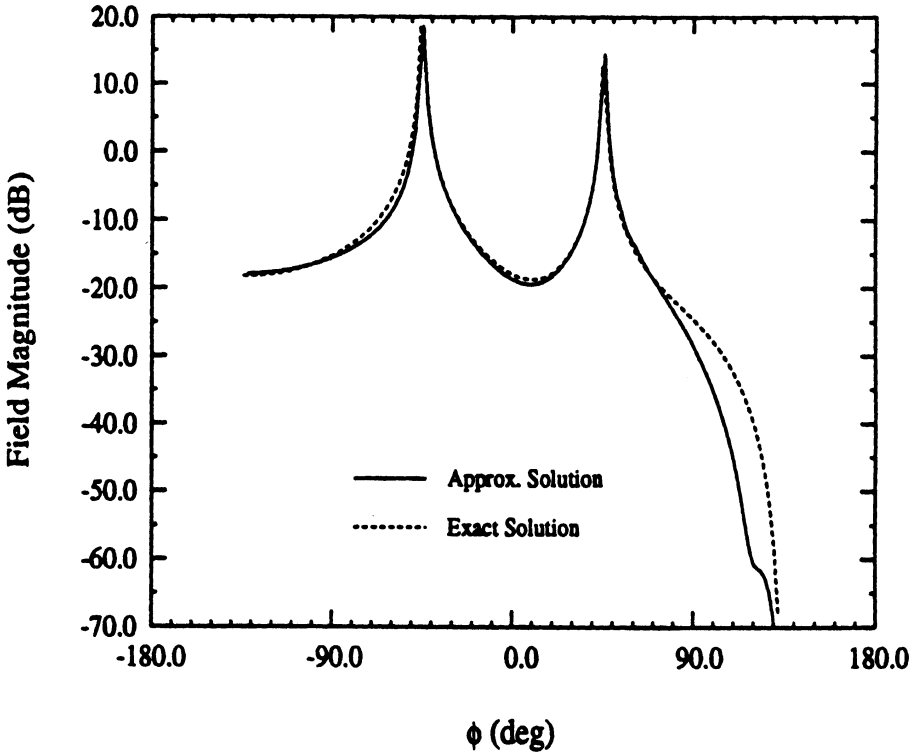

Figure 5.19: Far zone backscatter pattern for a right-angled wedge having $\eta_+ = 1.0 - j1.0$, $\eta_- = 0$, $\beta_o = 30°$, (a) $E_{\beta_o\beta_o'}$, (b) $E_{\phi\phi'}$.

(a)

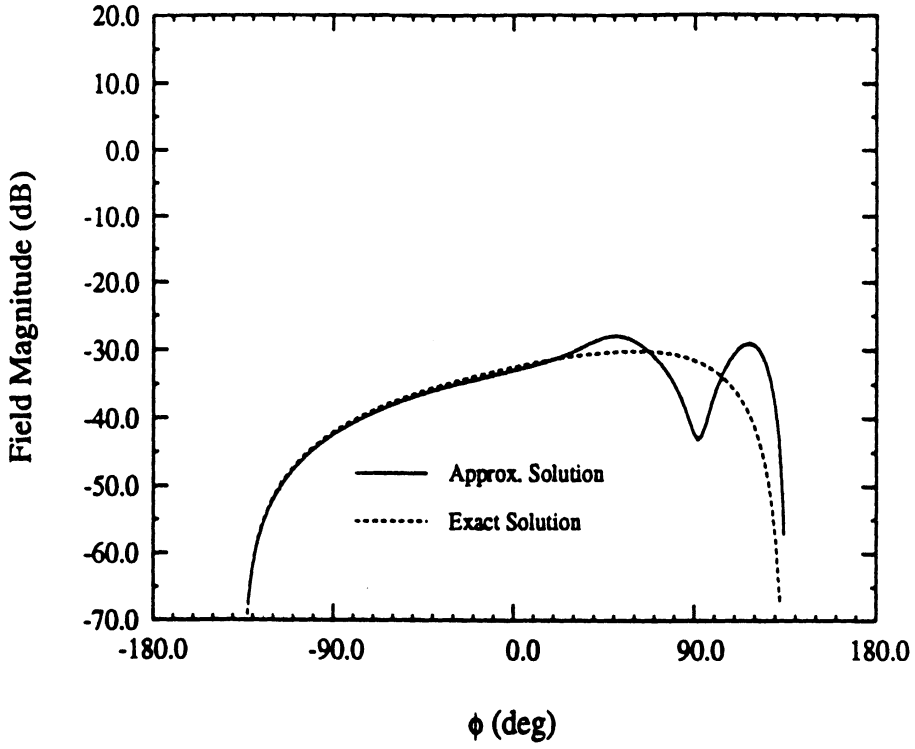

(b)

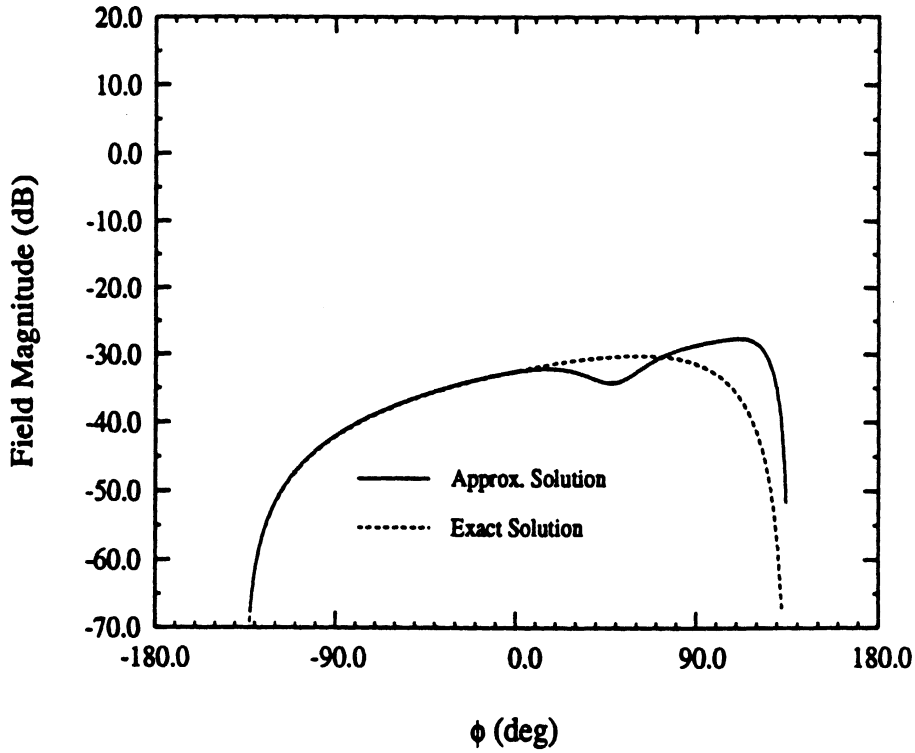

Figure 5.20: Far zone backscatter pattern for a right-angled wedge having $\eta_+ = 1.0 - j1.0$, $\eta_- = 0$, $\beta_o = 60°$, (a) $E_{\phi\beta'_o}$, (b) $E_{\beta_o\phi'}$.

(a)

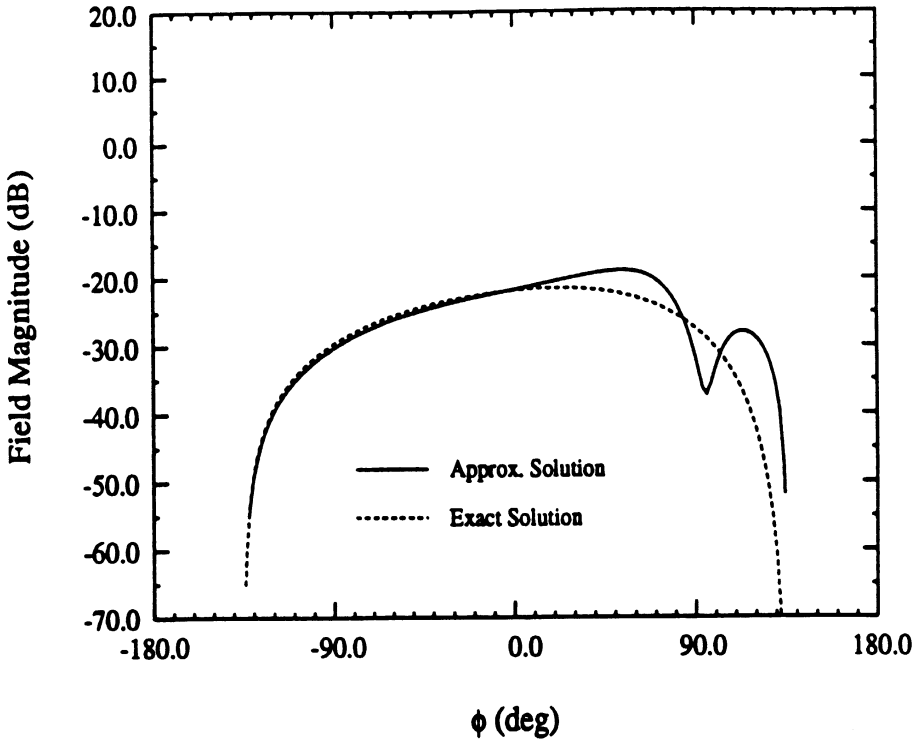

(b)

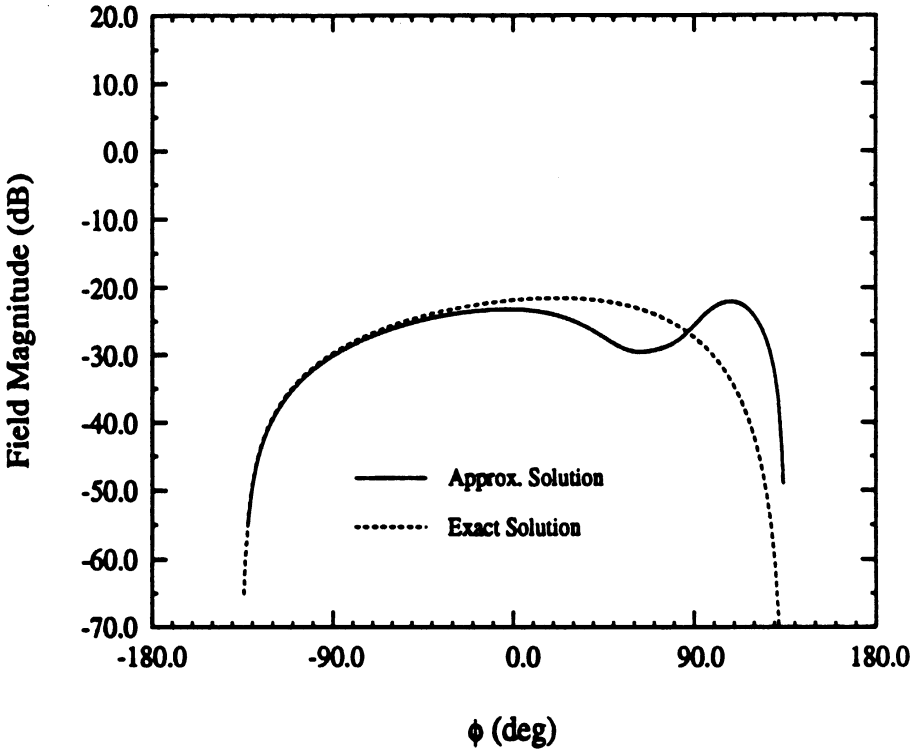

Figure 5.21: Far zone backscatter pattern for a right-angled wedge having $\eta_+ = 1.0 - j1.0$, $\eta_- = 0$, $\beta_o = 30°$, (a) $E_{\phi\beta'_o}$, (b) $E_{\beta_o\phi'}$.

CHAPTER VI

SKEW INCIDENCE SCATTERING FROM A COATED CYLINDER SIMULATED BY SIBC

The skew incidence dyadic diffraction coefficient developed in the previous chapter is an approximate one and it is necessary to establish the extent of its accuracy. This is achieved in this chapter by comparison with numerical data. These are obtained from a moment method solution of a coupled set of integral equations for skew incidence on an impedance cylinder of arbitrary shape. The surface currents obtained from the solution of the coupled integral equations are subsequently integrated to yield the scattered field on the diffraction cone. A corresponding first order high frequency solution for the far zone scattered field is then generated using the approximate diffraction coefficient and compared with the moment method data.

6.1 Integral Equation Formulation

Consider a closed cylindrical surface of infinite extent along the z-axis and having a constant cross section in the xy plane. Let C denote the contour enclosing the cylinder's cross section in the xy plane and $\hat{n}$ to be the outward normal to C. Also, we define $\hat{t} = \hat{z} \times \hat{n}$, so that $(\hat{t}, \hat{n}, \hat{z})$ form a right handed rectilinear system at each contour location as shown in figure 6.1.

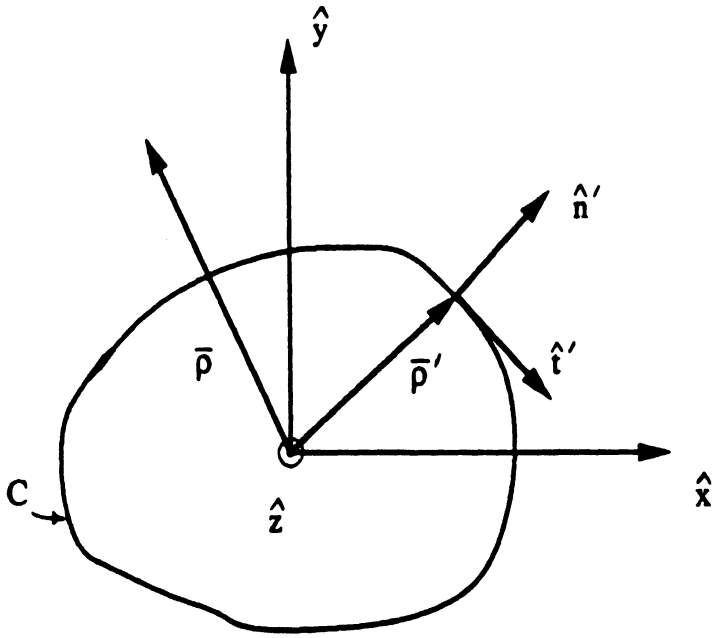

Figure 6.1: Geometry of a cylinder of arbitrary cross section.

Since the impedance cylinder is infinite along the z-direction, the scattered field will have the same z-dependence as the incident field. We assume the incident field to be the plane wave

$$\overline{E}^i = \overline{E}^i_o e^{jk(x\cos\phi'\sin\beta'_o + y\sin\phi'\sin\beta'_o - z\cos\beta'_o)} \tag{6.1a}$$

$$\overline{H}^i = Z\hat{s}^i \times \overline{E}^i \tag{6.1b}$$

where $\hat{s}^i$ denotes the unit vector along the direction of incidence. By invoking the equivalence principle, the scattered field from the impedance cylinder can then be given as the radiation of the surface electric $(\overline{J})$ and magnetic $(\overline{M})$ currents

$$\overline{J}(t) = \hat{n} \times \overline{H} = \hat{t}\overline{J}_t(t) + \hat{z}\overline{J}_z(t) \tag{6.2}$$

$$\overline{M}(t) = \overline{E} \times \hat{n} = \hat{t}\overline{M}_t(t) + \hat{z}\overline{M}_z(t) \tag{6.3}$$

in which $(\overline{E}, \overline{H})$ denote the total electric and magnetic fields in C and t is a measure of the arc length along C. From (6.2) and (6.3), it follows that

$$J_t = H_z, \qquad J_z = -H_t \tag{6.4}$$

$$M_t = -E_z, \qquad M_z = E_t \tag{6.5}$$

and when (6.4) and (6.5) are coupled with the SIBCs (see (2.1)-(2.3))

$$E_t = \eta Z H_z, \qquad E_z = -\eta Z H_t \tag{6.6}$$

to be enforced on C, they yield

$$M_t = -\eta Z J_z, \qquad M_z = \eta Z J_t \tag{6.7}$$

The scattered fields can in general be written in terms of the vector potentials as

$$\overline{E}^s = -\nabla \times \overline{F} - jkZ\overline{A} + \frac{1}{jkY}\nabla\nabla \cdot \overline{A} \tag{6.8}$$

$$\overline{H}^s = \nabla \times \overline{A} - jkY\overline{F} + \frac{1}{jkZ}\nabla\nabla \cdot \overline{F} \tag{6.9}$$

By using (6.7), we have

$$\overline{A} = -\frac{j}{4}\int_C \left\{\hat{t}J_t(t') + \hat{z}J_z(t')\right\} H_o^{(2)}(kr\sin\beta_o)e^{-jkz\cos\beta_o}dt' \tag{6.10}$$

$$\overline{F} = \frac{jZ}{4}\int_C \left\{\hat{t}J_z(t') - \hat{z}J_t(t')\right\} \eta(t') H_o^{(2)}(kr\sin\beta_o)e^{-jkz\cos\beta_o}dt' \tag{6.11}$$

in which $\hat{t}'$ denotes the unit tangent to C at the integration point, $H_o^{(2)}(\cdot)$ is the zeroth order Hankel function of the second kind and

$$r = |\overline{\rho} - \overline{\rho}'| \tag{6.12}$$

where $\overline{\rho}$ and $\overline{\rho}'$ denote the projection of the observation and integration points in the xy plane, respectively. Expanding (6.8) we find that the z-component of the scattered electric field is given by

$$\begin{aligned} YE_z^s &= -\frac{k\sin^2\beta_o}{4}\int_C J_z(t')H_o^{(2)}(kr\sin\beta_o)dt' \\ &\quad -\frac{jk\sin\beta_o}{4}\int_C \eta(t')J_z(t')(\hat{n}'\cdot\hat{r})H_o^{(2)}(kr\sin\beta_o)dt' \\ &\quad -\frac{jk\sin\beta_o\cos\beta_o}{4}\int_C J_{t'}(t')\left\{(\hat{t}\cdot\hat{t}')(\hat{t}\cdot\hat{r})\right. \\ &\quad \left.+(\hat{n}\cdot\hat{t}')(\hat{n}\cdot\hat{r})\right\}H_o^{(2)}(kr\sin\beta_o)dt' \end{aligned} \tag{6.13}$$

where $H_1^{(2)}(\cdot)$ denotes the first order Hankel function of the second kind,

$$\hat{r} = \frac{(\overline{\rho}-\overline{\rho}')}{|\overline{\rho}-\overline{\rho}'|} \tag{6.14}$$

and the factor containing the z-dependence has been suppressed. A similar expression for the scattered magnetic field is

$$\begin{aligned} H_z^s &= -\frac{k\sin^2\beta_o}{4}\int_C \eta(t')J_{t'}(t')H_o^{(2)}(kr\sin\beta_o)dt' \\ &\quad -\frac{jk\sin\beta_o}{4}\int_C J_{t'}(t')(\hat{n}'\cdot\hat{r})H_o^{(2)}(kr\sin\beta_o)dt' \\ &\quad +\frac{jk\sin\beta_o\cos\beta_o}{4}\int_C \eta(t')J_z(t')\left\{(\hat{t}\cdot\hat{t}')(\hat{t}\cdot\hat{r})\right. \\ &\quad \left.+(\hat{n}\cdot\hat{t}')(\hat{n}\cdot\hat{r})\right\}H_o^{(2)}(kr\sin\beta_o)dt' \end{aligned} \tag{6.15}$$

where $\hat{n}' = \hat{t}'\times\hat{z}$ and we have again suppressed the $e^{-jkz\cos\beta_o}$ factor.

A solution for J_t' and J_z can now be obtained by constructing a set of coupled integral equations to be solved numerically. A usual procedure in obtaining such a set is to enforce the boundary conditions (6.6) on C. Expressing the total field as a sum of the incident and scattered fields, in view of (6.4), (6.5) and (6.7) we have

$$E_z^i + E_z^s = \eta Z J_z \tag{6.16}$$

and

$$H_z^i + H_z^s = J_t \tag{6.17}$$

Substitution of (6.1)(without the z dependence),(6.13) and (6.15) into (6.16)- -(6.17) now yields a suitable set of integral equations, for the solution of J_z and J_t on C, as

$$\begin{aligned} YE_z^i &= \eta(t)J_z(t) + \frac{k\sin^2\beta_o}{4}\int_C J_z(t')H_o^{(2)}(kr\sin\beta_o)dt' \\ &+\frac{jk\sin\beta_o}{4}\int_C \eta(t')J_z(t')(\hat{n}'\cdot\hat{r})H_o^{(2)}(kr\sin\beta_o)dt' \\ &+\frac{jk\sin\beta_o\cos\beta_o}{4}\int_C J_{t'}(t')\left\{(\hat{t}\cdot\hat{t}')(\hat{t}\cdot\hat{r})\right. \\ &\left.+(\hat{n}\cdot\hat{t}')(\hat{n}\cdot\hat{r})\right\}H_o^{(2)}(kr\sin\beta_o)dt' \end{aligned} \tag{6.18}$$

$$\begin{aligned} H_z^i &= J_t(t) + \frac{k\sin^2\beta_o}{4}\int_C \eta(t')J_{t'}(t')H_o^{(2)}(kr\sin\beta_o)dt' \\ &+\frac{jk\sin\beta_o}{4}\int_C J_{t'}(t')(\hat{n}'\cdot\hat{r})H_o^{(2)}(kr\sin\beta_o)dt' \\ &-\frac{jk\sin\beta_o\cos\beta_o}{4}\int_C \eta(t')J_z(t')\left\{(\hat{t}\cdot\hat{t}')(\hat{t}\cdot\hat{r})\right. \\ &\left.+(\hat{n}\cdot\hat{t}')(\hat{n}\cdot\hat{r})\right\}H_o^{(2)}(kr\sin\beta_o)dt' \end{aligned} \tag{6.19}$$

To discretize the integral equations (6.18) and (6.19) it is, of course, necessary to discretize and evaluate the line integrals appearing in them. By employing a pulse basis expansion for J_z and J_t, a matrix system is generated whose impedance matrix elements can be evaluated numerically or analytically in terms of the functions defined in [32]. Upon evaluation of the surface currents $J_z(t)$ and $J_t(t)$, the far zone ($\rho \to \infty$) fields at (ρ, ϕ) can be obtained from (6.13) and (6.15) by letting $\hat{t} = -\hat{\phi}$, $\hat{n} \simeq \hat{\rho}$, $\hat{r} \simeq \hat{\rho}$, and making use of the large argument expansion for the Hankel functions. It is also to be noted that in the far zone, the above z- components of the scattered field are proportional to the corresponding β_o and ϕ components via the

relations

$$E_z^s = -\sin\beta_o E_{\beta_o}^s, \qquad ZH_z^s = -\sin\beta_o E_\phi^s \tag{6.20}$$

$$E_z^i = \sin\beta_o E_{\beta_o'}^i, \qquad ZH_z^i = \sin\beta_o E_{\phi'}^i \tag{6.21}$$

6.2 First Order High-Frequency Far Zone Field

To validate the approximate skew incidence diffraction coefficient developed in chapter five, we need to compute a first order high-frequency (GTD) far zone scattered field from a triangular impedance cylinder shown in figure 6.2. For this geometry, the first order high-frequency far zone field is represented by

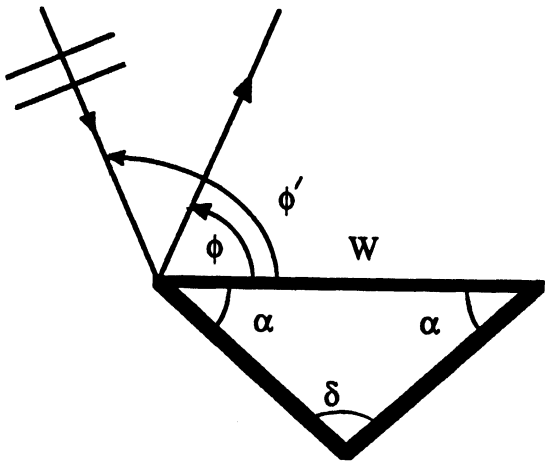

Figure 6.2: Geometry of a triangular impedance cylinder.

$$\overline{E}^s = \sum_{p=1}^{3} \frac{e^{-jks_p}}{\sqrt{s}} \overline{\overline{D}}_p \cdot \overline{E}^i \tag{6.22}$$

where

$$\overline{\overline{D}} = \hat{\beta}_o \hat{\beta}'_o D_{\beta_o \beta'_o} + \hat{\beta}_o \hat{\phi}' D_{\beta_o \phi'} + \hat{\phi} \hat{\beta}'_o D_{\phi \beta'_o} + \hat{\phi} \hat{\phi}' D_{\phi \phi'} \tag{6.23}$$

is the skew incidence dyadic diffraction coefficient for an impedance wedge, s is the distance between the diffraction and observation points and the subscript p simply denotes that the parameters are measured with respect to the pth edge of the triangular cylinder.

6.3 Test Results

To demonstrate the validity of the diffraction coefficient, we refer to figures 6.3–6.13 where the echowidth

$$\sigma = \lim_{s \to \infty} 2\pi s = \frac{|\overline{E}^s|^2}{|\overline{E}^i|^2} \tag{6.24}$$

is plotted as a function of scattering angle. In figures 6.3–6.7, bistatic scattering patterns are plotted for $\beta_o = 90°, 60°$ and $30°$ while the internal wedge angle α is kept constant at $30°$. Clearly, the agreement between the first order GTD solution and the moment method is quite good. The small disagreement observed at around $0°$, $180°$ and $360°$ is due to the absence of multiply diffracted fields as confirmed by the results for the normal incidence case (which is exact) shown in figure 6.3. Figures 6.8–6.13 show bistatic patterns for the triangular cylinder with the wedge angle $\alpha = 40°$ and $50°$. Again, the approximate GTD solution is found to be accurate even for β_o down to $30°$. The normal incidence ($\beta_o = 90°$) patterns 6.8 and 6.11 are given as a reference to show the regions of disagreement due to the absence of multiply diffracted field. The above test cases are only a sample from a rather large

set of validation data. In all cases, we found a remarkable agreement between the first-order GTD solution and the corresponding moment method data for internal wedge angles up to 50°.

6.4 Summary

To validate the approximate solution for an impedance wedge, a coupled set of integral equations for skew incidence on an impedance cylinder of arbitrary shape were derived and solved via moment method. The surface currents obtained from the solution of the coupled integral equations were subsequently integrated to yield the scattered field on the diffraction cone. A corresponding first order high frequency (GTD) solution for the far zone scattered field was then generated using the approximate diffraction coefficient and compared with the moment method data for a variety of different wedge angles. A remarkable agreement was found between the first order GTD solution and the corresponding moment method data for internal wedge angles upto 50°.

(a)

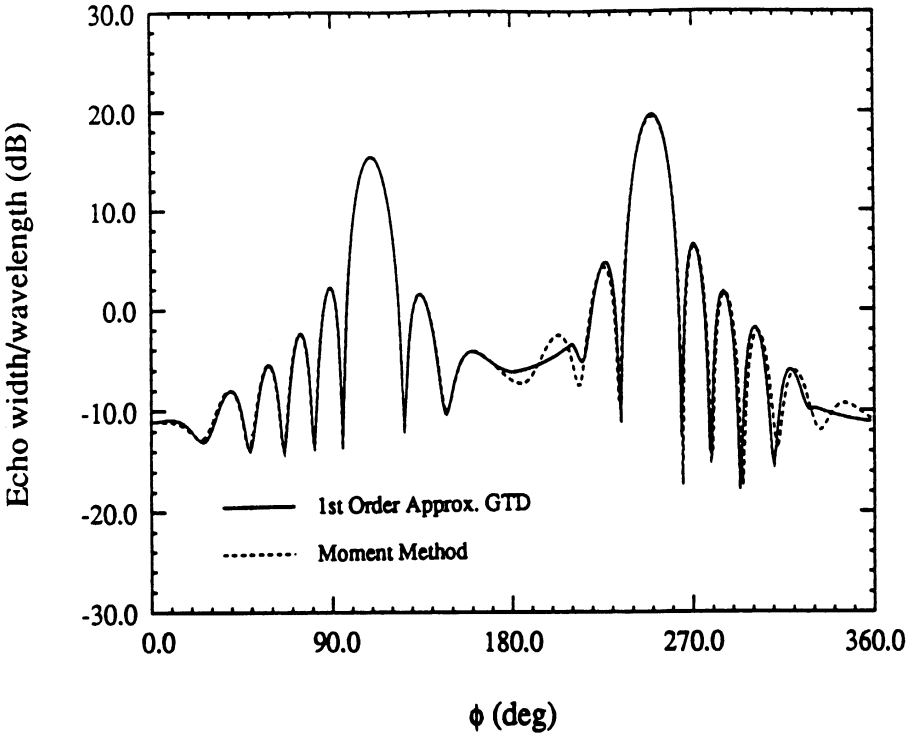

(b)

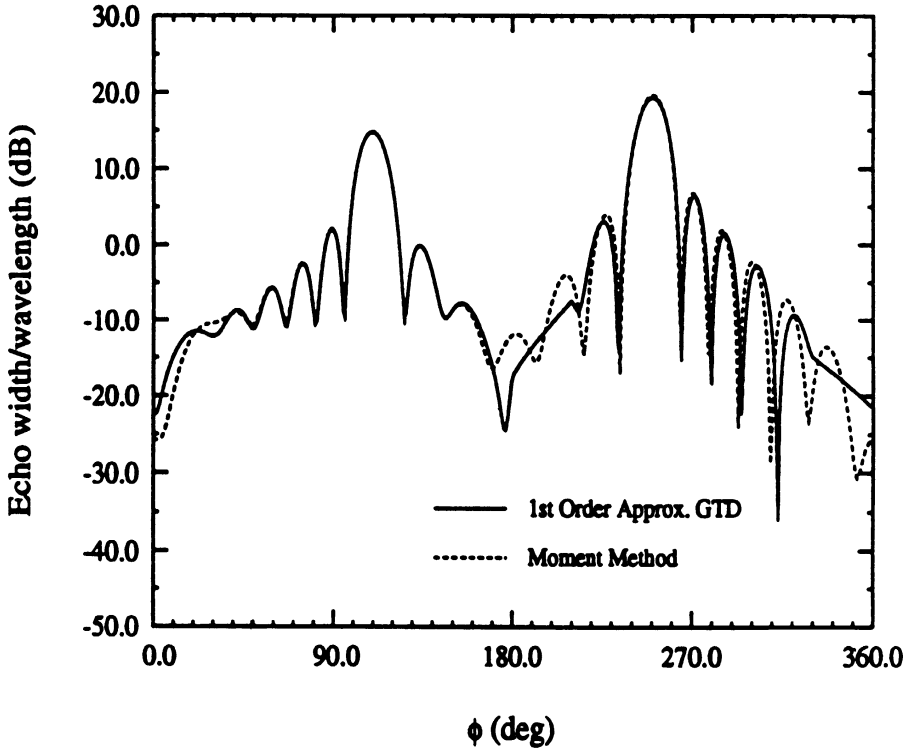

Figure 6.3: Far zone bistatic scattering pattern for a triangular cylinder with top side width $w = 4\lambda$, $\alpha = 30°$, $\beta_o = 90°$, $\phi' = 70°$, and its top face having $\eta = 0.25$, and the other having $\eta = 0.75 + j0.75$, (a) $E_{\beta_o\beta_o'}$, (b) $E_{\phi\phi'}$.

(a)

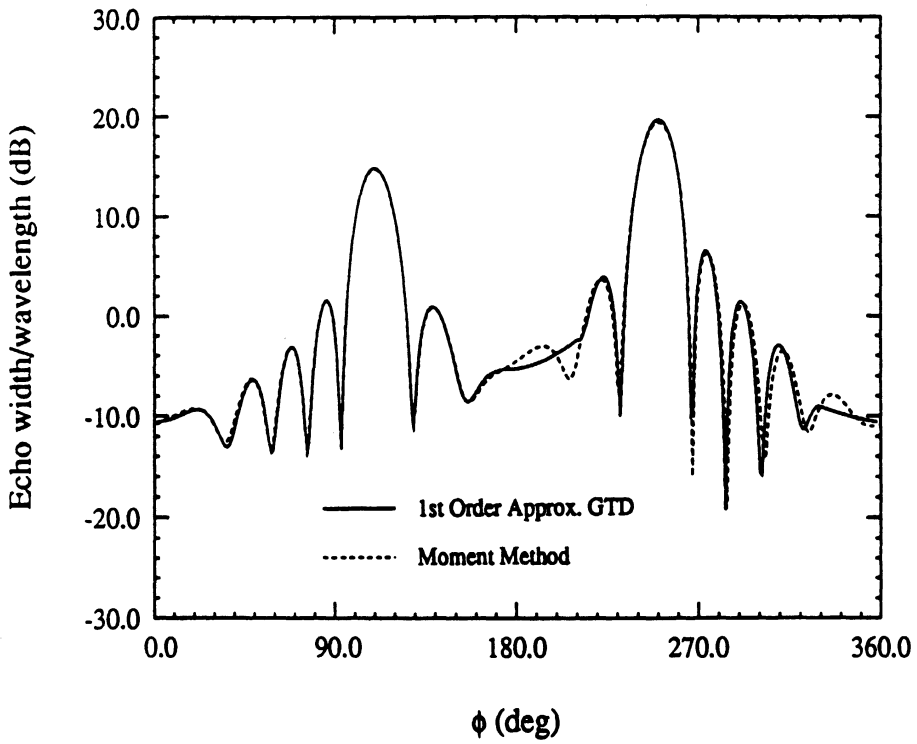

(b)

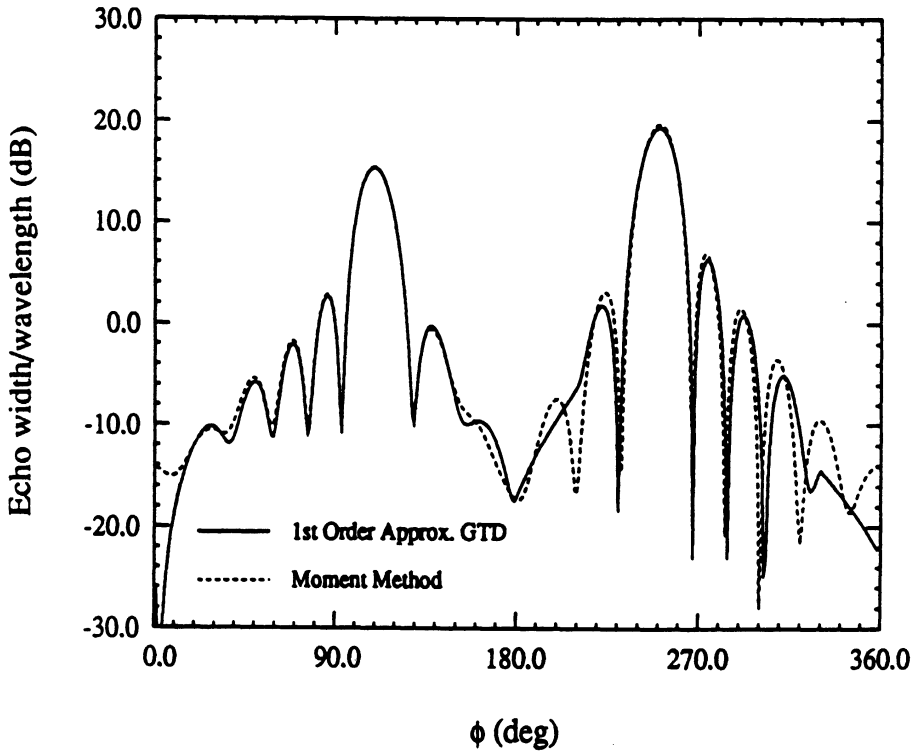

Figure 6.4: Far zone bistatic scattering pattern for a triangular cylinder with top side width $w = 4\lambda$, $\alpha = 30°$, $\beta_o = 60°$, $\phi' = 70°$, and its top face having $\eta = 0.25$, and the other having $\eta = 0.75 + j0.75$, (a) $E_{\beta_o\beta'_o}$, (b) $E_{\phi\phi'}$.

(a)

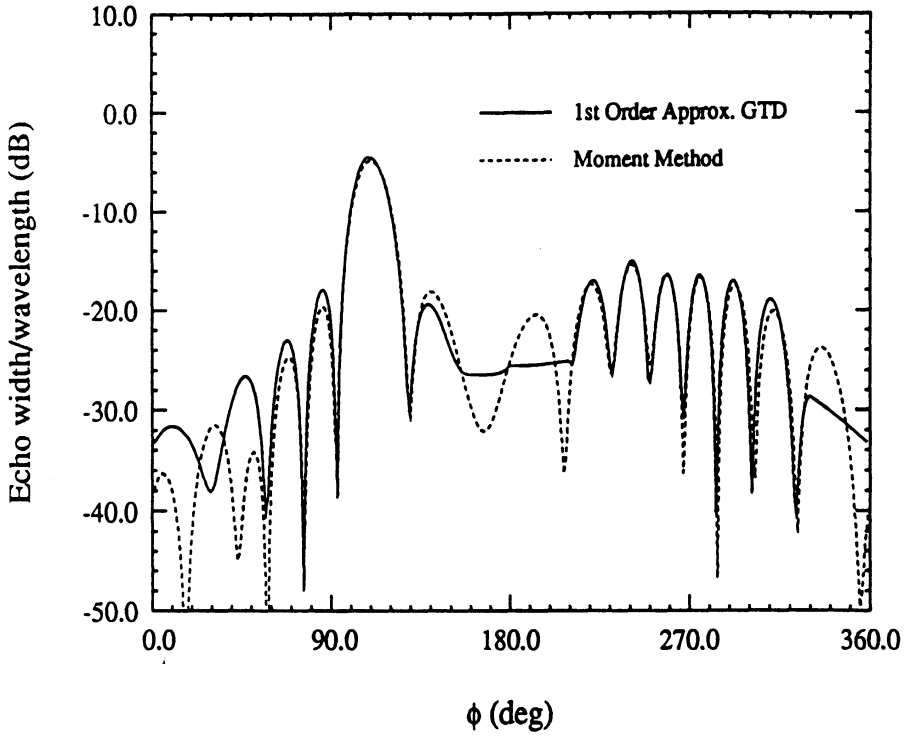

(b)

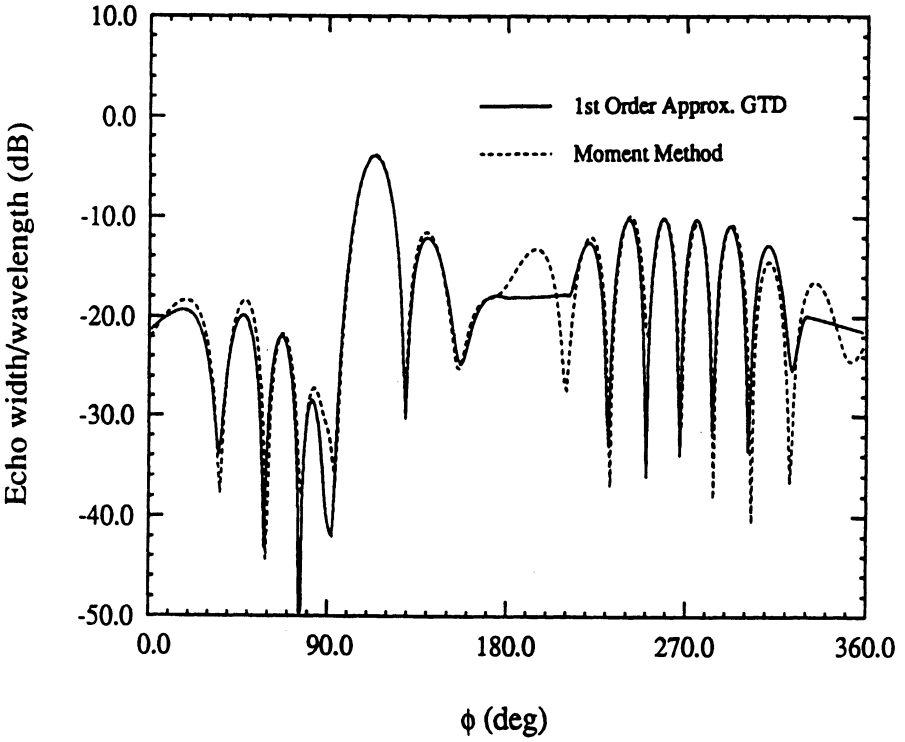

Figure 6.5: Far zone bistatic scattering pattern for a triangular cylinder with top side width $w = 4\lambda$, $\alpha = 30^o$, $\beta_o = 60^o$, $\phi' = 70^o$, and its top face having $\eta = 0.25$, and the other having $\eta = 0.75 + j0.75$, (a) $E_{\phi\beta'_o}$, (b) $E_{\beta_o\phi'}$.

(a)

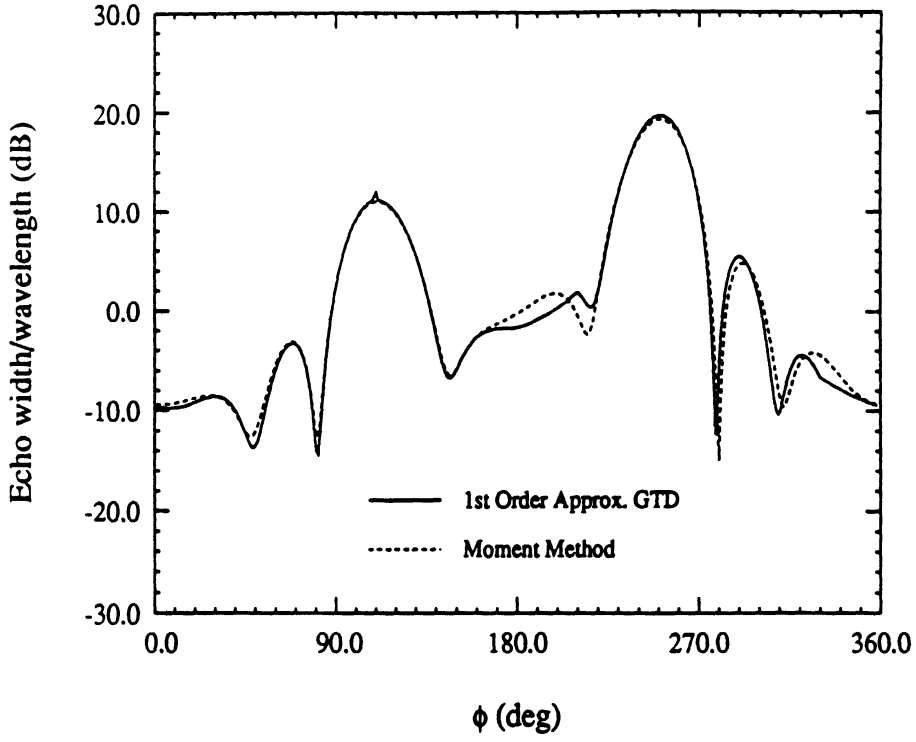

(b)

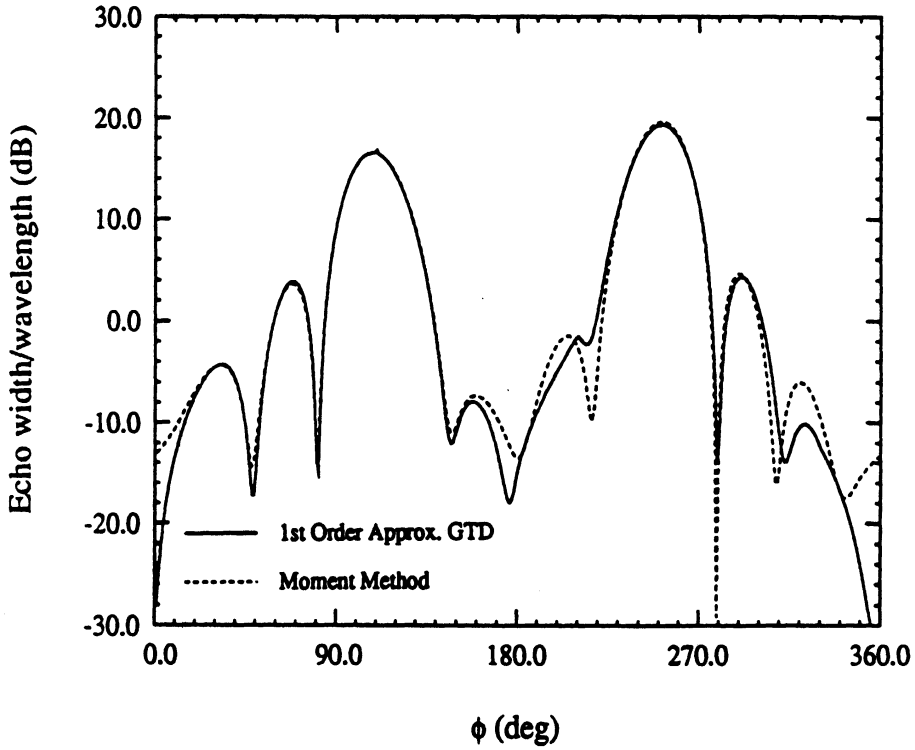

Figure 6.6: Far zone bistatic scattering pattern for a triangular cylinder with top side width $w = 4\lambda$, $\alpha = 30°$, $\beta_o = 30°$, $\phi' = 70°$, and its top face having $\eta = 0.25$, and the other having $\eta = 0.75 + j0.75$, (a) $E_{\beta_o\beta'_o}$, (b) $E_{\phi\phi'}$.

(a)

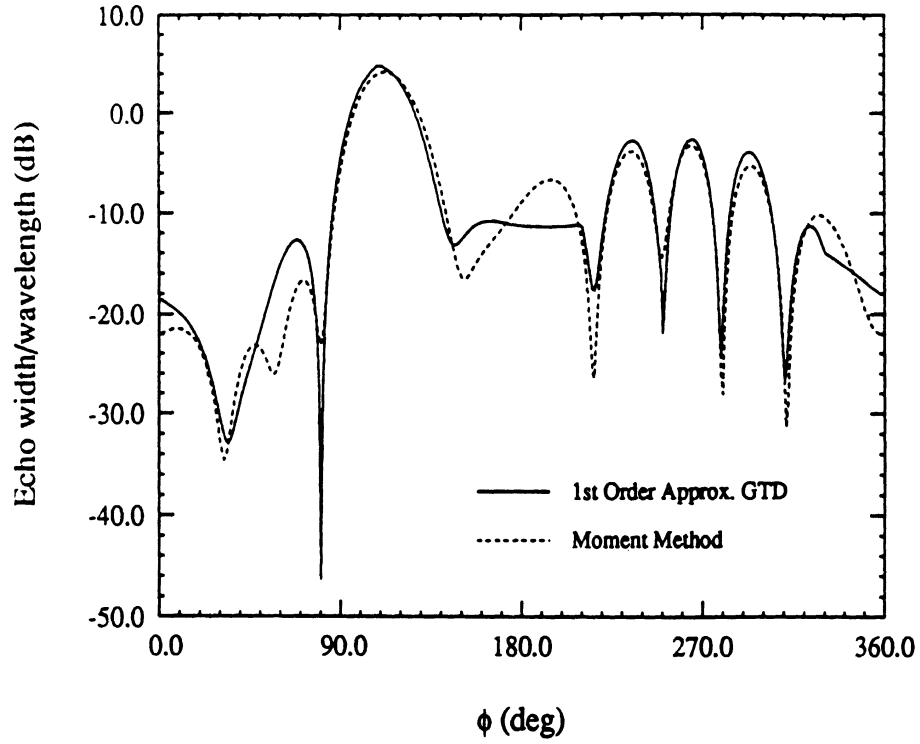

(b)

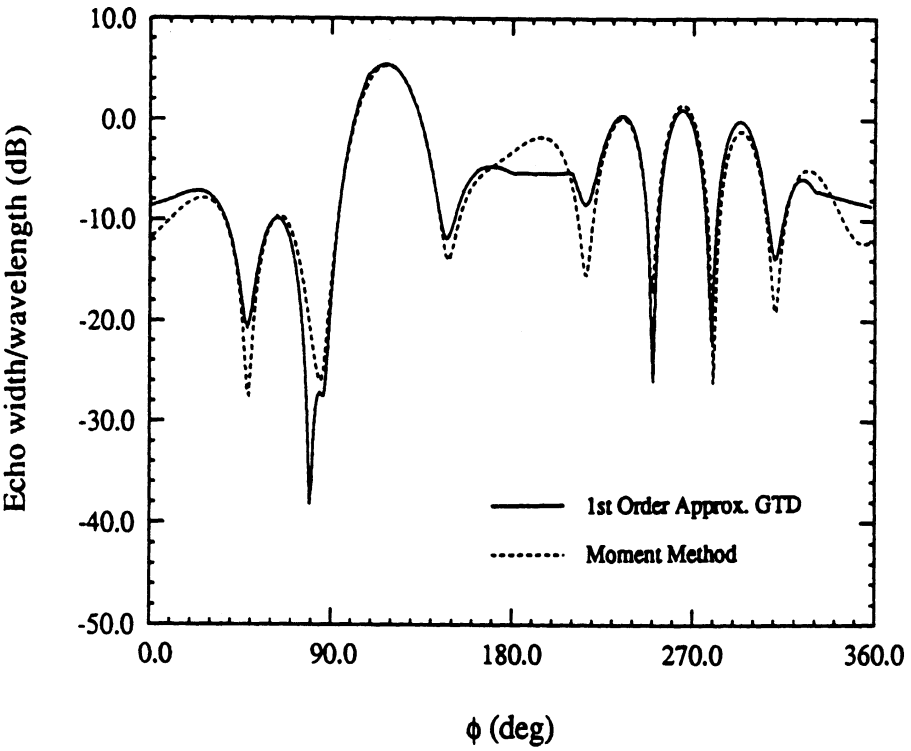

Figure 6.7: Far zone bistatic scattering pattern for a triangular cylinder with top side width $w = 4\lambda$, $\alpha = 30°$, $\beta_o = 30°$, $\phi' = 70°$, and its top face having $\eta = 0.25$, and the other having $\eta = 0.75 + j0.75$, (a) $E_{\phi\beta'_o}$, (b) $E_{\beta_o\phi'}$.

(a)

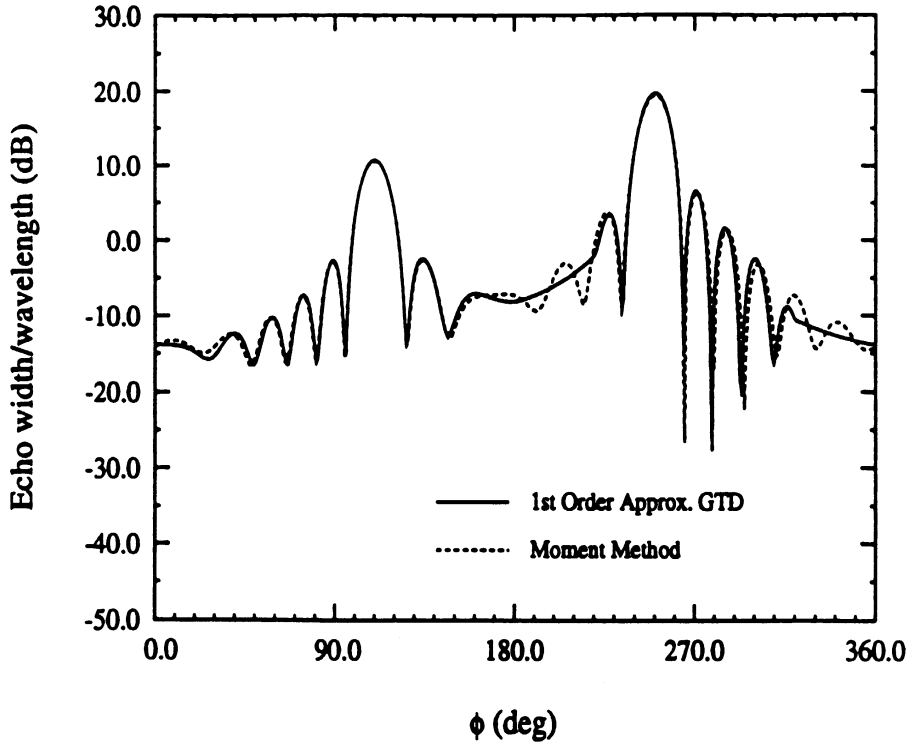

(b)

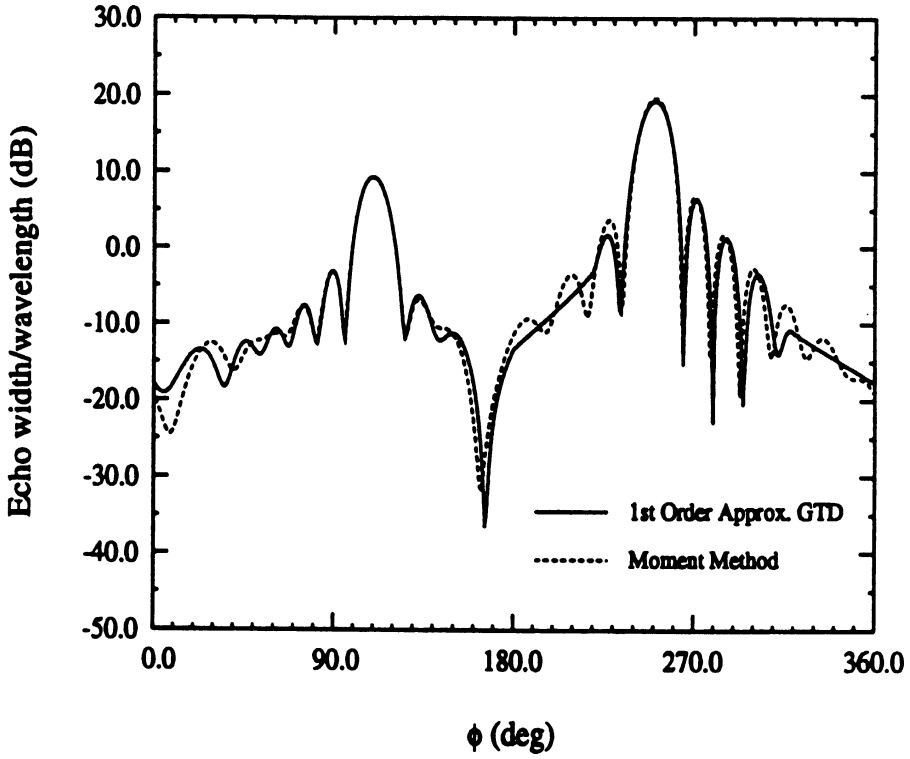

Figure 6.8: Far zone bistatic scattering pattern for a triangular cylinder with top side width $w = 4\lambda$, $\alpha = 40°$, $\beta_o = 90°$, $\phi' = 70°$, and its top face having $\eta = 0.5$, and the other having $\eta = 1.0 + j1.0$, (a) $E_{\beta_o\beta'_o}$, (b) $E_{\phi\phi'}$.

(a)

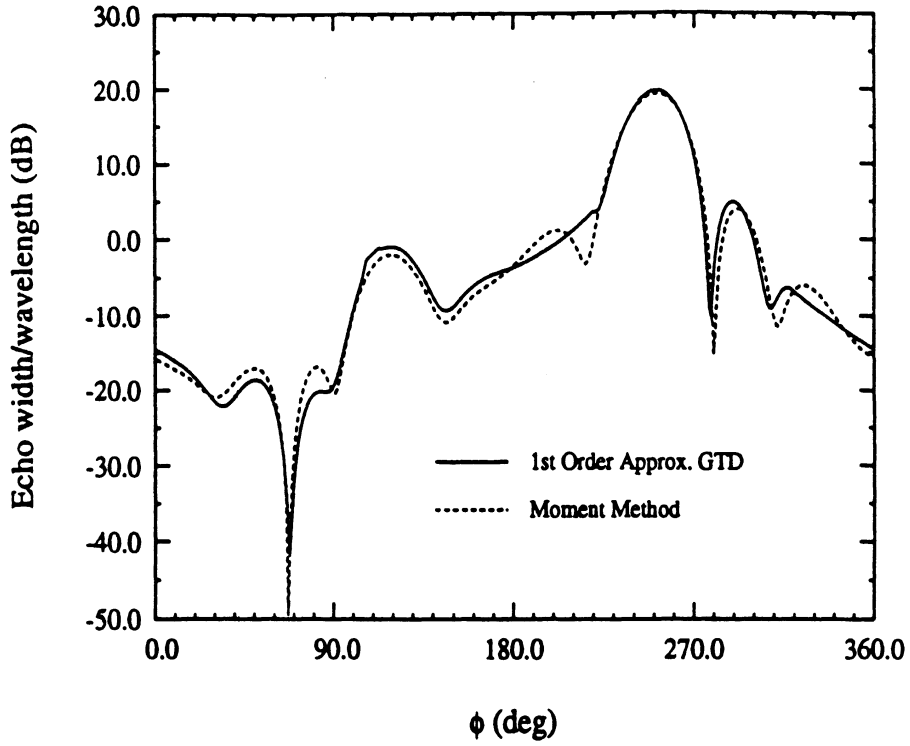

(b)

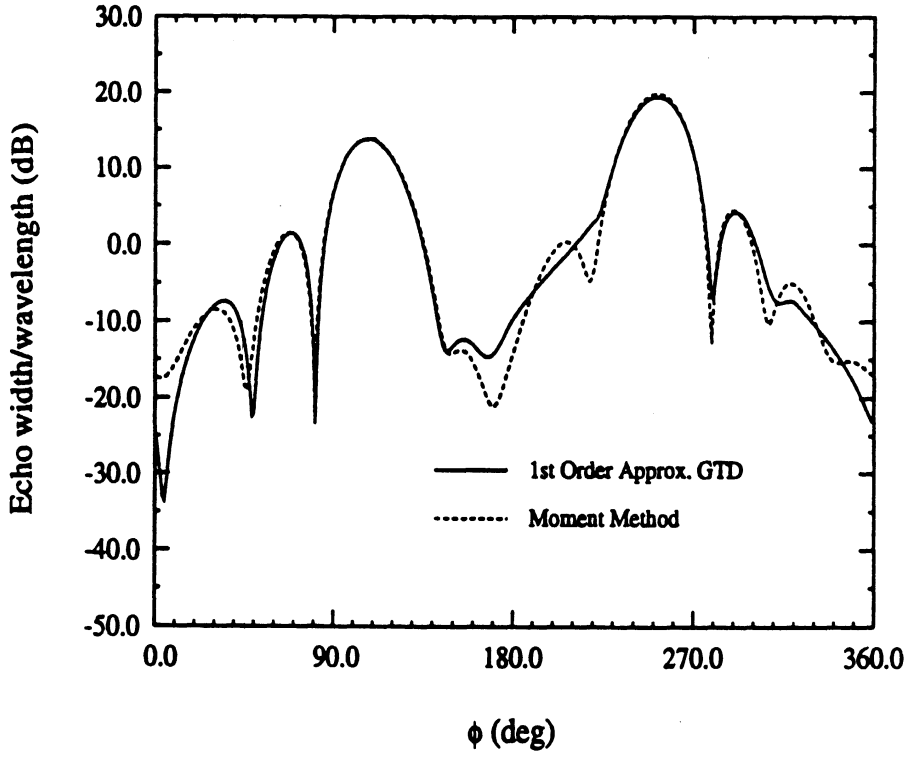

Figure 6.9: Far zone bistatic scattering pattern for a triangular cylinder with top side width $w = 4\lambda$, $\alpha = 40°$, $\beta_o = 30°$, $\phi' = 70°$, and its top face having $\eta = 0.5$, and the other having $\eta = 1.0 + j1.0$, (a) $E_{\beta_o\beta'_o}$, (b) $E_{\phi\phi'}$.

(a)

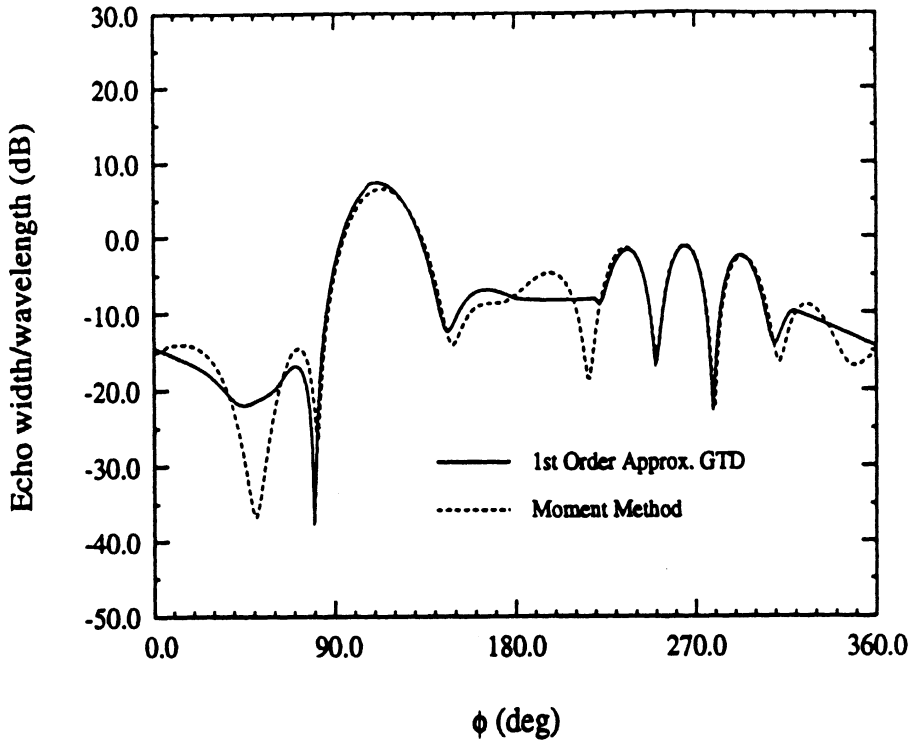

(b)

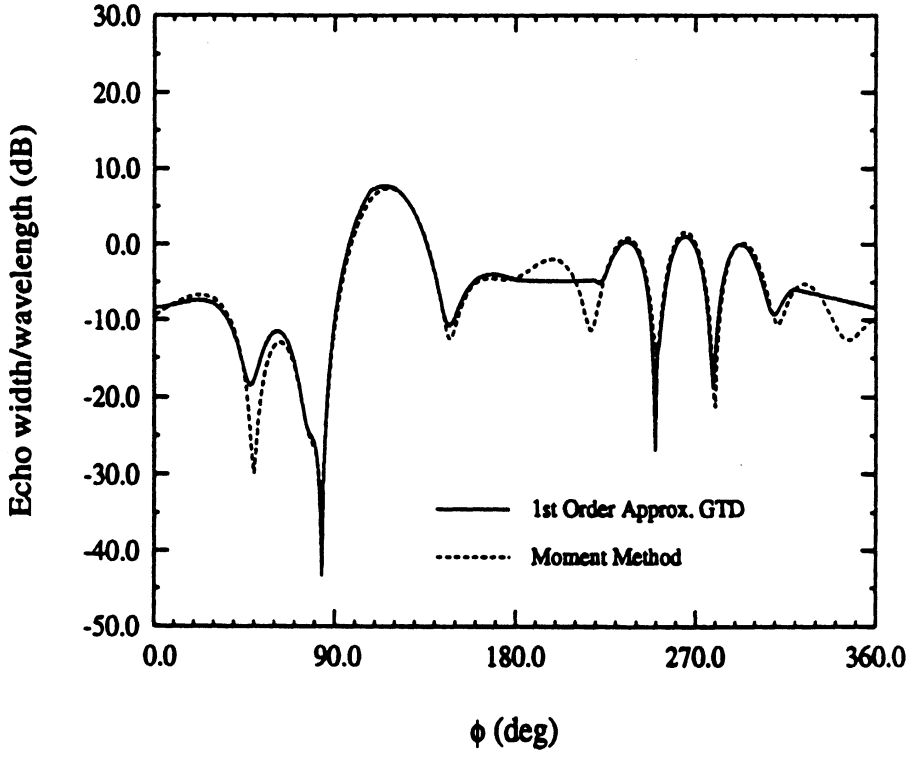

Figure 6.10: Far zone bistatic scattering pattern for a triangular cylinder with top side width $w = 4\lambda$, $\alpha = 40°$, $\beta_o = 30°$, $\phi' = 70°$, and its top face having $\eta = 0.5$, and the other having $\eta = 1.0 + j1.0$, (a) $E_{\phi\beta'_o}$, (b) $E_{\beta_o\phi'}$.

(a)

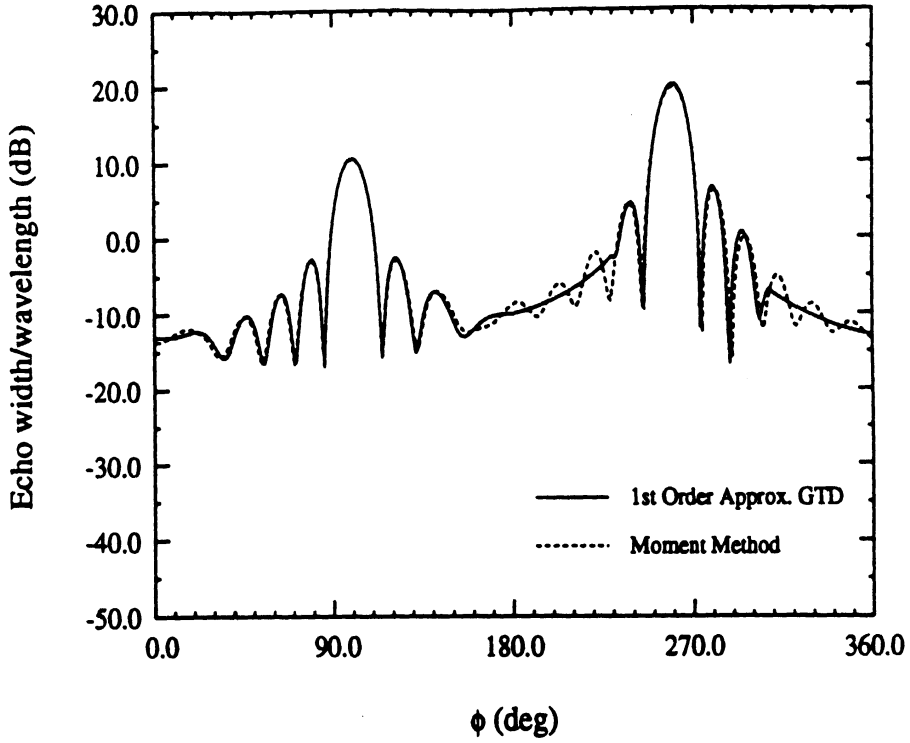

(b)

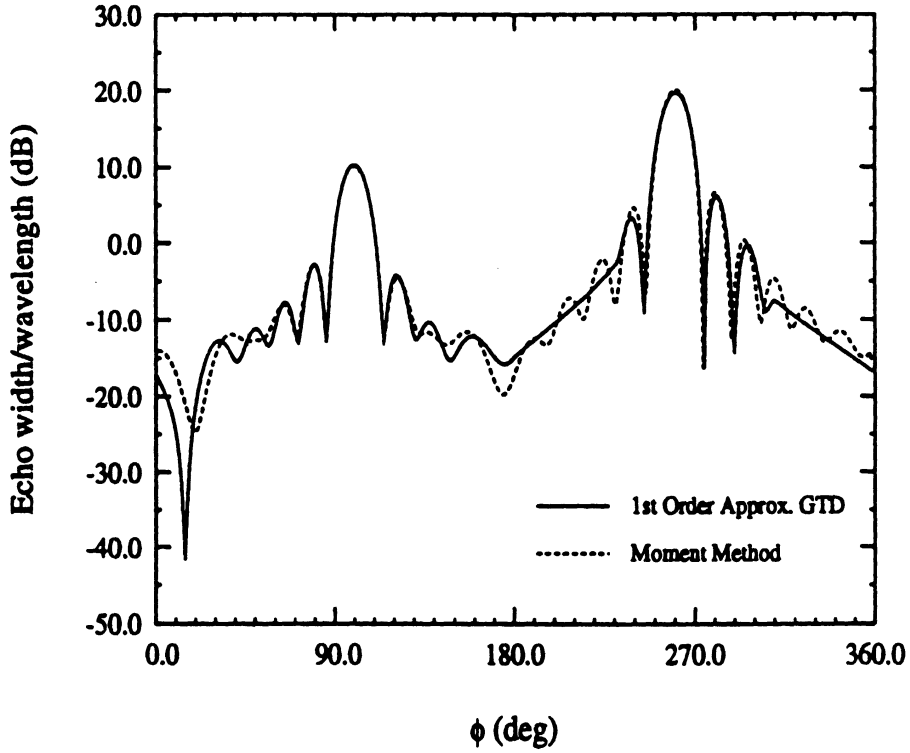

Figure 6.11: Far zone bistatic scattering pattern for a triangular cylinder with top side width $w = 4\lambda$, $\alpha = 50^o$, $\beta_o = 90^o$, $\phi' = 80^o$, and its top face having $\eta = 0.5$, and the other having $\eta = 1.0 + j1.0$, (a) $E_{\beta_o\beta'_o}$, (b) $E_{\phi\phi'}$.

(a)

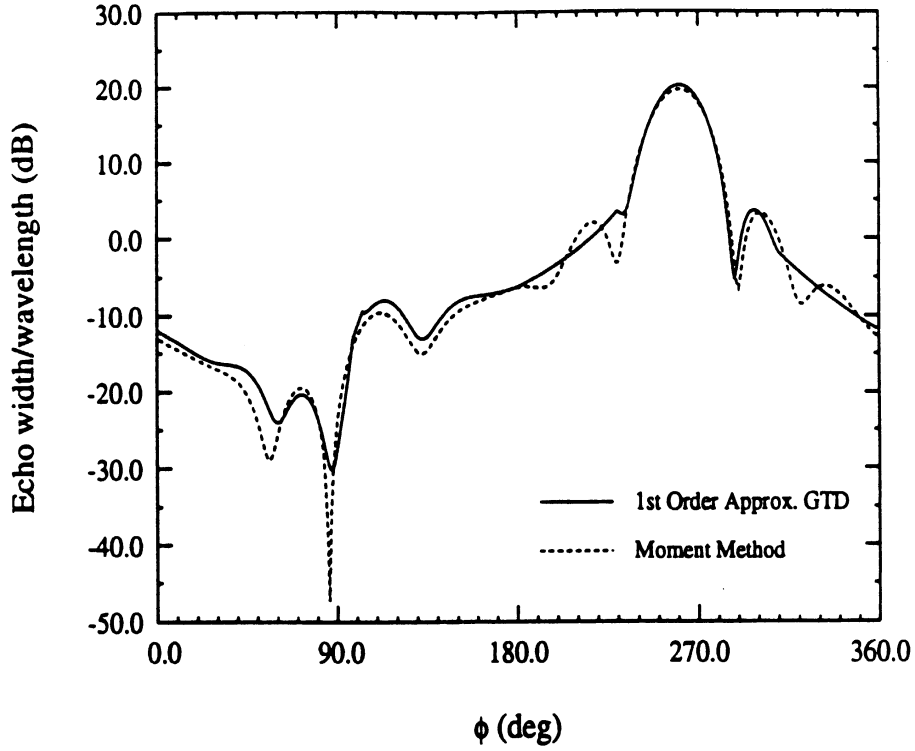

(b)

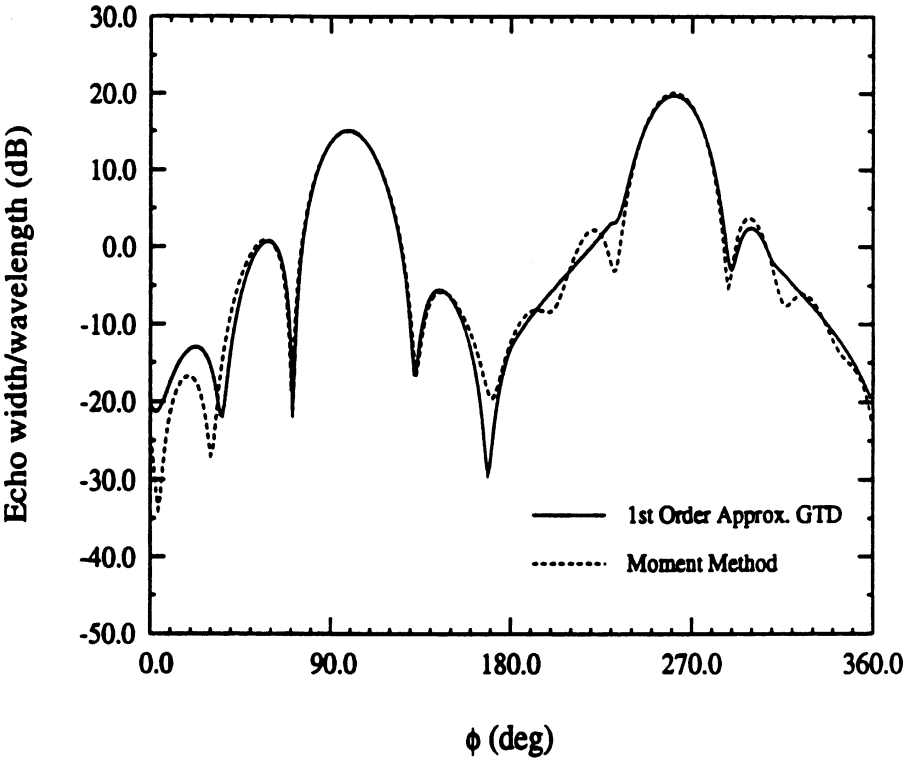

Figure 6.12: Far zone bistatic scattering pattern for a triangular cylinder with top side width $w = 4\lambda$, $\alpha = 50°$, $\beta_o = 30°$, $\phi' = 80°$, and its top face having $\eta = 0.5$, and the other having $\eta = 1.0 + j1.0$, (a) $E_{\beta_o\beta_o'}$, (b) $E_{\phi\phi'}$.

(a)

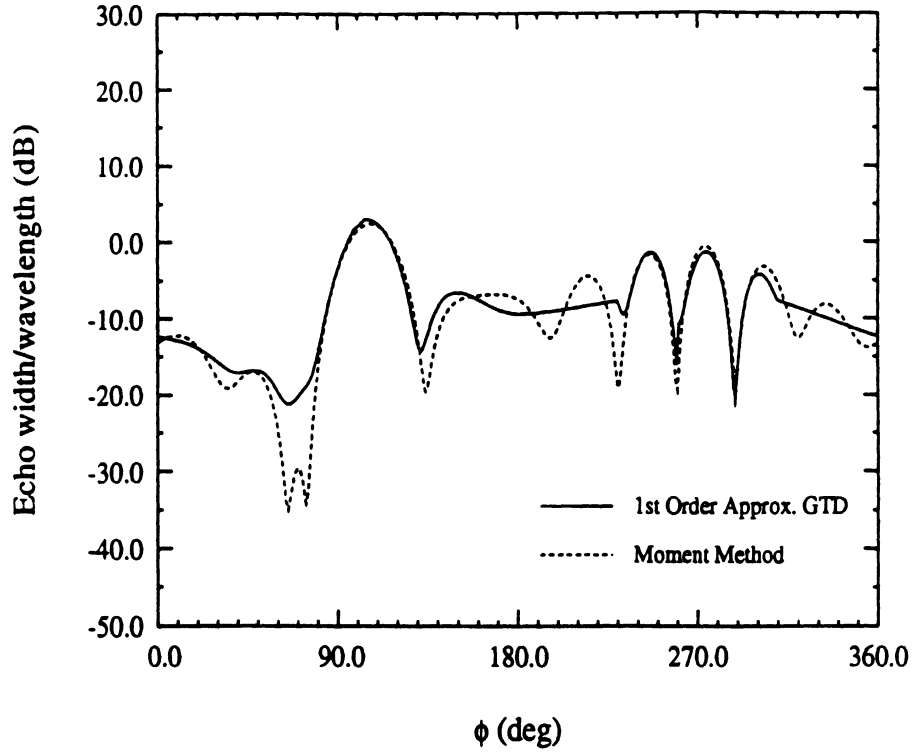

(b)

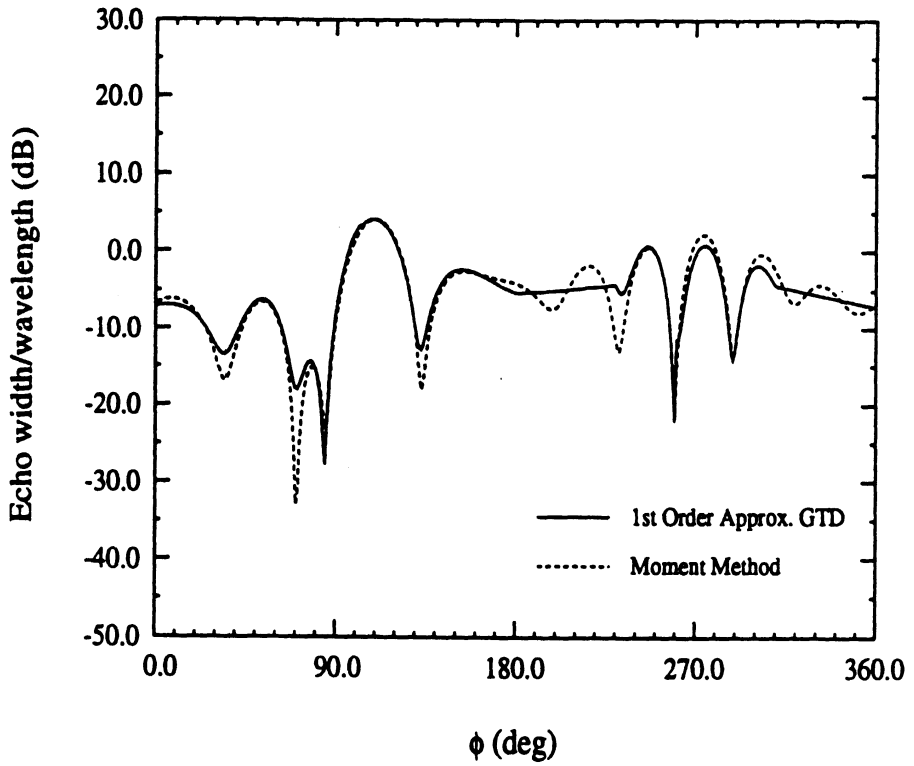

Figure 6.13: Far zone bistatic scattering pattern for a triangular cylinder with top side width $w = 4\lambda$, $\alpha = 50°$, $\beta_o = 30°$, $\phi' = 80°$, and its top face having $\eta = 0.5$, and the other having $\eta = 1.0 + j1.0$, (a) $E_{\phi\beta'_o}$, (b) $E_{\beta_o\phi'}$.

CHAPTER VII

PTD FORMULATION FOR SCATTERING BY IMPEDANCE STRUCTURES

The approximate solution developed in chapter five for an impedance wedge is essential for studying the scattering from practical three dimensional structures. In this chapter, equivalent currents are derived, based on the approximate dyadic diffraction coefficient, for computing the scattering by a finite length impedance wedge of arbitrary angle. The derived equivalent currents have been implemented in a standard general purpose PTD code [21] and results are presented demonstrating the accuracy of the formulation for a number of impedance and (dielectrically) coated structures. These include typical shapes such as plates, finite length cones and cylinders which have been partially or fully coated. The PTD type of implementation requires a dyadic physical optics diffraction coefficient which has been derived in appendix A.

7.1 Derivation of Equivalent Currents

Consider an impedance wedge of infinite length oriented along the z-axis of a spherical coordinate system as shown in figure 7.1. The normalized face impedances on the upper and the lower faces of the wedge are $\eta_+ = Z_+/Z$ and $\eta_- = Z_-/Z$, respectively, with Z being the free space intrinsic impedance. The incident electric

field on the wedge geometry is assumed to be a plane wave described by

$$\overline{E}^i(\overline{r}) = E^i e^{-jk\hat{s}^i \cdot \overline{r}} \hat{e}^i \tag{7.1}$$

where E^i is the constant complex amplitude of the incident field at the origin, $\hat{s}^i$ is the unit vector in the direction of propagation, $\overline{r}$ is the position vector of a point in space and $\hat{e}^i$ is a unit vector indicating the polarization of the incident electric field. The incident field at a point $z = z'$ on the edge can, therefore be expressed as

$$\overline{E}^i(z') = E^i e^{-jkz' \cos\beta_o'} \hat{e}^i \tag{7.2}$$

and to simulate the source of the field diffracted by the edge, we place a fictitious electric line current

$$\overline{I}^e(z') = I^e(z') e^{-jkz' \cos\beta_o'} \hat{t} \tag{7.3}$$

at the edge of the wedge, in which $\hat{t}$ denotes the unit vector tangent to the edge. The magnetic vector potential at the field point due to this current is given by

$$\overline{A}(\overline{r}) = \int_{-\infty}^{\infty} \overline{I}^e(z') \frac{e^{-jks^d}}{4\pi s^d} dz' \tag{7.4}$$

where s^d is the distance from a current element of incremental length dz' at $z = z'$ to the field point. Assuming that $\overline{I}^e(z')$ is slowly varying and k is large, (7.4) can be evaluated by the method of stationary phase to give

$$A_z(\overline{r}) \approx \frac{I^e(z_s') e^{-j\frac{\pi}{4}}}{2\sqrt{2\pi k} \sin\beta_o} e^{-jkz_s' \cos\beta_o} \frac{e^{-jks^d}}{\sqrt{s^d}} \tag{7.5}$$

where z_s' is the stationary point corresponding to the case when $\beta_o' = \beta_o$. Using this result the $\hat{\beta}_o$-polarized component of the far-zone radiated field due to the line current I^e, where $\hat{\beta}_o = \hat{s}^d \times \hat{\phi}$, is then found from

$$E_{\beta_o} = jkZ \sin\beta_o A_z \tag{7.6}$$

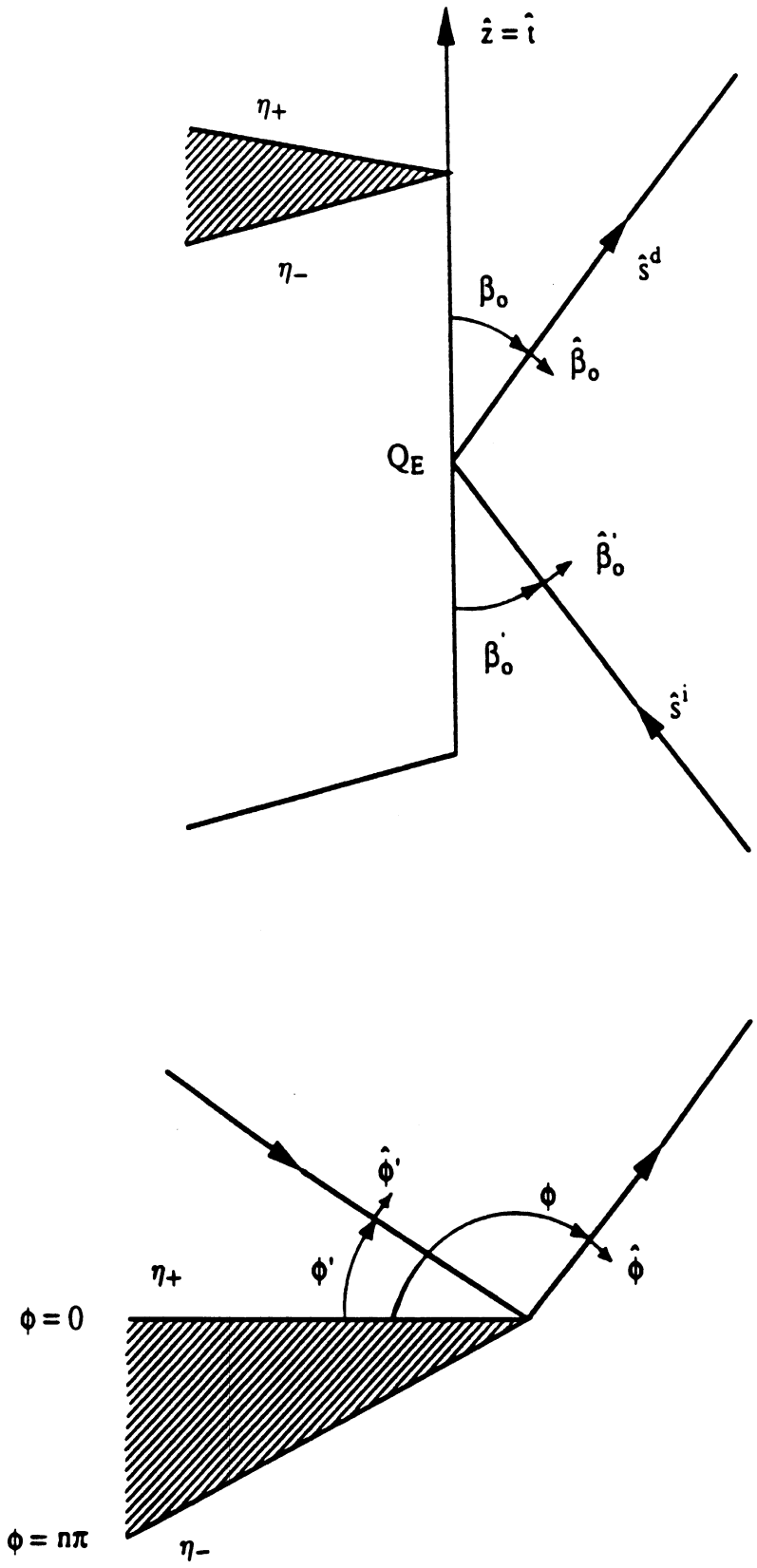

Figure 7.1: Edge-fixed coordinate system.

This must be equal to the known diffracted field from the wedge given by

$$E_{\beta_o} = -\left(E^i_{\beta'_o}\widetilde{D}_{\beta_o\beta'_o} + E^i_{\phi'}\widetilde{D}_{\beta_o\phi'}\right) e^{-jkz'_s\cos\beta_o}\frac{e^{-jks^d}}{\sqrt{s^d}}\frac{e^{-j\frac{\pi}{4}}}{\sqrt{2\pi k}} \tag{7.7}$$

where $\widetilde{D}_{\beta_o\beta'_o}$ and $\widetilde{D}_{\beta_o\phi'}$ are the diffraction coefficients of the wedge and will be defined later, $E^i_{\beta'_o}$ and $E^i_{\phi'}$ are the complex amplitudes of the $\hat{\beta}'_o$- and $\hat{\phi}'$-polarized components of the incident field at the phase origin with $\hat{\beta}'_o = \hat{s}^i \times \hat{\phi}'$. Comparing (7.6) and (7.7), the electric line current I^e is readily identified to be

$$I^e(z') = \frac{j2}{kz}\left[E^i_{\beta'_o}(z')\widetilde{D}_{\beta_o\beta'_o}(z') + E^i_{\phi'}(z')\widetilde{D}_{\beta_o\phi'}(z')\right] \tag{7.8}$$

Following a similar procedure one can obtain the expression for the magnetic line current I^m to be

$$I^m(z') = \frac{-j2}{k}\left[E^i_{\beta'_o}(z')\widetilde{D}_{\phi\beta'_o}(z') + E^i_{\phi'}(z')\widetilde{D}_{\phi\phi'}(z')\right] \tag{7.9}$$

7.2 Radiation from Equivalent Currents on a Finite Wedge

7.2.1 Straight Wedge

Consider a straight wedge of finite length ℓ oriented in the direction $\hat{t}$ as shown in figure 7.2. For this case, it is convenient to assume a local coordinate system (x', y', z') for the wedge so that $\hat{t}$ coincides with the z'-axis. The origin of this local system is chosen to be at the center of the wedge and is defined by the global position vector $\bar{r}'_o$.

We again postulate the existence of filamentary electric and magnetic currents I^e and I^m on the finite edge. The amplitudes of these equivalent currents are assumed to be the same as those found for the infinite wedge. The field diffracted by the finite wedge can then be computed by integrating these currents over the finite length of

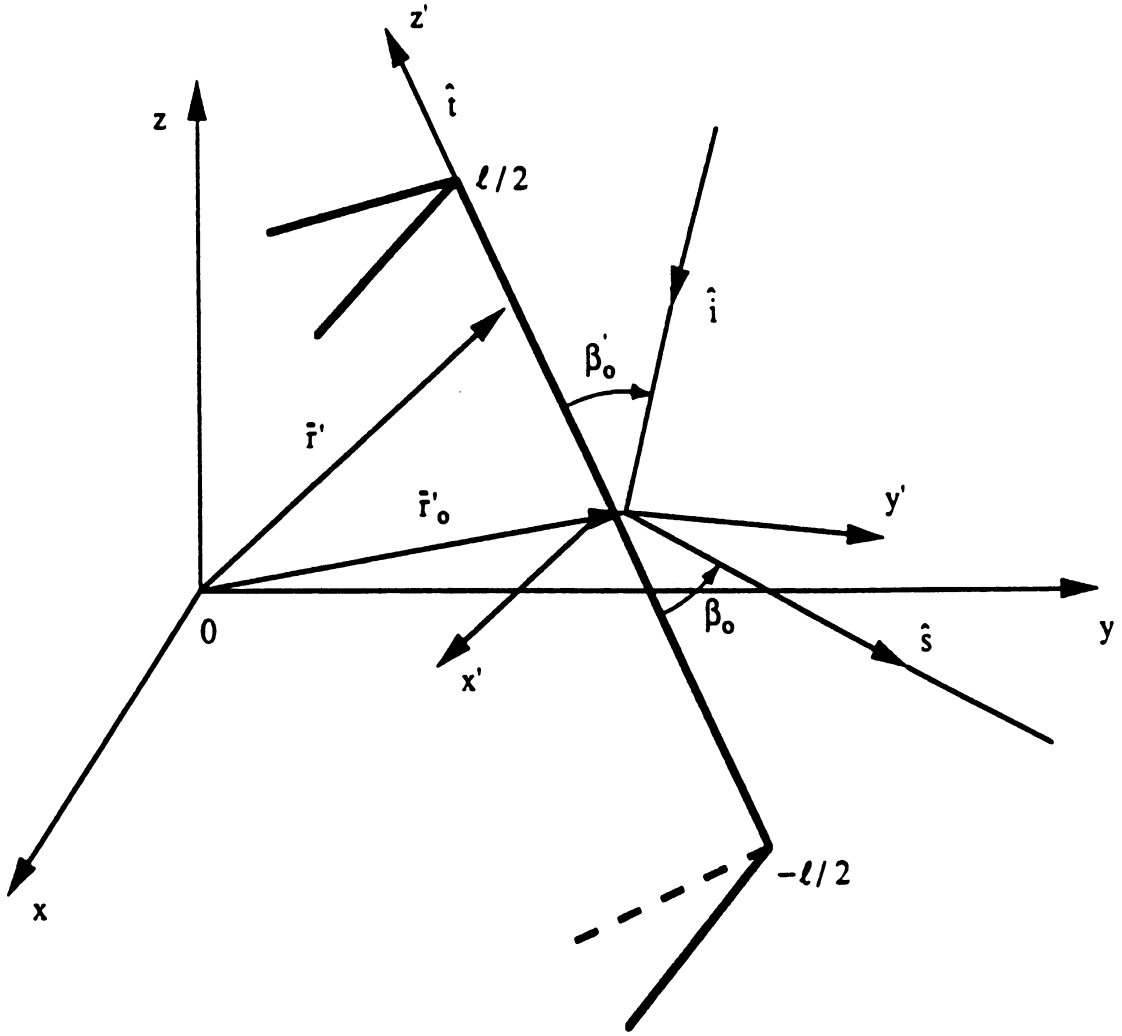

Figure 7.2: Finite impedance wedge geometry.

the wedge. In the far zone, we obtain the diffracted field

$$\overline{E}^d \approx jk \int_{-\ell/2}^{\ell/2} \left[ZI^e(\overline{r}')\hat{s} \times (\hat{s} \times \hat{t}) + I^m(\overline{r}')(\hat{s} \times \hat{t}) \right] \frac{e^{-jk(r-\hat{s}\cdot\overline{r}')}}{4\pi r} dz' \tag{7.10}$$

where $\overline{r}'$ is the position vector of a current filament on the wedge and the propagation direction of the radiated field is defined by the unit vector

$$\hat{s} = \hat{x}\sin\theta\cos\phi + \hat{y}\sin\theta\sin\phi + \hat{z}\cos\theta \tag{7.11}$$

Substituting the expression for $I^e(\overline{r}')$ and $I^m(\overline{r}')$ in (7.10) and noting that

$$E^i_{\beta'_o}(\overline{r}') = \frac{\hat{t}\cdot\hat{e}^i}{\sin\beta_o} E^i(\overline{r}') \tag{7.12}$$

and

$$E^i_{\phi'}(\overline{r}') = \frac{-(\hat{t}\times\hat{i})\cdot\hat{e}^i}{\sin\beta_o} E^i(\overline{r}') \tag{7.13}$$

the far-zone radiated field is more explicitly given by

$$\overline{E}^d = \frac{-e^{-jkr}}{2\pi r\sin\beta_o} \int_{-\ell/2}^{\ell/2} \Big[\hat{s}\times(\hat{s}\times\hat{t}) \Big\{ (\hat{t}\cdot\hat{e}^i)\widetilde{D}_{\beta_o\beta'_o} - (\hat{t}\times\hat{i})\cdot\hat{e}^i\widetilde{D}_{\beta_o\phi'} \Big\}$$

$$-(\hat{s}\times\hat{t}) \Big\{ (\hat{t}\cdot\hat{e}^i)\widetilde{D}_{\phi\beta'_o} - (\hat{t}\times\hat{i})\cdot\hat{e}^i\widetilde{D}\phi\phi' \Big\} \Big] e^{jk(\hat{s}-\hat{i})\cdot\overline{r}'} dz' \tag{7.14}$$

where the incident field on the edge is assumed to be

$$\overline{E}^i(\overline{r}') = E^i(\overline{r}')\hat{e}^i = e^{-jk\hat{i}\cdot\overline{r}'}\hat{e}^i \tag{7.15}$$

and $\hat{i}$ is the propagation direction of the incident field given by

$$\hat{i} = -\hat{x}\sin\theta^i\cos\phi^i - \hat{y}\sin\theta^i\sin\phi^i + \hat{z}\cos\theta^i \tag{7.16}$$

If required, one can write the $\hat{u}$-polarized component of the above field as

$$\hat{u}\cdot\overline{E}^d = \frac{e^{-jkr}}{2\pi r\sin\beta_o} e^{jk(\hat{s}-\hat{i})\cdot\overline{r}'_o} \Big[(\hat{u}\cdot\hat{t}) \Big\{ (\hat{t}\cdot\hat{e}^i)\widetilde{D}_{\beta_o\beta'_o} - (\hat{t}\times\hat{i})\cdot\hat{e}^i\widetilde{D}_{\beta_o\phi'} \Big\}$$

$$-\hat{u}\cdot(\hat{t}\times\hat{s}) \Big\{ (\hat{t}\cdot\hat{e}^i)\widetilde{D}_{\phi\beta'_o} - (\hat{t}\times\hat{i})\cdot\hat{e}^i\widetilde{D}_{\phi\phi'} \Big\} \Big] \int_{-\ell/2}^{\ell/2} e^{jkz'(\hat{s}-\hat{i})\cdot\hat{t}} dz' \tag{7.17}$$

where $\hat{u}$ is a unit vector transverse to $\hat{s}$ (the unit vector in the direction of propagation). Also in the above we have used the fact that

$$\overline{r}' = \overline{r}'_o + z'\hat{z}' \tag{7.18}$$

Performing the integration defined in (7.17) yields

$$\hat{u}\cdot\overline{E}^d = \frac{e^{-jkr}}{2\pi r\sin\beta_o}e^{jk(\hat{s}-\hat{i})\cdot\overline{r}'_o}\Big[(\hat{u}\cdot\hat{t})\left\{(\hat{t}\cdot\hat{e}^i)\widetilde{D}_{\beta_o\beta'_o}-(\hat{t}\times\hat{i})\cdot\hat{e}^i\widetilde{D}_{\beta_o\phi'}\right\}$$

$$-\hat{u}\cdot(\hat{t}\times\hat{s})\left\{(\hat{t}\cdot\hat{e}^i)\widetilde{D}_{\phi\beta'_o}-(\hat{t}\times\hat{i})\cdot\hat{e}^i\widetilde{D}_{\phi\phi'}\right\}\Big]\ell\,\mathrm{sinc}\left\{\frac{k\ell(\hat{s}-\hat{i})\cdot\hat{t}}{2}\right\} \tag{7.19}$$

In this the diffraction coefficients $\widetilde{D}$ can be chosen depending upon the type of high frequency theory to be employed. In particular,

$$\widetilde{D} = D^{GTD} - D^{PO} \qquad \text{(Physical Theory of Diffraction or PTD)} \tag{7.20a}$$

$$\widetilde{D} = D^{PO} \qquad \text{(Physical Optics)} \tag{7.20b}$$

$$\widetilde{D} = D^{GTD} \qquad \text{(Geometrical Theory of Diffraction)} \tag{7.20c}$$

where D^{GTD} is the approximate diffraction coefficient derived in chapter five and D^{PO} is the physical optics diffraction coefficient for an impedance wedge derived in appendix A.

7.2.2 Curved Wedge

Consider now the curved impedance wedge shown in figure 7.3. The curve describing the edge is arbitrary and may vary continuously. If a plane wave is incident on the edge, the total field diffracted from it can be calculated by first dividing the

edge into small straight segments and then summing the individual contributions, i.e.,

$$\overline{E}^d \text{ (total)} = \sum \overline{E}^d \text{ (segment)} \tag{7.21}$$

Suppose the excitation field at one of these small (incremental length) segments is given by

$$\overline{E}^i = e^{-jk\hat{i}\cdot\bar{r}}\left(\hat{\theta}^i a_{\theta^i} + \hat{\phi}^i a_{\phi^i}\right) \tag{7.22}$$

and the far-zone field associated with the diffracted field from this differential length along the edge may be written as

$$\overline{E}^d \approx \frac{e^{-jkr}}{r}\left(\hat{\theta} b_\theta + \hat{\phi} b_\phi\right) \tag{7.23}$$

From (7.19), the scattering amplitudes b_θ and b_ϕ of the diffracted field by each segment are then related to the incident field amplitudes through the matrix

$$\begin{bmatrix} b_\theta \\ \\ b_\phi \end{bmatrix} = \begin{bmatrix} f_{\theta\theta^i} & f_{\theta\phi^i} \\ \\ f_{\phi\theta^i} & f_{\phi\phi^i} \end{bmatrix} \begin{bmatrix} a_{\theta^i} \\ \\ a_{\phi^i} \end{bmatrix} \tag{7.24}$$

where

$$f_{ue^i} = \frac{e^{-jkr}}{2\pi r \sin\beta_o} e^{jk(\hat{s}-\hat{i})\cdot\bar{r}'_o}\Big[(\hat{u}\cdot\hat{t})\left\{(\hat{t}\cdot\hat{e}^i)\widetilde{D}_{\beta_o\beta'_o} - (\hat{t}\times\hat{i})\cdot\hat{e}^i\widetilde{D}_{\beta_o\phi'}\right\}$$

$$-\hat{u}\cdot(\hat{t}\times\hat{s})\left\{(\hat{t}\cdot\hat{e}^i)\widetilde{D}_{\phi\beta'_o} - (\hat{t}\times\hat{i})\cdot\hat{e}^i\widetilde{D}_{\phi\phi'}\right\}\Big]\ell \text{ sinc}\left\{\frac{k\ell(\hat{s}-\hat{i})\cdot\hat{t}}{2}\right\} \tag{7.25}$$

where $\hat{u}$ stands for $\hat{\theta}$ or $\hat{\phi}$ whereas $\hat{e}^i$ represents $\hat{\theta}^i$ or $\hat{\phi}^i$, and since the discretization segments are small we may set

$$\text{sinc}\left\{\frac{k\ell(\hat{s}-\hat{i})\cdot\hat{t}}{2}\right\} \to 1 \tag{7.26}$$

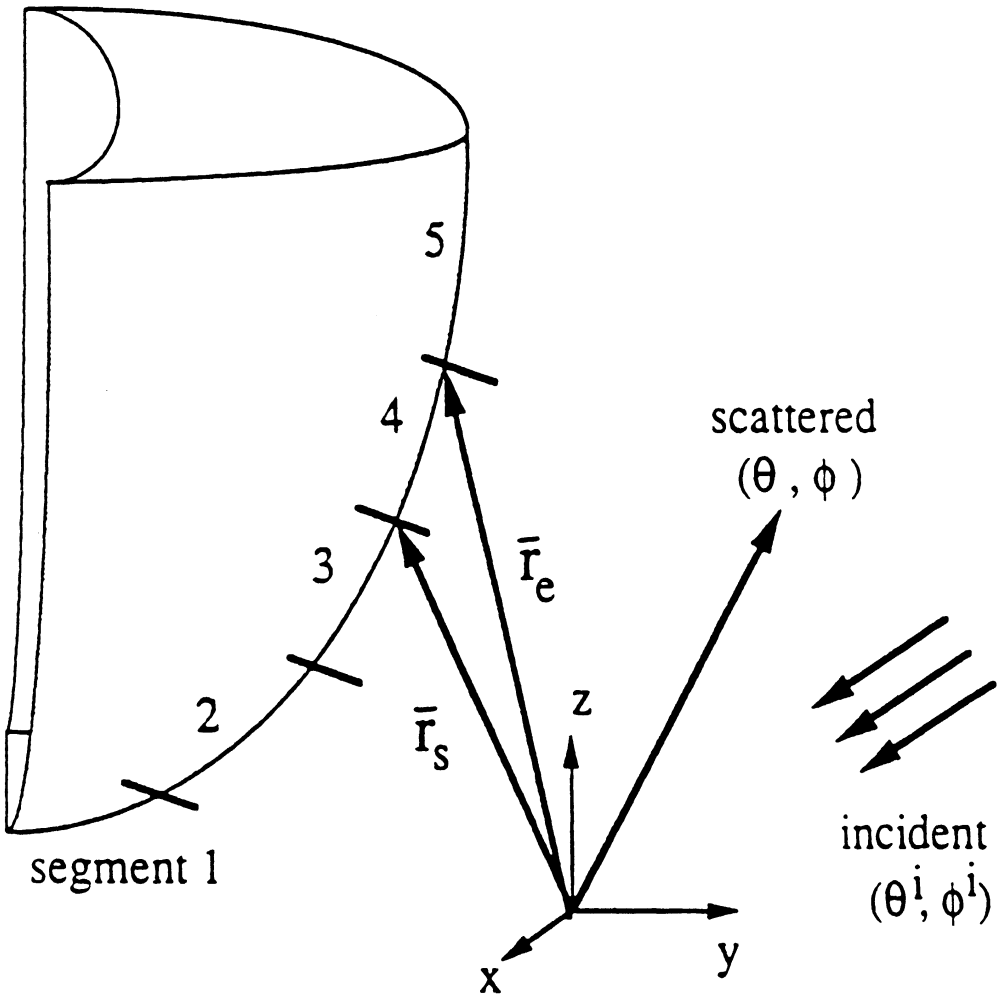

Figure 7.3: A curved three dimensional wedge illuminated by an incident plane wave.

Equations (7.21) in conjunction with (7.23)–(7.25) can be employed to calculate the total diffracted field from an arbitrary curved edge. The RCS due to the edge diffraction is then given by

$$\sigma_{ue^i} = 4\pi \left| f_{ue^i} \right|^2 \tag{7.27}$$

It should be noted that $\overline{E}^d$ in (7.21) is only the partial field and, therefore, the RCS in (7.27) is the partial RCS of the scatterer. To compute the total far-zone scattered field we must add a complementary field to the diffracted field. Since in this work we will pursue a PTD type of implementation, the complementary field will be a Physical Optics (PO) field and the total field will be

$$\overline{E}^t = \overline{E}^d + \overline{E}^{PO} \tag{7.28}$$

Hence, for the total RCS, the physical optics field must be calculated separately and then superimposed with the diffracted field to give

$$\sigma^t_{ue^i} = 4\pi \left| f^t_{ue^i} \right|^2 \tag{7.29}$$

where

$$f^t_{ue^i} = f_{ue^i} + f^{PO}_{ue^i} \tag{7.30}$$

7.3 Test Results

The derived equivalent currents have been implemented in a standard general purpose PTD code called McPTD [21] which employs only first order high-frequency far zone fields. In particular, the codes McWedge (for a general curved PEC wedge geometry), McLine (for long straight PEC wedges) and McRing (for a PEC wedge forming a ring) have been modified for the case of an impedance wedge. To test the accuracy of the equivalent current formulation, we refer to figures 7.4 – 7.8 where

the RCS of a number of different structures is plotted as a function of incident angle ϕ^i. The results obtained from McPTD have been compared with the measured and moment method data. The numerical data is obtained from a body of revolution code which does not employ any approximate boundary conditions and is, therefore, considered to be exact for coated structures. The RCS patterns given in figures 7.4 – 7.6 are for a flat base cone with half cone angle $\alpha = 15°$. Figures 7.4(a) and 7.4(b) display patterns due to incident $E^i_{\phi^i}$ (HH) polarization for a perfectly conducting and a coated cone, respectively, with base diameter of 2.0λ. A decrease in RCS in the case of the coated cone is observed because of the lossy coating. In figure 7.5, patterns for a larger cone having base diameter of 3.0λ have been presented. Figures 7.6(a) and 7.6(b) show RCS patterns of a partially coated cone, having a perfectly conducting base, due to incident $E^i_{\phi^i}$ (HH) and $E^i_{\theta^i}$ (VV) polarization, respectively. RCS patterns for a finite circular cylinder are displayed in figure 7.7 whereas figure 7.8 shows RCS patterns for a plate.

7.4 Summary

To demonstrate the usefulness of the approximate diffraction coefficient, obtained in chapter five, equivalent currents were presented in the context of PTD for a finite length impedance wedge of arbitrary internal angle. These were eventually incorporated in a standard general purpose physical theory of diffraction (PTD) code [21] and results were presented which demonstrated the accuracy of the formulation for a number of different impedance structures. These included typical shapes such as plates, finite length cones and cylinders which were partially or fully coated.

(a)

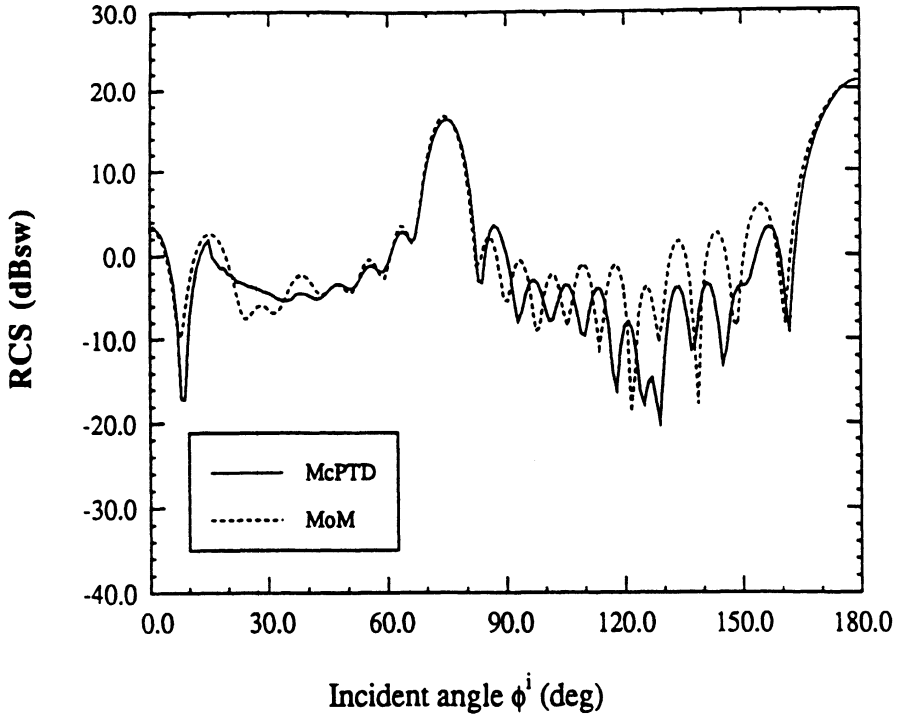

(b)

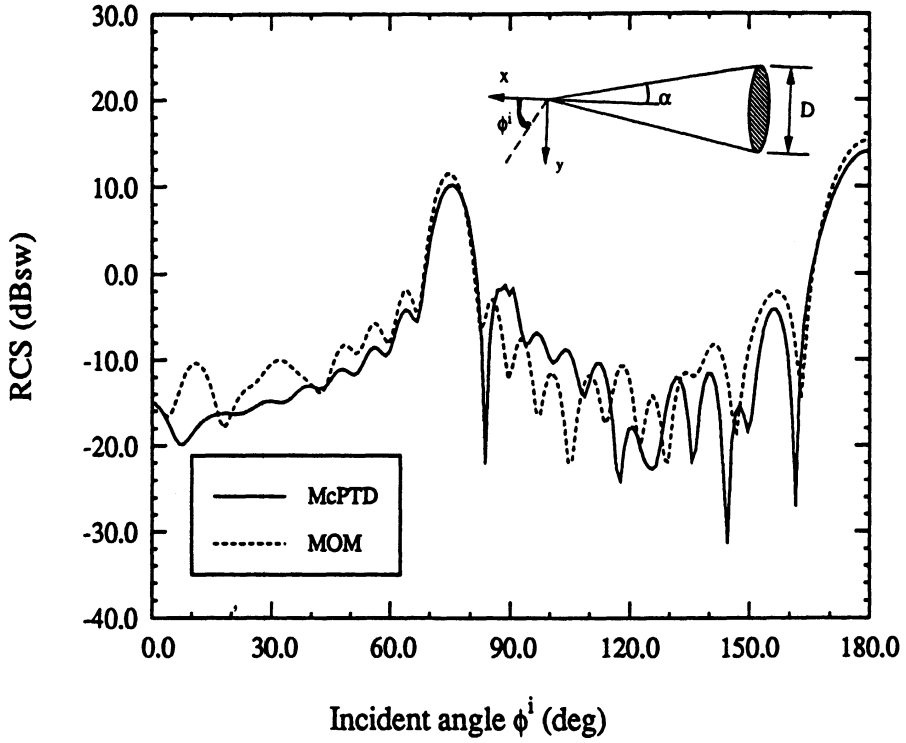

Figure 7.4: RCS of a flat base cone due to incident $E^i_{\phi^i}$ (HH) polarization with $\alpha = 15^o$, $D = 2\lambda$, $\theta^i = 90^o$, (a) perfectly conducting cone, (b) coated cone: ϵ_r=7-j1.5, μ_r=2- j1, coating thickness=0.04λ.

(a)

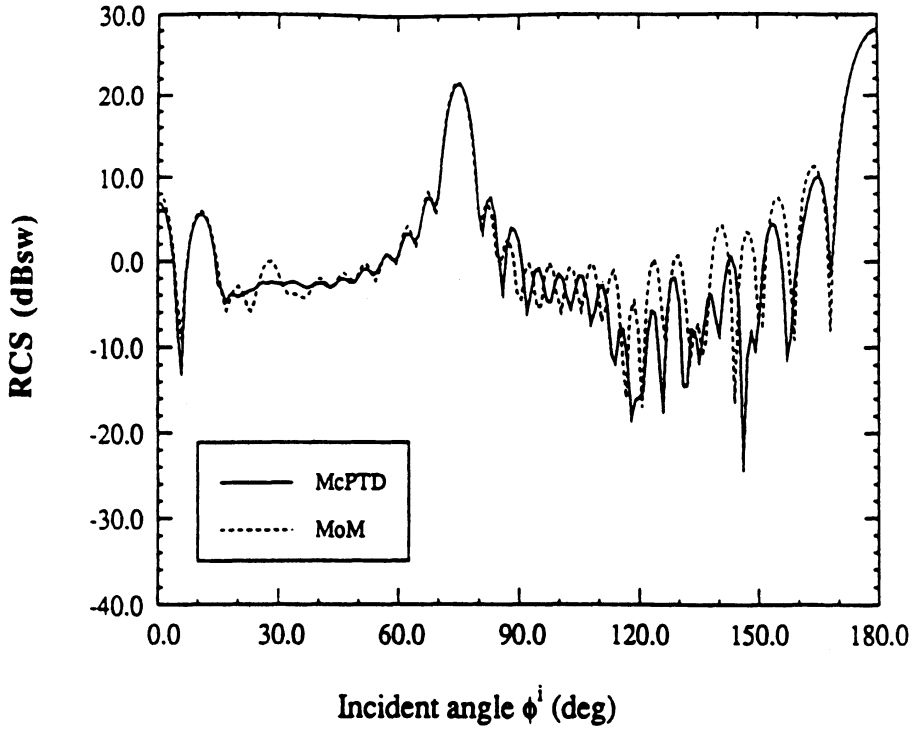

(b)

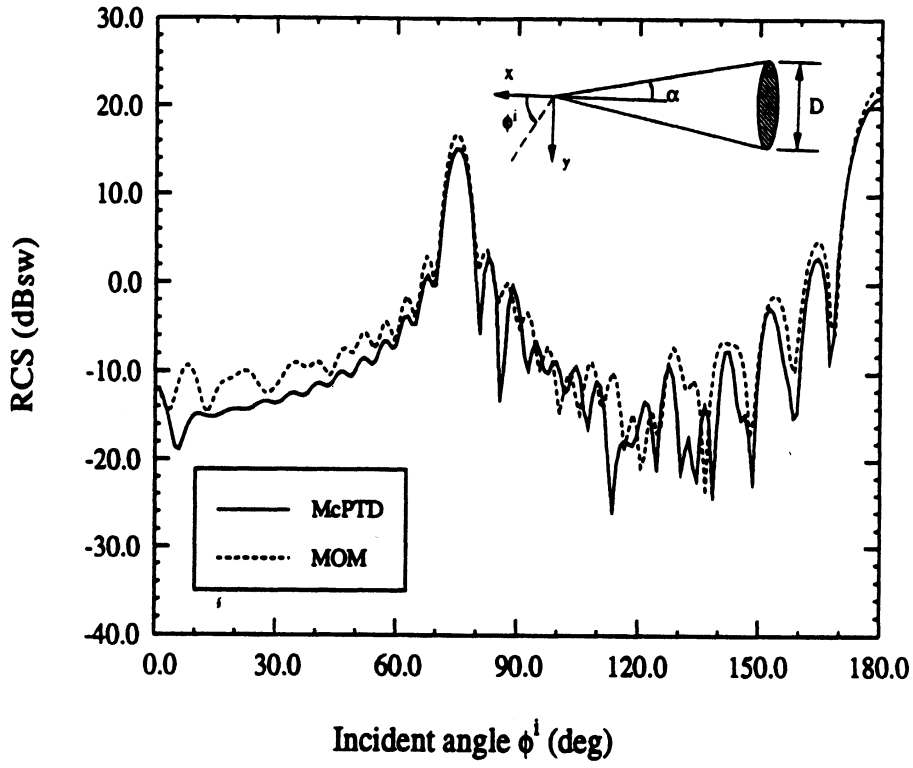

Figure 7.5: RCS of a flat base cone due to incident $E^i_{\phi^i}$ (HH) polarization with $\alpha = 15^o$, $D = 3\lambda$, $\theta^i = 90^o$, (a) perfectly conducting cone, (b) coated cone: ϵ_r=7-j1.5, μ_r=2- j1, coating thickness=0.04λ.

(a)

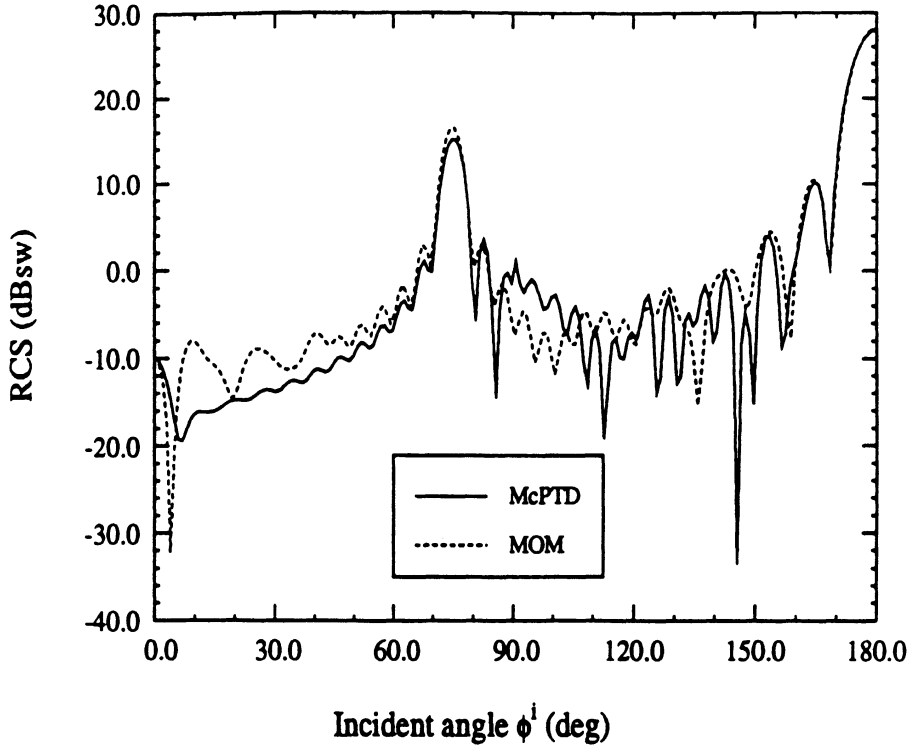

(b)

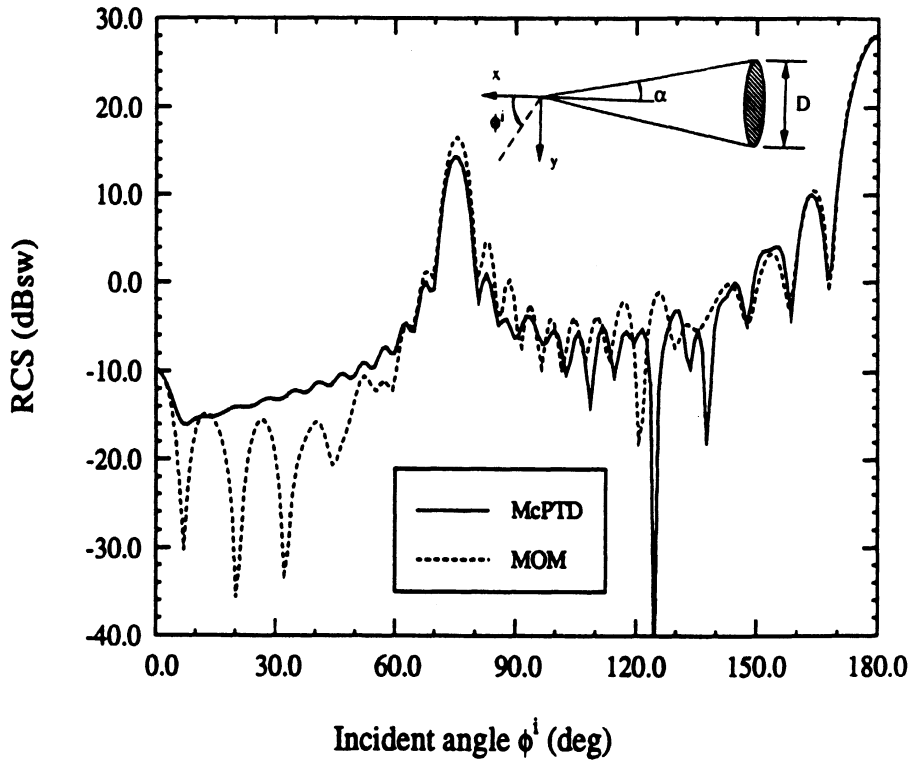

Figure 7.6: RCS of a partially coated flat base cone having perfectly conducting base with $\alpha = 15°$, $D = 3\lambda$, ϵ_r=7-j1.5, μ_r=2-j1, coating thickness=0.04λ, $\theta^i = 90°$, (a) $E^i_{\phi^i}$ (HH) polarization, (b) $E^i_{\theta^i}$ (VV) polarization.

(a)

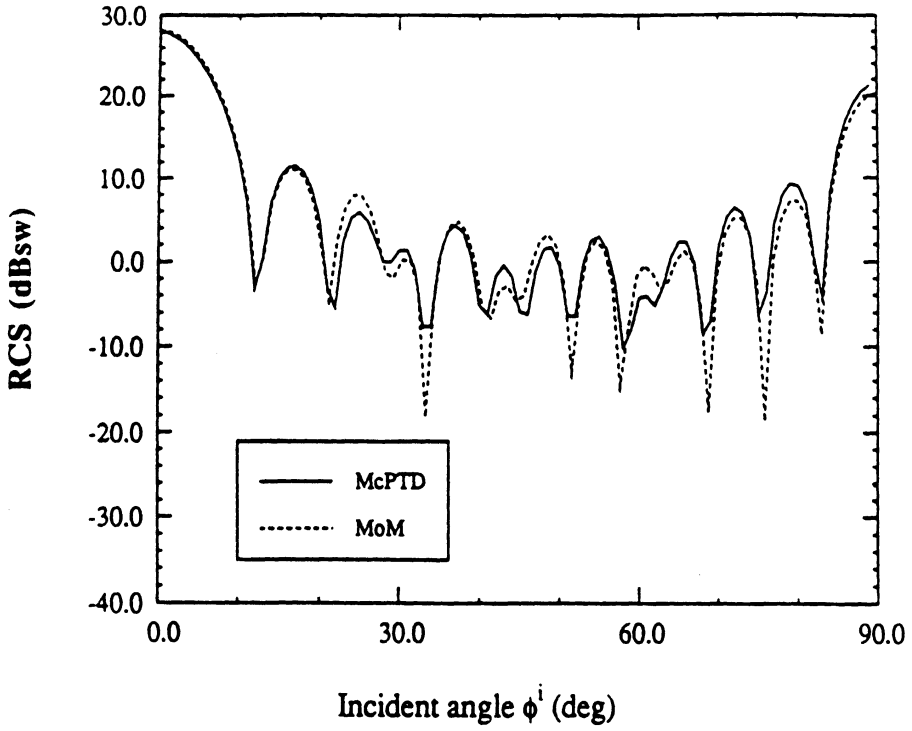

(b)

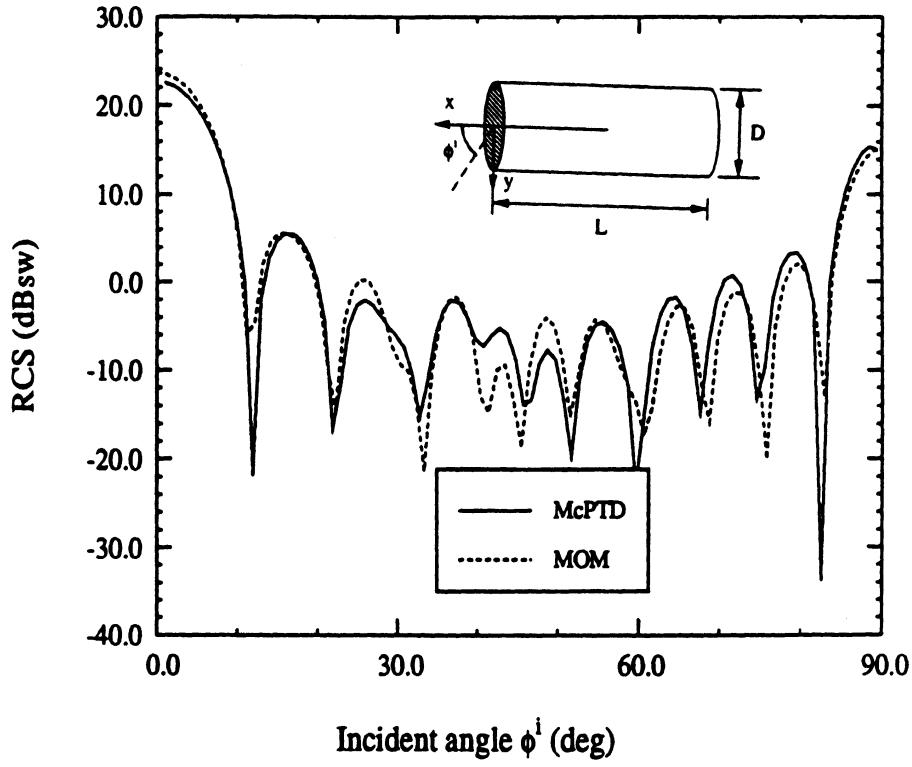

Figure 7.7: RCS of a finite circular cylinder due to incident $E^i_{\phi^i}$ (HH) polarization with $D = 3\lambda$, $L = 4\lambda$, $\theta^i = 90°$, (a) perfectly conducting cylinder, (b) coated cylinder: ϵ_r=4-j1.5, μ_r=2-j1, coating thickness=0.04λ.

(a)

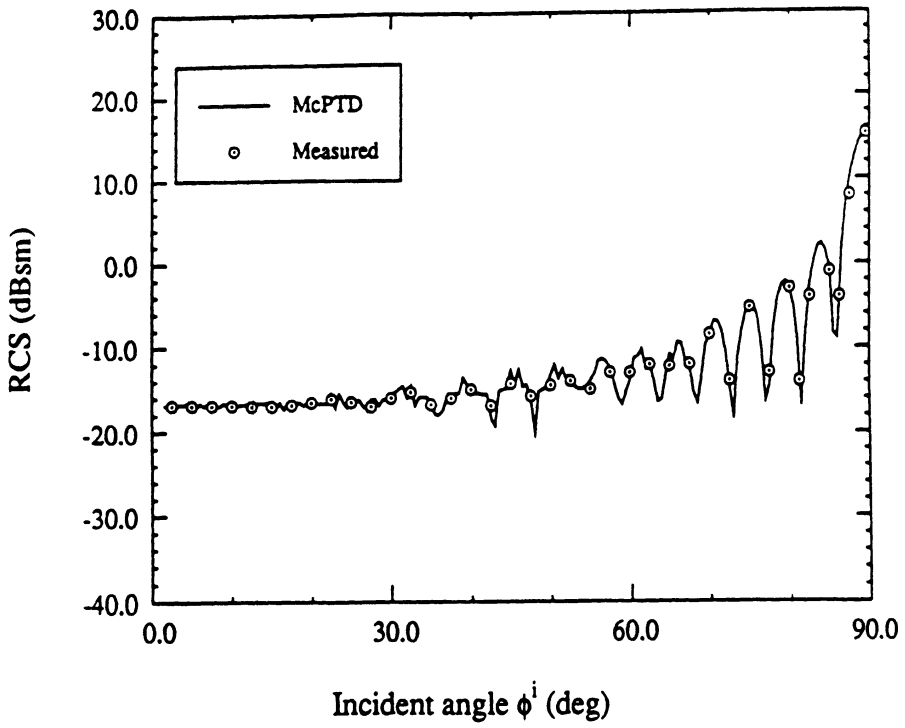

(b)

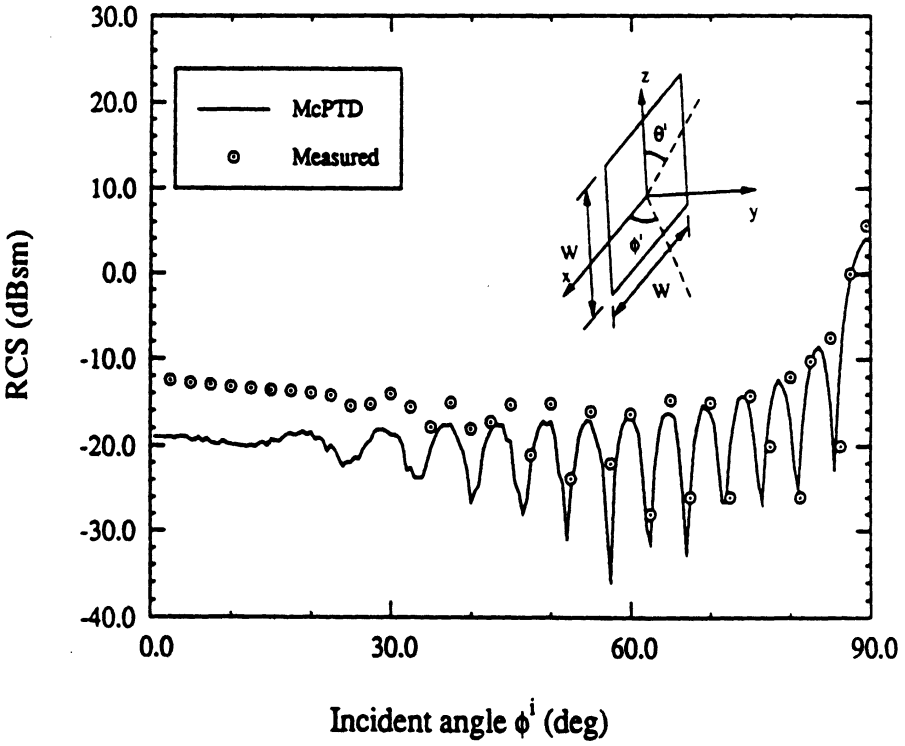

Figure 7.8: RCS of a square plate due to incident $E^i_{\theta i}$ (VV) polarization with $W = 10\lambda$, $\theta^i = 90^o$, (a) perfectly conducting plate, (b) coated plate: ϵ_r=12.1-j0.46, μ_r=2- j1.26, coating thickness=0.08 inches, frequency=8.004 GHZ.

CHAPTER VIII

CONCLUSIONS

In this study, asymptotic/high-frequency solutions were developed for analyzing some non-specular scattering mechanisms associated with coated convex surfaces and edges where the coating was simulated by approximate boundary conditions. Both the standard impedance boundary conditions (SIBCs) and the generalized impedance boundary conditions (GIBCs) were employed for a characterization of edge diffraction, creeping wave and surface diffracted wave contributions.

Second order generalized impedance boundary conditions (GIBCs) were derived in chapter two for a single and a three-layer coating and these were employed in chapter three to construct integral equations for scattering by two-dimensional coated structures of arbitrary cross-section. These integral equations were implemented via a moment method procedure and the results were compared with reference data based on analytical or other validated numerical solutions. It was found that the proposed second order boundary conditions provide an improved simulation of the coating in comparison with the traditional (first order) impedance boundary condition and guidelines were given for their region of validity. The primary reason for the improved simulation is because the second order GIBC accounts for the presence of polarization current components normal to the coating in addition to the tangential

ones. In general, the presence of edges or abrupt changes in the material leads to simulation inaccuracies which become more apparent as the coating thickness increases. This is due to the inherent non-uniqueness of these boundary conditions at abrupt terminations, a situation which can only be remedied by introducing additional field constraints at the terminations [51,52].

The non-specular scattering mechanisms like creeping waves and surface diffracted waves were considered in chapter four as applied to a coated convex cylinder. Rigorous ray solutions of the scattered fields were presented for a coated convex cylinder simulated by SIBCs and GIBCs. These were developed in the context of the uniform geometrical theory of diffraction and specific expressions were given for the scattered fields in the lit, shadow and transition regions as well as for observations in the near vicinity of the cylinder. Specifically, UTD expressions were derived for all regions exterior to the coated cylinder and these were shown to be suited for engineering computations. As expected, the derived UTD expressions were given in terms of the generalized Pekeris or Fock-type functions whose evaluation was efficiently performed via the Fourier Trapezoidal rule suggested by Pearson [45].

In comparison to the solution given by Kim and Wang [41], the ray representations given here, for the surface diffracted field, are based on a second order generalized impedance boundary condition which permits the simulation of thin multilayered coating as demonstrated in the included examples. Also, in our implementation of the transition fields we employed a rigorous rather than a heuristic evaluation of the Fock-type integrals. Further, we have presented accurate field representations for observations on or near the vicinity of the coated cylinder and these can also be used for computing the radiated fields by a source or an aperture on the surface of the convex cylinder.

In chapter five, a most important source of non-specular electromagnetic scattering, that of diffraction by an impedance wedge at skew incidence was considered. Application of the boundary conditions (SIBCs) on the wedge faces resulted in a set of four coupled functional difference equations. Three different approximate solutions were derived on the basis of these difference equations. Two of the approximate solutions were obtained by separating the difference equations associated with the upper and lower faces of the impedance wedge, respectively. These were found to recover the known solutions for three different sets of wedge angles and skewness angles, namely those corresponding to, normal incidence ($\beta_o = 90^o$) with arbitrary wedge angle, a half plane (arbitrary β_o, internal wedge angle = 0^o) and a two part plane (arbitrary β_o, internal wedge angle = 180^o). An important feature of our solution, lacked by the others [13,14,15,19], is that a single computer code can be employed to compute the scattered field for all three special cases mentioned above. A third approximate solution was constructed by approximating the trigonometric functions $\sin\alpha$ and $\cos\alpha$ appearing in the difference equations with functions having a period of 2Φ. This solution again was shown to reduce to the exact solutions of the half plane (arbitrary β_o, internal wedge angle = 0^o) and that of the normal incidence wedge ($\beta_o = 90^o$). For other β_o and wedge angles, the three approximate solutions were found to be of acceptable accuracy in certain regions of space and a scheme was suggested to combine all three approximate solutions for approximating the diffracted field in the entire angular section exterior to the wedge. Some comparisons with the exact solution for the right-angled wedge showed that the accuracy of the approximate solutions was still acceptable even for the internal wedge angle of 90^o which was quite far from that of a half plane.

To validate the approximate solution, developed in chapter five for an impedance

wedge, a coupled set of integral equations for skew incidence on an impedance polygonal cylinder of arbitrary shape were derived and solved via the moment method. The surface currents obtained from the solution of the coupled integral equations were subsequently integrated to yield the scattered field on the diffraction cone. A corresponding first order high frequency (GTD) solution for the far zone scattered field was then generated using the approximate diffraction coefficient and compared with the moment method data for a variety of different wedge angles. A remarkable agreement was found between the first order GTD solution and the corresponding moment method data for internal wedge angles up to 50°.

Finally, to test the usefulness of the approximate skew incidence wedge diffraction coefficients for practical three dimensional structures, equivalent currents were presented in the context of PTD for a finite length impedance wedge of arbitrary internal angle. These were incorporated in a standard general purpose physical theory of diffraction (PTD) code [21] and results were presented which demonstrated the accuracy of the formulation for a number of different impedance structures such as plates, finite length cones and cylinders which were partially or fully coated. The PTD implementation required a dyadic physical optics (PO) diffraction coefficient which was derived in appendix A.

For the future work, a characterization of the diffraction effects by impedance discontinuities in smooth convex cylinders should be pursued. Of interest is the case where the observer and the source are both at a finite distance away from the discontinuity. This will accommodate the situation when a creeping wave strikes the discontinuity and the observation point is also near or on the surface of the impedance cylinder. To treat this case, at first a parallel analysis should be carried out for an impedance insert on an impedance plane. The results of this analysis will then be

extended to the case of a similar impedance discontinuity on the convex cylinder on the assumption that the cylinder radius is large. Alternatively, a direct analysis could be pursued. The pertaining analysis will certainly be much more complex and the resulting diffraction coefficients may not, therefore, be of practical use. Using the diffraction coefficients based on the forementioned analysis, it will be possible to characterize the scattering and radiation by apertures and conformal antennas on a convex impedance cylinder. An analysis of the mutual coupling among such devices is another application of interest.

The proposed research in the above paragraph is concerned with the two dimensional applications. A natural extension of this work would be an analysis for three dimensional applications. In this case, the electric and magnetic fields are coupled on the cylinder surface and thus heuristic extensions of the two dimensional results to three dimensions, usually done in the case of perfectly conducting structures, are not applicable. In general, therefore, a separate analysis is required in the case of skew incidence.

The solutions developed in this work, for scattering by an impedance wedge at skew incidence, were obtained by solving a first order homogeneous functional difference equation. However, these solutions are approximate and a next step should be to improve the accuracy of these approximate solutions by employing, for example, an iterative procedure. Such a procedure will require a solution of a first order inhomogeneous functional difference equation and, therefore, will make the analysis more complicated. Another future task should be to pursue a rigorous solution for an impedance wedge of arbitrary wedge angle with GIBCs imposed on its faces.

APPENDICES

APPENDIX A

PHYSICAL OPTICS DIFFRACTION COEFFICIENT FOR AN IMPEDANCE WEDGE AT SKEW INCIDENCE

The impedance wedge diffraction coefficient presented in chapter five predicts infinite diffracted field at the incident and reflection shadow boundaries. However, this difficulty can be overcome by subtracting a physical optics diffraction coefficient from it resulting in a finite field at the shadow boundaries. The diffracted field obtained in this manner is only a partial field and is called a fringe field. The total scattered field for a particular finite structure having edges can be computed by calculating the physical optics field for the structure, separately, and then adding it to the fringe field.

In this appendix, a dyadic diffraction coefficient, for an impedance wedge, is derived using physical optics. In other words, we seek a physical optics approximation to the diffraction tensor given in chapter five.

Consider a plane wave incident on the upper face of an impedance wedge (see figure A.1) and is represented by

$$\overline{E}^i = \overline{e}e^{-jk\hat{s}^i\cdot\overline{r}}, \quad z\overline{H}^i = \overline{h}e^{-jk\hat{s}^i\cdot\overline{r}} \tag{A.1}$$

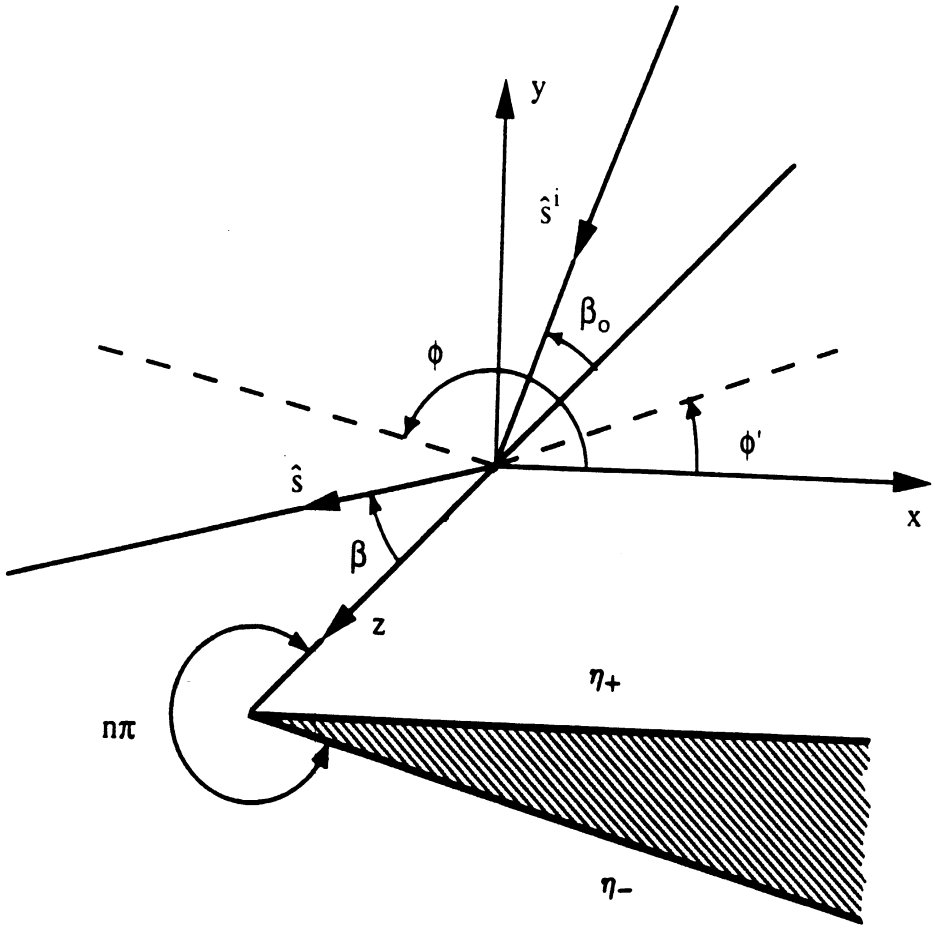

Figure A.1: Edge geometry and angle definitions.

where

$$\hat{s}^i = -\hat{x}\sin\beta_o\cos\phi' - \hat{y}\sin\beta_o\sin\phi' + \hat{z}\cos\beta_o \qquad (A.2)$$

with ϕ' measured from the upper face of the wedge. It is convenient to proceed with just the z-components, e_z and h_z, of the incident field. The rest of the components can be expressed in terms of the z- components, using Maxwell's equations, as

$$e_x = \frac{1}{\sin\beta_o}(\cos\beta_o\cos\phi' e_z + \sin\phi' h_z) \qquad (A.3)$$

$$e_y = \frac{1}{\sin\beta_o}(\cos\beta_o\sin\phi' e_z - \cos\phi' h_z) \qquad (A.4)$$

$$h_x = \frac{1}{\sin\beta_o}(-\sin\phi' e_z + \cos\beta_o\cos\phi' h_z) \qquad (A.5)$$

$$h_y = \frac{1}{\sin\beta_o}(\cos\phi' e_z + \cos\beta_o\sin\phi' h_z) \qquad (A.6)$$

The total field is a sum of the incident field and a reflected field. We assume the z-component of the reflected field to be of the form

$$E_z^r = R_e e_z e^{-jk\hat{s}^r\cdot\bar{r}}, \quad zH_z = R_h h_z e^{-jk\hat{s}^r\cdot\bar{r}} \qquad (A.7)$$

where R_e and R_h are the reflection coefficients for the z- components of the electric and magnetic field, respectively, and $\hat{s}^r$ denotes the propagation direction of the reflected field and is defined as

$$\hat{s}^r = -\hat{x}\sin\beta_o\cos\phi' + \hat{y}\sin\beta_o\sin\phi' + \hat{z}\cos\beta_o \qquad (A.8)$$

The upper face of the wedge satisfies the impedance boundary conditions (at $y = 0$)

$$E_x = \eta_+ Z\, H_z, \quad E_z = -\eta_+ Z\, H_x \qquad (A.9)$$

and using these, the expressions for R_e and R_h can be derived to be

$$R_e e_z = \gamma\left[\left\{(\sin\phi' + \eta_+ \sin\beta_o)\left(\sin\phi' - \frac{\sin\beta_o}{\eta_+}\right) - \cos^2\beta_o \cos^2\phi'\right\} e_z - 2\cos\beta_o \sin\phi' \cos\phi' h_z\right] \tag{A.10}$$

$$R_h h_z = \gamma\left[2\cos\beta_o \cos\phi' \sin\phi' e_z + \left\{(\sin\phi' - \eta_+ \sin\beta_o)\left(\sin\phi' + \frac{\sin\beta_o}{\eta_+}\right) - \cos^2\beta_o \cos^2\phi'\right\} h_z\right] \tag{A.11}$$

with

$$\gamma = \frac{\eta_+}{(1 + \eta_+ \sin\beta_o \sin\phi')(\eta_+ + \sin\beta_o \sin\phi')} \tag{A.12}$$

Now the surface electric and magnetic currents induced on the upper face ($y = 0$) of the wedge are

$$\overline{J}_s = \hat{n} \times \overline{H}^t, \quad \overline{M}_s = -\hat{n} \times \overline{E}^t \tag{A.13}$$

where $\hat{n} = \hat{y}$ for the upper face and $\overline{H}^t$ and $\overline{E}^t$ denote the total field which is the sum of the incident and reflected fields. It is convenient to write these currents in the form

$$z\overline{J}_s = \overline{j} e^{-jk(z\cos\beta_o - x\sin\beta_o\cos\phi')} \tag{A.14}$$

$$\overline{M}_s = \overline{m} e^{-jk(z\cos\beta_o - x\sin\beta_o\cos\phi')} \tag{A.15}$$

where $\overline{j}$ and $\overline{m}$ are determined, using (A.10) - (A.15), to be

$$\overline{j} = 2\gamma \sin\phi'\left[\left\{\cos\beta_o \cos\phi' e_z + \left(\sin\phi' + \frac{\sin\beta_o}{\eta_+}\right) h_z\right\}\hat{x} + \frac{1}{\eta_+}\left\{(\sin\phi' + \eta_+ \sin\beta_o) e_z - \cos\beta_o \cos\phi' h_z\right\}\hat{z}\right] \tag{A.16}$$

$$\overline{m} = -2\gamma \sin\phi' \Bigg[\{(\sin\phi' + \eta_+ \sin\beta_o)e_z - \cos\beta_o \cos\phi' h_z\}\, \hat{x} - \eta_+ \left\{ \cos\beta_o \cos\phi' e_z + \left(\sin\phi' + \frac{\sin\beta_o}{\eta_+} \right) h_z \right\} \hat{z} \Bigg] \qquad (A.17)$$

The far-zone scattered field due to the induced surface currents on the upper face ($y = 0$) of the wedge is given by

$$\overline{E}^s = \frac{jk}{4\pi} \int\int_{S'} \left\{ z\hat{s} \times \left[\hat{s} \times \overline{J}_s(\overline{r}') \right] + \hat{s} \times \overline{M}_s(\overline{r}') \right\} \frac{e^{-jk|\overline{r} - \overline{r}'|}}{|\overline{r} - \overline{r}'|} ds' \qquad (A.18)$$

where the integration is performed over the upper face of the wedge. The $\hat{s}$ unit vector is defined as

$$\hat{s} = \hat{x} \sin\beta_o \cos\phi + \hat{y} \sin\beta_o \sin\phi + \hat{z} \cos\beta_o \qquad (A.19)$$

with ϕ measured from the upper face of the wedge. Assuming now that the edge diffraction is mainly due to the surface currents concentrated on a narrow strip along the edge, the edge diffracted part of the field $\overline{E}^s$ can be written as

$$\overline{E}^d \sim \frac{jk}{4\pi} \int_0 \int_{-\infty}^{\infty} \left\{ z\hat{s} \times \left[\hat{s} \times \overline{J}_s(x', z') \right] + \hat{s} \times \overline{M}_s(x', z') \right\} \cdot \frac{e^{-jk\sqrt{(x-x')^2 + y^2 + (z-z')^2}}}{\sqrt{(x-x')^2 + y^2 + (z-z')^2}} dz'dx' \qquad (A.20)$$

where the absence of the upper limit, in the above integral, on the x' integration denotes that only the asymptotic endpoint contribution at $x' = 0$ is taken into account. Employing the method of stationary phase for the z' integration, one can evaluate the integral in equation (A.20) and the expression for the diffracted field is given by

$$\overline{E}^d \sim -\sqrt{\frac{2}{\pi k \rho \sin\beta_o}}\, \frac{e^{-j\frac{\pi}{4}} e^{-jk\hat{s}\cdot\overline{r}}}{4\sin\beta_o(\cos\phi + \cos\phi')} \left\{ \hat{s} \times (\hat{s} \times \overline{j}) + \hat{s} \times \overline{m} \right\} \qquad (A.21)$$

with $\bar{j}$ and $\overline{m}$ defined in (A.16) and (A.17) respectively. The edge diffraction tensor given in (A.21) can now be transformed into the edge-fixed coordinate system [43] and the resultant diffracted field from the edge is given by

$$\begin{bmatrix} E^d_{\beta_o}(s) \\ \\ E^d_{\phi}(s) \end{bmatrix} \sim -A_1(s) \begin{bmatrix} D^{PO}(\phi,\phi';\beta_o,\eta_+) & D^{PO}_c\left(\phi,\phi';\beta_o,\frac{1}{\eta_+}\right) \\ \\ -D^{PO}_c(\phi,\phi';\beta_o,\eta_+) & D^{PO}\left(\phi,\phi';\beta_o,\frac{1}{\eta_+}\right) \end{bmatrix} \begin{bmatrix} E^i_{\beta'_o}(Q_E) \\ \\ E^i_{\phi'}(Q_E) \end{bmatrix} \tag{A.22}$$

where s is the distance between the diffraction and obervation points and $A_1(s)$ is

$$A_1(s) = \frac{e^{-jks}}{\sqrt{s}} \frac{e^{-j\frac{\pi}{4}}}{\sqrt{2\pi k}} \tag{A.23}$$

The 2×2 matrix in (A.22) represents the physical optics dyadic diffraction coefficient similar to the one presented in chapter five. The components of the diffraction matrix can be expressed as

$$D^{PO}(\phi,\phi';\beta_o,\eta_+) = A_2(\phi,\phi';\beta_o)\left[E(\phi,\phi';\beta_o,\eta_+) + \cos\beta_o F\left(\phi,\phi';\beta_o,\frac{1}{\eta_+}\right)\right] \tag{A.24}$$

$$D^{PO}_c(\phi,\phi';\beta_o,\eta_+) = A_2(\phi,\phi';\beta_o)\left[G(\phi,\phi';\beta_o,\eta_+) + \cos\beta_o H\left(\phi,\phi';\beta_o,\frac{1}{\eta_+}\right)\right]$$

with

$$A_2(\phi,\phi';\beta_o) = (1-\sin^2\beta_o\sin^2\phi')^{-1}(1-\sin^2\beta_o\sin^2\phi)^{-1} \tag{A.25}$$

and

$$\begin{bmatrix} E^\eta \\ \\ G^\eta \end{bmatrix} = - \begin{bmatrix} \cos\phi\cos\phi' & -\cos\beta_o\sin\phi\cos\phi' \\ \\ \cos\beta_o\sin\phi\cos\phi' & \cos\phi\cos\phi' \end{bmatrix} \begin{bmatrix} U^\eta \\ \\ V_\eta \end{bmatrix} \tag{A.26}$$

$$\begin{bmatrix} F_\eta \\ \\ H_\eta \end{bmatrix} = - \begin{bmatrix} \cos\beta_o \sin\phi \sin\phi' & \cos\phi \sin\phi' \\ \\ -\cos\phi \sin\phi' & \cos\beta_o \sin\phi \sin\phi' \end{bmatrix} \begin{bmatrix} U_\eta \\ \\ V^\eta \end{bmatrix} \tag{A.27}$$

where the notation $E(\phi, \phi'; \beta_o, \eta_+) = E^\eta$, $E\left(\phi, \phi'; \beta_o, \frac{1}{\eta_+}\right) = E_\eta$, etc., has been employed for simplicity. The U and the V functions are given by

$$U^\eta = U^{PO}(\phi, \phi'; \beta_o, \eta_+) = \frac{\sin\phi'}{\cos\phi + \cos\phi'}$$

$$(\cos^2\beta_o - \sin^2\beta_o \cos\phi \cos\phi') \frac{(1 - \eta_+ \sin\beta_o \sin\phi)}{(1 + \eta_+ \sin\beta_o \sin\phi')} \tag{A.28}$$

$$V^\eta = V^{PO}(\phi, \phi'; \beta_o, \eta_+) = -\sin\beta_o \cos\beta_o \sin\phi' \frac{(1 - \eta_+ \sin\beta_o \sin\phi)}{(\eta_+ + \sin\beta_o \sin\phi')} \tag{A.29}$$

For the case when the lower face of the impedance wedge is illuminated the above expressions will be applicable with the replacement $\eta_+ \rightarrow \eta_-$, $\phi' \rightarrow n\pi - \phi'$, $\phi \rightarrow n\pi - \phi$ and $\beta_o \rightarrow \pi - \beta_o$.

BIBLIOGRAPHY

BIBLIOGRAPHY

[1] Volakis, J. L., and T. B. A. Senior, "Diffraction by a thin dielectric half plane," *IEEE Trans. Antennas and Propagat.*, Vol. AP-35, pp. 1483-1487, September 1987.

[2] Volakis, J. L., "High frequency scattering by a thin material half plane and strip," *Radio Science*, Vol. 23, pp. 450-462, May-June 1988.

[3] Volakis, J. L., and T. B. A. Senior, "Application of a class of generalized boundary conditions to scattering by a metal-backed dielectric half plane," *Proceedings of the IEEE*, Vol. 77, pp. 796-804, May 1989.

[4] Senior, T. B. A., "Approximate boundary conditions," *IEEE Trans. Antennas and Propagat.*, Vol. AP-29, pp. 826-829, 1981.

[5] Senior, T. B. A., and J. L. Volakis, "Derivation and application of a class of generalized impedance boundary conditions," *IEEE Trans. Antennas and Propagat.*, Vol. AP-37, pp. 1566-1572, December 1989.

[6] Bowman, J. J., T. B. A. Senior and P. L. E. Uslenghi, *Electromagnetic and Acoustic Scattering by Simple Shapes*, New York: Hemisphere Publishing Co., 1987.

[7] Sommerfeld, A., "Mathematische theone der diffraction," *Math. Ann.*, Vol. 47, pp. 317-374, 1986.

[8] MacDonald, H. M., *Electric Waves*, Cambridge: Cambridge Univ. Press, 1902.

[9] Kaminetsky, L., and J. B. Keller, "Diffraction coefficients for higher order edges and vertices," *SIAM J. Appl. Math.*, Vol. 22, pp. 109-134, 1972.

[10] Senior, T. B. A., "Diffraction matrix for a discontinuity in curvature," *IEEE Trans. Antenna and Propagat.*, Vol. AP-20, pp. 326- 333, May 1972.

[11] Maliuzhinets, G. D., "Excitation, reflection and emission of surface waves from a wedge with given face impedances," *Sov. Phys. Doke.*, Vol. 3, pp. 752-755, 1958.

[12] Senior, T. B. A., "Diffraction tensors for imperfectly conducting edges," *Radio Science*, Vol. 10, pp. 911-919, October 1975.

[13] Bucci, D. M., and G. Franceschetti, "Electromagnetic scattering by a half plane with two face impedances," *Radio Science*, Vol. 11, 212-218, January 1976.

[14] Rojas, R. G., "Electromagnetic diffraction of an obliquely incident plane wave field by a wedge with impedance faces," *IEEE Trans. Antennas and Propagat.*, Vol. AP-36, pp. 956-970, July 1988.

[15] Senior, T. B. A., "Solution for a class of imperfect wedge problems for skew incidence," *Radio Science*, Vol. 21, pp. 185-191, March-April 1986.

[16] Senior, T. B. A., and J. L. Volakis, "Scattering by an imperfect right angled wedge," *IEEE Trans. Antennas and Propagat.*, Vol. AP-34, pp. 681-689, May 1986.

[17] Weinstein, A. L., *The Theory of Diffraction and the Factorization Method*, Boulder: Golem Press, 1969.

[18] Rojas, R. G., and Z. Al-hekail, "Generalized impedance/resistive boundary conditions for electromagnetic scattering problems," *Radio Science*, Vol. 24, pp. 1-12, Jan-Feb. 1989.

[19] Vaccaro, V. G., "The generalized reflection method in electromagnetism," *AEU*, Vol. 34, pp. 493-500, 1980.

[20] Vaccaro, V. G., "Electromagnetic diffraction from a right- angled wedge with soft conditions on one face," *Opt. Acta*, Vol. 28, pp. 293-311, March 1981.

[21] Lee, S. W., *McPTD-1.4: A high-frequency RCS computation code based on physical theory of diffraction*, DEMACO, July 1990.

[22] Kane, J., and S. N. Karp, "An accurate boundary condition to replace transition condition at dielectric-dielectric interfaces," Institute of Mathematical Sciences Division of E.M. Research, New York University, New York, N.Y., Research Report EM-153, May 1960.

[23] Karp, S. N., and Karal, Jr., "Generalized impedance boundary conditions with application to surface wave structures," in *Electromagnetic Wave Theory*, part 1, ed. J. Brown, pp. 479-483, New York: Pergamon Press, 1965.

[24] Fock, V. A., "Solution of the problem of propagation of electromagnetic waves along the earth's surface by the method of parabolic equation," *J. Phys. USSR*, Vol. 10, pp. 13-24, 1946.

[25] Senior, T. B. A., "Impedance boundary conditions for imperfectly conducting surfaces," *Appl. Sci. Res.*, Sec. B, Vol. 8, pp. 418-436, 1960.

[26] Senior, T. B. A., "A note on impedance boundary conditions," *Can. J. Phys.*, Vol. 40, pp. 663-665, 1962.

[27] Senior, T. B. A., "Approximate boundary conditions," *IEEE Trans. Antennas and Propagat.*, Vol. AP-29, pp. 826-829, September 1981.

[28] Volakis, J. L., T. B. A. Senior and J. M. Jin, "Derivation and application of a class of generalized impedance boundary conditions - II," University of Michigan Radiation Laboratory Report 025921-1-T, 1989.

[29] Knott, E. F., V. V. Liepa and T. B. A. Senior, "Non-specular radar cross section study," University of Michigan Radiation Laboratory Report 011062-1-F, 1973.

[30] Knott, E. F., V. V. Liepa and T. B. A. Senior, "Non-specular radar cross section study," University of Michigan Radiation Laboratory Report 011764-1-T, 1974.

[31] Medgyesi-Mitschang, L. N., and J. M. Putnam, "Integral equation formulations for imperfectly conductive scatterers," *IEEE Trans. Antennas and Propagat.*, Vol. AP-33, pp. 206-214, February 1985.

[32] Ricoy, M. A., and J. L. Volakis, "Integral equations with reduced unknowns for the simulation of two-dimensional composite structures," *IEEE Trans. Antennas Propagat.*, Vol. AP-37, pp. 362-372, March 1989.

[33] Jin, J. M., and V. V. Liepa, "Application of hybrid finite element method to electromagnetic scattering from coated cylinders," *IEEE Trans. Antennas Propagat.*, Vol. AP-36, pp. 50-54, January 1988.

[34] Wang, N., "Regge poles, natural frequencies, and surface wave resonance of a circular cylinder with a constant surface impedance," *IEEE Trans. Antenna Propagat.*, Vol. AP-30, November 1982.

[35] Wang, N., "Electromagnetic scattering from a dielectric coated circular cylinder," *IEEE Trans. Antenna Propagat.*, Vol. AP-33, September 1985.

[36] Wait, J. R., and A. M. Conda, "Pattern of an antenna on a curved lossy surface," *IEEE Trans. Antennas Propagat.*, Vol. AP-6, pp. 348- 359, October 1958.

[37] Wait, J. R., and A. M. Conda, "Diffraction of electromagnetic waves by smooth obstacles for grazing angles," *J. Res. Bur. Stand.*, Vol. 63D, pp. 181-197, 1959.

[38] Pathak, P. H., "An asymptotic Analysis of the scattering of plane waves by a smooth convex cylinder," *Radio Sci.*, Vol. 14, pp. 419-435, 1979.

[39] Keller, J. B., "Geometrical theory of diffraction," *J. Opt. Soc. Am.*, Vol. 52, pp. 116-130, 1962.

[40] Keller, J. B., "Diffraction by a convex cylinder," *IEEE Trans. Antenna Propagat.*, Vol. AP-24, pp. 312-321, 1956.

[41] Kim, H., and N. Wang, "UTD solution for electromagnetic scattering by a circular cylinder with thin lossy coatings," *IEEE Trans. Antenna Propagat.*, Vol. AP-37, pp. 1463-1472, November 1989.

[42] Felson, L., and N. Marcuvitz, *Radiation and Scattering of Waves*, Prentice Hall, 1973.

[43] Kouyoumjian, R. G., and P. H. Pathak, "A uniform geometrical theory of diffraction for an edge in a perfectly conducting surface," *Proc. IEEE*, Vol. 62, pp. 1448-1461, November 1974.

[44] Logan, N. A., and K. S. Yee, *Electromagnetic Waves*, edited by R. E. Langer, Madison: University of Wisconsin Press.

[45] Pearson, L. W., "A scheme for automatic computation of Fock-type integrals," *IEEE Trans. Antenna Propagat.*, Vol. AP-35, pp. 1111-1118, October 1987.

[46] Tuck, O. A., "A simple 'Finlon-trapezoid' rule," *Math. Comp.*, Vol. 21, pp. 239-241, 1967.

[47] Ricoy, M. A., and J. L. Volakis, "Derivation of generalized transition/boundary conditions for planar multiple layer structures," *Radio Sci.*, Vol. 25, pp. 391-405, July-August 1990.

[48] Volakis, J. L., and H. H. Syed, "Application of higher order boundary conditions to scattering by multilayered coated cylinders," *J. of Electromagnetic Waves and Applications*, Vol. 4, pp. 1157-1180, 1990.

[49] Singaraju, B. K., D. V. Giri and C. E. Baum, "Further development in the application of contour integration to the evaluation of the zero of analytical functions and relevant computer programs," Math. Note 42, March 1976.

[50] Herman, M. I., J. L. Volakis and T. B. A. Senior, "Analytic expressions for a function occuring in diffraction theory," *IEEE Trans. Antenna Propagat.*, Vol. AP-35, pp. 1083-1086, September 1987.

[51] Ricoy, M. A., and J. L. Volakis, "Diffraction by a symmetric material junction simulated with GSTC," *IEEE Trans. Antenna Propagat.*, Vol. AP-40, 1992.

[52] Senior, T. B. A., "Generalized boundary and transition conditions, and the question of uniqueness," submitted for publication.